Les nouvelles stratégies de contrôle d'onduleurs pour un système électrique 100% interfacé par électronique de puissance

Guillaume Denis

N° d'ordre : 336

Centrale Lille

Thèse

présentée en vue

d'obtenir le grade de

Docteur

En

Spécialité: Génie Électrique

Par

Guillaume Denis

Doctorat délivré par Centrale Lille

Titre de la thèse:

From grid-following to grid-forming:

The new strategy to build 100 % power-electronics interfaced transmission system with enhanced transient behavior

Les nouvelles stratégies de contrôle d'onduleurs pour un système électrique 100% interfacé par électronique de puissance

Soutenue le 23 Novembre 2017 devant le jury d'examen:

M. Thierry Van Cutsem	Professeur, FNRS, Université de Liège	**Président**
M. Istvan Erlich	Professeur, IEPS, Université de Duisbourg-Essen	**Rapporteur**
M. Antonello Monti	Professeur, RWTH Université d'Aix-la-Chapelle	**Rapporteur**
Mme. Vera Paiva Da Silva	Docteur, EDF Paris Saclay	**Examinatrice**
M. Jon Are Suul	Docteur, SINTEF Trondheim	**Examinateur**
M. Thibault Prevost	Research Engineer, RTE R&D Versailles	**Membre invité**
M. Xavier Guillaud	Professeur, L2EP, École Centrale Lille	**Directeur de thèse**
M. Xavier Kestelyn	Professeur, L2EP, ENSAM Lille	**Co-Encadrant**

Thèse préparée dans le laboratoire L2EP

Ecole Doctorale SPI 072 (Lille I, Lille III, Artois, ULCO, UVHC, Centrale Lille)

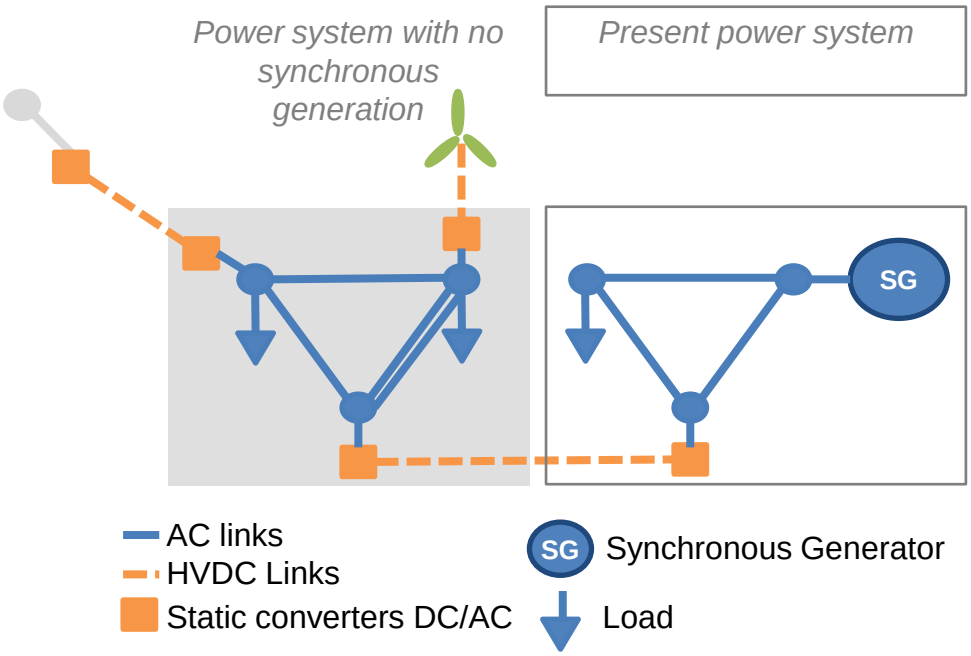
Power system with no synchronous generation
Present power system
SG
AC links
HVDC Links
Static converters DC/AC
SG
Synchronous Generator
Load

Abstract

Analysis tool & control design method of parallel grid-forming converters for proper operation of power system

The present work on *Grid-forming converters*, takes place in the context of renewable energy development in power systems. Prospective scenarios of 100% of renewables are getting more and more realistic. In those scenarios, wind power and solar photovoltaics are expected to supply more than 50% of annual electricity consumption, and interconnection with HVDC links are more frequent. These scenarios have been studied to take into account the variability of renewables in assessing the needs for power reserve and storage in future grids. Here, the main concern is related to the technical operations of such systems. As wind power, solar photovoltaics and HVDC are interfaced to the transmission grid with power-electronics, can the system be operated in the extreme case where the load is fed only through static converters?

The power system behavior has been based on synchronous generators physical characteristics for years. Driving a power system only based on power electronic interfaced generation is a tremendous change of the power system paradigm that must be clearly understood by transmission grid operators. These questions have barely been treated at transmission level and deserve a specific investigation regarding the original issues, system stability conditions, designing tools and analysis methods.

The traditional "grid-feeding" control strategy of inverters exhibits a stability limit when their proportion becomes too important in the power system supply. To cope with the extreme case of a power system with only converter based generators, the inverter control strategy must be turned into a "parallel grid-forming" strategy.

This thesis first analyses the bulk power system needs, proposes the requirements for “parallel grid-forming” converters and describes the associated challenges. Accordingly, the thesis describes a method for designing a stable autonomous synchronization controls so that grid-forming sources can operate in parallel with a good level of reliability. Then, a method is proposed to design a voltage control for a grid-forming PWM source taking into account the limited dynamic of powerful converters. The robustness of the solution is discussed for different configuration of the grid-topology, with the impedance-based method. A current limiting strategy is presented to solve the current sensitivity issue of grid-forming converters, subject to different stressing events of the transmission grid. The ideas developed on a single converter are then applied on small grids with a limited number of converters to allow a physical interpretation on the simulation results.

Keyswords : Converters, Distributed control, Overcurrent protection, Power system dynamic stability, Power system transients, Droop control, Voltage control.

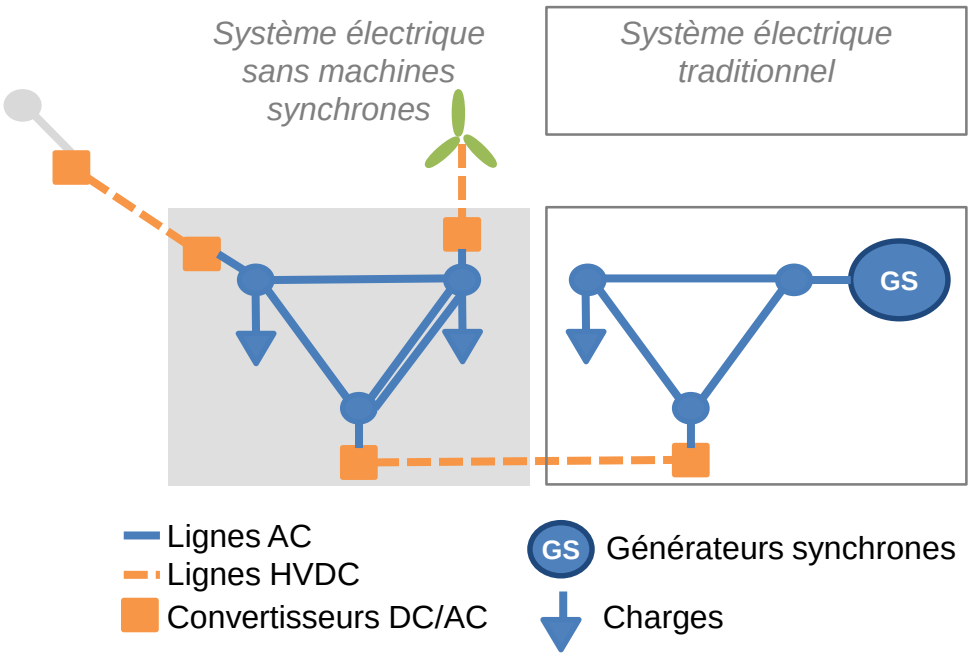
Système électrique sans machines synchrones
Système électrique traditionnel
GS
Lignes AC
Lignes HVDC
Convertisseurs DC/AC
GS
Générateurs synchrones
Charges

Résumé étendu

Outils d'analyse & méthode de construction de convertisseurs "Grid-forming" contrôlés en parallèle pour un fonctionnement sûr du système électrique

A l'échelle du réseau de transport, la majorité des ouvrages raccordant des productions éoliennes, photovoltaïques, et les liaisons à courant continu s'interface avec des convertisseurs statiques de tension type VSC. Alors que la capacité installée des VSC s'accroît, les opérateurs du réseau de transport, comme RTE, s'inquiètent de potentielles instabilités soulevées par leur fonctionnement. Dans les systèmes électriques les plus concernés, comme le réseau irlandais, une limite règlementaire fixe à 60 % la participation maximale de cette génération non-synchrone à la demande globale. L'origine de ces instabilités est liée à la stratégie de contrôles de type "grid-following". Ces contrôles équipent la quasi-totalité des VSC connectés au réseau de transport actuellement. Ils s'appuient sur une mesure de l'amplitude, de la fréquence et de la phase de la tension au point de raccordement, pour injecter un courant synchrone dont le déphasage avec la tension mesurée fixera les échanges de puissances actives et réactives avec le réseau. Dans le cas extrême où 100% de la capacité de génération électrique serait interfacée par des VSCs, aucun dispositif ne serait responsable du maintien de la tension ou de la fréquence. Le comportement du système serait imprévisible. Plutôt qu'améliorer les contrôles "grid-following" existant pour augmenter la pénétration de VSCs, on propose ici une approche opposée: peut-on construire directement un système électrique 100% VSC, en s'affranchissant du comportement dicté par les générateurs synchrones.

Une telle situation paraît hypothétique dans un horizon temporel proche, au regard du développement actuel du réseau de transport. Mais il n'est pas exclu que localement, ou temporairement, une poche de réseau ne se retrouve alimenté que par des sources interfacées, en particulier après

la perte du dernier lien synchrone avec le reste du réseau. A supposer que cette poche isolée dispose de suffisamment d'adéquation entre sa capacité productive, ses réserves d'énergie, et sa demande, comment doter les VSCs d'une fonction "parallel grid-forming" qui leur permettrait de faire fonctionner le système électrique en totale autonomie? Répondre à cette question nécessite à définir ce qu'on attend d'une fonction "parallel grid-forming" et ouvre une interrogation fondamentale sur la nature des sources électriques dont le système a besoin.

Définition du problème, état de l'art

La fonction "grid-forming", donne de la "rigidité" au caractère source de tension, telle qu'elle est exigée du réseau de transport. Ce caractère source de tension assure que les unités de production et les charges puissent être connectées en parallèle. Ce caractère est d'autant plus affirmé, ou fort, qu'il permet de maintenir l'amplitude et la fréquence de l'onde de tension, quelques soient les transits de courant auquel le réseau est soumis. A ce jour, ce sont les générateurs synchrones qui apportent au réseau ce caractère source de tension, en limitant la dynamique de la tension en amplitude et en fréquence, comme l'illustre la figure 1. En réponse à la connexion d'une charge active, la chute initiale de fréquence est limitée par l'inertie mécanique H du générateur (fig. 1.a). Cette limite se quantifie usuellement par le "rate-of-change of frequency", $ROCOF = \frac{1}{2H} \approx 0.1\, rad.s^{-1}.(p.u.)^{-1}$. La chute d'amplitude de tension transitoire suivant la connexion d'une charge réactive est limitée par les faibles valeurs de réactances transitoire $x^{'}$ et sous-transitoire $x^{''}$ (fig. 1.b). Cette rigidité de l'amplitude peut être caractérisée par la puissance de court-circuit $S_{cc} = \frac{V_0}{x^{'}} \approx 5\, p.u.$ Ces caractéristiques sont permises par la très forte capacité de surcourant des alternateurs (fig. 1.c).

D'autre part, les rotors des générateurs synchrones convergent naturellement à une vitesse identique lorsqu'ils opèrent en parallèle. Ils partagent donc une fréquence électrique commune sur l'ensemble du réseau, en régime permanent. Un contrôle de leur puissance mécanique "en droop" fait réagir les générateurs à un écart statique global de la fréquence. Ils compensent alors la variation de la demande qui est responsable de cet écart, dans la mesure de leurs capacités nominales.

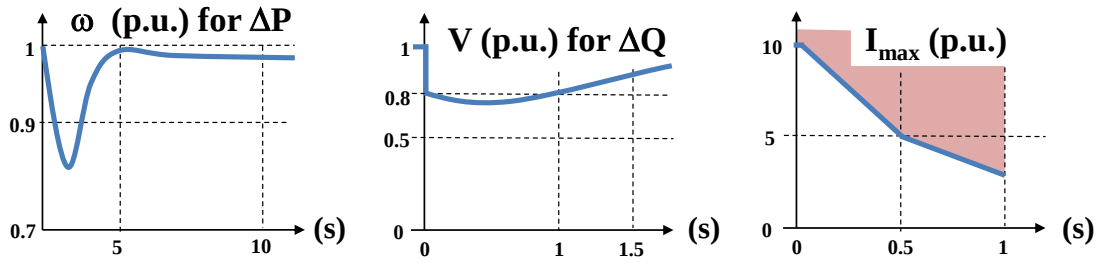

(a) Dynamique de la fréquence (b) Dynamique de l'amplitude (c) Capacité de surcourant

Figure 1 – La fonction grid-forming du générateur synchrone

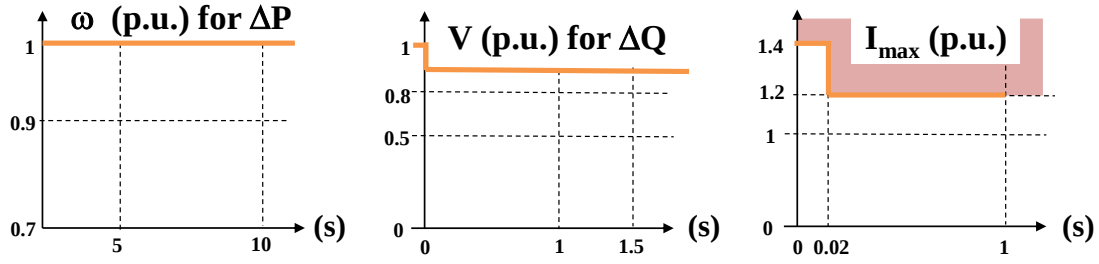

(a) Dynamique de la fréquence (b) Dynamique de l'amplitude (c) Capacité de surcourant

Figure 2 – Les caractéristiques du VSC en open-loop

Un convertisseur de tension VSC module une tension continue, supposée idéale, en une tension alternative triphasée de fréquence et d'amplitude choisies. Théoriquement, ce fonctionnement lui confère un caractère source de tension meilleur que celui du générateur synchrone comme le décrit la figure 2. Contrôlé en boucle ouverte, la tension de sortie du VSC présente un ROCOF possiblement nul (fig. 2.a), une tension uniquement affectée par l'impédance du filtre de sortie, soit une puissance de court-circuit théorique de $\frac{V_0}{x_f} \approx 8\,p.u$ (fig. 2.b). En pratique, ces capacités sont limitées par un surcourant admissible dans les semi-conducteurs qui dépasse à peine le courant nominal (2.c). Le contrôle du VSC en boucle ouverte le rendrait très exposé aux surcourants.

Par ailleurs, il serait illusoire de donner une référence identique fréquence à chaque convertisseur, qui ne dévierait pas dans le temps. Or, il est impossible de faire fonctionner un système électrique avec des sources de fréquences différentes. Dès lors, seul un contrôle adapté de l'amplitude de la tension et de la fréquence permettrait de faire des VSC des sources grid-forming autonomes fonctionnant en parallèle. Il reste alors à en définir les dynamiques. Enfin, on ambi-

tionne qu'un VSC grid-forming soit capable de partager la charge selon la même loi statique que les générateurs synchrones en embarquant la même loi de droop.

La présente thèse poursuit donc l'objectif de répondre aux questions suivantes:

- Comment un contrôle synchronisant des VSCs redéfinit-il la dynamique de fréquence du système?
- Comment la dynamique de contrôle de la tension de sortie des VSCs doit-elle être fixée?
- Comment peut-on protéger le VSC des larges appels de courant sans un surdimensionnent coûteux?

Les solutions apportées doivent de plus tenir compte des contraintes suivantes:

- La compatibilité avec les caractéristiques du réseau de transport: Dispositifs de haute puissance, environnement et topologie de réseau variable, évènements réseau critiques.
- La simplicité des solutions sera privilégiée en raison de la vocation industrielle de leur application.
- L'indépendance de toute mesure de fréquence (ex: PLL), ou d'un signal GPS.

Des solutions de contrôle "grid-forming" existent dans la littérature, principalement pour trois types d'applications: les microgrids, ces réseaux réduits à l'échelle d'un navire ou d'un quartier, la connexion "weak-grid", lorsque le point de raccordement est éloigné de la production, et enfin, dans les parcs éoliens offshores. Comme en témoigne le tableau suivant, aucune des solutions disponibles n'est aujourd'hui suffisante pour couvrir l'ensemble des objectifs et des contraintes listés plus haut.

La problématique émergente de ce premier travail d'analyse consiste à trouver comment combiner les trois composantes fondamentale de la fonction grid-forming, à savoir: la synchronisation des sources, le contrôle de tension du VSC dans un environnement variable, et la protection contre les surcourants en transitoire.

	Microgrids	Weak grid connection	Offshore Windfarm
Synchronization (with no PLL)	✔	✔	✖
Flexible Voltage Control (Grid-connected/standalone)	✔	✖	✔
Protection against large disturbances	✔	✖	✔
Compliance with transmission grid level	✖	✔	✔

✔:Aspect treated in the literature
✖:Aspect not treated in the literature

Table 1 – Les sous-fonctions des VSCs grid-forming dans la littérature

Synchronisation de sources de tension pour opération en parallèle

Pour élaborer les conditions nécessaire et suffisante à la synchronisation des sources, un système simple de deux sources de tension idéales a été étudié. La dynamique du système a été modélisée par l'expression linéarisée des flux de puissances entre les sources: les variations de puissances active $\Delta P_1(s)$ et réactive $\Delta Q_1(s)$ sont liées aux variations de différence d'angles intantanés entre les sources $\Delta\delta = \Delta\theta_1 - \Delta\theta_2$ et à la variation de l'amplitude instantanée de la tension $\Delta E_1(s)$. Le couplage entre les grandeurs est exprimée par une matrice de fonction de transfert:

$$\begin{bmatrix} \Delta P_1(s) \\ \Delta Q_1(s) \end{bmatrix} = \begin{bmatrix} F_{P\delta 0}(s) & F_{PE0}(s) \\ F_{Q\delta 0}(s) & F_{QE0}(s) \end{bmatrix} \begin{bmatrix} \Delta\delta(s) \\ \frac{\Delta E_1(s)}{E_1 0} \end{bmatrix}$$

De cette analyse, il apparaît que des variations rapides d'angles et d'amplitudes des sources produisent indistinctement des varations de puissances active et réactive. Le découplage entre les puissances active et réactive est obtenu lorsque la dynamique de variation de l'angle et de l'amplitude de la tension est modérée. Dans ce but, un filtrage de puissance avec une fréquence de coupure 10 fois inférieure à la fréquence fondamentale est introduit. Pour assurer la synchronisation, le contrôle de la fréquence par la puissance active se présente comme sur la fig. 3.

Le gain m_{p1} fixe la relation statique puissance-fréquence dans les même proportions que celles des générateurs synchrones traditionnels ce qui assure l'interopérabilité des sources pour

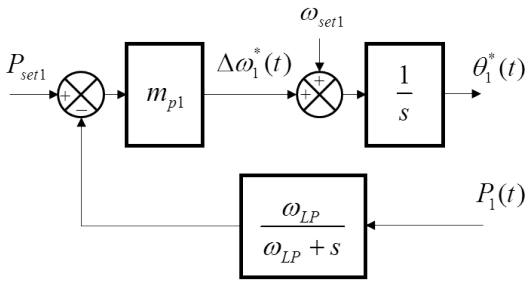

Figure 3 – Contrôle en droop de la fréquence pour les opérations parallèle de VSCs

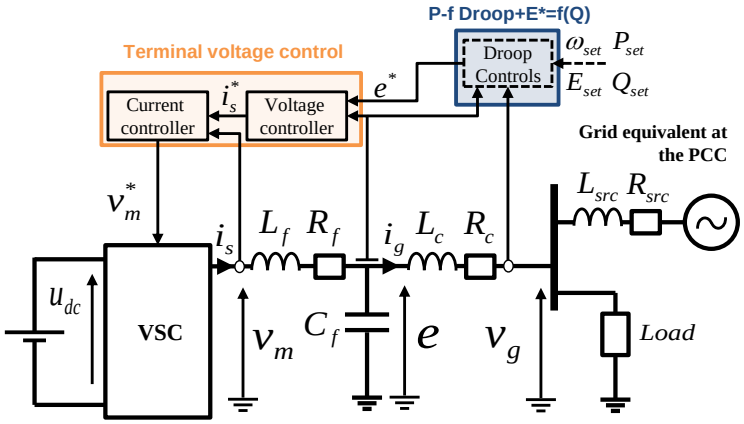

Figure 4 – Contrôle complet d'un VSC-PWM par boucles cascadées.

le partage de la charge. La fréquence de coupure du filtre ω_{LP} fixe quant à elle la dynamique de la fréquence de consiqne des VSCs selon des critères de stabilité du système interconnecté.

Contrôle de tension d'un VSC-PWM

Le système électrique exige que le VSC grid-forming soit capable de contrôler la tension, qu'il soit connecté à une charge passive ou à un réseau d'une puissance variable. D'un autre côté, les VSCs ont des limitations dynamiques à forte puissance qui contraignent le design de son hardware et de ses contrôles. En conséquence, le dimensionnement du système et le paramétrage d'un contrôle par boucle cascadé est proposé comme l'illustre la figure 4.

Le paramétrage du contrôleur s'appuie sur un découplage temporel entre les différentes boucles. Les performances sont satisfaisantes lors de l'alimentation d'une charge isolée, mais ne sont pas robustes lorsque que le VSC contrôlé est connecté à un réseau équivalent de forte

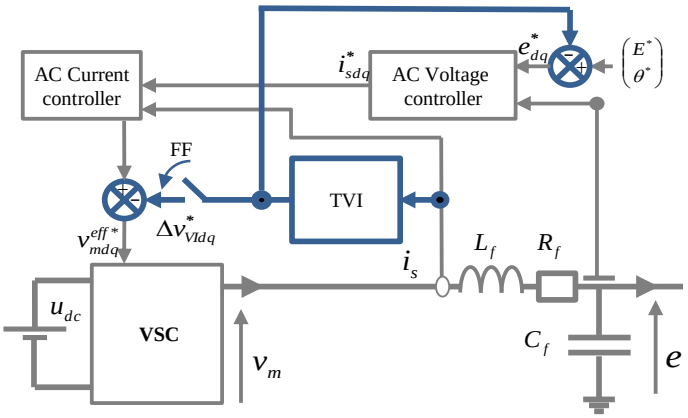

Figure 5 – Contrôle complet d'un VSC-PWM par boucles cascadées.

puissance. L'instabilité qui peut apparaître dans cette configuration "grid-connected" est analysée avec deux méthodes différentes. Par analyse du lieu des pôles du système, et par analyse fréquentielle de l'impédance équivalente formée par le filtre et le contrôleur. Cette approche circuit aide à appréhender le comportement d'un VSC contrôlé et connecté au réseau.

Amélioration du comportement transitoire par nouvelle stratégie de limitation du courant

Le contrôle de la tension par boucles cascadées permet une limitation explicite du courant de sortie de l'onduleur. Néanmoins, la saturation du courant de référence rend inopérant le contrôle de la tension et du droop en puissance nécessaire à la synchronisation. En conséquence, le système perd sa stabilité après un large transitoire. Pour palier ce problème, une impédance virtuelle (TVI) activable sur seuil de courant, a été ajoutée. Ainsi, dès que le courant de sortie de l'onduleur dépasse sa limite, la tension de référence de l'onduleur baisse très rapidement pour le protéger durant les transitoires exigeant. Un schéma de fonctionnement est proposé en figure 5.

La stabilité transitoire apportée par cette solution est validée par différentes simulations EMT sur des réseaux d'un, deux et trois onduleurs fonctionnant, en autonomie, sur un réseau de transport typique.

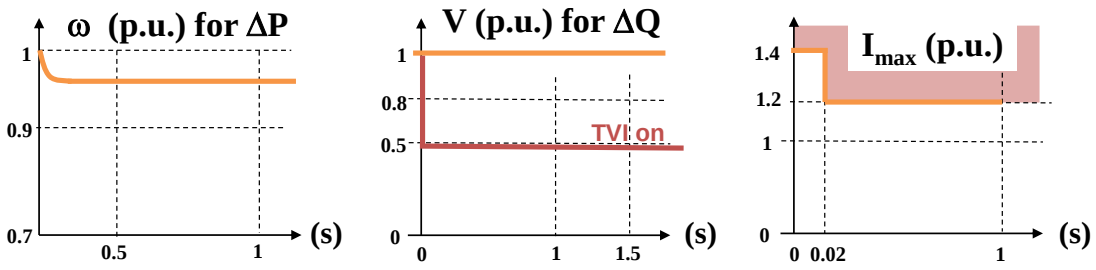

(a) Dynamique de la fréquence (b) Dynamique de l'amplitude (c) Capacité de surcourant

Figure 6 – Les caractéristiques du VSC en parallel grid-forming

Conclusions

Les présents travaux ont permis de définir un contrôle "parallel grid-forming" pour le VSC qui remplit à la fois les fonctions exigées par le système électrique et les contraintes de l'onduleur. Le comportement de cette source est synthétisé schématiquement sur la figure 6. Ces contrôles donnent une nouvelle dynamique de fréquence lors de la connexion d'une charge unitaire (fig. 6.a), une nouvelle dynamique d'amplitude de tension qui diffère selon que l'onduleur est loin de ses limites, ou que l'onduleur atteint son courant maximum (fig. 6.b). On tire alors bénéfice de la rigidité de la source de tension apportée par le VSC tout en le protégeant dans les cas critiques.

En particulier, cette thèse met en évidence la limitation dynamique que doit observer le contrôle de la fréquence pour garantir la stabilité de la synchronisation. Pour le design du contrôle d'amplitude de tension, l'accent est porté sur la nécessité de minimiser les interactions négatives que le contrôle local pourrait avoir avec le reste du réseau. Pour cela la modélisation de l'impédance équivalente au filtre et au contrôle est proposée afin d'adopter une approche circuit qui donne aisément la sensibilité de la tension aux perturbations du réseau. Par ailleurs, la propriété de passivité du contrôle apparaît comme désirable car elle assure une condition suffisante de stabilité. Enfin, la TVI apporte une réponse au compromis vitesse-stabilité de la synchronisation en offrant une réponse lente de la fréquence aux petites perturbations du réseau, mais une réaction rapide lors des larges transitoires qui risqueraient d'endommager le matériel.

Mots-clés : Convertisseur, Contrôle distribué, Protection contre les surcourants, Stabilité dynamique du système électrique, Transitoires du système électrique, Source de tension, Control de tension.

Acknowledgements

This thesis is the result of three-years research activities conducted under the collaboration of the laboratory of electrical engineering of Lille, and RTE, the french transmission system operator. This work would not have been possible without the support of many people.

First of all, I would like to thank Patrick Panciatici, the scientific adviser of RTE, who gave me the opportunity to candidate with such advanced and timely topic. His expertise and passionate discussions have been a deep source of inspiration during three-years. Also, I express my entire gratitude to my PhD supervisor, Professor Xavier Guillaud, for his unfailing patience with my numerous questions, his understanding, and most important, his guidance to emphasize the ideas we supported.

A special thanks goes to Pr. Xavier Kestelyn for providing so much support during the first years, investigating with me the fundamental concepts of power system through lengthy discussions, and teaching me how to to get a foot in the door of research activities.

I also would like to thank my Ph.D. examination committee members, Prof. Thierry Van Cutsem for accepting to preside the jury, Prof. Antonello Monti, Dr. Vera Paiva Da Silva, Dr. Jon Are Suul, for the sincere interest you showed for my work and the highly constructive questions, comments and discussions you formulated on my results. Your remarks improved significantly my understanding of the topic. Particularly, I am truely indebted to Prof. Istvan Erlich who hosted me in his Institute of Electrical Power System, as one of its own student. I really appreciated our scientific debates on synchronization process and I whish I could continue these fruitful exchanges in the future.

→

Another big thanks goes to the members of L2EP lab, who accepted my monthly visits in Lille as if I was a permanent member. Special attention for the Phd Student office where Juliette, Julian, Jérôme, Quentin, Taoufik who created a pleasant atmosphere to share the joyes and the pitfalls of doctoral studies, but also for Moez, Frederic and Hicham and the football team.

My biggest thanks go to the RTE R&D team who accompanied for the last three-years. More than simple colleagues, Marie-Sophie, Thibault, Florent, Carmen, Marjorie, Phillipe, and Sébastien followed my work closely. I express my heartfelt appreciation for their involvement in promoting my results, offering a critical eyes on my questions. The role of Thibault Prevost was particularly fundamental for driving the success of my doctoral studies.

Last but not least, I would like to thank my parents, my sister, and my close family for their continual support even when the difficulties of the exercise affected my mood. Along with my family, I always am thankful to my closest friends, the Paradisios, for providing me confidence and pride. Special mention to Margaux who had the courage to proofread part of this manuscript.

Contents

1 Introduction **33**

1.1 Background and motivation 33

1.2 Scope of the Thesis 38

1.3 Thesis contribution & outline 40

2 Problem statement: Challenges of a full VSC-interfaced transmission grid system **43**

2.1 Analysis of large power systems needs 44

2.1.1 Technical needs from the transmission grid infrastructure 44

2.1.2 Technical needs for good quality electricity 45

2.1.3 Technical needs from transmission grid operating constraints 47

2.1.4 Synthesis on demanded functions to electrical sources forming a transmission grid 49

2.2 Power system based on synchronous generators electrical sources 51

2.2.1 The grid-forming capability of synchronous generators 52

2.2.2 Parallel grid-forming capability of synchronous generators 60

2.2.3 Conclusion on the parallel grid-forming capability of synchronous generators 65

2.3 Power system based on VSC-based electrical sources 66

2.3.1 Model of a Voltage Source Converter 66

2.3.2 The grid-forming capability of a VSC 68

2.3.3 Parallel grid-forming capability of VSC 74

2.3.4 Conclusion on the parallel grid-forming capability of VSCs 75
2.4 State-of-the-art of grid-forming VSC 76
2.4.1 Grid-forming VSCs in small, medium-voltage systems 77
2.4.2 Grid-forming VSCs in weak grid or low inertia power system 78
2.4.3 Grid-forming VSCs in Offshore windfarm park 80

3 Synchronization and power exchange control of two voltage-sources on a transmission grid 83

3.1 Dynamic modeling of a full VSC-based power system 84
3.1.1 Voltage sources model 85
3.1.2 AC Transmission line model 85
3.1.3 Power system loads model 87
3.1.4 Power system dynamic representation 88
3.1.5 Power flows between two voltage-sources 89
3.1.6 Conclusions on power flow dynamics on the power system 94
3.2 Synchronization one voltage source with the other fixed voltage source ("infinite bus") 96
3.2.1 Structure of the active power feedback control 97
3.2.2 Synchronization mechanism of the active power feedback control 98
3.2.3 Small-signal stability of the synchronization 100
3.3 Synchronization of two voltage sources and link with droop control 103
3.3.1 Static analysis: from double power-synchronization to droop control . . 103
3.3.2 Small-signal stability of the droop-controlled system 106
3.3.3 Physical considerations around the droop control parameters 108
3.3.4 Reactive power droop control 111
3.4 Toward generalization of small-signal and large-signal stability of multiple droop-controlled VSCs, in a scalable, radial or meshed grid 112
3.4.1 Small-signal stability studies based on linearized models of multiple-converters network 112

3.4.2 Singular perturbation techniques for non-linear modeling and large-signal stability studies . . . 114
3.5 Transient load-sharing capabilities of droop-controlled voltage-sources . . . 117
3.5.1 Transient load-sharing during a line tripping in the transmission grid . 117
3.5.2 Limits of available solutions to improve the transient-load sharing . . . 122

4 Building a grid-forming VSC-PWM for the transmission grid system 125
4.1 Design requirements and method . . . 126
4.1.1 Design requirements of grid-forming control from PWM-VSC perspective 126
4.1.2 Design requirements of grid-forming control from power system perspective . . . 128
4.1.3 VSC grid-forming capability design method . . . 129
4.2 Design of the VSC output filter . . . 129
4.2.1 Criterion for rated power delivery . . . 131
4.2.2 Criterion of PWM harmonics attenuation . . . 133
4.2.3 Criterion of limitation of output current ripples . . . 134
4.2.4 Filter design synthesis . . . 134
4.3 Design of the terminal voltage control in closed loop . . . 136
4.3.1 Filter model in dq-frame . . . 136
4.3.2 Design of the cascaded structure of the VSC voltage control . . . 138
4.3.3 Setting the dynamic performance of the cascaded voltage and current loop 141
4.3.4 Current limitation in cascaded loop . . . 145
4.3.5 Conclusion on the voltage control design . . . 147
4.4 Robustness of the voltage control in various grid configurations . . . 149
4.4.1 Grid stiffness and short-circuit capacity definition . . . 149
4.4.2 Small-signal stability limit of the voltage controlled VSC in various grid-connected situations . . . 150
4.4.3 Improving the robustness against grid stiffness with the voltage feedforward gain . . . 151
4.4.4 Conclusion on VSC voltage control robustness . . . 154

4.5 Analysis of the control robustness through the impedance-based approach . . . 155
4.5.1 Concept of passivity of the equivalent output impedance 155
4.5.2 Output impedance shape and passivity of a VSC in open-loop 157
4.5.3 Output impedance shape and passivity of voltage-controlled VSC in closed-loop 164
4.5.4 Interaction between the closed-loop output impedance and the grid impedance 167
4.5.5 Output impedance shaping to improve its passivity 170
4.5.6 Conclusion on impedance-based approach 173

5 Enhancing the large-signal stability of parallel grid-forming converters 177
5.1 Overcurrent limiting strategy for improving the VSC transient stability 178
5.1.1 The loss of transient stability with conventional current limitation . . . 178
5.1.2 Threshold-virtual impedance concept for limiting the overcurrent 179
5.1.3 Implementation of the Threshold-virtual impedance in the parallel grid-forming VSC 185
5.1.4 Conclusion on the new overcurrent limiting strategy 190
5.2 Simulation EMT of a two-VSCs parallel grid-forming system 190
5.2.1 System model and parameters 190
5.2.2 Response to a line switch, load change, and power setpoint modification 193
5.2.3 Response to islanding 195
5.3 Simulation EMT of a three-VSCs parallel grid-forming system in a meshed grid 195
5.3.1 System model and parameters 198
5.3.2 Response to line switches and power setpoints modification 198
5.3.3 Response to a VSC-based generator outage 199

6 Conclusion and perspectives 205
6.1 Summary and discussion around the achievements 205
6.2 Perspectives 209

A Appendix 213
A.1 Electromechanical model of a synchronous generator 213

A.1.1 The mechanical equation 213
A.1.2 The electrical equations 214
A.1.3 Steady-state representation of the synchronous generators at fixed speed 215
A.1.4 Transient electrical representation of the synchronous generators at fixed speed 217
A.2 Impedance-based Nyquist criterion 218

List of Figures

1 La fonction grid-forming du générateur synchrone 9

2 Les caractéristiques du VSC en open-loop 9

3 Contrôle en droop de la fréquence pour les opérations parallèle de VSCs 12

4 Contrôle complet d'un VSC-PWM par boucles cascadées. 12

5 Contrôle complet d'un VSC-PWM par boucles cascadées. 13

6 Les caractéristiques du VSC en parallel grid-forming 14

1.1 Annual electrical energy consumption share for a 90% of renewables in US in 2050 [1]. 34

1.2 Annual electrical energy consumption share for a 100% of renewables in France in 2050 [2]. 34

1.3 Wind penetration duration curves for nominally 27% annual energy system. Source: NSPI Renewable Integration [3]. 35

1.4 Representation of the present power system loosing its last synchronous link. . 36

2.1 The considered grid-connected synchronous generator system with the primary mechanical source. The electromotive force is produce along the q-axis. 51

2.2 Stator windings and rotor windings relative positions. 52

2.3 Terminal phase-voltages of the synchronous generator following a load connection. The curves are plotted after the park transform of eq. (2.7) 55

2.4 Simplified scheme of the long-term control of the synchronous generator terminal voltage 57

2.5 The output phase-current of the synchronous generator following a three-phase short-circuit. . . . 58

2.6 Simplified scheme of the long-term control of the rotor speed of synchronous generators . . . 61

2.7 Details of the speed-governor controller with an integration for non-error control in steady-state. . . . 61

2.8 Details of the speed-governor controller with an integration for non-error control in steady-state. . . . 64

2.9 Properties of the grid-forming function of a synchronous generator . . . 65

2.10 The considered grid-connected VSC system comprises a DC primary source, a DC capacitor, and a VSC. . . . 66

2.11 Two main layout of switches in VSC for two modulation types. . . . 67

2.12 A VSC modeled by a modulated voltage source behind the filter inductance (choke). . . . 68

2.13 The terminal phase-voltages of the VSC following a load connection. . . . 70

2.14 The output phase-current of the synchronous generator following a three-phase short-circuit. . . . 72

2.15 2 VSCs represented by three-phase voltage sources behind inductive filters, connected at their terminal. . . . 75

2.16 Properties of the VSC in open-loop . . . 76

2.17 Offshore wind farms linked through an HVDC to the continental transmission grid [4] . . . 79

3.1 Basic VSC-based power system . . . 84

3.2 Basic VSC-based power system . . . 87

3.3 Basic VSC-based power system dynamic model . . . 88

3.4 Rotating dq-frame compared relative to the natural frame abc. . . . 89

3.5 Comparison between the linearized model of active power to voltage-angle difference dependency $F_{P\delta 0}(s)$ implemented in Matlab, and an EMT simulation of the same system, following a voltage-angle difference step. $L\omega_n = 0.45$ p.u. and $R = 0.025$ p.u. 92

3.6 Frequency-response comparison of $F_{P\delta 0}(s)$ and $F_{PE0}(s)$ at different operating points with $L\omega_n = 0.45$ p.u. and $R = 0.045$ p.u. 95

3.7 Active power feedback control 96

3.8 Small-signal representation of the active power transfer in closed loop between the controlled voltage source 1 with power-frequency droop control. 98

3.9 Comparison of margins on the open-loop transfer voltage angle difference response (3.24). Gain margins on the upper axis and the phase margins on the lower axis are marked with dots. Base values: $P_0 = 1$, $L\omega_n = 0.45pu$, $R = 0.045pu$, $\omega_{LP} = \omega_n/10$, $m_p = 0.05\omega_n$. 104

3.10 Representation of the two sources with each an autonomous conventional droop control. Loads are neglected. 107

3.11 Comparison of voltage angle difference dynamics $\Delta\delta(s)$ between two voltage-sources following a disturbance. An EMT model time-domain response is plotted with dashed line, the linearized model (3.31) plotted on Matlab with plain line. System parameters are: $\sigma = 0.04$ p.u., $\omega_{LP} = \omega_n/10$, $P_0 = -0.9$ p.u. for $L\omega_n = 0.45$ p.u. and $R = 0.025$ p.u. 108

3.12 Two voltage-sources system interfaced by a double overhead line, subject to a line tripping 118

3.13 Active power response of two droop-controlled voltage-source following a line opening 119

3.14 Current envelopes of two droop-controlled voltage-source following a line opening 119

3.15 Equivalent circuit describing the initial power sharing 120

4.1 Layout of the PWM-VSC with its output filter and parallel grid-forming controls. Single-phase equivalent representation 126

4.2 Power delivery in steady-state depending on the total filter inductance. The normal operation area is filled in grey. Dot lines delimits the accessible points for a given value of x_{tot}. 132

4.3 EMTP simulation of VSC output phase-current (a), and filter output capacity phase-to-ground voltage (b). The full VSC switched model is compared with the averaged model over a switching period. Initially no load is connected. At $t = 0.06$ s, a load of $P_{load} = 1$ p.u. and $Q_{load} = 0.3$ p.u. is connected to the PCC. 137

4.4 Scheme of the inner control of AC filter output voltage. Two cascaded loops in dq-frame including cross-decoupling terms, capacitor voltage and grid current feedforward. 139

4.5 Bode diagram of three current closed-loop transfer functions. With ideal e_{dq} voltage feedforward ($g_{ffv} = 1$), no voltage feedforward at no-load ($g_{ffv} = 0$, $\boldsymbol{i}_{gdq} = 0$), and no voltage feedforward at full load ($g_{ffv} = 0$, $r_{load} = 1$ p.u.). . . . 143

4.6 Bode diagram of two voltage closed-loop transfer functions: considering a perfect inner current control ($i_{sdq} = i^*_{sdq}$) and taking into account the closed-loop current dynamic ($i_{sdq} = G_c(s)i^*_{sdq}$). 145

4.7 Time-domain response of the voltage closed-loop. (a) The load (r_{load}=0.5 p.u., l_{load}=0.3 p.u.) is connected at 0.01 s, and Δe^*_d=-0.1 p.u. at t=0.11 s. 146

4.8 Current-limiting strategy during short-circuit at terminal voltage ($R_{fault} = 1\Omega$). (a) Terminal voltages. (b) VSC output currents. (c) VSC output currents in dq-frame. 148

4.9 Poles-map of a grid-connected VSC with voltage-control with *SCR* growing from 0.25 blue (dark) to 20 orange (light),($g_{ffv} = 1$). (a) The whole eigenvalues. (b) Zoom on slower modes. 152

4.10 Poles-map of a grid-connected VSC with voltage-control with *SCR* growing from 0.25 blue (dark) to 20 orange (light) ($g_{ffv} = 0.5$). (a) The whole eigenvalues. (b) Zoom on slower modes. 153

4.11 Equivalent representation of the VSC in open-loop modeled by a voltage-source, and a open-loop output impedance $\boldsymbol{Z}^{ol}_{out}(s)$. 157

4.12 Bode diagram of the VSC open-loop output impedance for positive frequencies. $\left[Z_{out}^{ol}(j\omega)\right]_{abc}$ is expressed in the natural abc-frame, and $\left[Z_{out}^{ol}(j\omega)\right]_{dq}$ is expressed in the dq-frame rotating at $\omega^* = \omega_n$. 159

4.13 Real-part of the VSC open-loop output impedance for positive frequencies. $\left[Z_{out}^{ol}(j\omega)\right]_{abc}$ is expressed in the natural abc-frame, and $\left[Z_{out}^{ol}(j\omega)\right]_{dq}$ is expressed in the dq-frame rotating at $\omega^* = \omega_n$. 159

4.14 Bode diagram of the VSC open-loop output impedance for positive and frequencies. $\left[Z_{out}^{ol}(j\omega)\right]_{abc}$ is expressed in the natural abc-frame, and $\left[Z_{out}^{ol}(j\omega)\right]_{dq}$ is expressed in the dq-frame rotating at $\omega^* = \omega_n$. 163

4.15 Real-part of the VSC open-loop output impedance for positive and frequencies. $\left[Z_{out}^{ol}(j\omega)\right]_{abc}$ is expressed in the natural abc-frame, and $\left[Z_{out}^{ol}(j\omega)\right]_{dq}$ is expressed in the dq-frame rotating at $\omega^* = \omega_n$. 163

4.16 Representation of the voltage-controlled VSC with its reference tracking transfer gain $G_v(s)$ and its closed-loop output impedance $Z_{out}^{cl}(s)$. 164

4.17 Frequency-response comparison of the closed-loop and open-loop output impedance models in dq-frame. 166

4.18 Real-part comparison of the closed-loop and open-loop output impedance models. $\omega_1 = 24\,rd.s^{-1}$ and $\omega_2 = 319\,rd.s^{-1}$. 166

4.19 Frequency-response in dq-frame of the closed-loop output impedance of the controlled VSC $Z_{out}^{cl}(j\omega)$ and of two values of the grid impedance $Z_{src}(j\omega)$. $\omega_1 = 24\,rd.s^{-1}$ and $\omega_2 = 319\,rd.s^{-1}$. 167

4.20 Frequency-response in dq-frame of the closed-loop output impedance of the controlled VSC $Z_{out}^{cl}(j\omega)$ and of two values of the grid impedance $Z_{src}(j\omega)$. The negative real-part of $Z_{out}^{cl}(j\omega)$ is delimited by $\omega_1 = 24\,rd.s^{-1}$ and $\omega_2 = 319\,rd.s^{-1}$. 169

4.21 Real part of the frequency-response of $Z_{out}(j\omega)$ for three different voltage feed-forward gains. 171

4.22 Real part of the frequency-response of $Z_{out}(j\omega)$ for three different voltage loop designed bandwidths. 171

4.23 Real part of the frequency-response of $Z_{out}(j\omega)$ for three different integral gain of the current loop controller. 172

4.24 Frequency-response of $G_v(j\omega)$ for $g_{ffv} = 0$ and $\omega_{nv} = \omega_{nc}/50$, compared to the originally designed function. 173

5.1 Time-domain response of fully controlled VSC after a grid voltage phase-angle shift at 0.2 s. (a) VSC output phase-currents (b) Magnitude of the VSC output current (c) Frequency reference. 180

5.2 The threshold virtual impedance control scheme is implemented in dq-frame. The virtual impedance is active only if the VSC output current magnitude (I_s) exceeds the defined threshold value I_{tresh}. 182

5.3 Steady state representation of the system after short-circuit, for the calculation of k_R value. 183

5.4 Considered system for the tuning of the TVI. The terminal voltage-control is disregarded. The source impedance value is taken as $l_{src} = 0.15$ p.u. $r_{src} = 0.15$ p.u. 184

5.5 Poles map of the simplified system in the presence of a real additional series impedance compared to the presence of the equivalent TVI. $\rho_{X/R} = 10$, $I_s = I_{max}$. 185

5.6 Poles trajectories of the simplified system with the presence of an active TVI (a) and zoom on the slowest modes (b). $\rho_{X/R}$ = is moving from 10 (orange/light) to 0.1 (blue/dark), $Z_{VI} = Z_{VI}(I_s = I_{max})$. 186

5.7 Poles trajectories of the simplified system with the presence of an active TVI (a) and zoom on the slowest modes (b). $\rho_{X/R}$ =5, Z_{VI} is moving from $Z_{VI}(I_s = 1)$ (orange/light) to $Z_{VI}(I_s = I_{max})$ (blue/dark). 187

5.8 Implementation of the TVI within the cascaded loops of the voltage-control. . . 188

5.9 Time-domain response of fully controlled VSC with the TVI after a grid voltage phase-angle shift at 0.2 s. (a) Amplitude of the VSC output current (b) Amplitude of the VSC terminal voltage (c) Frequency reference. 189

5.10 Layout of a power system based on two parallel grid-forming VSC 191

5.11 Time-domain response of electrical quantities of the two-VSC system (fig. 5.10) expressed in respective per-unit base S_{b1}=261 MVA, S_{b1}=1044 MVA. At t=0.1 s, S_1 opens, t=0.8 s P_{load} = +150 MW, t=1.5 s P_{set2} = +0.1 p.u. 194
5.12 Time-domain responses of the frequency references of the two VSCs (fig. 5.10). At t=0.1 s, S_1 opens, t=0.8 s P_{load} = +150 MW, t=1.5 s P_{set2} = +0.1 p.u. 195
5.13 Time-domain response of electrical quantities of the two-VSC system (fig. 5.10) expressed in respective per-unit base S_{b1}=261 MVA, S_{b2}=1044 MVA. At t=0.1 s, S_2 opens. 196
5.14 Time-domain responses of the frequency references of the two VSCs (fig. 5.10). At t=0.1 s, S_1 opens, t=0.8 s P_{load} = +150 MW, t=1.5 s P_{set2} = +0.1 p.u. 197
5.15 Layout of a power system based on three parallel grid-forming VSC 197
5.16 Time-domain responses of electrical quantities of the three-VSC system (fig. 5.15) expressed in respective per-unit base S_{b1}=261 MVA, S_{b2}=1044 MVA, S_{b3}=522 MVA. At t=0.1 s, S_3 opens, t=0.8 s S_1 opens, t=1.5 s P_{set2} = +0.1 p.u. 200
5.17 Time-domain responses of the frequency references for the three VSCs (fig. 5.15). At t=0.1 s, S_3 opens, t=0.8 s S_1 opens, t=1.5 s P_{set2} = +0.1 p.u. 201
5.18 Time-domain responses of electrical quantities of the three-VSC system (fig. 5.15) expressed in respective per-unit base S_{b1}=261 MVA, S_{b2}=1044 MVA, S_{b3}=522 MVA. At t=0.1 s, S_2 opens 202
5.19 Time-domain responses of the frequency references for the three VSCs (fig. 5.15). At t=0.1 s, S_2 opens. 203

6.1 Properties of the grid-forming fonction of the controlled VSC 205

A.1 Stator windings and rotor windings relative positions. 214
A.2 Nyquist diagram of the ratio $Z_{out}(j\omega)$ to $Z_{srcm}(j\omega)$ for $g_{ffv} = 0$ and $g_{ffv} = 1$. . 219

List of Tables

1 Les sous-fonctions des VSCs grid-forming dans la littérature 11

2.1 Technical needs from transmission grid infrastructure 45
2.2 Technical needs for a good quality of electricity 46
2.3 Technical needs from operating constraints 48
2.4 Grid-forming capability 50
2.5 Additional functions for parallel grid-forming capability 50
2.6 Typical parameters of synchronous generators with round poles in power system [5] 54
2.7 Typical parameters of synchronous generators with round poles in power system [5] 55
2.8 VSC output filter inductance typical values 68
2.9 VSC output current limits 71

3.1 Typical nominal values of electrical sources connected on transmission grid . . 86
3.2 Typical 400 kV overhead line on transmission grid 86
3.3 Numerical application 122

4.1 Definition of PWM nominal values fig. 4.1 in a common voltage base (U_b =320 kV) 130
4.2 LCL filter parameters 135
4.3 Numerical values 142
4.4 Numerical values 144

5.1 Comparison of eigenvalues from fig. 5.5 184
5.2 Nominal values of two VSC based sources 191
5.3 LCL filters parameters 191
5.4 Control parameters 192
5.5 Typical 400 kV overhead line on transmission grid 192
5.6 Nominal values of three VSC based sources 198
5.7 Chosen lines length 198

A.1 Typical parameters of synchronous generators with round pole in power system [5] 217

Chapter 1

Introduction

Contents

1.1 Background and motivation 33

1.2 Scope of the Thesis 38

1.3 Thesis contribution & outline 40

1.1 Background and motivation

Toward a 100% power-electronics power system In most of the developed countries, the share of renewable generation in power system has raised drastically. In the US or in France, scenarios of 90% and 100% of renewables in 2050 have been explored respectively by the NREL [1] or the ADEME [2]. In both projections shown in fig. 1.1 and 1.2, the wind power and solar photovoltaics are expected to supply more than 50% of the annual electricity consumption. The largest wind and photovoltaic generators will be connected to the transmission grid. They are interfaced through power-electronic based converters to extract the maximum energy from wind and solar flux. As a consequence, the power-electronic based generation will be dominant over traditional synchronous generation in the future.

Further more, the construction of HVDC links are stimulated by two main drivers. First, these links can interconnect asynchronous power systems such as continental Europe with Scandinavia and British islands. Second, embedded HVDC links, such as between France and Spain [6], are an alternative to traditional overhead lines that face a low social acceptance in the trans-

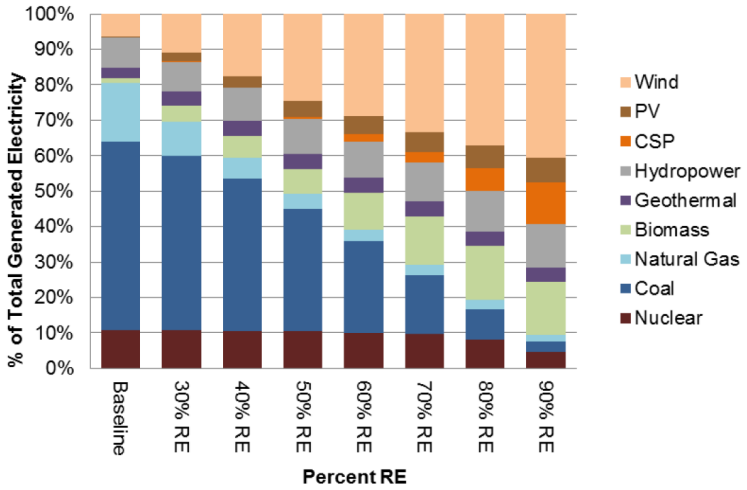

Figure 1.1 – Annual electrical energy consumption share for a 90% of renewables in US in 2050 [1].

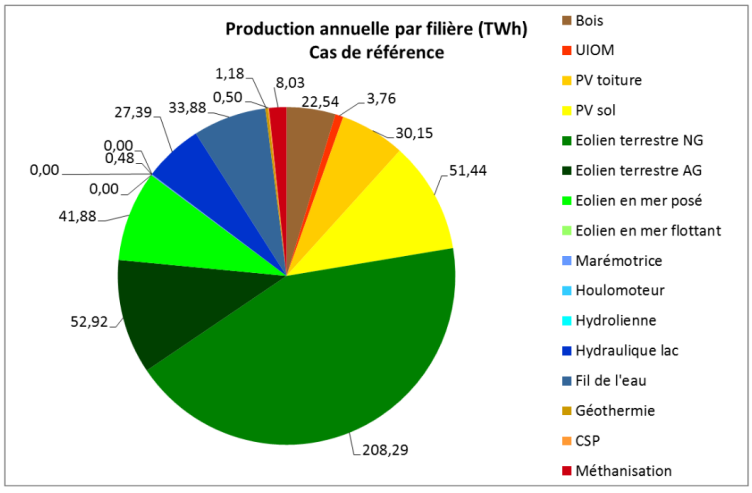

Figure 1.2 – Annual electrical energy consumption share for a 100% of renewables in France in 2050 [2].

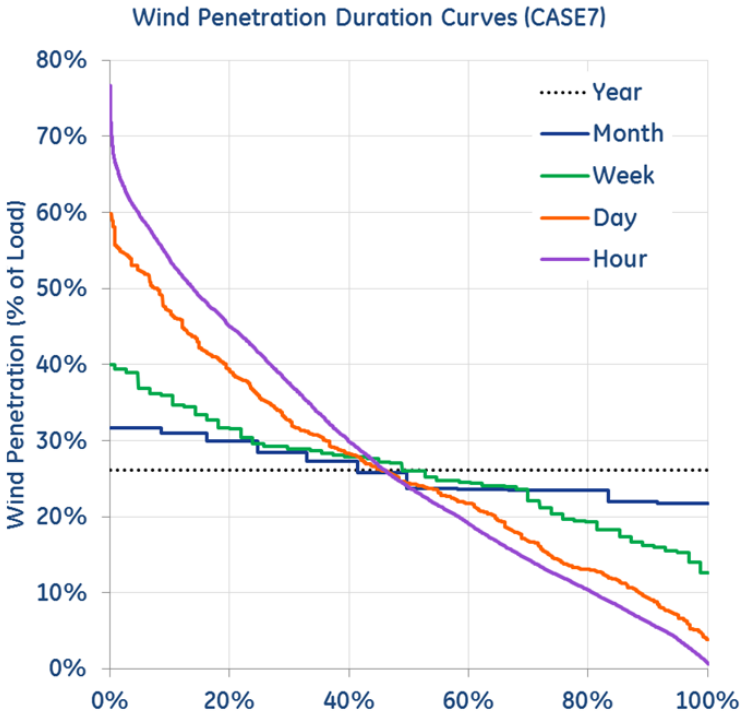

Figure 1.3 – Wind penetration duration curves for nominally 27% annual energy system. Source: NSPI Renewable Integration [3].

mission grid development. HVDC links have one AC/DC converter at each end, and thus are not considered as natural synchronous links. Consequently, the probability to lose the last synchronous link between two areas is higher.

A 100% power-electronics interfaced power system seems hypothetical as synchronous generation remains connected, even in 2050. However, looking at instantaneous electrical energy production, only interfaced-based generation is likely to feed the load temporary or locally. As noted in [3] and illustrated in fig. 1.3, 27% annual wind energy in a hypothetical power system exceeds 70% hourly production few times a year. In case where 50% of the load is annually fed by converter-based generation, 100% of instantaneous production could be reach temporary. Moreover, since wind and photovoltaic generations are concentrated where the wind blows and the sun shines, a large area of transmission system fed through power-electronics can lose the last synchronous link connecting it to the rest of the system as depicts on the fig. 1.4. The transmission grid operators must adapt their practice to run the islanded system with no synchronous generation, under sufficient reliability and economical effectiveness.

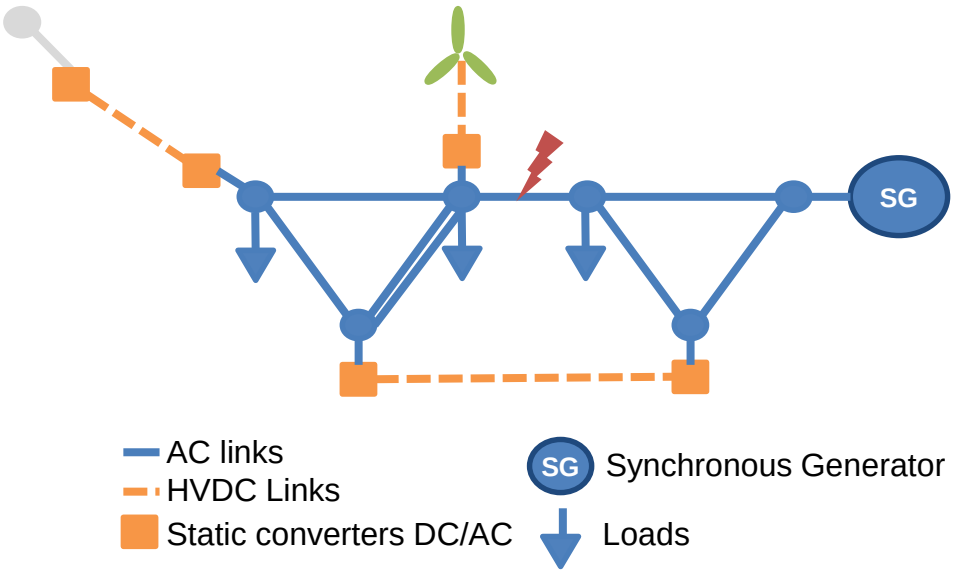

Figure 1.4 – Representation of the present power system loosing its last synchronous link.

Converter-based electrical sources connected to the transmission grid Static converter technology for renewables or HVDC interface is mostly based on Voltage Source Converter (VSC). Compared to previous LCC technologies, the VSC has an extra degree of freedom to decouple its active power injection from its reactive current injection.

At transmission level, the main role of grid-connected VSCs is to provide AC active power that follows a setpoint, depending on the level of wind, of sun, or of the planed transfer on HVDC links. Power setpoint injection requires measurement of the sinusoidal voltage at the connection point. From the value of the voltage amplitude, frequency and initial phase angle, a controlled AC current can be injected with a shifted phase-angle, to establish the desired active and reactive power exchange with the grid. This VSC current-controlled strategy is the state-of-the-art for controlling distributed power generation system nowadays [7]. The control relies on a synchronization unit based most frequently on a "phase-lock-loop" to estimate the system frequency and phase angle, and on a fast loop current control. This strategy is inherited from motor drive, as the PLL estimates the rotational speed of an equivalent synchronous machine that would be connected at the point of common coupling with the converter. The active power injection supports the synchronous generators rotation and replaces part of their mechanical

power supply. In this sense, the control strategy is called "grid-feeding" strategy (equivalently "grid-following" strategy) [8, 9].

The characteristic behavior of grid-feeding converters is their apparent lack of so-called "inertia". The inertia quantifies the capability of the power system based on synchronous generators to withstand fluctuation in net load and generation, through the presence of kinetic energy reserve in their rotating parts. As the grid-feeding converters only inject fixed power setpoints, regardless of the load level, they cannot guarantee the stability of the system frequency and voltage magnitude, the key variables of the power system.

Control requirements for grid-feeding converters are currently fixed by the transmission grid operators in grid-codes. These grid-codes are based on the assumption that synchronous generators dynamic dominates the system. However, the increasing share of grid-feeding converter in the power generation changes the resulting dynamics and endangers the system stability.

Existence of a penetration limit of grid-feeding VSC at the transmission grid-level In the present situation, the transmission grid operators estimate a stability limit is reached for a penetration level of grid-feeding converter between 60% to 80% [10, 11]. In Ireland, the maximum penetration level is currently limited to 60% in their 5 GW system. A precise limit is impossible to draw as it depends on the localization of the converter-based generation and on the dispatch.

The stability issues caused by high penetration of power-electronic devices have been extensively documented in [12]. One factor involved is the poor stability of grid-feeding controls in weak-grid situation. Another factor is linked to the low frequency stiffness when the remaining inertia of synchronous generators decreases.

Improvements in the grid-feeding control have been suggested to participate to the primary control of voltage and frequency, similarly to what is already implemented in synchronous generators. Such controlled converters are called "grid-supporting" [9]. Grid-supporting converters offer flexibility to the primary reserves management, but they do not provide the first cycles of a sinusoidal voltage waveform as synchronous generators naturally do. In other words, at an extreme point, if the output voltage collapses suddenly, following an outage or a large load connection, there will be nothing left to measure or adjust to.

Additional controls have been suggested to speed up the dynamic of frequency control. The idea is to inject or absorb active power when the measured frequency has a high rate of change. It takes advantage of the energy immediately available in the wind turbine rotation [13], or in fast DC storage devices [14]. Because this add-on contributes to a better frequency stability by limiting the transient frequency excursion, it has been called "synthetic inertia". However, this effect is temporary, and [11] showed that such control does not allow to expand the stability limit of the penetration level.

If one tried to push the limit up to the 100% of grid-feeding/grid-supporting converters, it is unclear how the voltage amplitude and frequency would be regulated as the grid-feeding converters are forced to behave as current-source within ten milliseconds, the characteristic time of the current loop. Particularly, once synchronous generators are removed, the frequency dynamic does not depend on rotational speed but on PLLs parameters. Interaction between PLLs is not yet fully understood. The non-linearity of the PLL is difficult to analyze properly, and stability limits on PLL parameters are hard to generalized to networks with unknown topologies.

Instead of trying to expand the stability boundaries of penetration level, this thesis takes the challenge of building directly a full VSC-based power system. To that end, the control strategy of VSC should be turned from a grid-feeding strategy to a "grid-forming" strategy. The grid-forming capability refers to the ability of VSCs to precisely control their output voltage amplitude and frequency and thus to create the grid by their own.

1.2 Scope of the Thesis

Opposed to the approach of maximizing the penetration level of VSC-based generators in the system, the thesis focused on the necessary and sufficient conditions to build a 100% VSC-based power system from scratch with, at least, the same level of reliability than today. A 100% VSC-based power system considers that all the electrical generators are interfaced through VSC devices. Further, the thesis considers that no synchronous motor remains in the load.

Thesis objectives The task of guaranteeing a stable and reliable operation of power system is tremendous. Hence, the ambitious problematic of the thesis has been decomposed in three subsidiary questions that must be addressed.

1. What are the fundamental services the electrical sources must provide to operate the fundamental functions in a power system?

2. How the analysis of these services from the transmission grid perspective could define the "parallel grid-forming" requirements for future static converter?

3. From the VSC-device perspective, what are the technical challenges to offer the "parallel grid-forming" service?

4. What are the designing methods and recommendations to cope with these challenges while ensuring that VSCs operate with sufficient level of reliability?

Constraints on the objectives The technical solutions found in this thesis consider the following contextual constraints

1. The industrial context of this work is conservative. The chosen approach gives the priority to the simplicity of the developed controls, whenever it is possible. Ideally, the proposed controls should be an upgrade of the existing VSC systems, allowing retrofit.

2. The system must be easy to understand and to analyze in its resulting phenomena. The power system is formed of thousand of nodes, the possible interactions must be minimized.

3. The solutions must be compatible with the highest voltage, and the highest power rate of the existing VSCs.

4. With no synchronous generators, the definition of system frequency is no more linked with the rotation speed of rotors. As a consequence, frequency estimation is not fully reliable, especially under the fundamental period or during transients. Thus, it has been chosen not to rely on frequency measurements. In particular, all the PLL-based solutions will be avoided.

1.3 Thesis contribution & outline

The main contributions of the present thesis are fourfold

1. An analysis of the technical challenges for operating a full VSC-based power system that results in requirements for parallel grid-forming capabilites.

2. An analysis of the trade-off between the stability of the synchronization control of grid-forming sources and the sensitivity to transient grid events.

3. A design method and recommendations for a high-power VSC-PWM based grid-forming sources for the transmission system.

4. An overcurrent limitation strategy to preserve the synchronization stability during grid-events.

The contributions are organized in the following structure:

- Chapter 2, To state the problem, this preliminary chapter investigates the power system needs and the technical services required by the transmission system operators. A comparison between the nature of an electrical source based on synchronous generators or VSC underscores the challenges to fulfill the mentioned services. A literature survey on similar technical problems in others application such as Microgrids or offshore windfarm networks emphasizes the specific and original issues associated with the transmission network application.

- Chapter 3, From a power system perspective, the second chapter identifies the stability constraints of a network interfacing only grid-forming VSCs. The grid-forming VSCs are represented by fully controllable voltage-sources. Based on a simplified model of transmission lines, an analytic study justifies the use of a power-frequency droop-control because it provides the necessary and sufficient conditions to synchronize the sources at a common frequency. The chapter closes on the trade-off illustration between the stability margins droop control and the sensitivity to transient overcurrents following grid events.

- Chapter 4, From the VSC device perspective, this chapter provides a method and recommendations to size and control the terminal voltage of a VSC-PWM with its filter. The controlled VSC is expected to satisfy grid-forming function requirements on a wide range of grid situations. Especially, the small-signal stability limit of a tight voltage control is highlighted when the VSC is connected to a strong grid. Consequently, the influence of control parameters on potential small-signal instabilities is studied through the frequency dependent model of the equivalent output impedance of the voltage-controlled VSC.

- Chapter 5, The last chapter tackles the large-signal stability of the developed control while the VSC faces stressing grid events. A post-fault overcurrent limiting strategy is designed to avoid the saturation of the control reference to keep the VSC system under

control. The ideas developed on a single converter are simulated on small transmission systems with a limited number of converters to allow a physical interpretation on the simulation results. The simulations are conducted on a EMT software.

Chapter 2

Problem statement: Challenges of a full VSC-interfaced transmission grid system

Contents

2.1 Analysis of large power systems needs 44

2.2 Power system based on synchronous generators electrical sources . . . 51

2.3 Power system based on VSC-based electrical sources 66

2.4 State-of-the-art of grid-forming VSC 76

The chapter is dedicated to the problem statement of this thesis, rising the main technical challenges: defining stable synchronization of VSC based grid-forming sources, building robust and flexible grid-forming sources with a PWM-VSC, protecting the VSC against overload during grid events. Those three challenges reveal themselves from the following methodology. First some of the fundamental power system needs and constraints have been analyzed to define a parallel grid-forming capability required for the sources. Then, the traditional synchronous generators behavior has been compared to the nature of VSC-based electrical sources, underlining their lacking features to fulfill power system needs. Finally, the VSC requirements are compared to available solutions in the literature. As an output, the chapter gives the original technical challenges that this thesis must address to operate a full VSC-interfaced transmission grid system.

2.1 Analysis of large power systems needs

Anywhere in a power system, the transmission grid operators (TSOs) have a fundamental responsibility among others: provide electrical energy of good quality to the consumers [15]. Pursuing this goal, the TSOs use the grid infrastructure, built in the last century, as well as constructive capacity of electrical sources owned by the producers. This section analyses some of the fundamental technical functions, required from the electrical sources, to allow electrical energy transport through the grid, a good electrical quality, and safe operations of the power system. The section ends with a synthesis of some technical needs, gathered under the definition of "parallel grid-forming capability", that electrical sources must meet in order the TSOs to fulfill their mission. The quantification of power system needs in future power system will be, at minimum, as good as today from the consumer point of view.

2.1.1 Technical needs from the transmission grid infrastructure

Historically, electrical generation units have been centralized and located far from consumption centers. To transport electrical energy over long distances, the existing transmission grid is based on AC-line and transformers. Compared to DC transmission, AC transmission have been preferred in the past for the following technical advantages:

- AC voltages can be readily transformed to higher voltages, with robust copper coil. High-voltage minimizes current and losses for a given power transfer amount.
- AC-lines are easy to switch-off when the current values cross zero. Line switching is desirable to eliminate faults, as short-circuit.
- Brushless AC motors can be employed.

In contrast, one point stands in favor of the DC transmission: there is no limitation of the transmission distance, especially when using cables that can be buried, and thus, hidden. However, the existing interconnected European transmission assets are worth billions of euros with long life expectancy. Reasonably, the grid-structure of AC transmission lines will remain in the future, even in the case of a 100% power electronics based system.

Table 2.1 – Technical needs from transmission grid infrastructure

Services	Main technical functions	Conditions
Electrical energy transport on AC line	Three-phase sinusoidal currents injection	$\omega_{min} < \omega < \omega_{max}$

As a consequence, the AC transmission grid nature constraints the electrical energy to be carried through the network under alternative quantities. Three-phase transmission results from a cost minimization of the line investment compared to the transmitted power. Lines and coils have been sized for 50 Hz currents in Western Europe. Therefore, actual alternative currents flowing through the AC grid should present a frequency in the vicinity of the nominal frequency. This main requirement on frequency is reported in table 2.1. During normal operation, the frequency is expected to remain between 49.5 Hz and 50.5 Hz [16], but those limits are mainly driven by the synchronous generators technical limits. Transmission grid hardware have also rated AC voltage amplitude, connected through transformers. In France, the transmission grid gathers the voltage levels of 63 kV, 90kV, 225 kV, and 400 kV. At all voltage levels, the transmission grid shares a common structure of mainly overhead lines, often doubled-lines, connected in a meshed topology.

2.1.2 Technical needs for good quality electricity

One of the fundamental missions of TSOs is to guarantee the electrical supply of all consumers, at any point of the managed grid, with a good quality. Basically, electrical energy of good quality means that the energy is available instantaneously, without interruption, under a well defined sinusoidal form [15]. This mission of qualitative supply can be decomposed in four subsidiary services provided by the transmission grid and its operator:

1. **Load adequacy**: The TSOs must ensure that there is enough energy generation, reserve or storage, to feed the load demand variation at any time (no generation shortfalls).

2. **Parallel load connection**: Consumers must be connected in parallel on the same network otherwise, the electrical circuit should be opened for each new connection.

Table 2.2 – Technical needs for a good quality of electricity

Services	Main technical functions	Conditions
Parallel load connection	Control of grid nodes RMS voltages	$V_{min} < V(i) < V_{max}$
System security	Load-sharing between parallel generators	$P_{gen(i)} = P_{set(i)} + \Delta P_{load}/P_{nom(i)}$
Hardware Security	Overload limitation	$I_{gen(i)} < I_{max(i)}$

3. **System security**: To avoid the system collapse following a random grid event, the load must be fed from, at least, two different generators operating in parallel, and interconnected in a meshed network.

4. **Hardware Security**: All the grid-connected devices must be protected from grid events. These events can be faults, outages, or normal operation and can result in high-voltages or high-currents, destructive for the connected devices.

Among the listed services, the first one regarding load adequacy will not be treated in this thesis. The load adequacy depends on long term planning. It is then assumed here, that there is always sufficient primary energy production or reserve to be converted into electricity to fulfill the load demand. The three remaining services necessitate technical functional conditions. This thesis treats only some fundamental needs of interest that are summarized in the table 2.2 and quantified in the next paragraphs.

Control of grid nodes RMS voltages is fundamental to feed loads under their rated power conditions when loads are connected in parallel to the grid. Today, a steady-state voltage control is required to reach a reference value of ±5 % in less than 10 s, with a static error of less than 0.2 % of the reference value [16].

The load sharing ensures the generators in parallel to share load variation in proportion to their rated power ($\Delta P_{load}/P_{nom(i)}$), or according to another predefined law. Mainly steady-state requirements are expected, as long as the sources can handle overload before the load-sharing

action. In AC electrical system, a prerequisite for load-sharing is the synchrony of all generation units.

The overload limitation concerns all protective functions that must be implemented depending on the intrinsic physical capability of the electrical sources. The limitation is often a thermal limit, that depends on a couple current magnitude and over-current period. Voltage limitations also might exist but they are not taken into account in this work.

Other TSOs missions should be kept in mind while looking at potential technical solutions. Economical optimum for the society implies that generation operating points $P_{set(i)}$ (the steady-state power references of each units) can be market driven. Also, only the necessary hardware investment must be proposed. Whenever possible, intelligent computed solution should be favored instead. At last, for the sake of transparency and simplicity, the system behavior must be kept as simple as possible to let stakeholders understanding the underlying dynamics. Simple solutions are all the more necessary as TSOs must operate a very large system of thousand nodes with the highest possible level of reliability.

2.1.3 Technical needs from transmission grid operating constraints

The power system is subject to numerous contingencies and physical disturbances, resulting from normal operations (load changes, generation variations, grid reconfiguration), as well as from hazardous outages. The consequences on grid operating constrains are twofold. First, the transmission grid can have multiple configurations, from large interconnection of multiple generators, to standalone situations where only passive loads must be fed by one generator. Standalone situations might appear when the last AC link between two synchronized areas is lost. Second, the generators connected to the transmission grid are subject to stressing events. Example of what is considered as stressing events are listed below:

1. Connection of a large load close to a small generation unit
2. Loss of the last AC line between two areas
3. Line switch or transformer disconnection
4. Generator outage

Table 2.3 – Technical needs from operating constraints

Constraints	Main technical functions	Conditions
Feeding sudden load changes	Transient voltage stiffness	Guarantee limited amplitude and frequency transients
Surviving in separated areas	Autonomous operation	Use local measurements
Ensuring stable normal operation	Small-signal stability in various grid configurations	Sufficient damping
Surviving transmission grid events	Large-signal stability	Remain connected after fault

5. Short-circuit

The events listed above are considered to be instantaneous and to affect the three-phases simultaneously. The power system must be robust enough to remain stable in any situations during normal operation, and to converge to an acceptable steady-state following each of these large disturbances.

The fundamental technical functions summed up in tables 2.1 and 2.2 must be fulfilled with a sufficient level of robustness to face the transmission grid operating constraints. These operating constraints require additional technical functions listed in table 2.3 to be achieved. These expected technical functions are further explained in details.

Transient voltage stiffness ensures that the voltage does not collapse in amplitude or in frequency when a reasonable load is connected. Even if no specifications exist in present grid-codes for instantaneous voltage limits, it is expected in future grids that the voltage conserves at least the same transient voltage stiffness as nowadays. Present criteria for evaluating the transient voltage waveform stiffness are the "short-circuit power", and the "rate of change of frequency" (ROCOF). The short-circuit power describes the ability of the grid to provide current to the fault in order to maintain the voltage magnitude as much as possible. The short-circuit

power is also said to characterize the strength of the grid. The ROCOF evaluates the frequency variation in respect to the load current, in the first moments following the connection. In a synchronous generators-based system, the ROCOF is often mixed up with the level of inertia of the system.

Autonomous operation is needed because electrical sources can not depend on additional communication link for reliability reasons. Consequently, the sources have no information on whether they are linked to a large synchronous area or passive network. In any case, they must feed the load if they are supplied with enough energy.

The small-signal stability in various grid configurations characterizes the ability of the system to maintain normal operations after small changes from initial conditions (load changes, generation variations). Particularly, the small-signal stability implies that critical resonances of the system must be damped. It is particularly challenging, as electrical sources must operate in stable manner in an unknown environment. From standalone situations with only passive loads, to large power system with numerous other electrical generation units.

Large-signal stability ensures the electricity sources to remain connected after a severe event to reach an acceptable operating point, without exceeding their overload capabilities.

2.1.4 Synthesis on demanded functions to electrical sources forming a transmission grid

The three previous subsections reviewed the main technical needs that should be met by electrical sources, required by the structure, the quality services, and the operating constraints of a transmission grid. To build a transmission grid that fulfills its mission, TSOs require the electrical generators, to embed these functions rearranged in two separate tables 2.4 and 2.5.

The ability of electrical generator to feed a passive load under controlled voltage and frequency in steady-state but also with sufficient stiffness during transient will be referred as "grid-forming" capability. The associated functions are described in table 2.4. The ability of such grid-forming generator to operate in parallel, in a stable manner, will be referred as "parallel

Table 2.4 – Grid-forming capability

Technical needs	Description
Sinusoidal waveform generation	Conversion of a primary energy resource into electrical energy on three-phase alternating currents
Transient voltage stiffness	The first voltage cycles following an event should have a limited amplitude and frequency drop from the nominal values
Hard transient resilience	The device must survive when stressing event occurs
Autonomous operation	Critical functions must be ensured only based on measurements available locally
Steady-state voltage amplitude control	The steady-state terminal voltage amplitude must be kept into acceptable range
Steady-state voltage frequency control	The steady-state terminal voltage frequency must be kept into acceptable range

Table 2.5 – Additional functions for parallel grid-forming capability

Technical needs	Description
Synchronization	All the electrical sources must converge into a consensus frequency
Load sharing	Load variation must be shared among generation units according to their ratings or a predefined law
Stability	Parallel electrical sources must remain stable after small or large disturbances

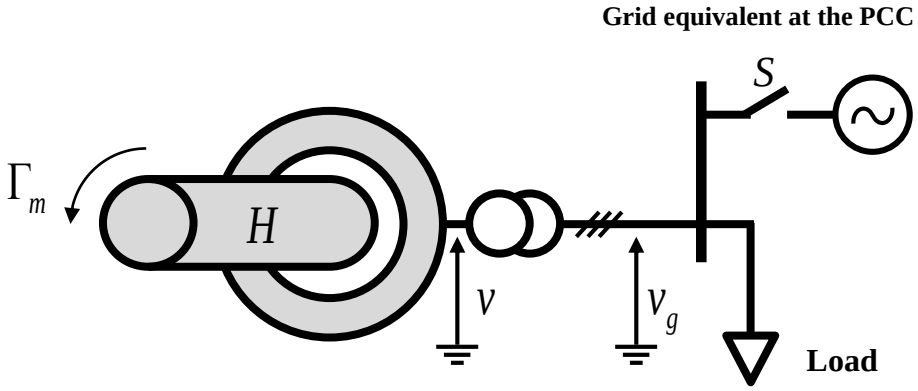

Figure 2.1 – The considered grid-connected synchronous generator system with the primary mechanical source. The electromotive force is produce along the q-axis.

grid-forming capability", gathering the grid-forming functions with the additional features described in table 2.5. The following sections show how the synchronous generators have historically fulfilled these parallel grid-forming functions through their physical behavior and their controls, and what are the missing functions to be developed to turn VSCs into parallel grid-forming sources.

2.2 Power system based on synchronous generators electrical sources

Traditionally, TSOs have been driving the power system through the action of the electromechanical energy converters based on the synchronous generators. Intrinsic physical properties associated with suitable controls were used to provide parallel grid-forming capabilities to the grid.

Based on the representation of stator and rotor windings in fig. 2.2, equations of the synchronous generators are recalled in appendix A.1. Equations (A.1), (A.2), (A.3), (A.4), (A.5), (A.6) and (A.8) describe completely the synchronous generator instantaneous behavior under the given assumptions.

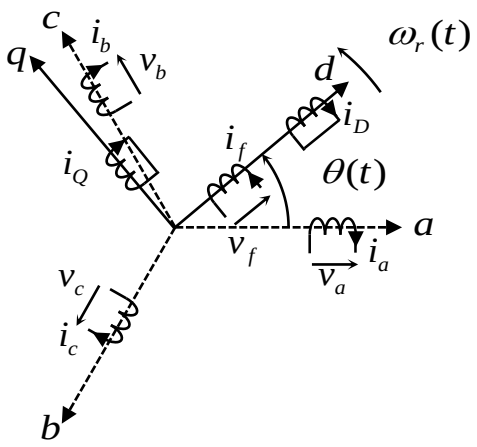

Figure 2.2 – Stator windings and rotor windings relative positions.

2.2.1 The grid-forming capability of synchronous generators

Based on the steady-state and transient model of the synchronous generator, this section details how the electrical source fulfills all the functions to provide grid-forming capability to a passive load (S open in fig. 2.1). Analytic study is, however, difficult, because of the non-linearity since the stator electrical quantities depend on the rotor speed, and since the electromagnetic torque is the product of electrical quantities. To easily demonstrate the synchronous generator properties, the electrical behavior of the converter is first studied assuming a fixed rotation speed. Then, variation of the rotational speed is quantified.

Source of sinusoidal waveform voltage When the rotor rotates at fixed speed $\omega_r = \omega_0$, all the stator quantities, currents, flux, and voltages have sinusoidal waveforms in steady-state with an angular frequency of ω_0, because of the assumption of the sinusoidal distribution of stator windings. In case a multi-polar generator, the relationship between mechanical speed and electrical frequency is affected by the number of poles.

Transient voltage amplitude stiffness Before the field current control can react, the terminal voltages must be stiff enough to handle strong load variation or grid disturbance without collapsing the system. The transient voltage stiffness of a synchronous generator only depends on its physical equations. As the terminal voltage is mainly affected by a reactive current, the

magnitude stiffness is investigated by looking at the magnitude evolution of the first voltage cycles following a step of a reactive current (d-axis current):

$$\begin{cases} \Delta i_d(t > 0) = i_{d1} \\ \Delta i_q(t) = 0 \end{cases} \tag{2.1}$$

In Laplace domain:

$$\begin{cases} \Delta i_d(s) = \frac{i_{d1}}{s} \\ \Delta i_q(s) = 0 \end{cases} \tag{2.2}$$

The corresponding flux and voltage variation are deduced from eq. (A.15) and (A.3). In the short-time scale following the event, the stator resistance r_a is neglected because of its small influence, and the field voltage is considered constant ($\Delta v_f(s) = 0$).

$$\begin{cases} \Delta \psi_d(s) = -l_d(s) \Delta i_d(s) \\ \Delta \psi_q(s) = 0 \end{cases} \tag{2.3}$$

$$\begin{cases} \Delta v_d(s) = s\Delta \psi_d(s) = -s l_d(s) \frac{i_{d1}}{s} \\ \Delta v_q(s) = \omega_0 \Delta \psi_d(s) = -\omega_0 l_d(s) \frac{i_{d1}}{s} \end{cases} \tag{2.4}$$

The frequency dependent inductance $l_d(s)$ expression from eq. (A.16) is decomposed in simple fractional elements, introducing the steady-state reactance x_d, the transient reactance x'_d, and the subtransient reactance x''_d. These equivalent reactances are calculated from the characteristics time constants of table 2.6, considering operations close to the nominal frequency ($\omega_0 \approx \omega_n$). Typical reactances values are reported in table 2.7. Voltages from eq. (2.4) are thus rewritten [5]:

$$\begin{cases} \Delta v_d(s) = -i_{d1} \left[\frac{x''_d}{\omega_0} + \frac{1}{\omega_0} \frac{(x_d - x'_d)}{(1 + T'_{d0} s)} + \frac{1}{\omega_0} \frac{(x'_d - x''_d)}{(1 + T''_{d0} s)} \right] \\ \Delta v_q(s) = -i_{d1} \left[\frac{x_d}{s} - T'_{d0} \frac{(x_d - x'_d)}{1 + T'_{d0} s} - T''_{d0} \frac{(x'_d - x'_{d-})}{1 + T''_{d0} s} \right] \end{cases} \tag{2.5}$$

In the $\Delta v_d(s)$ expression, the constant term in Laplace domain is an impulsion in time-domain. The physical meaning of the impulsion could be discussed regarding the model because a current step applied in an inductive circuit has no physical reality. As it belongs to the model limit, the impulsion is neglected [5]. Further recalling from 2.6 that:

Table 2.6 – Typical parameters of synchronous generators with round poles in power system [5]

Parameters	Value
r_a	0.003 p.u.
$l_d\omega_n$	2 p.u.
$l_q\omega_n$	2 p.u.
T'_d	1.2 s
T''_d	0.04 s
T'_q	0.6 s
T''_q	0.04 s
T'_{d0}	10 s
T''_{d0}	0.05 s
T'_{q0}	2 s
T''_{q0}	0.4 s
T_D	0.02 s

$$\begin{aligned} \frac{1}{\omega_0} &<< T'_{d0} \\ \frac{1}{\omega_0} &<< T''_{d0} \end{aligned} \tag{2.6}$$

The expression of $\Delta v_d(s)$ can be neglected as compared to $\Delta v_q(s)$ [5]. In time domain, the voltage variation can be deduced from (2.5):

$$\Delta v_q(t) = -i_{d1}\left[x_d + \left(x'_d - x_d\right)e^{-t/T'_{d0}} + \left(x''_d - x'_d\right)e^{-t/T''_{d0}}\right] \tag{2.7}$$

Applying the inverse Park transform to $v_q(t) = E_0 + \Delta v_q(t)$ give the temporal expression of phase-voltage just after the load connection:

$$v_a(t) = \left\{E_0 - i_{d1}\left[x_d + \left(x'_d - x_d\right)e^{-t/T'_{d0}} + \left(x''_d - x'_d\right)e^{-t/T''_{d0}}\right]\right\} sin\left(\omega_0 t + \theta_0\right) \tag{2.8}$$

The three-phases are plotted in fig. 2.3. Analyzing the phase voltage expression (2.8) with parameters value of table 2.6 and 2.7 distinguishes three voltage behaviors following the load step in three separated time scales visible in fig. 2.3:

Table 2.7 – Typical parameters of synchronous generators with round poles in power system [5]

Parameters	Value
x_d	2 p.u.
x_q	2 p.u.
x'_d	0.25 p.u.
x''_d	0.2 p.u.
x''_q	0.2 p.u.

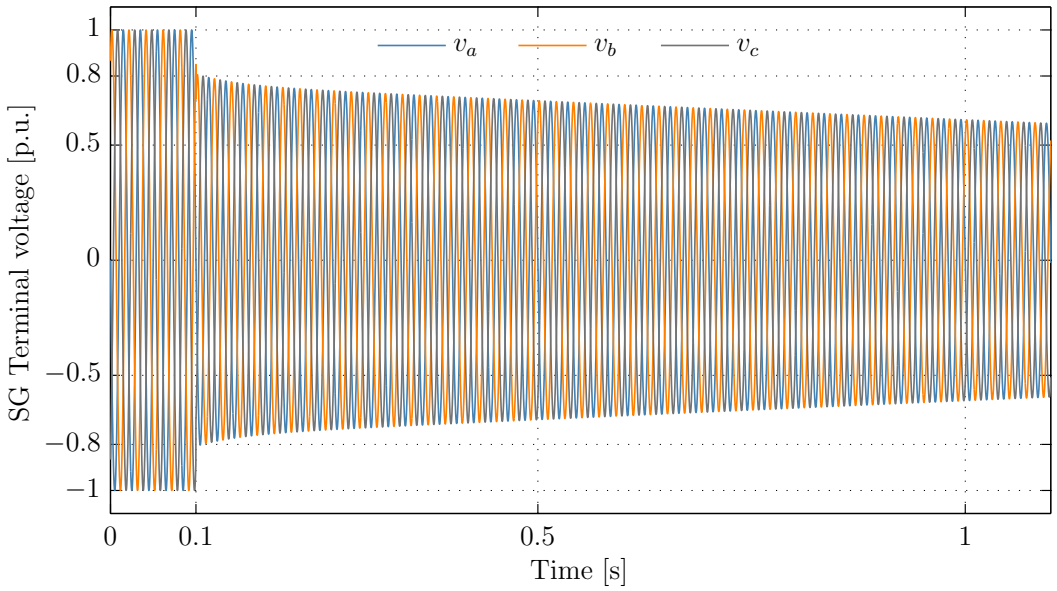

Figure 2.3 – Terminal phase-voltages of the synchronous generator following a load connection. The curves are plotted after the park transform of eq. (2.7)

- In the very first moment ($t > 0^+$), the current step of $i_{d1} = 1\,p.u.$ drops the terminal voltage magnitude of $x''_d i_{d1} = 0.2\,p.u.$.
- For the following short-term duration ($0 < t < T''_{d0} = 0.05\,s$) the voltage drop increases until $x'_d i_{d1} = 0.25\,p.u.$
- Then, for $T''_{d0} < t < T'_{d0} = 10\,s$, the voltage amplitude decays slowly until steady-state.

The ability of the synchronous generators to reasonably maintain its terminal voltage amplitude during the first cycles can be characterized by the traditionally short-circuit current that use only the transient reactance characteristic.

$$I_{cc} = \frac{E_0}{x'_d} = 5\,p.u. \tag{2.9}$$

Or by the short-circuit power:

$$S_{cc} = \frac{E_0^2}{x'_d} = 5\,p.u. \tag{2.10}$$

In steady-state voltage magnitude is slowly decaying, but can be kept in acceptable range if a slow acting control reacts within seconds.

Steady-state voltage amplitude control Eq. (A.13) shows how the terminal voltage is affected in steady-state by the load current. To maintain a long-term terminal voltage magnitude, a feedback control can be applied to adjust the field current i_f through the field voltage v_f, to adapt the electromotive force to the load variation as suggested by (A.12). Applying a field current is not straightforward because it depends on the field circuit dynamics and limitation of the so called "exciter". Many control schemes have been developed. A very simplified principle of the closed-loop control scheme is given here in fig. 2.4.

Hard transient resilience The ability of the synchronous generators to withstand hard transients is illustrated in the case of a three-phase short-circuit at no load. From transfer functions expressions (A.16), the line currents expression is computed just after a bold three-phase fault is applied to the terminal voltage. Detailed derivation can be found in [5]. Given an initial terminal

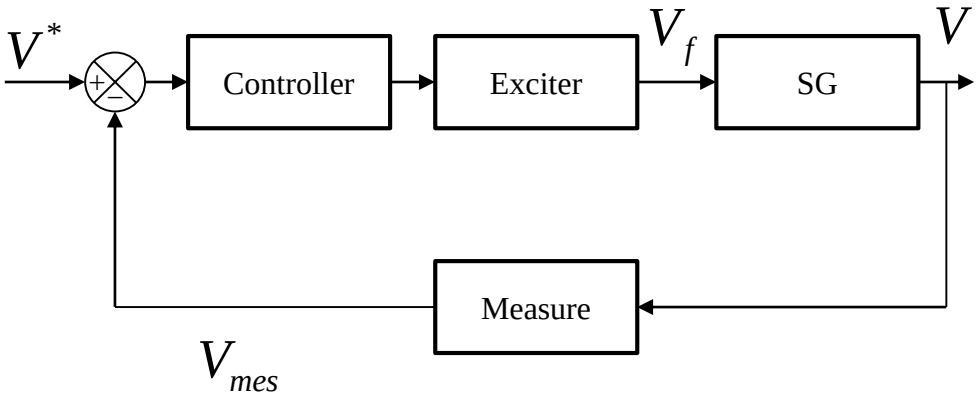

Figure 2.4 – Simplified scheme of the long-term control of the synchronous generator terminal voltage

voltage magnitude at no load of $V = E_{emf} = E_0 = 1\,p.u.$, the time-domain currents for round poles synchronous generators (saliency neglected) are given by:

$$i_a(t) = -E_0 \left[\frac{1}{x_d} + \left(\frac{1}{x'_d} - \frac{1}{x_d} \right) e^{-t/T'_d} + \left(\frac{1}{x''_d} - \frac{1}{x'_d} \right) e^{-t/T''_d} \right] cos\left(\omega_0 t + \theta_0\right) + \frac{E_0}{x''_d} e^{-\alpha t} cos\theta_0 \quad (2.11)$$

Where α is the damping term associated with the stator windings dynamics (their resistance is not neglected in this case), defined as the inverse of the time-constant $T_a \approx 0.2\,s$ (from table 2.7):

$$\alpha = \frac{r_a \omega_0}{x''_d} = \frac{1}{T_a} \quad (2.12)$$

The current expression (2.11) gives the magnitude during the first cycles following the fault. Note that a DC component in the phase-current is superimposed with a fundamental frequency component. The DC component appears when the phase-voltage is not equal to 0 when the short-circuit occurs, because the flux in the corresponding stator winding cannot vary instantaneously. The three-phases are plotted in fig. 2.5.

- When $t < T''_d = 0.05\,s$, and in the phase with worst case initial angle $\theta_0 = 0$, the current magnitude reaches up to $\frac{2E_0}{x''_d} = 10\,p.u.$

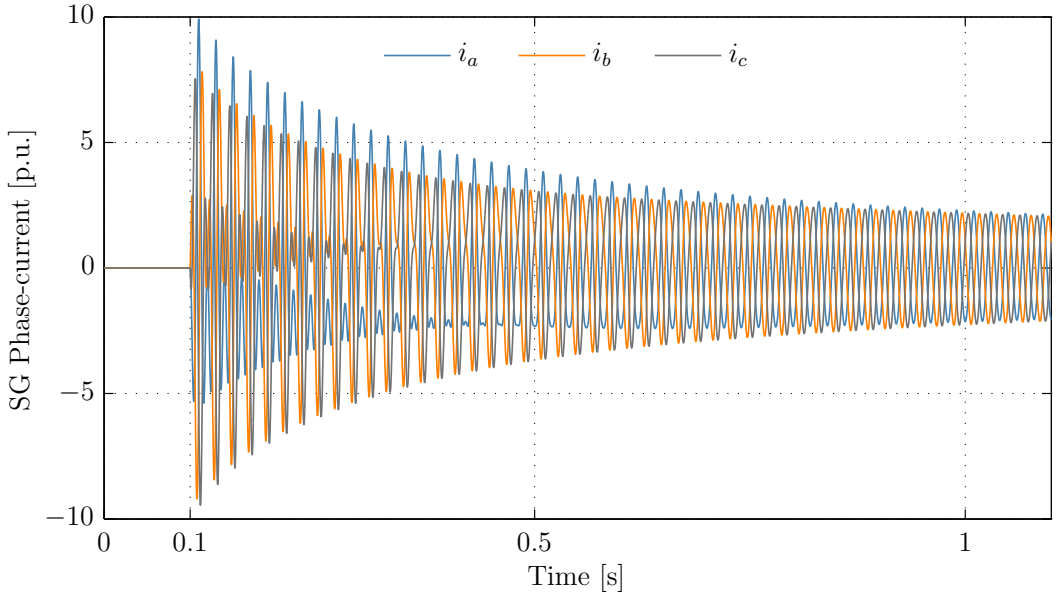

Figure 2.5 – The output phase-current of the synchronous generator following a three-phase short-circuit.

- Once $T_a = 0.2\,s << t < T'_d = 1.2\,s$, the DC transient vanishes and the current magnitude is limited under $\frac{E_0}{x'_d} = 4\,p.u.$
- In steady-state, the output current magnitude is maintained at $\frac{E_0}{x_d} = 0.5\,p.u.$

The synchronous generator stator is made of large coils with a large thermal inertia. They can handle temporary the 10 p.u. currents in the first cycles. Transient currents are therefore not a challenging constraint for the hardware of synchronous generators.

Note that faults can theoretically be even worst during three-phase grid-connection if the synchronous generator is connected in opposite phase-direction to an other voltage source. In this case, the current magnitude in (2.11) is multiplied by 2.

Variation of rotor speed and frequency stiffness In practice, the rotor speed varies during operation. The fixed frequency assumption must be validated by proving the frequency stiffness of the electrical source based on synchronous generator. After a full load current connection from no load, one can consider the torque $\Delta\Gamma_e$ is set to 1 p.u. This is a conservative assumption as the terminal voltage would drop noticeably before the voltage regulation compensates for it.

The mechanical equation of (A.1) gives the variation of the rotor speed $\Delta\omega_r$ for a single pole generator.

$$\frac{2H}{\omega_n}\frac{d\Delta\omega_r}{dt} = -\Delta\Gamma_e \tag{2.13}$$

$$\Delta\omega_r(t) = \omega_0 - \frac{\omega_n}{2H}\Delta\Gamma_e t \tag{2.14}$$

The parameter H depends on the physical inertia of the synchronous generator. H is expressed in seconds, representing the time after which the rotors loses half of its nominal speed, under nominal electromagnetic torque. Symmetrically, $2H$ is seen as the time to bring the rotor at its nominal speed, at no electrical load, when the nominal mechanical torque is applied. With a typical value of $H = 5\,s$, the variation $\Delta\omega_r$ in respect with the time under the nominal load ($\Delta\Gamma_e = 1$) gives the ROCOF of the system:

$$ROCOF = \frac{\Delta\omega_r}{\omega_n} = -\frac{1}{2H} = -0.1\,s^{-1} \tag{2.15}$$

Intrinsic inertia of the synchronous generator gives stiffness to the electrical frequency by guaranteeing a slow variation of rotor speed during load variation. Eq. (2.15) shows that for t<100 ms, the frequency is maintained in the range of ±1%. This value justifies neglecting the frequency variation during the study of electrical transients in the synchronous generator. Limiting the frequency drop over longer time requires a speed regulation by acting on the governor of the primary mechanical source and thus control the steady-state frequency.

Steady-state frequency control Transient limitation of the frequency drop following a load increase is guaranteed by the inertia of the synchronous generator as shown by equation (2.15). For longer time-scale, a load increase slows down the rotor speed and thus decreases the frequency. It is convenient to consider the power instead of the torque. For small deviation from initial state ($\Gamma_{m0} = \Gamma_{e0}$):

$$\begin{aligned}\Delta P_m - \Delta P_e &= \omega_0\left(\Delta\Gamma_m - \Delta\Gamma_e\right) + \left(\Gamma_{m0} - \Gamma_{e0}\right)\omega_r \\ \Delta P_m - \Delta P_e &= \omega_0\left(\Delta\Gamma_m - \Delta\Gamma_e\right)\end{aligned} \tag{2.16}$$

Assuming the initial rotating speed equals the nominal ($\omega_0 = \omega_n$), the eq. (A.1) is rewritten for small deviation:

$$2H\frac{d\Delta\omega_r}{dt} = \Delta P_m - \Delta P_e \tag{2.17}$$

In reality, the load power will drop with the frequency. Indeed, part of the loads are dependent of the frequency because of the presence of motors. The dependency of ΔP_e on the frequency is traditionally modeled by the coefficient D [17]:

$$\Delta P_e = \Delta P_L - D\Delta\omega_r \tag{2.18}$$

The D coefficient damps the electromechanical equation (2.17)

$$2H\frac{d\Delta\omega_r}{dt} = \Delta P_m - \Delta P_L - D\Delta\omega_r \tag{2.19}$$

According to the eq. (2.19), the frequency decreases to an extremely low frequency. To avoid large frequency deviation, the rotor speed must be controlled in closed-loop to limit the frequency drop by adjusting the mechanical power applied to the rotor shaft. A simplified closed-loop control scheme of a speed-governing action is illustrated in fig. 2.6. In case of standalone operation, an integral compensation can be included in the controller (see fig. 2.7) to cancel the frequency error in steady-state.

Speed control brings maintain the rotor speed close to the nominal value in several within seconds. When multiple generators are connected in parallel, pure integral control would result in conflicts because each speed-governors would try to control the frequency with its own dynamic characteristics. For parallel grid-forming capability, the speed-governor controller example of fig. 2.7 can be modified with a droop strategy as detailed in the next subsection.

2.2.2 Parallel grid-forming capability of synchronous generators

The grid-forming capability of the controlled synchronous generators must be completed by the function of table 2.5 to operate jointly on a transmission grid. The properties of the synchronous generators connected with an other voltage source (S closed in fig. 2.1) are analyzed here.

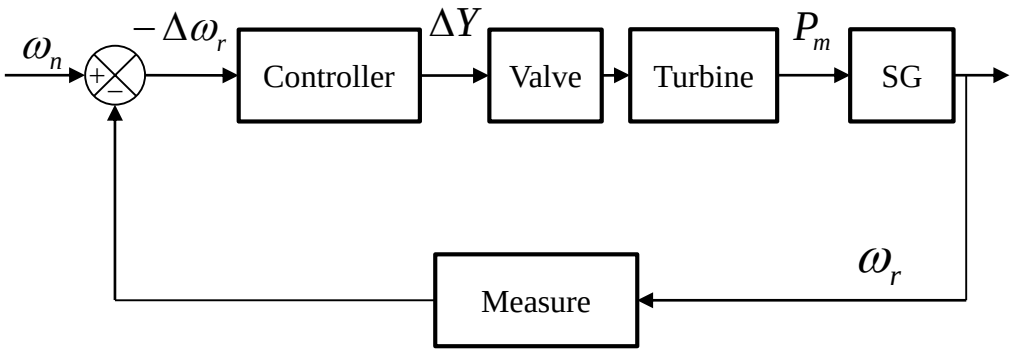

Figure 2.6 – Simplified scheme of the long-term control of the rotor speed of synchronous generators

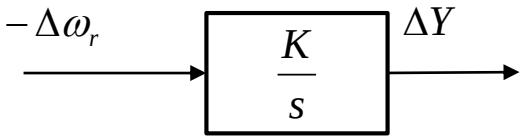

Figure 2.7 – Details of the speed-governor controller with an integration for non-error control in steady-state.

Synchronization The ability of the synchronous generator to stay synchronized with an other voltage comes from its intrinsic physical property. When a synchronous generator is connected to a voltage source, it forms a voltage-angle difference of δ_e, called the total internal angle, between the emf vector $\boldsymbol{e}_{emf}$ of the synchronous generator and the vector of the voltage source $\boldsymbol{v}_g$.

$$\delta_e = \omega t + \theta_{g0} - \theta + \frac{\pi}{2} \tag{2.20}$$

Where θ_{g0} denotes the initial phase-angle of the voltage source. The corresponding derivatives are:

$$\omega_r = \frac{d\theta}{dt} = \omega + \frac{d\delta_e}{dt} \tag{2.21}$$

$$\frac{d\omega_r}{dt} = \frac{d^2\delta_e}{dt^2} \tag{2.22}$$

One could demonstrate, as [5] that the electromagnetic torque depends only on total internal angle:

$$\Gamma_e = \Gamma_{es}(\delta_e) + \Gamma_{ed}(\frac{d\delta_e}{dt}) \tag{2.23}$$

$$\Gamma_m = \frac{2H}{\omega_n}\frac{d^2\delta_e}{dt^2} + \Gamma_{es}(\delta_e) + \Gamma_{ed}(\frac{d\delta_e}{dt}) \tag{2.24}$$

The eq. (2.24) exhibits a synchronizing torque Γ_{es} and a damping torque Γ_{ed}. The synchronizing torque is due to the interaction of the rotor field created by the field current and the stator field created by the connection to the voltage source. The damping torque is mainly due to the damping windings.

The generic expressions of Γ_{es} and Γ_{ed} are complex to derive, but they could be simplified when δ_e varies closely to the pseudo-oscillation given by the eq. (2.24), typically around 1 Hz for the considered size of synchronous generator. In this case:

$$\Gamma_{es} = \frac{\left(v_{d0} - x'_d i_{d0}\right) V_g}{x'_d + x_c} sin(\delta_e) + \frac{V_g^2}{2} sin(2\delta_e)\left(\frac{1}{x_q + x_c} - \frac{1}{x'_d + x_c}\right) \tag{2.25}$$

$$\Gamma_{ed} \approx \frac{V_g^2 T_q''}{x_q''} \frac{d\delta_e}{dt} \tag{2.26}$$

For a small variation of the total internal angle, eq. (2.24) becomes:

$$\Delta\Gamma_m = \frac{2H}{\omega_n}\frac{d^2\Delta\delta_e}{dt^2} + \frac{v_g^2 T_q''}{x_q''}\frac{d\Delta\delta_e}{dt} + \left[\frac{\left(\left(v_{d0} - x_d' i_{d0}\right) v_g}{x_d' + x_c} cos(\delta_{e0}) + \frac{v_g^2}{2} cos(2\delta_{e0}) \left(\frac{1}{x_q + x_c} - \frac{1}{x_d' + x_c}\right)\right] \Delta\delta_e \tag{2.27}$$

The small-signal dynamic of $\Delta\delta_e$ depends on physical parameters of the synchronous generator such as the inertia, the transient d-axis reactance, the subtransient q-axis reactance, the connection inductance value, and the initial steady-state. Numerical application for the following values:

$$\begin{aligned} v_{d0} - x_d' i_{d0} &= V_g = 1\,p.u. \\ \delta e0 &= 45 deg. \\ H &= 5\,s \\ x_c &= 0.15\,p.u. \\ x_d' &= 0.25\,p.u. \\ x_q'' &= 0.4\,p.u. \\ T_q'' &= 0.04\,s \end{aligned} \tag{2.28}$$

$$\Delta\Gamma_m = 0.03\frac{d^2\Delta\delta_e}{dt^2} + 0.1\frac{d\Delta\delta_e}{dt} + 1.8\Delta\delta_e \tag{2.29}$$

Giving roots of the characteristic equation:

$$s \approx -1.7 \pm j7.6 \tag{2.30}$$

The roots values (2.30) show that δ_e has an oscillating but damped dynamic, keeping the rotor angle synchronized with the voltage-source angle. The pseudo-oscillation of at 7.6 $rad.s^{-1}$ (1.21 Hz) validates the approximations of almost 1 Hz variation, in the simplified expression of the damping torque and the synchronous torque. The intrinsic physical oscillating behavior of synchronous generators in parallel is responsible for subsynchronous oscillations in the power

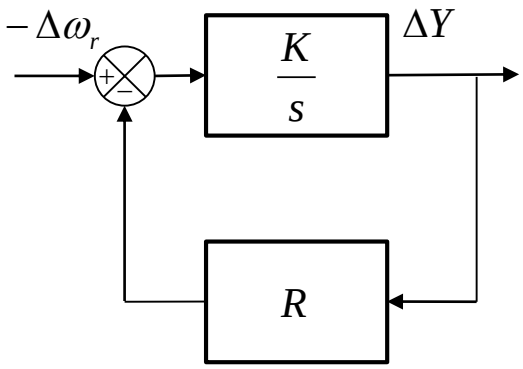

Figure 2.8 – Details of the speed-governor controller with an integration for non-error control in steady-state.

system. This phenomenon is highly undesirable and still provoke stability concerns at large geographical scales nowadays. There is a hope that converter based system can get ride of this issue.

Load share As previously noted, the integral speed control does not allow a load sharing between synchronous generators units. In case of different closed-loop dynamics, the controls will fight each other to imposed the final frequency. To effectively share the load, a static droop control is introduced into the speed control shown in fig. 2.8. In practice, there is no integral compensation in the speed control of actual power plant. A proportional controller is sufficient to implement the droop law. The steady-state error is corrected through a centralized secondary frequency control.

Stability of a synchronous generator based power system The stability of interconnected synchronous generators have been extensively documented over the years. In small-signal sens, additional controls, such as the power system stabilizer, have been included to increase the damping. Those controls also contribute to a better large-signal stability. In the case of synchronous machine, the large-signal stability is called traditionally the transient stability and concerns the ability of the synchronous generator to stay synchronized after a fault.

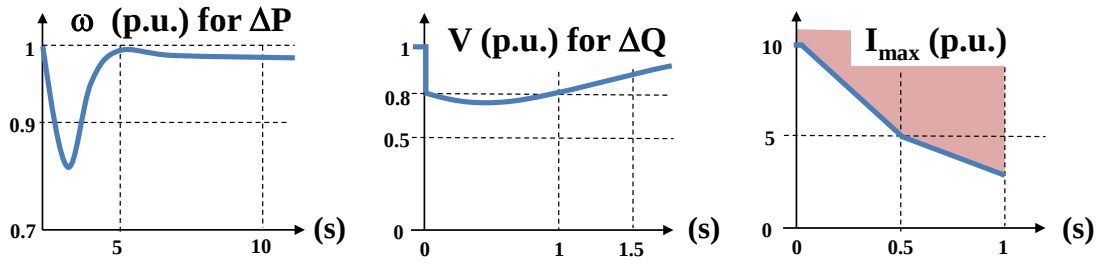

(a) Frequency dynamic (b) Voltage magnitude dynamic (c) Overcurrent capability

Figure 2.9 – Properties of the grid-forming function of a synchronous generator

2.2.3 Conclusion on the parallel grid-forming capability of synchronous generators

The grid-forming capability of a synchronous generator is formed by its physical properties and its rather slow acting controls. Transiently, the stiffness of the voltage source behavior is illustrated roughly on fig. 2.9. In response to a nominal load connection, the frequency dynamic is limited by the large mechanical inertia H of the synchronous generator (fig. 2.9.a). The frequency dynamic is often quantified by the "rate-of-change of frequency", $ROCOF = \frac{1}{2H} \approx 0.1\,rad.s^{-1}.(p.u.)^{-1}$. The transient voltage drop following a reactive load connection is limited by the low transient $x^{'}$ and sub-transient reactances $x^{''}$ (fig. 2.9.b). The short-circuit capacity is commonly used to characterize this stiffness of the voltage magnitude: $S_{cc} = \frac{V_0}{x^{'}} \approx 5\,p.u.$ Meanwhile, the consequence is high transient overcurrent that the synchronous generator can easily withstand because of its large thermal capacity (fig. 2.9.c). In electrical steady-state, the field current control regulates the RMS value of the terminal voltage within seconds, whereas the rotation speed control maintains the frequency in acceptable range.

The parallel grid-forming capability is performed through the natural presence of the synchronizing and damping torques when the synchronous generator is linked by an AC line to another voltage source. Load-sharing is further obtained by introducing a steady-state power to frequency droop characteristic in the rotor speed regulation. The small-signal and large-signal stability of interconnected synchronous generators has been proved and improved over the years.

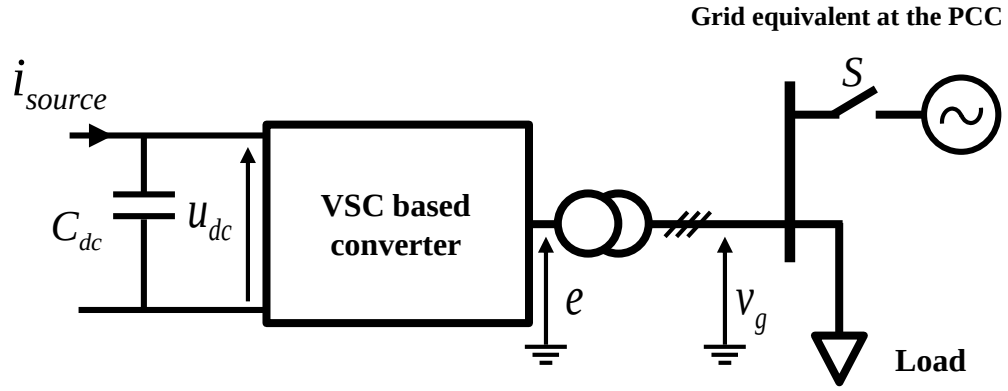

Figure 2.10 – The considered grid-connected VSC system comprises a DC primary source, a DC capacitor, and a VSC.

2.3 Power system based on VSC-based electrical sources

Last two decades have seen the emergence of static electrical converters able to create autonomously a sinusoidal voltage waveform, provided a DC voltage source. Initially developed for motor drives in various applications, they have been adapted in power system to interface renewable generation or HVDC link. VSC-based converters are candidates to provide grid-forming functions to the grid. The sections analyses the physical properties of the VSC system of fig. 2.10 based on its model to derive the control requirements for parallel grid-forming applications in an interconnected network.

2.3.1 Model of a Voltage Source Converter

Voltage Source Converters (VSCs) are different from Line Commutated Converters (LCCs) because of their ability to force self-commutation on their switches with no assistance from the grid. Therefore, the VSCs produce their own AC voltage waveform from a DC voltage source, independently of the rest of the connected system. One could have also talked about a "voltage-sourced converter".

Basically, two main layout of switches exist between a DC voltage source and an AC system. The two-level (or three-level) converter principle is based on a temporal modulation, the pulse-width-modulation (PWM). Each phase is connected alternatively to the upper DC voltage and

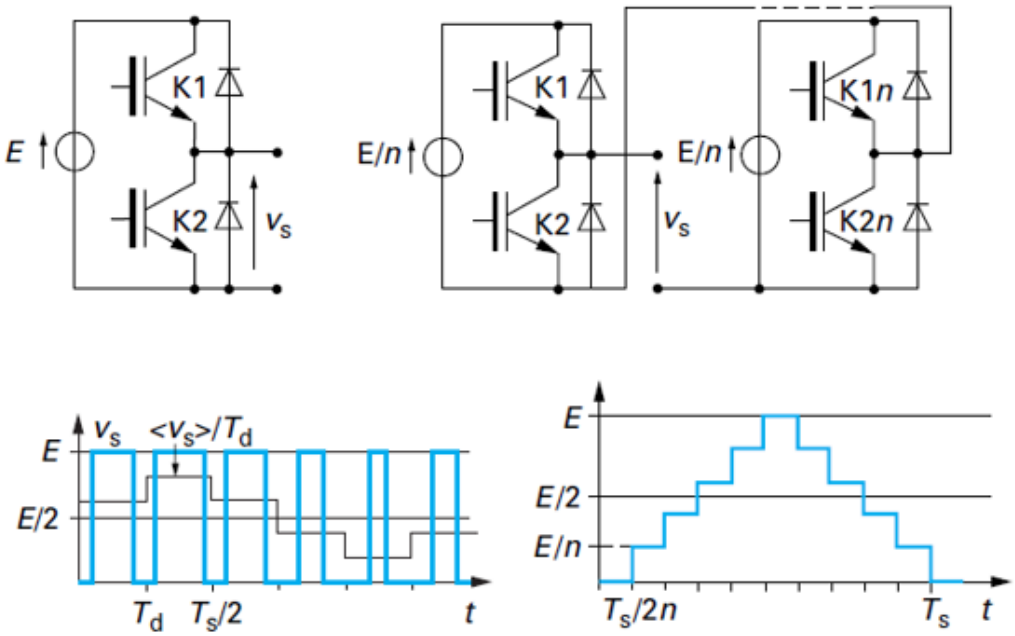

Figure 2.11 – Two main layout of switches in VSC for two modulation types.

to the lower DC voltage, following a chosen sequence, such that the fundamental component of the modulated voltage has the desired form. After the filter stage, the VSC terminal voltage resembles to the fundamental voltage component of the VSC modulated voltage.

The MMC converter distributes the DC source between a certain amount of voltage levels and realizes an amplitude modulation. Each phase are connected to the voltage level corresponding to the sinewave value at a given time. The harmonic purity of the modulated voltage requires a smaller filter than for a two-level converter. One advantage of the MMC is to have an extra degree of freedom on the DC side to manage the stored energy in the distributed capacitors, for example in [18]. The MMC technology spreads in power system applications, since its modular structure easily scales up to high-voltage and high-power with low losses. The interested readers will find more information on converters topologies and modulations techniques in [19]. The rest of the thesis refers to the PWM technology when needed.

As looked from the AC side, at the terminal voltage (see fig. 2.12), both VSC technologies can be treated as a modulated voltage source behind a filter stage:

$$v_{mabc}(t) = m_{abc}(t)\frac{v_{dc}(t)}{2} \tag{2.31}$$

Where $m_{abc}(t)$ is the chosen modulation signal for each phases.

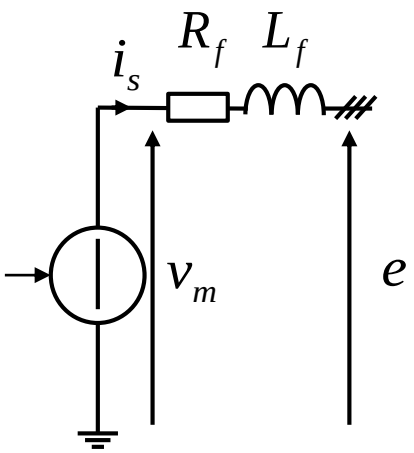

Figure 2.12 – A VSC modeled by a modulated voltage source behind the filter inductance (choke).

Table 2.8 – VSC output filter inductance typical values

Parameter	Value
$x_f = l_f \omega_n$	$0.15\,p.u.$
r_f	$0.005\,p.u.$

In practice, the controllable voltage source is not an ideal voltage source but has a limited dynamic because of the computation and switching delays in PWM technology. The rated voltage and current limitations must also be taken into account.

2.3.2 The grid-forming capability of a VSC

From the VSC model of fig. 2.12, the expression of the modulated voltage (2.31) and typical filter parameters in table 2.8, the grid-forming functions of table 2.4 are assessed in standalone (S open). The eq. (2.31) is non-linear. To study the grid-forming behavior of VSC, the DC voltage is first assumed to be constant, and then, the variation of the voltage is taken into account.

Source of sinusoidal waveform voltage A three-phase sinusoidal waveform can be obtained with a suited modulation $m_{abc}(t)$, with instantaneously controllable amplitude, frequency and initial phase angle. In this case, the modulated voltage $v_m(t)$ can be replaced by its fundamental component that impacts similarly the terminal voltage, after the filter stage. For example, the

phase "a" of the modulated voltage can be replaced by the expression:

$$v_{ma}(t) = M(t)cos\left(\omega^* t + \theta_0\right)\frac{v_{dc}(t)}{2} \tag{2.32}$$

Provided that the DC voltage is maintained at a constant value and that the VSC dynamics are neglected, the VSC behaves as a sinusoidal voltage source behind the filter inductance, with controllable voltage amplitude and frequency:

$$v_{ma}(t) = V_m^*(t)cos\left(\omega^* t + \theta_0^*\right) \tag{2.33}$$

VSC terminal voltages can then be expressed in per-unit, in a dq-rotating frame. For a direct comparison with the synchronous generator expressions, the rotating angle $\theta^*(t)$ is taken such that $v_{mq} = 1$ and $v_{md} = 0$.

$$\begin{cases} e_d = v_{md} - l_f\frac{di_{sd}}{dt} + l_f\omega^* i_{sq} - r_f i_{sd} \\ e_q = -l_f\frac{di_{sq}}{dt} - l_f\omega^* i_{sd} - r_f i_{sq} \end{cases} \tag{2.34}$$

In steady-state, the VSC terminal voltage e has the same fundamental frequency component as the modulated voltage v_m. Provided sufficient harmonic filtering, the terminal voltage assimilated to a pure three-phase sinusoidal voltage.

Transient frequency stiffness By definition, the fundamental frequency of the VSC modulated voltage is fixed after the reference ω^*. The VSC has theoretically an infinite frequency stiffness as the frequency does not depend on the load currents. If the frequency reference is provided by a feedback control, it may introduce a load dependence, and thus a non-infinite frequency stiffness.

Transient voltage amplitude stiffness The transient voltage drop following a reactive current demand can be calculated with (2.34). To study the equation in Laplace domain, the VSC frequency reference is fixed at the nominal frequency: $\omega^* = \omega_n$.

$$\begin{cases} e_d = v_{md} - l_f s i_{sd} + l_f\omega_n i_{sq} - r_f i_{sd} \\ e_q = -l_f s i_{sq} - l_f\omega_n i_{sd} - r_f i_{sq} \end{cases} \tag{2.35}$$

Similarly to section 2.2.1, the response to a load current step $i_{sd}(t > 0) = \Delta i_{d1}$ is studied. The resistances are neglected:

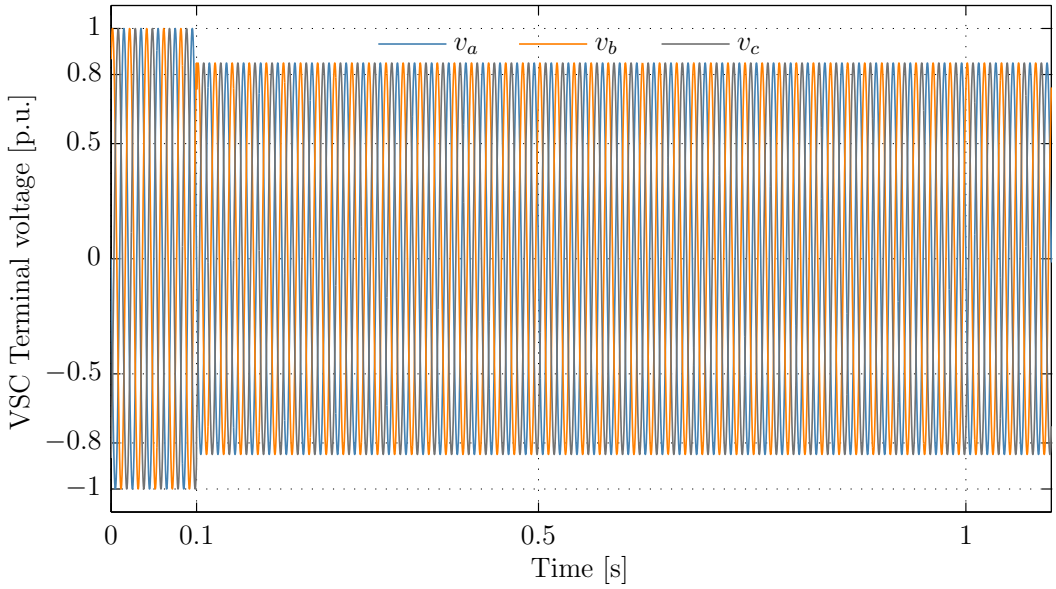

Figure 2.13 – The terminal phase-voltages of the VSC following a load connection.

$$\begin{cases} \Delta e_d(s) = -l_f s \Delta i_{sd}(s) \\ \Delta e_q(s) = -l_f \omega_n \Delta i_{sd}(s) \end{cases} \tag{2.36}$$

With $\Delta i_{sd}(s) = \frac{\Delta i_{d1}}{s}$

$$\begin{cases} \Delta e_d(s) = -l_f s \Delta i_{sd}(s) \\ \Delta e_q(s) = -l_f \omega_n \Delta i_{sd}(s) \end{cases} \tag{2.37}$$

The expression form of the terminal voltage variation (2.37) is similar to the expression in the synchronous generator case (2.4). The differences is that l_f is not frequency dependent as $l_d(s)$ is. The resulting time domain phase voltage (2.8) can then be transposed by taking $x_d = x'_d = x''_d = x_f$.

$$v_a(t) = \left\{ v_{mq0} - i_{d1} x_f \right\} \cos\left(\omega_n t + \theta_0\right) \tag{2.38}$$

The three-phases are plotted in fig. 2.13. Eq. (2.38) and fig. 2.13 indicate that the voltage magnitude drop occurs directly after the load connection and stays the same until the steady-state. Compared to the synchronous generator, the short-term voltage transient is smaller following a load increase as the filter inductance x_f is usually inferior to the subtransient reactance x''_d. Consequently, the VSC basically provides a stiffer voltage amplitude. This natural property of VSC

Table 2.9 – VSC output current limits

Current	Limit
First cycle magnitude limit	$i_s(t) < 1.4\,p.u.$
Steady-state magnitude limit	$I_s < 1.2\,p.u.$

is, however, not reachable in practice. As seen later, the device protection constraints requires the instantaneous voltage to be controlled in closed-loop.

Steady-state voltage control In steady-state, when the frequency reference ω^* is kept close to the nominal frequency, the terminal voltages are:

$$\begin{cases} e_d = v_{md} + x_f i_{sq} - r_f i_{sd} \\ e_q = -x_f i_{sd} - r_f i_{sq} \end{cases} \tag{2.39}$$

Eq. (2.39) shows that a full load connection results in a small amplitude drop of the steady-state terminal voltage. Using typical output reactance value of table 2.8, and neglecting the resistance, a voltage drop of 0.15 p.u. is expected, from no load to full reactive current. Only small regulation efforts are needed to keep the terminal voltage within acceptable limits in steady-state, by acting on the reference VSC voltage amplitude V_m^*.

Hard transient resilience The VSC devices connected to the grid are subject to high transients, during line tripping or short-circuit. The sensitivity of the VSC to hard transients is illustrated in the case of a three-phase short-circuit at no load. With similar developments as in section 2.2, the line current expression following a three-phases short-circuit at the VSC terminal is:

$$i_{sa}(t) = \frac{V_m^*}{x_f} sin\left(\omega_n t + \theta_0\right) + \frac{V_m^*}{x_f} e^{-\alpha_f t} sin\theta_0 \tag{2.40}$$

Where α_f is the damping term associated with the filter dynamics (the filter resistance is not neglected in this case), the inverse of the time-constant $T_f \approx 0.1\,s$ (from table 2.8):

$$\alpha_f = \frac{r_f \omega_n}{x_f} = \frac{1}{T_f} \tag{2.41}$$

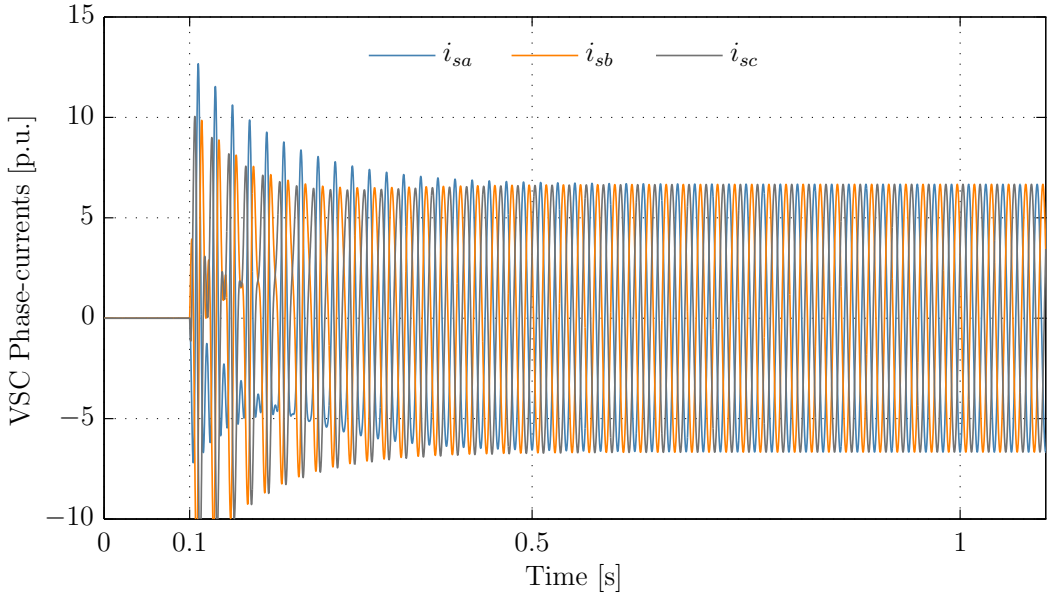

Figure 2.14 – The output phase-current of the synchronous generator following a three-phase short-circuit.

The three-phases are plotted in fig. 2.14. Depending on the initial phase-angle, the phase current could theoretically raise up to $\frac{2V_m^*}{x_f} = 13\,p.u.$ in the first 100 ms after the short-circuit. Such overcurrent would lead to instantaneous destruction of the device, as the VSCs are based on semiconductor switches with very low thermal inertia. In this thesis, acceptable overcurrent limits are defined in table 2.9. These values are arbitrary chosen to be realistic for high-power applications, at reasonable costs. Compared to the admissible current of the synchronous generators, the overcurrent capacity of VSC are very limited.

The VSC must be actively protected from overload when the load impedance is very low [20]. The way the current is limited has a strong influence on a full VSC based power system stability.

DC voltage variation during full-load connection In practice, the storage device on DC side is limited in power rating and cannot react instantaneously to load changes. Consequently, a current load change in the AC side induces a variation of the DC voltage. If the voltage variation is large, the fixed DC voltage assumption does not hold, and the AC voltage amplitude stiffness is not guaranteed. The paragraph analyses the DC voltage variation during a full load connection

to deduce a design requirement on the DC short-term storage to maintain short-term DC voltage in acceptable range.

An active power consumption on the AC side causes the DC voltage to decrease with the energy stored in the DC capacitor. The simplified DC dynamics is ruled by the equation:

$$\frac{1}{2}C_{dc}\frac{dv_{dc}^2(t)}{dt} = P_{source}(t) - P_e(t) \tag{2.42}$$

Where $P_{source}(t)$ is the DC power fed by the primary source and the DC storage device, and $P_e(t)$ is the active power demand on the AC side. In small deviation from an initial operating point where $P_{source}(0) = P_e(0)$, and $v_{dc} = v_{dc0}$ gives:

$$C_{dc}v_{dc0}\frac{d\Delta v_{dc}}{dt} = \Delta P_e \tag{2.43}$$

The electrostatic constant H_{dc} is often defined from the nominal DC voltage v_{dcn} and the nominal AC power P_n by:

$$H_{dc} = \frac{1}{2}C_{dc}\frac{v_{dcn}^2}{P_n} \tag{2.44}$$

Combining eq. (2.44) and (2.43) yields:

$$2H_{dc}\frac{v_{dc0}}{v_{dcn}^2}\frac{d\Delta v_{dc}}{dt} = \frac{\Delta P_e}{P_n} \tag{2.45}$$

Considering an initial state at nominal value ($v_{dc0} = v_{dcn}$), a DC voltage drop of $\Delta v_{dc} = 10\%v_{dcn}$ following an AC load variation of $\Delta P_e = P_n$ is reached after a time $t_{10\%}$ determined by:

$$t_{10\%} = \frac{2H_{dc}}{10} \tag{2.46}$$

The value of H_{dc} ranges typically between 40 ms and 80 ms considering the natural capacitance of DC cables and the DC filter capacitor [18]. Hence, $t_{10\%}$ is situated around 10ms.

Limiting the DC voltage drop to 10% following an 100% of load increase requires DC fast storage device (batteries, supercapacitor, etc.) to react within 10 ms. This power source dynamic requirement is hundred times higher than for synchronous generator.

The VSC reference can be adjusted from DC voltage measurements to compensate for remaining variations on the voltage of the DC side. Thus the AC side amplitude can keep a fixed

value $V_m^*(t)$.

$$M(t) = \frac{V_m^*(t)}{v_{dc_mes}(t)} \tag{2.47}$$

With DC voltage compensation, the non-linearity in eq. (2.31) is avoided, and AC controls can be applied independently from DC voltage. On the other hand, the DC voltage compensation removes the passive behavior of the DC capacitance that decreases the voltage during AC current demand. This behavior is interesting during transients to limit the current spike. The impact of the DC voltage regulation from storage device as well as the DC voltage compensation should have an impact on stability of the AC system in the case of grid-forming controls and deserve more investigation on how strongly ac and dc dynamics are coupled. In this thesis, a constant DC voltage is always assumed.

2.3.3 Parallel grid-forming capability of VSC

The prerequisite for parallel grid-forming capability listed in table 2.5 are assessed in the case of VSCs to highlight the missing features.

Synchronization All the interconnected VSC follow on their own frequency reference. The frequency reference could be fixed at the nominal frequency to operate a isochronous system. This solution is, however, technically impossible. The frequency reference accuracy is dependent on the VSC internal clock-rate. The processor clock-rate is determined by a resonator, usually based on quartz-oscillator. The short-term accuracy of quartz-oscillators is excellent, but all resonators suffer from long-term accuracy, caused by aging, pressure or temperature or by technological dispersion. As a consequence, the frequency references can drift over the time.

The problem of frequency drift can be observed on a system of two interconnected VSCs of fig. 2.15 connected by their terminals. The frequency difference between the two VSCs would result in unacceptable power oscillations through the grid.

Some authors suggested to use GPS signal as a re-synchronizing link the references periodically [21],[22], [23], [24]. These solutions, however, are not compatible with the requirement for autonomous operation of units in transmission grid because they rely on a critical GPS signal. The synchronization between converters is not natural compared to synchronous generators,

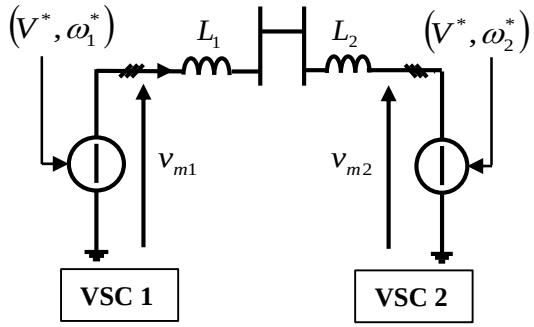

Figure 2.15 – 2 VSCs represented by three-phase voltage sources behind inductive filters, connected at their terminal.

but different techniques based on local measurements could be employed as shown in the next chapter.

Load sharing As soon as the interconnected VSCs share a common frequency, they can share any load. The load sharing technique will depend on the synchronization mechanism.

Small-signal and large-signal stability of a VSC-based power system VSC devices have no moving parts but rely on forced commutations. They do not have intrinsic stability issues without feedback controls. However, when the VSC are controlled as parallel grid-forming source, they need additional controllers. Each of these controls interact with the grid dynamics, and other VSC controls inducing stability issues. Three potential sources of instabilities are suspected: the synchronization strategy, the voltage control strategy, and the current-limiting strategy. It is strongly believed that the DC voltage control also plays a role in the AC stability but this aspect is out of the scope of the thesis.

2.3.4 Conclusion on the parallel grid-forming capability of VSCs

The VSC based devices are good candidate to provide parallel grid-forming function to the transmission grid as illustrated roughly on fig. 2.16 because its following characteristics in open-loop:

- Sinusoidal voltage-source with fast controllable amplitude, frequency and phase-angle

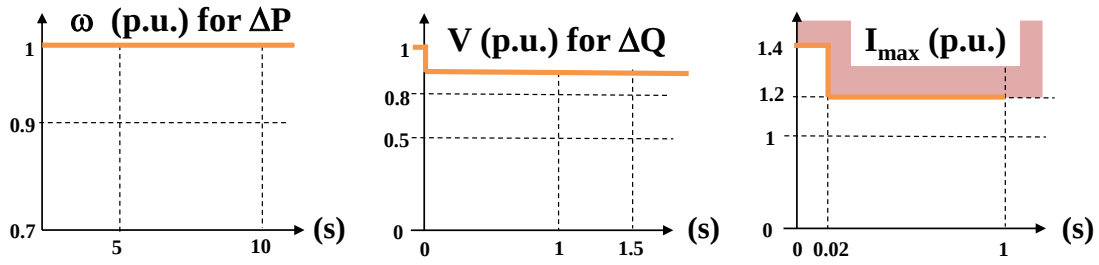

(a) Frequency dynamic (b) Voltage magnitude dynamic (c) Overcurrent capability

Figure 2.16 – Properties of the VSC in open-loop

- Theoretically infinite frequency stiffness (fixed frequency) (fig. 2.16.a)
- Strong voltage amplitude stiffness in during transient (fig. 2.16.b)

However, owing to the VSC nature and to its poor overload capability (c), the following functions must be added by the control:

- Closed-loop instantaneous voltage control including a current limiting action
- Synchronization mechanism
- Steady-state voltage control
- Small-signal stability of the voltage and synchronization controls
- Large-signal stability during current limiting action.

The next section reviews the control solution presented in the literature to provide those functions.

2.4 State-of-the-art of grid-forming VSC

Historically, the VSC have been developed for the drive of electrical machines. Some applications, though, have seen the emergence of VSC controlled in grid-forming mode. The application scope is wide from local standalone system for back-up generation, to transmission grid interfaces. The developments of grid-forming converters in different fields have been conducted and studied apart, following two-different approaches, but answering the same challenges. The first direction

started from a standalone system in small Uninterrupted Power System to build a larger system of multi-devices operating in parallel, until creating a Microgrid. The other direction started from developing power system support in critical cases where the grid lacks from frequency or voltage support. The section reviews the main trends in the literature for VSC controlled in grid-forming to evaluate how both research fields can contribute to answer the power system needs presented in the chapter.

2.4.1 Grid-forming VSCs in small, medium-voltage systems

Early developments on paralleling grid-forming VSC in line interracting UPS started with [25], [26]. A first implementation of frequency droop control is tested successfully as a synchronization mechanism that also ensures load sharing. From this preliminary results, several droop scheme improvements are reported to provide faster reaction to load changes. It includes transient droop controller, adaptive droop, angle droop function, adaptation to resistive output impedance in low voltage grid seen by the VSC control [27], [28], [29], [30], [31], [32].

Larger and heterogeneous systems of multi-power sources called Microgrid have been next deeply investigated. Microgrids could be considered as a future feature of power system aggregating distributed energy resources at the local scale, encouraged by all smart-grid initiatives [33]. As the microgrids must be able to operate autonomously, apart from the main grid, the fundamental role of grid-forming converters (also called VSI for Voltage Source Inverter) has been underlined [34], [35], [36], [37],[38],[39], [9], [40], [41], [42], [43]. In all these reference works, the inner control of the converters dynamics are neglected and microgrid stability analysis focused on power controls interaction [44], [37], [45].

Some authors focused specifically on the inner voltage control design of grid-forming converters in Microgrids [46], [47] [48], but they based the design on internal model of the filter rather than on stability of the whole system. To adapt to every situation, a common solution in Microgrid is to switch from an islanded control mode to a grid-connected mode, based on a centralized breaker information [46], [49], [50]. Thus, the challenge is to build a "flexible" inner voltage control, with a fixed structure, that can survive to islanding and grid-connected situations. This challenge has been also noted in [51]. The proposed solutions are often complex [52], [53], or based on estimation of the grid frequency by a PLL [54], [55], [56], [57].

When the terminal voltage control is taking into account in stability studies in [58, 31, 59], they are shown to have less influence on stability than power controls, even in the presence of active load [60]. Indeed, the results have been validated with medium-sized with very fast dynamics that are quickly damped.

The impact of current-limiting strategies of grid-forming VSCs during faults in the Microgrid has been marginally studied, for example in [61], [62], [20], [50], [55], [63], [64], [65]. Among these studies, [20], [63] were concerned only by the power quality issues during limitation and not on the induced stability problems cause by the loss of power control of VSC.

2.4.2 Grid-forming VSCs in weak grid or low inertia power system

In high power application, grid-forming VSCs control have been proposed to support respectively the voltage amplitude or frequency when the grid is considered respectively as weak or with low inertia. A weak grid is a connection node far from a grid-forming generation units, so, far from the last tightly controlled voltage node. As a consequence, a current injection in a weak grid results in a large voltage variation. When the VSCs are controlled in grid-feeding mode, instabilities could arise [66], [67]. Particularly, the destabilizing role of the PLL in weak grid conditions has often been underlined [68], [69], [70], [71], [72], [73], [74], [75], [76]. Accordingly, several attempts tried to mimic the behavior of synchronous generation to stay synchronized with the grid without PLL. Different name have been given to those controls structure: "power-synchronization" [66], "Virtual Synchronous Machine" (VSM) [77], [78], [79], "Virtual Synchronous Generator" (VSG) [80], [81], [82], "Synchroverter" [83], "Swing-Equation-Based-Inertial-Response" (SEBIR) [11]. All the control schemes consist in adjusting the frequency reference according to the output power measurement. The power-frequency dependence recreates virtually the synchronization torque that stabilizes the voltage angle, and thus, the frequency. A discussion around these different control schemes is proposed in the next chapter 3. When the VSCs are controlled in grid-forming with a frequency reference deduced from an active power measurement, the system exhibits a better stability in weak grid conditions [66], [74], and also support the frequency in low-inertia system [84], [11]. Note that the "VSG" concept, as proposed by [85], [86], [87], [88], [89], is based on a PLL associated with grid-feeding VSC. As no grid-forming capability is included, such control scheme cannot feed a passive load. These types of

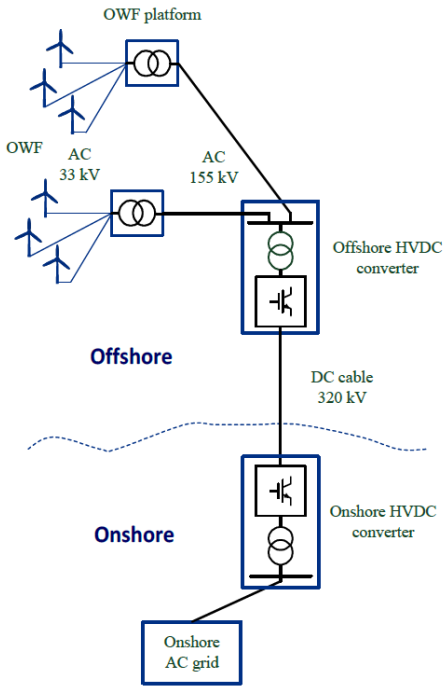

Figure 2.17 – Offshore wind farms linked through an HVDC to the continental transmission grid [4]

VSG are more related to "virtual (synthetic) inertia emulation" concept, where converters react to fast ROCOF by power injection [90], [14]. Note further that, the original VISMA concept from [91] uses a detailed model of the synchronous generator to inject emulated stator currents from voltage measurement, without the need of PLL. The VISMA based on current injection showed limits to preserve a pure sinusoidal waveform in islanded conditions, especially at no load [92]. Alternatively, [92] suggests a direct voltage control of the VSC, closer to the one proposed by [83], providing grid-forming capability.

Removing the PLL is interesting to keep an easier understanding of a large power system dynamics. The blind emulation of synchronous generators with their advantages and disadvantages is, however, not believed to be the best approach. In all the presented scheme, the parameters of VSG are tuned to recreate fast synchronous generators, not to expand the stability limits of large interconnected system.

2.4.3 Grid-forming VSCs in Offshore windfarm park

Several offshore wind farms have been built lastly in the north of Europe. The main connection scheme layout is represented in fig. 2.17. Traditionally wind turbines are interfaced with converters of type 4, controlled in grid-feeding mode, whereas the offshore converter of the HVDC acts as the only master grid-forming converters. In the case where the HVDC converter blocks, the system is prone to resonnance instabilities because of the current injection of wind turbines [4, 93]. Consequently, a novel grid-forming control for wind turbine converters has been suggested recently in [94, 93] to withstand faults on the HVDC. The proposed control defines a new standard approach for large grid-connected converters that can survive islanding. The chosen approach uses a terminal voltage estimation still based on a PLL. The PLL is associated with a power control that includes droop characteristic to stay synchronized. This promising approach is, however, not compatible the choice of removing all the PLLs of our system.

Conclusions on the new challenges of VSC based transmission system

In this chapter, the fundamental requirements of electrical sources have been formulated to provide the transmission grid services summarized in table 2.2. The first requirement is to provide grid-forming capabilities, to supply the loads with enough quality. The grid-forming capability is defined as the ability to apply a stiff voltage sinusoidal waveform to the sources terminal, with regulated amplitude and frequency in steady-state.

The second requirement is to operate grid-forming sources in parallel to ensure redundancy of feeding paths. Parallel operations are obtained if all electrical sources converge to a consensus frequency in steady-state, if the load demand is shared between sources, and if the interconnected system is stable.

These requirements must be observed by the sources in compliance with their intrinsic physical constraints and with the transmission grid operating needs. These needs are summarized in table 2.3. Traditionally, the synchronous generators fulfilled the above requirements, because of their physical properties (a sinusoidal windings distribution, a small transient reactance, mechanical inertia) and slow acting controls of the terminal voltage and of the rotation speed.

VSCs are good candidates to provide grid-forming capabilities to the transmission system but some complementary features do not naturally exist and must be designed properly for parallel operation on transmission grid:

- A stable power-frequency control based on local measurements must ensure that all units converge to the same frequency,
- A load sharing function,
- A voltage control in steady-state,
- A tight regulation of instantaneous output electrical quantities in closed-loop to avoid overcurrent during normal operation or fault,

- A careful design of control parameters to keep the system stable and damped in any configurations, from standalone, to grid-connected in a large system.

A large diversity of grid-forming controls of VSC have been proposed in the literature. Either for full-VSC based system in local application like UPS, Microgrids, and offshore wind farms, or for transmission grid-connected application for voltage or frequency support. The present thesis aims at taking advantage of these two distinct research fields to draw a design methodology to construct a full-VSC transmission grid.

Compared to local application like UPS, Microgrids, and offshore wind farms, the additional transmission grid constraints are:

1. High-power converters, which limit the inner closed loop control bandwidth, specifically in the case of PWM-VSC
2. Variable grid topology and situations. The VSCs must operate in standalone or in grid-connected situation, seamlessly, in stable manner, with a fixed control structure.
3. Unpredictable grid events
4. Large transient stress

Compared to grid-connected application, the grid-forming VSC in full-VSC transmission grid must be able to operate in parallel as well as in standalone situation. In this context, the output current limitation has not been studied yet.

Chapter 3

Synchronization and power exchange control of two voltage-sources on a transmission grid

Contents

3.1 Dynamic modeling of a full VSC-based power system 84

3.2 Synchronization one voltage source with the other fixed voltage source ("infinite bus") 96

3.3 Synchronization of two voltage sources and link with droop control . 103

3.4 Toward generalization of small-signal and large-signal stability of multiple droop-controlled VSCs, in a scalable, radial or meshed grid 112

3.5 Transient load-sharing capabilities of droop-controlled voltage-sources 117

Regardless their technology, the VSC converters are naturally controllable AC voltage-sources as they modulate a DC voltage source. In this sense, they provide the function grid-forming by creating a sinusoidal waveform at their terminals. On a power system, the voltage angular frequency and amplitude of the fundamental wave, applied to the transmission grid, are independently controllable by the VSCs, with a bandwidth twenty to fifty times higher than the nominal frequency. Interfacing independent and autonomous controllable voltage-sources on the transmission grid requires understanding their interaction in terms of power exchanges. This

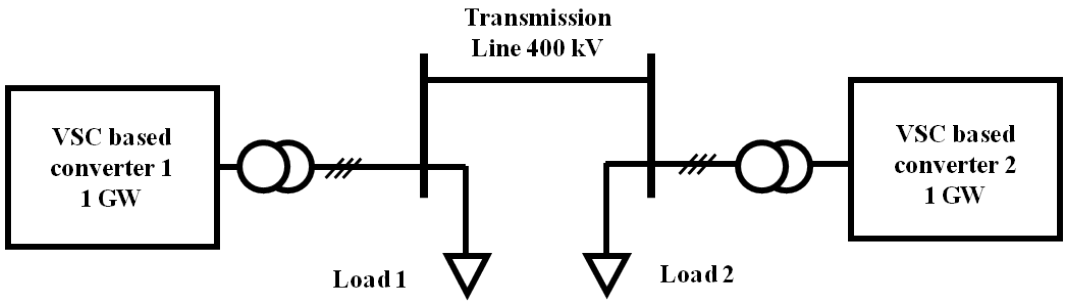

Figure 3.1 – Basic VSC-based power system

chapter recalls some founding principles about power exchange between two voltage sources and explores the control opportunities to make the voltage-sources operate in parallel through a transmission grid network. It claims that fast-acting power electronics are an opportunity for tight regulation of power flows through the network, but also excite new dynamics. Based on this observation, it is shown why droop-controlled voltage-sources give the system a locally stable synchronization between VSCs, under certain conditions that shall be observed. To scale up the stability conditions of the two voltage-sources system, the recent analytic studies on generalization toward a random meshed grid of multiple VSCs are reviewed. The chapter closes on transient capability limits of droop-controlled voltage-sources while facing typical transmission grid events such as sudden line opening. The trade-off between the synchronization stability margin offered by droop control, and the ability of VSCs to cope with transient overloading is identified as the major challenge for a future full VSC-based transmission grid system.

3.1 Dynamic modeling of a full VSC-based power system

The basic power system under study in the chapter gathers two loads, two VSC-based electrical sources for redundancy and an interconnection line between sources.

In this chapter, the VSC rating is supposed to be $P_{nom} = 1\ GW$, corresponding to the biggest VSC converter connected to the transmission grid nowadays [6]. The AC voltage nominal value is U_{nom} =400 kV, rms, phase-to-phase, corresponding to the highest voltage level on the french system. The objective of the first section is to detail the model of each component of the network

and then to derive an analytic expressions of the dynamics power transfer between the two sources.

3.1.1 Voltage sources model

As mentioned previously in section 2.3, the VSC-based electrical source can be assumed to be a pure voltage source. This representation is a common assumption to study interactions between them [95]. The fundamental sinusoidal voltage waveform applied to the output of each voltage-source i is totally determined by its time-varying amplitude $E_i(t)$, and time-varying instantaneous phase angle $\theta_i(t)$. Depending on the VSC technology, amplitude and phase-angle quantities can be controlled with a limited dynamic inherent to the modulation techniques, and the power ratings of the devices. To produce a sinusoidal waveform out of the voltage-source, the phase-angle is continuously defined by integration of the instantaneous angular frequency reference:

$$\theta_i(t) = \int_0^t \omega_i(\tau) d\tau \qquad \forall t > 0, \tag{3.1}$$

From instantaneous amplitude and phase-angle information, the three-phase sinusoidal, direct, and balanced voltages are defined by:

$$\begin{bmatrix} e_{ia}(t) \\ e_{ib}(t) \\ e_{ic}(t) \end{bmatrix} = \begin{bmatrix} E_i(t)\cos(\theta_i(t)) \\ E_i(t)\cos(\theta_i(t) - \frac{2\pi}{3}) \\ E_i(t)\cos(\theta_i(t) + \frac{2\pi}{3}) \end{bmatrix} \tag{3.2}$$

At the transmission level, typical power sources have the characteristics gathered in table 3.1. Those nominal values are used to define relative values of the electrical quantities in per-unit.

3.1.2 AC Transmission line model

In case of short-length distance (under 80km), an overhead power line has a negligible capacitive effect [17]. Under balanced conditions, the line can be represented by its resistive and inductive effect for electrical quantities propagation around fundamental frequency. Between 80km and 240km, pi-equivalent model of line should be used. Rigorously, the series impedance line model

Table 3.1 – Typical nominal values of electrical sources connected on transmission grid

Parameter	Quantity	Value	per-unit
P_n	Nominal active power	$1\,GW$	0.96
Q_{min}, Q_{max}	Reactive power at rated power	$\pm 300 MVAR$	± 0.29
S_{base}	Base apparent power	$1044\,MVA$	1
U_{base}	Base voltage	$400\,kV$	1
Z_{base}	Base impedance	$160\,\Omega$	1
ω_n	Nominal angular frequency	$2\pi 50\,rad.s^{-1}$	1
X_c	Transformer leaks reactance at ω_n	$24\,\Omega$	0.15

Table 3.2 – Typical 400 kV overhead line on transmission grid

Parameter	Quantity	Value
r_{line}	distributed line series resistance	$0.024\ \Omega.km^{-1}$
x_{line}	distributed line series reactance at ω_n	$0.24\ \Omega.km^{-1}$
b_{line}	distributed line shunt susceptance at ω_n	$3.974.10^{-6}\ \Omega^{-1}.km^{-1}$

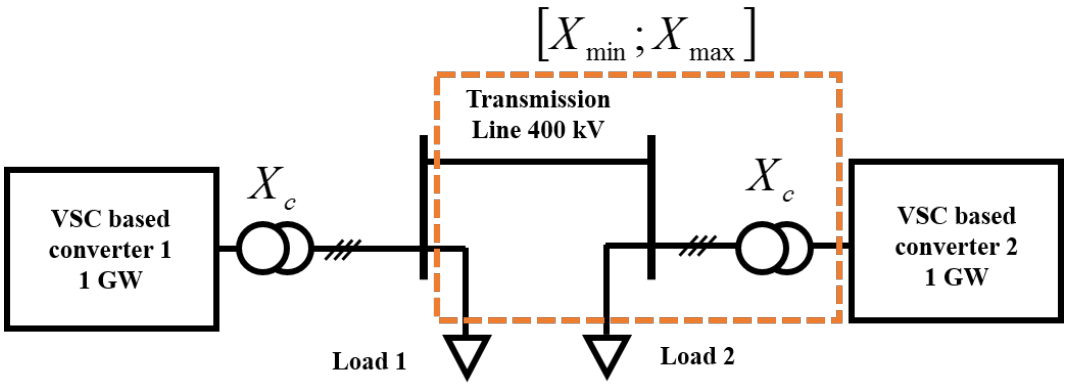

Figure 3.2 – Basic VSC-based power system

is only valid for dynamics slower or equal to the nominal frequency and below. Higher dynamical studies must consider more complex models (frequency-dependant model), or shorter lines. However, the approach presented hereafter could be easily extended to all line models. Typical values for high-voltage overhead lines are summarized in table 3.2.

The overhead line length variation is deduced from current grid-codes. In typical transmission grids, highest powered generation units (>800 MW) see a total connection equivalent series reactance, that can range between X_{min}=0.05 p.u. and X_{min}=0.6 p.u., from their point of coupling (PCC) after the transformer, and the infinite bus model of the rest of the grid [16]. This equivalent reactance variation is adapted to the studied system studied as seen in fig. 3.2. Given the line parameters of table 3.2, it would correspond approximately to an overhead line connection, up to 300 km between two VSC-based sources of 1 GW.

3.1.3 Power system loads model

The load models are diverse, depending on load types (heating, lightning, motors, or electronic appliance). Under a given voltage waveform, the diversity of load models leads to various absorbed current dynamics, and the consequent disturbances are unpredictable. In high-power studies (at 400 kV) loads are usually represented in the system model under an impedance model [16]. However, loads impedance contribute positively to the damping of the system as they dissipate energy [60], especially at high frequencies [58]. In power control stability studies, neglecting load impedances places the system in critical damping situation, which is interesting to assess the stability limits in the worst conditions case. Besides, the characteristic-time $\tau_{load} = L_{load}/R_{load}$

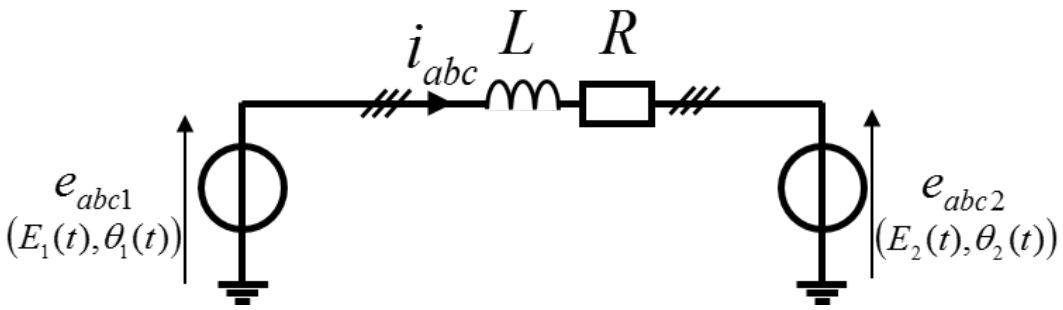

Figure 3.3 – Basic VSC-based power system dynamic model

of linear loads can often be neglected relatively to the line characteristic time $\tau_{line} = L_{line}/R_{line}$ [96].

More complex and non-linear load models, as ZIP models, could be employed as proposed by [42] at the expense of additional analytic computation efforts. In particular, constant-power load model are suspected to destabilize the system [97, 98]. Although the impact on the system stability is real, the effect of the load dynamics is not investigated in this chapter and therefore, the loads are removed whenever it comes to the power dynamics between sources.

For the dynamic model of power flow between units derived in this section, the loads influence is disregarded, so that the study consider dynamical interactions between sources on a non-loaded system. In practice, such system could represent a AC area only fed by VSC-interfaced wind generation which is exported through a VSC-based HVDC.

3.1.4 Power system dynamic representation

Using the description of the components models, the basic power system of fig. 3.1 is represented solely by the dynamic model in fig. 3.3 with two perfect and independent voltage-sources and a series impedance link.

Assuming the transmission line is represented only by its resistive and inductive series impedance, the impedance link between the two sources of fig. 3.3 is represented by an equivalent *R-L* impedance, including the transformers leaks. A transformer has a typical leakage reactance of 0.15 $p.u.$ that gives the extreme values for the total impedance link between the two voltage-sources: $X_{min} + 0.15 = 0.2 < L\omega_n < 0.75 = X_{max} + 0.15$ (see fig. 3.2). At high voltage, all

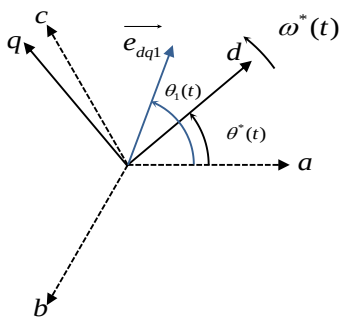

Figure 3.4 – Rotating dq-frame compared relative to the natural frame abc.

the overhead lines present low losses, for all voltage classes. The interconnection links are then considered dominated by their reactive behavior, with the ratio $5 < L\omega_n/R < 20$.

The transmission grid dynamic model determines the current flowing between the two sources connected at both terminals.

$$\left(L\frac{d}{dt} + R\right)\begin{bmatrix} i_a(t) \\ i_b(t) \\ i_c(t) \end{bmatrix} = \begin{bmatrix} e_{1a}(t) \\ e_{1b}(t) \\ e_{1c}(t) \end{bmatrix} - \begin{bmatrix} e_{2a}(t) \\ e_{2b}(t) \\ e_{2c}(t) \end{bmatrix} \tag{3.3}$$

As we assumed that lines, loads and more generally all the electrical system is balanced over the three-phase, the flowing currents are also symmetric with sinusoidal waveform in steady-state.

3.1.5 Power flows between two voltage-sources

Power flow is the principal quantity of interest through out a power system because they are conservative values over different voltage-level. As illustrated in the previous chapter 2.3, two voltage-sources only can exchange power in steady-state, if they operate at a common frequency. To understand the dynamic relationship between power and frequencies deviation, the instantaneous active and reactive power expressions out of source 1 are derived, following the definitions provided in the instantaneous power theory [99, 100]. The power expressions are then linearized at the vicinity of a steady-state operating point by small-signal approximation.

The three-phases quantities are expressed in per-units by their coordinates in dq-rotating frame, turning at the phase-angle reference $\theta^*(t)$, by using complex space vector $\boldsymbol{x}_{dq}(t) = x_d(t) + jx_q(t)$. Using this formalism equation (3.3) is re-written as:

$$\left(L\frac{d}{dt} + R + j\omega^*(t)L\right)\boldsymbol{i}_{dq}(t) = \boldsymbol{e}_{1dq}(t) - \boldsymbol{e}_{2dq}(t) \tag{3.4}$$

$$\begin{aligned}\boldsymbol{e}_{1dq}(t) &= E_1(t)\left(\cos(\theta_1(t) - \theta^*(t)) + j\sin(\theta_1(t) - \theta^*(t))\right),\\ \boldsymbol{e}_{2dq}(t) &= E_2(t)\left(\cos(\theta_2(t) - \theta^*(t)) + j\sin(\theta_2(t) - \theta^*(t))\right).\end{aligned} \tag{3.5}$$

The angle frequency $\omega^*(t)$ in (3.4) is the time-derivative of the phase-angle reference $\theta^*(t)$. A convenient choice of $\theta^*(t) = \theta_1(t)$ aligns the dq-frame with the first voltage-source output. Moreover, to manipulate fixed quantities in steady-state, the voltage-angle difference between sources $\delta(t)$ has been defined by:

$$\delta(t) = \theta_1(t) - \theta_2(t) = \theta^*(t) - \theta_2(t), \tag{3.6}$$

Voltage coordinates in dq-frame from (3.5) simplify then in:

$$\begin{aligned}\boldsymbol{e}_{1dq}(t) &= E_1(t),\\ \boldsymbol{e}_{2dq}(t) &= E_2(t)\left(\cos(-\delta(t)) + j\sin(-\delta(t))\right).\end{aligned} \tag{3.7}$$

Instantaneous active and reactive powers, defined according to [99, 100], are further given by the combination of (3.4) and (3.7):

$$\begin{aligned}P(t) &= \mathrm{Re}\{\boldsymbol{e}_{1dq}(t)\boldsymbol{i}_{dq}(t)^*\},\\ Q(t) &= \mathrm{Im}\{\boldsymbol{e}_{1dq}(t)\boldsymbol{i}_{dq}(t)^*\}.\end{aligned} \tag{3.8}$$

The power expressions in (3.11) are non-linear differential equations where $P(t)$ and $Q(t)$ are inter-dependent. To use linear control theory, the expressions must be linearized around a steady-state operating point, following the method of [101, 102, 103]. The steady-state is reached when the frequencies $\omega^*(t)$, $\omega_1(t)$, and $\omega_2(t)$ tend to the same value ω_0. In this case, the dq-coordinates are time-invariant and the steady-state active power and reactive expressions are:

$$\begin{aligned}P_0 &= \mathrm{Re}\{\boldsymbol{e}_{1dq0}\boldsymbol{i}^*_{dq0}\},\\ Q_0 &= \mathrm{Im}\{\boldsymbol{e}_{1dq0}\boldsymbol{i}^*_{dq0}\},\\ P_0 &= \frac{R\left(E_{10}^2 - E_{10}E_{20}\cos(\delta_0)\right) + E_{10}E_{20}\left(L\omega_0\right)^2\sin(\delta_0)}{(R) + \left(L\omega_0\right)^2},\\ Q_0 &= \frac{\left(L\omega_0\right)\left(E_{10}^2 - E_{10}E_{20}\cos(\delta_0)\right) - E_{10}E_{20}R\sin(\delta_0)}{(R)^2 + \left(L\omega_0\right)^2}.\end{aligned} \tag{3.9}$$

Assuming such a synchronized situation at $t = 0$, the dynamical linearized power expressions expression are obtained by small-signal variations of $\Delta\delta(t)$ and $\Delta E_1(t)$ from this operating point. The second voltage-source amplitude E_2 is kept constant. In small-signal sense, the sinus and cosinus from (3.5) in the current expression (3.4) can be replaced by their first order approximation :

$$\left(L\frac{d}{dt} + R + j\omega_0 L\right)\Delta \boldsymbol{i}_{dq}(t) = \Delta E_1(t) - E_{20}\left(-\sin(\delta_0)\Delta\delta(t) - j\cos(\delta_0)\Delta\delta(t)\right) \tag{3.10}$$

Note that $\omega^*(t)$ potentially can change transiently. However, if the variation of $\omega^*(t)$ are smooth and contained in a small range (up to 5% of ω_0), the variation can be neglected to keep the equation (3.10) linear. Further linearizing the product, in the instantaneous active and reactive powers expressions, yields:

$$\begin{aligned}\Delta P(t) &= \mathrm{Re}\{\Delta E_1(t)\boldsymbol{i}^*_{dq0} + E_{10}\Delta \boldsymbol{i}_{dq}(t)^*\},\\ \Delta Q(t) &= \mathrm{Im}\{\Delta E_1(t)\boldsymbol{i}^*_{dq0} + E_{10}\Delta \boldsymbol{i}_{dq}(t)^*\}.\end{aligned} \tag{3.11}$$

Inserting (3.10) in (3.11) and replacing the derivative operator $\frac{d}{dt}$ by the Laplace variable "s" gives the transfer functions from small variations of the voltage-angle difference and the amplitude to the active and reactive power variations. The four transfer functions of the linearized system system constitute a multi-input multi-output system (MIMO):

$$\begin{bmatrix}\Delta P(s)\\ \Delta Q(s)\end{bmatrix} = \begin{bmatrix}F_{P\delta 0}(s) & F_{PE0}(s)\\ F_{Q\delta 0}(s) & F_{QE0}(s)\end{bmatrix}\begin{bmatrix}\Delta\delta(s)\\ \frac{\Delta E_1(s)}{E_10}\end{bmatrix} \tag{3.12}$$

With:

$$\begin{aligned}F_{P\delta 0}(s) &= E_{10}E_{20}\frac{\sin(\delta_0)(R+Ls) + \cos(\delta_0)(L\omega_0)}{(R+Ls)^2 + (L\omega_0)^2},\\ F_{Q\delta 0}(s) &= E_{10}E_{20}\frac{\sin(\delta_0)(L\omega_0) - \cos(\delta_0)(R+Ls)}{(R+Ls)^2 + (L\omega_0)^2},\\ F_{PE0}(s) &= E_{10}E_{20}\frac{\sin(\delta_0)(L\omega_0) + \left(2\frac{E_{10}}{E_{20}} - \cos(\delta_0)\right)(R+Ls)}{(R+Ls)^2 + (L\omega_0)^2},\\ F_{QE0}(s) &= E_{10}E_{20}\frac{\sin(\delta_0)(R+Ls) + \left(2\frac{E_{10}}{E_{20}} - \cos(\delta_0)\right)(L\omega_0)}{(R+Ls)^2 + (L\omega_0)^2},\end{aligned} \tag{3.13}$$

The model has been validated by EMT simulation with the EMTP-RV software. As an illustration, the active power exchange variation following a step of $\Delta\delta = 0.1$ rad is shown in fig.

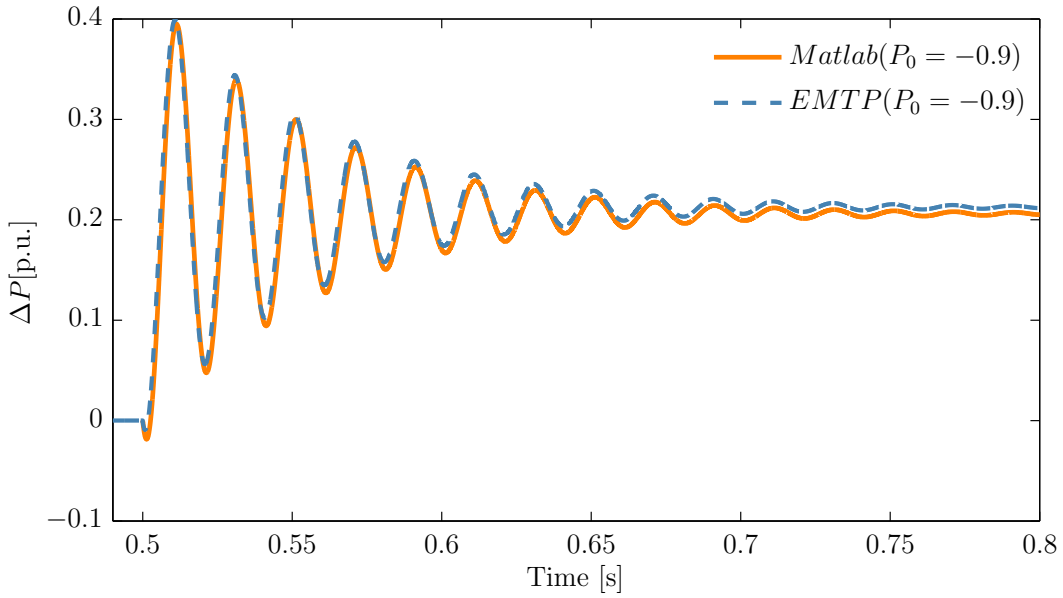

Figure 3.5 – Comparison between the linearized model of active power to voltage-angle difference dependency $F_{P\delta 0}(s)$ implemented in Matlab, and an EMT simulation of the same system, following a voltage-angle difference step. $L\omega_n = 0.45$ p.u. and $R = 0.025$ p.u.

3.5. The initial active power transfer between sources is set at $P_0 = -0.9$ p.u. Both curves are similar, but one can notice a slightly difference in steady-state due to the linearization and the dependence on the initial point.

Several observations from these power expressions can be made:

1. The linearized relationships are dependent on the initial operating point.

2. The voltage-angle difference must respect the steady-state stability criterion of power transfer defined by [17]. This criterion states that the sign of $F_{P\delta_0}(0)$ must stay positive, inducing the limit on the voltage-angle:

$$\forall \delta_0 \in]-\frac{\pi}{2};\frac{\pi}{2}[\qquad F_{P\delta_0}(0) > 0 \Rightarrow \delta_0 > \arctan(-\frac{L\omega_0}{R}) \tag{3.14}$$

When $F_{P\delta_0}(0) > 0$, a closed loop control on the active power can be stable in small-signal sense. If $L\omega_0 >> R$, the criterion is (3.14) respected for all the operating points respecting the conditions $\delta_0 \in]-\frac{\pi}{2};\frac{\pi}{2}[$. Out of these limits, the sign of $F_{P\delta 0}(0)$ changes and the closed loop regulation diverges. This requirement is developed further, as a necessary condition

for the stability of the chosen power control. In practice, for the model of fig. 3.3 and in the worst case of a rated active power exchange on a interconnection line of $L\omega_0 = 0.75$ p.u. and $R = 0.15$ p.u., the voltage-angle difference in steady-state remains in $[-\frac{\pi}{4}; \frac{\pi}{4}]$.

3. All the transfer functions contain two conjugate poles with resonance at the initial frequency ω_0:

$$p_{1,2} = -\frac{R}{L} \pm j\omega_0 \tag{3.15}$$

This resonance is visible on the time-response of fig. 3.5. The resonance is due to the DC current component of the line currents.

4. At very low frequencies, the transfer functions ($F_{P\delta 0}(s \approx 0)$, $F_{Q\delta 0}(s \approx 0)$, $F_{PE0}(s \approx 0)$, $F_{QE0}(s \approx 0)$) simplify in the classical quasi-static relationships between power and angle and voltage amplitude of phasors circuit theory [17]. Quasi-static relationships are simpler, as the line dynamics are neglected, but they hide the resonance and potential instabilities [101, 104, 102, 105].

5. One right-half-plane zero appears under certain conditions. For example, the active power to the voltage phase-angle difference transfer function $F_{P\delta 0}(s)$ have a real zero at:

$$z = -\frac{R}{L} + \frac{\omega_0}{-\tan(\delta_0)} \tag{3.16}$$

The zero have a positive real-part if the initial active power transfer is negative:

$$z > 0 \Rightarrow -\frac{L\omega_0}{R} < \tan(\delta_0) < 0 \tag{3.17}$$

Systems with the right-half-plane zeros are called non-minimal-phase system. Their short-term time-response to an excitation has an opposite direction than to the long-term response. The effect is visible in fig. 3.5. The non-minimal-phase systems are non-trivial to control as they induce a bandwidth limitation in their excitation to remain stable in closed loop [106]. However, the effect of the zero is only significant for very high total reactances between sources, for high voltage-angle differences, and/or high voltage amplitude differences. These conditions are out of the scope of the thesis, but the RHP zeros limitation must be handled properly when it comes to weak grid situations.

6. Recalling that $L\omega_0 >> R$, and considering frequencies below the nominal frequency, the off-diagonal transfer functions gains ($F_{Q\delta 0}(s \approx 0)$,$F_{PE0}(s \approx 0)$) in (3.12) are negligible compared to diagonal transfer functions gains $F_{P\delta 0}(s \approx 0)$, $F_{QE0}(s \approx 0)$. The comparison at low frequencies of $F_{P\delta 0}(s \approx 0)$ and $F_{PE0}(s \approx 0)$ is well illustrated in fig. 3.6, for three different initial power operating points. The dominance of $F_{P\delta 0}(s \approx 0)$ over $F_{PE0}(s \approx 0)$ is obvious at $P_0 = 0$, as shown on the case (a). In the case where $P_0 = 1$ (b) or $P_0 = -1$ (c), the comparison $F_{P\delta 0}(s \approx 0) > F_{PE0}(s \approx 0)$ is still effective, although the difference between the gains is reduced. However, the domination of diagonal terms is not true around ω_0, yielding to coupled dynamics between active and reactive power. As a consequence, only slow dynamics (below ω_0) of active and reactive power could be controlled independently with a feedback control on respectively the voltage phase-angle and the voltage amplitude. A faster control of the active and reactive power is theoretically possible for a MIMO system [107, 100] but it comes at the expense of increased complexity of the controller structure and parameters tuning. In addition, the increased complexity of the large power system analysis under MIMO controls is a corollary. For this reason, the choice has been made to stimulate the transmission grid below the steady-state frequency to prevent the coupled dynamics between active and reactive power. In practice, a low-pass filter at $\omega_{LP} < \omega_0$ is introduced in the feedback loop as explained in the next section.

3.1.6 Conclusions on power flow dynamics on the power system

The section described an elementary model of a power system of two ideal VSC-based voltage-sources interfaced through a basic transmission grid-system. The instantaneous power transfer between the sources are modeled as a response to a voltage-angle difference between the units, and to the voltage magnitude differences. The power expressions have been linearized, from a credible operating point, giving the power system response to small variation of voltage-sources references in the form of a MIMO system (3.12).

Among the four transfer functions, $F_{P\delta 0}(s)$ in (3.13) gives the instantaneous real power transfer, in response to a small voltage angle change $\Delta\delta(s)$ between the two sources. For any operating points, the function $F_{P\delta 0}(s)$ dominates the transfer function $F_{PE0}(s)$ provided that the voltage-

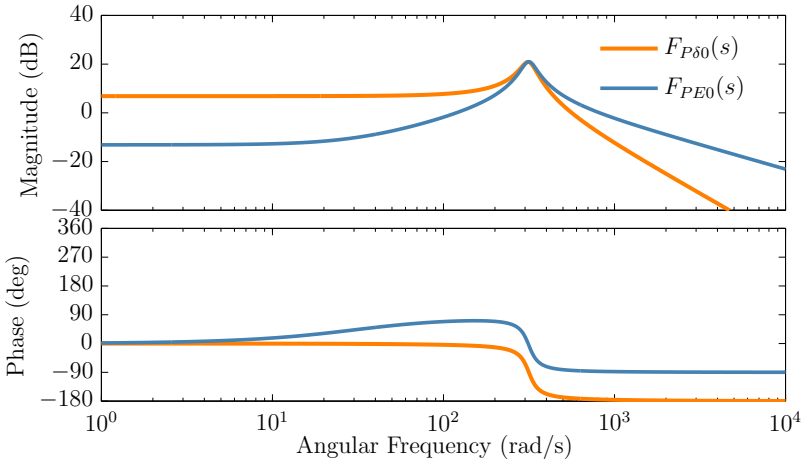

(a) $P_0 = 0\,p.u.$

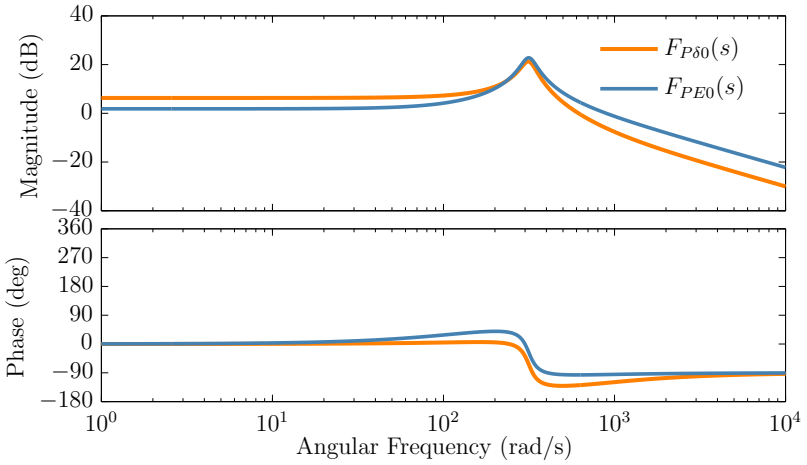

(b) $P_0 = 1\,p.u.$

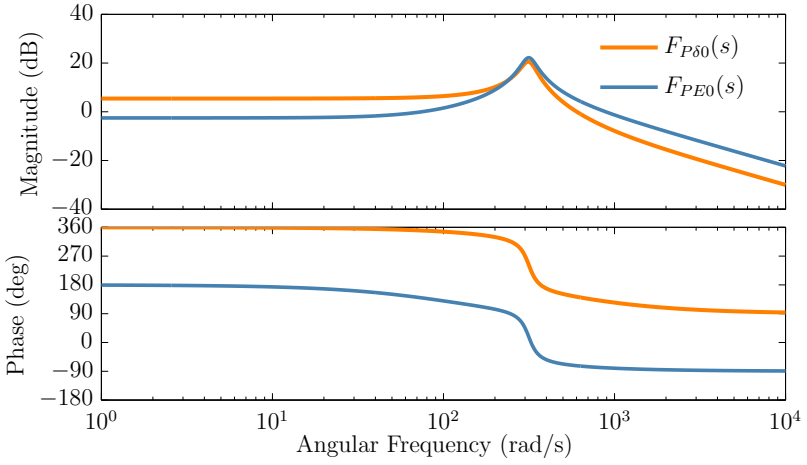

(c) $P_0 = -1\,p.u.$

Figure 3.6 – Frequency-response comparison of $F_{P\delta 0}(s)$ and $F_{PE0}(s)$ at different operating points with $L\omega_n = 0.45$ p.u. and $R = 0.045$ p.u.

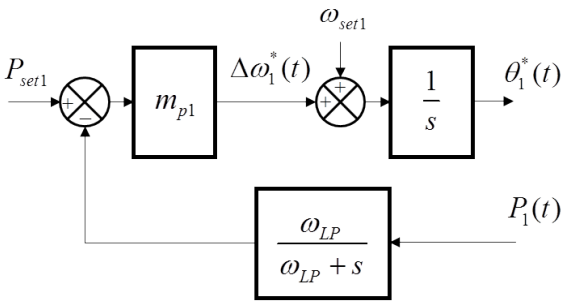

Figure 3.7 – Active power feedback control

sources references vary slowly compared to the nominal frequency. As a consequence, an instantaneous variation of the observed active power transfer $\Delta P(s)$ between units reveals a variation of the voltage angle reference $\Delta\delta(s)$ between units. A variation of $\Delta\delta(s)$ occurs when one of the interconnected sources is subject to a phase-angle deviation, or a frequency deviation from the other. From a technological point of view, the frequency references of autonomous voltage-sources cannot not be equal over the time, because they are provided by independent internal oscillators. To compensate the phase-angle or frequency deviation, a control feedback on active power measurement of one converter can adjust its frequency reference $\omega_i^*(t)$, and so the phase angle $\theta_i^*(t)$, to keep the sources synchronized together.

3.2 Synchronization one voltage source with the other fixed voltage source ("infinite bus")

Given the model of the active power transfer between two voltage-sources, this section shows how a conventional feedback droop control on the frequency on one voltage-source can keep it synchronized with the other source. The section considers that the left-hand source in fig. 3.3 is equiped with an active power feedback control, and that the right-hand source is a fixed voltage-source with constant voltage amplitude and fixed frequency reference over the time. This consideration corresponds to the classic infinite bus assumption in power system analysis. The system and control parameters impact the local stability of the synchronization.

3.2.1 Structure of the active power feedback control

Fig. 3.7 shows the structure of the output active power feedback control of voltage source 1 that modifies the voltage frequency reference $\omega_1^*(t)$ through the phase-angle θ_1^*:

The real power measurement $P_1(t)$ is first processed through a low-pass filter. This filtering stage is desirable to limit the bandwidth of the voltage phase-angle reference variations, and to remain in the quasi-static domain of power transfer expression. A limited bandwidth contributes to a good decoupled behavior between the phase-angle variation and the voltage angle variation in power response given by (3.13).

Other reasons motivate the use of a power filter, such as: Calculating the average power calculation in case of single-phase converters [108, 109], filtering the power harmonics at $2\omega_0$ in case of unbalanced currents [110], taking into account the sensor and computation delays [96], time-decoupling with faster inner VSC dynamics [111, 44], [58, 31, 50], introducing a degree of freedom to damp the active power response [112], or facilitating the analysis based on dominant poles [96]. In any case, to pursue those objectives, the filter cut-off frequency must be taken between:

$$\frac{\omega_n}{20} < \omega_{LP} < \frac{\omega_n}{5} \tag{3.18}$$

The set-points P_{set1} and ω_{set1} are the desired value for the active power output and frequency of the converter in normal operation. The set-points can be provided to each converter by an external and centralized control, based on low-bandwidth communication, as a function of an energy management strategy or an optimal load-flow dispatch [35, 113]. Such a global control is out of the scope of the present thesis but is of major interest for a full VSCs interfaced power system operation. Accordingly, the active power P_{set1} and angular frequency ω_{set1} set-points in fig. 3.7 are assumed to be fixed and equal to the initial steady-state output real power P_0 and frequency ω_0. A proportional gain of m_{p1} adjusts the output frequency whenever the measured real power does not equal its set-point. From steady-state, small-signal variation in the measured active power leads to variation of frequency reference:

$$\Delta\omega_1(s) = -\frac{m_{p1}\omega_{LP}}{\omega_{LP} + s}\Delta P_1(s) \tag{3.19}$$

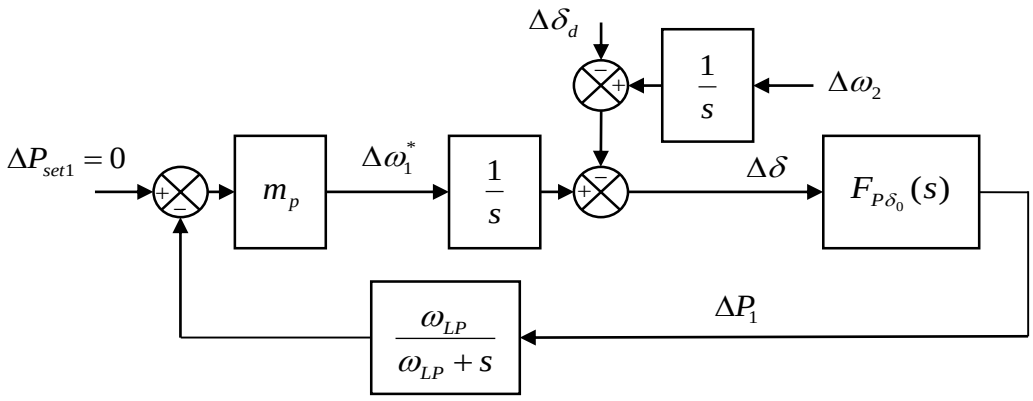

Figure 3.8 – Small-signal representation of the active power transfer in closed loop between the controlled voltage source 1 with power-frequency droop control.

3.2.2 Synchronization mechanism of the active power feedback control

Recalling that the active power response originates from a voltage angle difference variation given by (3.13) when both voltage sources fixed amplitude, the small-variation of active power output from voltage-source 1 is given by:

$$\Delta P_1(s) = F_{P\delta 0}(s)\Delta\delta(s) \tag{3.20}$$

By combining the equations (3.20) and (3.19), the small-signal representation of the active power transfer in closed loop between the controlled voltage source 1 with active power feedback and the fixed voltage source 2 is drawn in fig. 3.8.

The closed loop in fig. 3.8 helps to understand the synchronization mechanism provided by the active power feedback control on the left-hand voltage source when the second source is subject to either an arbitrary phase angle jump $\Delta\delta_d$ or a frequency step $\Delta\omega_2$. The effect of the voltage angle disturbance $\Delta\delta_d$, and of the frequency variation in voltage-source 2 ($\Delta\omega_2$), are studied separately. In both cases, the system is able to reach a new steady-state. Assuming first a constant frequency of the voltage source 2 ($\Delta\omega_2 = 0$), the closed loop response of $\Delta\delta(s)$ to $\Delta\delta_d$ is deduced from the block diagram in fig. 3.8:

$$\begin{aligned}\Delta\delta(s) &= \frac{\Delta\omega_1(s)}{s} + \Delta\delta_d \\ \Delta\delta(s) &= \frac{1}{s}\left(-\frac{m_{p1}\omega_{LP}}{\omega_{LP}+s}F_{P\delta 0}(s)\Delta\delta(s)\right) + \Delta\delta_d \\ \Delta\delta(s) &= \frac{1}{1+\frac{m_{p1}}{s}\frac{\omega_{LP}}{\omega_{LP}+s}F_{P\delta 0}(s)}\Delta\delta_d,\end{aligned} \tag{3.21}$$

The closed loop transfer function (3.21) contains an integration in the loop due to the phase-angle computation from the frequency reference. The integration compensates the voltage angle difference disturbance $\Delta\delta_d$ in steady-state [101]. As the voltage angle difference converges to its initial value $\Delta\delta(s=0)=0$, also goes the frequency variation $\Delta\omega_1(s=0)$ to zero, meaning that the output real power returns to $P_1(s=0)=P_{set1}=P_0$. In other words, the controlled voltage-source 1 regulates its power output by rejecting voltage angle disturbance $\Delta\delta_d$, in the case where the frequency of voltage-source 2 is fixed.

Secondly, the voltage source 2 is subject to a small variation of its frequency reference $\Delta\omega_2(s) = \Delta\omega_2$, and $\Delta\delta_d = 0$.

$$\Delta\delta(s) = \frac{\Delta\omega_1(s) - \Delta\omega_2}{s} \tag{3.22}$$

The response of the controlled frequency reference of voltage source 1 is given by (3.19), (3.20) and (3.22):

$$\begin{aligned}\Delta\omega_1(s) &= -\frac{m_{p1}\omega_{LP}}{\omega_{LP}+s}F_{P\delta 0}(s)\left(\frac{\Delta\omega_1(s)-\Delta\omega_2}{s}\right) \\ \Delta\omega_1(s) &= \frac{\frac{m_{p1}}{s}\frac{\omega_{LP}}{\omega_{LP}+s}F_{P\delta 0}(s)}{1+\frac{m_{p1}}{s}\frac{\omega_{LP}}{\omega_{LP}+s}F_{P\delta 0}(s)}\Delta\omega_2,\end{aligned} \tag{3.23}$$

The equation (3.23) shows the synchronizing action of the active power feedback control. The frequency $\Delta\omega_1(t)$ converges to the same frequency variation of $\Delta\omega_2$.

To conclude, the proportional gain control m_{p1} on the frequency in fig. 3.7 ensures a tight control output power with no steady-state error if the frequency of the other source is constant. Also, the integration in the active power closed loop serves to follow a frequency variation of the other source with no error in steady-state. The control realizes then the synchronization of voltage-source 1 in closed loop, with the rest of the system. Regarding these steady-state considerations, the control structure builds the necessary conditions for an effective synchronization action. The

control principle, based on active power-feedback, has been called the "power-synchronization" [66, 67]. The dynamic stability of the synchronization is, however, dependent on the system dynamics modeled by equation (3.20). A careful tuning of control parameters m_{p1} and ω_{LP} must be realized to ensure the local stability of an operating point.

3.2.3 Small-signal stability of the synchronization

The parameters m_{p1} and ω_{LP} of the controller in fig. 3.7 must be chosen carefully to ensure the stability of the synchronization action in the whole range of network parameters and accessible operating points described in section 3.1. This paragraph gives insight on how to tune parameters considering the linearized model of power transfer (3.20). The model is only valid locally, close to an operating point. The local stability is assessed in small-signal sense by the ability of the system to reach a steady-state following a small disturbance. [111] conducted a similar analysis but did not take into account the line dynamics.

The analysis of small-signal stability limits of the power-synchronization is conducted by plotting the Bode diagrams of the open-loop transfer:

$$\frac{m_{p1}}{s}\frac{\omega_{LP}}{\omega_{LP}+s}F_{P\delta 0}(s) \tag{3.24}$$

The Bode diagrams of fig. 3.9 illustrate the influence of network parameters L and R, as well as of the control parameters m_{p1} and ω_{LP}, at a rated active power transfer between sources and fixed nominal voltage amplitude. On each plot, the gain margins on the upper axis and the phase margins on the lower axis are marked with dots. When not subject to the parametric variations, the parameter values are taken as follows: $P_0 = 1$, $L\omega_n = 0.45$ p.u., $R = 0.045$ p.u., $\omega_{LP} = \omega_n/10$, $m_p = 0.05\omega_n$.

Comparing the phase margin for different parameters set, several conclusions can be drawn. in fig. 3.9 (a), the phase margin decreases with the active power control gain m_p. The result was predictable as high gain means fast excitation of the line, increasing the risk to fall into line resonance area. To preserve stability margin but also a time response below 0.25 s, the variation of m_p should be restricted to $[0.01\omega_n; 0.1\omega_n]$. An additional static constraint will give the value of m_p in the next section. The impact of the power filter cut-off frequency ω_{LP} is further shown in fig. 3.9 (b), using a median value of $m_p = 0.05\omega_n$. As expected, if the low-pass filtering

action is not far enough from the nominal frequency ($\omega_{LP} = \omega_n$), the damping of the resonance is not achieved and the closed-loop system is unstable. On the other hand, a very low power filter cut-off frequency ($\omega_{LP} = \omega_n/100$) introduces an early phase lag in the open loop response, leading to low phase margin. An acceptable trade-off is ($\omega_{LP} = \omega_n/10$), which stands for a widely used value for power filtering. Regarding the network parameters impact, the variation of total inductance between both voltage-sources is illustrated in fig. 3.9 (c), whereas the total resistance is kept at a constant ration $R = L\omega_n/10$. Higher is the inductance value, lower are the phase margins. As long as the inductance stays in the operating limits $0.2\,p.u. < L\omega_n < 0.75\,p.u.$, the stability margins remain acceptable. The last figure 3.9 (d) looks at the evolution of stability margin for three reactance-to-resistance ratios $L\omega_n/R$. Obviously, adding more resistance damps the resonance peak, but the impact on the stability margins is not significant.

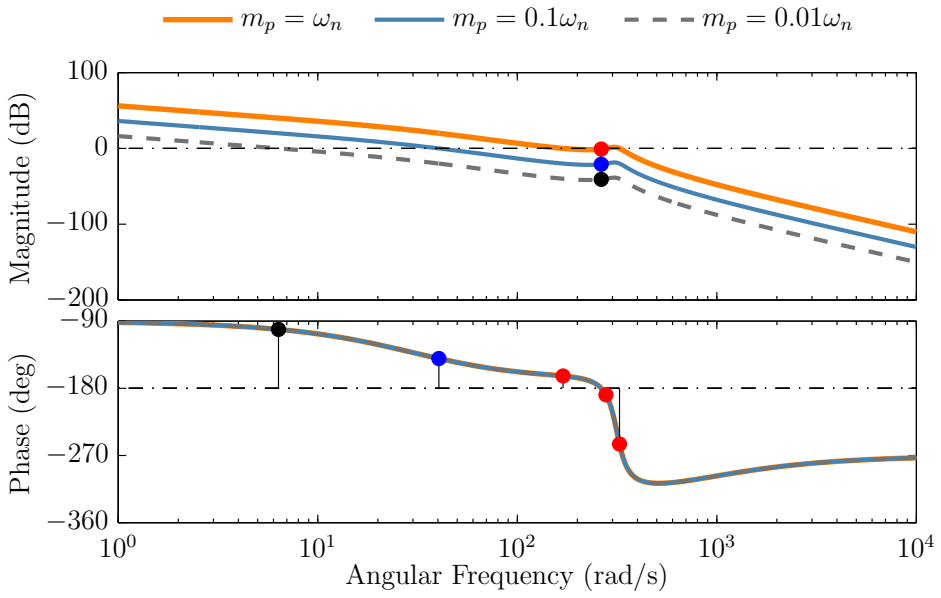
$m_p = \omega_n$
$m_p = 0.1\omega_n$
$m_p = 0.01\omega_n$
Magnitude (dB)
100
0
−100
−200
Phase (deg)
−90
−180
−270
−360
10^0
10^1
10^2
10^3
10^4
Angular Frequency (rad/s)

(a)

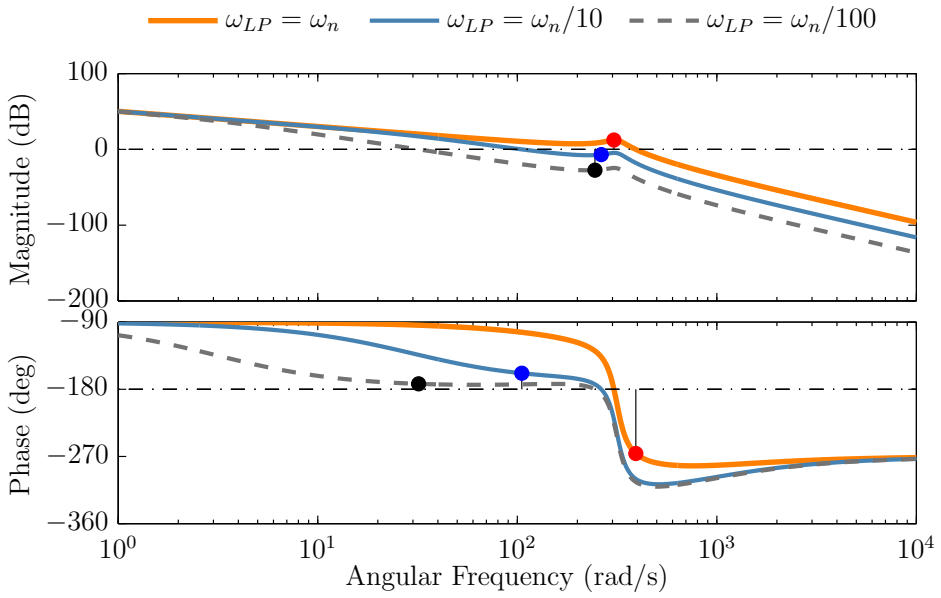
$\omega_{LP} = \omega_n$
$\omega_{LP} = \omega_n/10$
$\omega_{LP} = \omega_n/100$
Magnitude (dB)
100
0
−100
−200
Phase (deg)
−90
−180
−270
−360
10^0
10^1
10^2
10^3
10^4
Angular Frequency (rad/s)

(b)

3.3 Synchronization of two voltage sources and link with droop control

In this section, neither of the two voltage sources have a fixed voltage frequency anymore, but they both embed a power-synchronization control. Besides the property of the controls to keep the two sources synchronized, the section emphasizes the load-sharing property of the controls and the steady-state frequency-drop behavior of the system following a load increase. In a large power system, one electrical source cannot be designated as the master, imposing the frequency reference over the other sources. The loss of the master unit would be fatal for the rest of the system. Instead, all the sources must have symmetrical roles in the network. From static considerations, the two controlled sources form a droop-controlled system similar to the current synchronous generators based power system. In contrast with synchronous generators, the control parameters do not depend on physical electromechanic characteristics. The control parameters must be chosen to maintain the steady-state frequency in the defined operation range. Small-signal stability analysis is then conducted to ensure that the chosen parameters keep the local stability defined in the previous paragraph.

3.3.1 Static analysis: from double power-synchronization to droop control

The system of two controlled voltage-sources exhibits a static frequency-droop following a load increase. If both sources are controlled with power-synchronization scheme in fig. 3.7, their frequency references are guided by the equations:

$$\begin{aligned} \omega_1 &= \omega_{set1} - m_{p1}\left(\frac{\omega_{LP}P_1}{(\omega_{LP}+s)} - P_{set1}\right), \\ \omega_2 &= \omega_{set2} - m_{p2}\left(\frac{\omega_{LP}P_2}{(\omega_{LP}+s)} - P_{set2}\right). \end{aligned} \tag{3.25}$$

For the static analysis, the total steady-state load connected to the system of fig. 3.3 is taken into account as a purely active power load P_{load}. The initial operating point is fixed by load-flow and $\omega_{set1} = \omega_{set2} = \omega_0$. The initial active power transfer on the line is P_0 and the total power delivered by the sources is $P_{set1} + P_{set2} = P_{load}$. After a power demand increase of ΔP_{load}, the voltage-sources fulfill the new load, while assumed to stay synchronized by the

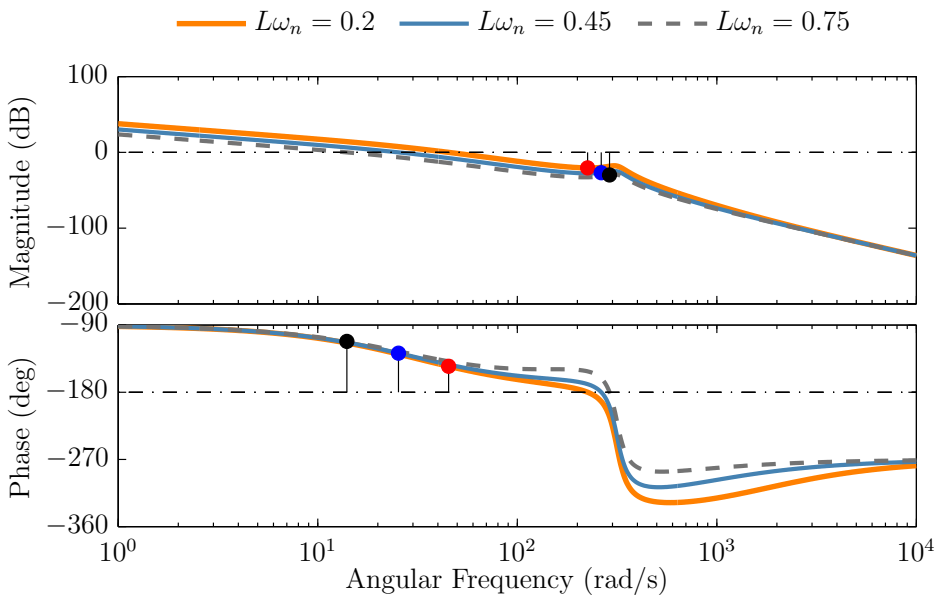

(c)

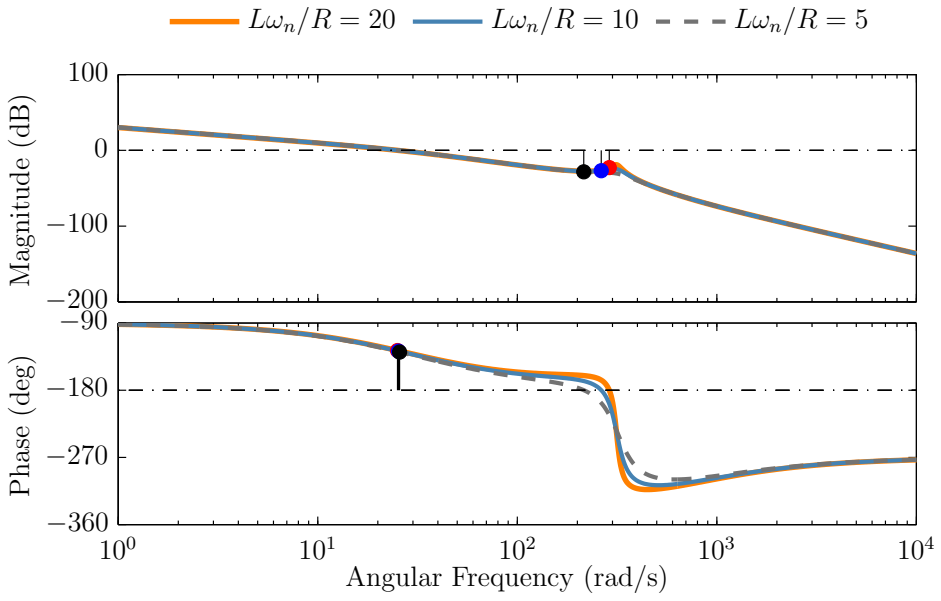

(d)

Figure 3.9 – Comparison of margins on the open-loop transfer voltage angle difference response (3.24). Gain margins on the upper axis and the phase margins on the lower axis are marked with dots. Base values: $P_0 = 1$, $L\omega_n = 0.45pu$, $R = 0.045pu$, $\omega_{LP} = \omega_n/10$, $m_p = 0.05\omega_n$.

power-synchronization control. This assumption supposes that a new stable operation point exists, and the frequencies converges to a new a common value ω_f:

$$\begin{aligned} \Delta\omega_1 &= \Delta\omega_2 = \omega_f - \omega_0, \\ \Delta P_1 &+ \Delta P_2 = \Delta P_{load}. \end{aligned} \tag{3.26}$$

Equations (3.25) drive the load-share among ΔP_1 and ΔP_2, and the final steady-state frequency (ω_f):

$$\begin{aligned} -m_{p1}\Delta P_1 &= -m_{p2}\Delta P_2, \\ \Delta P_1 &= \frac{m_{p2}}{m_{p1}+m_{p2}}\Delta P_{load}, \\ \Delta P_2 &= \frac{m_{p1}}{m_{p1}+m_{p2}}\Delta P_{load}, \\ \omega_f - \omega_0 &= -\frac{m_{p1}m_{p2}}{m_{p1}+m_{p2}}\Delta P_{load}. \end{aligned} \tag{3.27}$$

From (3.27), note that the coefficients m_{p1} and m_{p2} determine the final active load-share of the load increase ΔP_{load} among the two sources. The last equation of (3.27) quantifies the system frequency drop following a load increase. This static behavior is similar to the current power system. The frequency drop gave its name to this type of parallel control of VSC-based sources: "the conventional droop control" as early defined by [25].

In a general power system where the two sources have different power rates, it is highly desirable that each source handles the load according to their own capability. The parameters m_{pi} are therefore defined in respect with the nominal power P_{ni}, for each source.

$$m_{pi} = \sigma\frac{\omega_n}{P_{ni}}. \tag{3.28}$$

The nominal frequency ω_n is introduced to give the proportional droop coefficient σ no dimension. Considering that all the sources control have an identical droop coefficient σ, the final steady-state after the load change (3.27) can be rewritten with (3.28):

$$\begin{aligned}\Delta P_1 &= \frac{P_{n1}}{P_{n1}+P_{n2}}\Delta P_{load},\\ \Delta P_2 &= \frac{P_{n2}}{P_{n1}+P_{n2}}\Delta P_{load},\\ \omega_f - \omega_0 &= -\frac{\sigma\omega_n}{P_{n1}+P_{n2}}\Delta P_{load}.\end{aligned} \tag{3.29}$$

The system reaches an effective active load share in steady-state, and the frequency drop is completely determined by the value of the droop coefficient σ. This final state only depends on the initial set-points, and on the droop coefficient. For example, if the normal power system operation limits the frequency to $\omega_n \pm 5\%$, σ must be chosen between 0 and 0.05, limiting the accessible values of m_{pi}. From the previous analysis, the power-synchronization control of an unique source stayed stable for the all these possible values m_{pi}. On the current power system, a droop static slope of σ=4% is common.

3.3.2 Small-signal stability of the droop-controlled system

To assess the local stability of the synchronization of the two interconnected voltage-sources under droop control, the system is assumed to be in an accessible steady-state. Around this operating point, a small-signal stability analysis reveals the impact of droop parameters on the system stability. Compared to the previous section, the introduction of a second power-synchronized source might tighten the parameters choice to ensure stability.

Assuming two identical sources $P_{n1} = P_{n2}$, with equal droop coefficients, so that $m_{p1} = m_{p2} = m_p$. When the sources have equal droop coefficients, [45] identifies the situation as the most critical case for the stability of interfaced VSCs. Fig. 3.10 shows the equivalent model under study. From this model, the expression of $\Delta P_1(s)$ is given by (3.20). As the system is symmetric, the active power variation $\Delta P_2(s)$, out of the source 2 is:

$$\Delta P_2(s) = F_{P(-\delta 0)}(s)(-\Delta\delta(s)) \tag{3.30}$$

The characteristic equation on the voltage angle difference is obtained combining (3.20), (3.30) and (3.19):

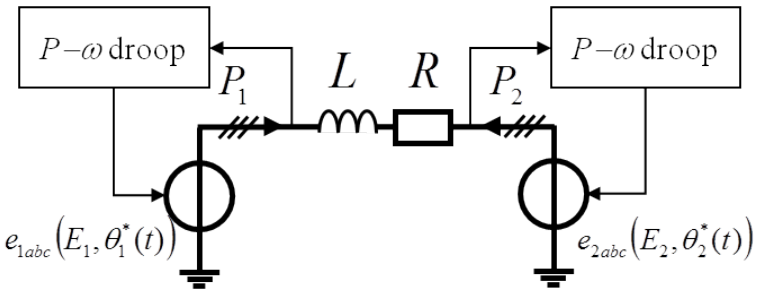

Figure 3.10 – Representation of the two sources with each an autonomous conventional droop control. Loads are neglected.

$$
\begin{aligned}
\Delta\delta(s) &= \frac{1}{s}\left(\Delta\omega_1(s) - \Delta\omega_2(s)\right), \\
\Delta\delta(s) &= \frac{1}{s}\left(-\frac{m_p\omega_{LP}}{\omega_{LP}+s}\Delta P_1(s) - \left(\frac{m_p\omega_{LP}}{\omega_{LP}+s}\Delta P_2(s)\right)\right), \\
\Delta\delta(s) &= -\frac{1}{s}\frac{m_p\omega_{LP}}{\omega_{LP}+s}\left(F_{P\delta 0}(s)\Delta\delta(s) - F_{P(-\delta 0)}(s)(-\Delta\delta(s))\right), \\
\Delta\delta(s) &= \frac{-m_p}{s}\frac{\omega_{LP}}{\omega_{LP}+s}\left(F_{P\delta_0} + F_{P(-\delta_0)}\right)\Delta\delta(s),
\end{aligned}
\tag{3.31}
$$

With

$$
\left(F_{P\delta_0} + F_{P(-\delta_0)}\right) = E_0 V_0 \frac{2\cos(\delta_0)\left(L\omega_0\right)}{\left(R+Ls\right)^2 + \left(L\omega_0\right)^2}, \tag{3.32}
$$

The small-signal expression of the voltage angle dynamics (3.31) has been validated through EMT simulation in fig. 3.11 and illustrates the convergence of the simplified system of two droop-controlled voltage-sources.

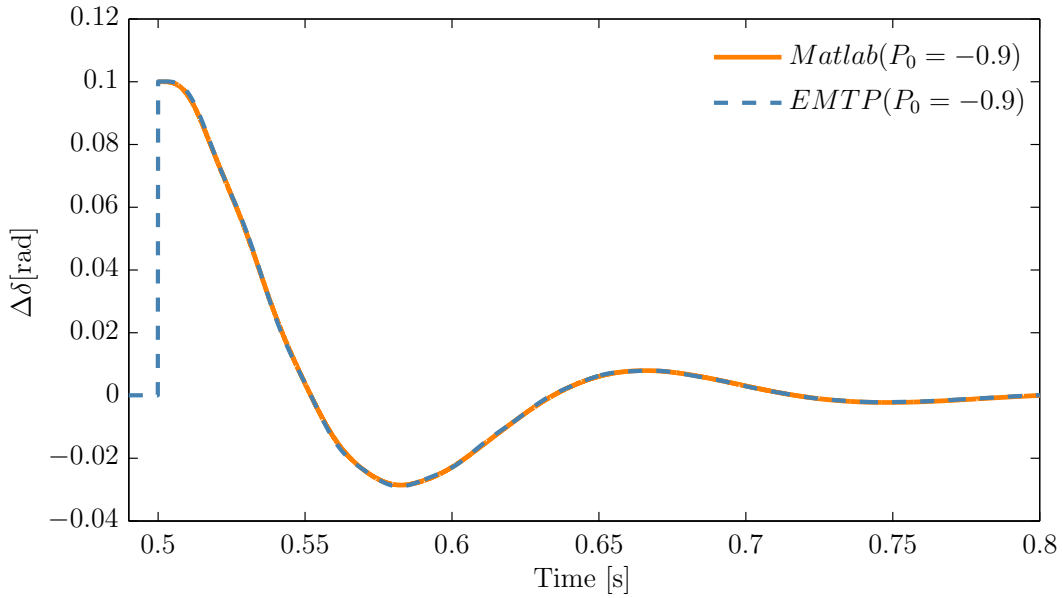

Figure 3.11 – Comparison of voltage angle difference dynamics $\Delta\delta(s)$ between two voltage-sources following a disturbance. An EMT model time-domain response is plotted with dashed line, the linearized model (3.31) plotted on Matlab with plain line. System parameters are: σ = 0.04 p.u., $\omega_{LP} = \omega_n/10$, $P_0 = -0.9$ p.u. for $L\omega_n = 0.45$ p.u. and $R = 0.025$ p.u.

3.3.3 Physical considerations around the droop control parameters

The frequency-droop controlled system has a behavior close to the current synchronous generation based power system. The parameters of the droop control can be compared to the physical characteristic of synchronous generators and their control. The droop control, as described in fig. 3.7, has two parameters of interest, namely σ defined from m_p by equation (3.28) and ω_{LP}. First, the normalized droop coefficient σ represents the ability of one source to change its frequency reference in response to a real power demand change. The value of σ changes the behavior of the controlled voltage-source:

- $\sigma = 0$ builds a fixed frequency voltage-source irrespective to load demand. The delivered active power satisfies the load presented at its output, with no load-sharing capacity. In traditional power system representation, this is the behavior of an infinite bus or of a synchronous generator with infinite inertia. An ideal voltage source.

- $\sigma = \infty$ forms a theoretically instant frequency-changing voltage-source. In response to a load change, the controlled voltage-source adapts directly its voltage angle to maintain its active output power at $P = P_{set}$. Such controlled voltage-source corresponds to an ideal power source or sink, that follows immediately frequency changes of the others sources connected in the same network. An ideal grid-following source.

- $0 < \sigma < 0.05$ makes frequency reference elastic to load demand changes, with a configurable degree of elasticity. A real power change creates a synchronization torque to adjust the voltage angle of the source with a certain dynamic. It has therefore, a static behavior that results in a frequency drop as expressed in equation (3.29), and a dynamic effect which determines the synchronization speed.

Note that the parameter σ is involved in the static final state, and in the convergence dynamics toward this final state. Secondly, the power filter parameters introduces an additional degree of freedom to decouple static objective from the dynamic behavior. With the power filter at ω_{LP} cut-off frequency, the droop-controlled voltage-sources behavior resembles to those of synchronous generators, in small-signal sense. On one hand, the frequency reference expression is deduced directly from equation (3.19), and applied for small variation of the angle difference $\Delta\delta(s)$:

$$\left(\frac{s}{\sigma\omega_{LP}} + \frac{1}{\sigma}\right)\frac{\Delta\omega_1^*(s)}{\omega_n} = -F_{P\delta_0}(s \approx 0)\Delta\delta(s) \tag{3.33}$$

On the other hand, the simplified electromechanical model of synchronous generators from chapter 2 is obtained by neglecting the turbine dynamics, the speed control dynamics, and considering slow variation of the internal angle δ_e:

$$\left(2Hs + \frac{1}{R} + \Gamma_{ed}\omega_n\right)\frac{\Delta\omega_r(s)}{\omega_n} = -\Gamma_{es}(\delta_{e0})\Delta\delta_e(s) \tag{3.34}$$

The right hand sides are made equivalent by taking a situation where $F_{P\delta_0} \approx \Gamma_{es}(\delta_{e0})$, eg. with $\delta_{e0} = \delta_0 = \frac{\pi}{4}$ and $L\omega_0 = x_c + x'_d$. It is worth noting that the damping effect of the load frequency sensibility has been removed ($D = 0$), as it is similar in both cases. A quick comparison of both expressions reveals their similarity and highlights the comparable role of $\frac{1}{\sigma}$ and $\frac{1}{R} + \Gamma_{ed}\omega_n$ on one

side, and $\frac{1}{\sigma\omega_{LP}}$ and $2H$ on the other side. Thus, the normalized droop coefficient in $\frac{1}{\sigma}$ is related to the asynchronous damping, as well as to the droop slop. As seen from equation (3.33), the power-filter cut-off frequency multiplicated by the normalized droop coefficient ($\sigma\omega_{LP}$) represents the initial sensibility of the frequency reference ω^* to an active power variation, namely the ROCOF.

In this sense droop-controlled voltage-sources recreate the synchronization mechanism of interconnected synchronous generators, around an operating point. The order of magnitude of the parameters, however, are different. For synchronous generators, the commonly used values in per-units are $\frac{1}{R} = 25\,p.u.$, $\Gamma_{ed}\omega_n = 31\,p.u.$ and $2H = 10\,s$ for classic thermal generators. Following the tuning recommendations of previous paragraphs, $\frac{1}{\sigma} = 25\,p.u.$ and $\frac{1}{\sigma\omega_{LP}} = 0.8\,s$. Consequently, the values of R and σ give the same droop characteristic in steady-state, but the dynamic damping in synchronous generation is completed by the damping torque Γ_{ed}. Droop-controlled voltage-sources bring an equivalent "inertia" to the power system of $0.8\,s$ compared to the ten time higher $10\,s$ inertia of the synchronous generators. Equivalent "inertia" should be understand as latency time given to the other controls or devices to react on events. This ensures that the whole system will not collapse instantaneously after a random grid event. In other words, the physical inertia of synchronous generators limits the dynamics of the frequency with a characteristic time of 10s, even though no one asked for. As developed in previous sections, grid stability requirements lead to a limited frequency dynamic with a characteristic time of only $0.8\,s$. The consequences are visible on the ROCOF. In the case of droop-controlled inverters, a ROCOF=$\sigma\omega_{LP}$ is also ten times higher than with synchronous generators. This might have consequences on protection based on ROCOF, but not on system security. The frequency will indeed converge quickly to its steady-state value with an higher damped response. Thus, the frequency deviation is expected to be lower during transients.

The lower characteristic time of the droop controlled VSC means that lower energy reserve from the DC bus are required for stability, compared to the traditionnal "spinning reserve". During the latency time, the voltage-sources must ensure to have enough energy stored on the DC side to feed the load without an excessive DC voltage drop (max 10%). The ratio $\frac{1}{\sigma\omega_{LP}} = 0.8\,s$ determines the level of energy reserve needed on the DC storage unit. When the droop coefficient increases, the need for DC energy reserve is lower, but so are the stability margins.

The conventional active power frequency droop control has been adapted in various situations with a wide diversity of alternative droop control schemes. Among them, [31, 114] introduce a control gain on the power derivative. The resulting "transient droop control" adds supplementary degree of freedom to damp the power response. Similar objective are pursued by [82], with an additional lead-lag filter that emulates a generator governor, or by [57] who adds a PLL. On the other hand, the power filter can have better performance than first-order filter, improving the system dynamic and stability [115, 116]. Besides, Virtual Synchronous Machine (VSM) controls have received a growing interest recently by implementing small-signal model of SGs in the VSC-based voltage-sources control [117], or directly the non-linear equations of the synchronous generators [83]. VSM controls result in similar dynamics than SGs and droop-controlled voltage-sources. They form the droop-like control family. [77, 78, 115, 118] brought a comprehensive comparison between frequency droop control scheme, VSM, and synchronous generators. The matching results confirm that they can all be considered as one droop-like control family.

To conclude, most of the autonomous solutions for parallel operation of voltage-sources in the literature rely on the basic synchronization mechanism provided by the frequency droop control. They can be gathered in a droop-like family. The synchronization mechanism of frequency droop control is the one of traditional synchronous generators. The parameters values of σ and ω_{LP}, however, are not physically constrained, but must fulfill the stability constraints of the system. The small-signal stability of one droop-controlled voltage-sources has been analytically analyzed in the previous subsection, but the generalization to large multi-source system, or to large-signal stability is a highly challenging topics.

3.3.4 Reactive power droop control

In a real power system, the voltage plan depends on the load level and must be handled by an appropriate strategy. The transmission grid operator must have the control on voltage reference set point provided by the VSC-based voltage source. The regulation strategy of voltage level in a 100 % PE grid could be comparable to the existing one. Additionally, a $E - Q$ voltage-droop is often presented as a simple control method to share locally the reactive power exchange on two sources closely bounded [17]. In the thesis, the conventional voltage-droop (3.35) is implemented

to give the voltage-amplitude reference to the voltage-sources, but the voltage-droop coefficients are taken low enough $n_q < 0.1$ p.u. and preserve stability of the frequency droop control [119].

$$E_i = E_{set} - n_q (Q_i - Q_{seti}) \tag{3.35}$$

Note that the reactive power Q_i must also be filtered for decoupling reasons. For the interested readers, the literature explores a bench of innovative solutions [120, 121, 122], for voltage management and control.

3.4 Toward generalization of small-signal and large-signal stability of multiple droop-controlled VSCs, in a scalable, radial or meshed grid

This section details the attempts in the literature to prove the existence of such an equilibrium, to generalize local stability of the equilibrium to an arbitrary number of interconnected devices, to extend local stability to large-signal stability. Power-frequency droop controls have been successfully tested in microgrid and showed sufficient robustness in the studied test cases [25, 58, 31]. However, investigations on local stability for large, meshed, and multi-VSCs system has been identified as a crucial research in the past, as pointed out by [40, 123], and are still hot topics nowadays. Moreover, transient stability after large signal perturbation is even harder to investigate analytically owing to non-linear behavior of the power-flow equations. Previous works on the topic are analyzed with a specific attention on the underlying assumptions.

3.4.1 Small-signal stability studies based on linearized models of multiple-converters network

Analytic studies of small-signal stability on a generalized network are based on linearization of power expression and rely on approximations to reduce the model size. Different approximation approaches and associated stability analysis are listed below.

In classical works on microgrid, two or three converters with droop controls are interfaced on a radial grid. The whole system small-signal stability is often studied focusing dominant

poles observation [44, 27, 36, 114, 31, 45, 109, 50, 64]. They detail a state-space model system, including the VSC output filter, the VSC inner controls, the loads and line dynamics, and droop controls. The power equation are linearized around an existing steady-state operating point. The eigenvalues are gathered by clusters, defined by mode frequency and damping. The focus is turned on less-damped poles as they will drive the critical behavior of the system. In all works, dominant poles are found to be related with the active power droop coefficients, the reactive droop coefficients, and power filters time constants. For example, the contribution of droop controls on less-damped modes can be evaluated by participation factor analysis [17, 36, 58] or by sensitivity analysis [124]. The dominant impact of droop controls on small-signal stability originate from a time decoupling between low-pass filters of power measurement, and high VSCs dynamics, lines dynamics, loads impedance or even fast active loads [97]. When the dynamics are timely decoupled, the system model can be reduced to perfect controlled voltage-sources connected with static impedances or admittances, written with algebraic expressions [44, 27, 114, 31, 45, 109, 59, 50]. While considering only dominant poles, the small-signal stability of droop is said to be acquired for a purely inductive radial grid, as long as the droop gains are reasonable and do not violate the time-decoupling with the VSC inner loops, regardless the size of the network [26, 40]. Lossy networks require more care while tuning the voltage droop coefficient [40]. [59] expands the reduced model techniques to generalized, scalable, meshed networks. He assumed inductive lines and neglected the VSC innercontrol dynamics, the loads and the power filters impact. Further considering small line impedance, then small voltage angle differences and small voltage amplitude dips between nodes in steady-state, he states that each droop control stability can be studied independently and that the stability of the whole system is obtained by the superposition theory facilitating the stability analysis on large systems. In such approximation, he emphasizes that only high frequency-droop gains compromise the stability of the overall grid, but the voltage droop have no significant impact on the stability if the system has only reactive lines.

When the different network components have no timely decoupled dynamics, conclusions are harder to draw. It has been shown in [102] than neglecting the lines dynamics in the reduced model by dominant poles failed to predict unstable regions. Furthermore, when the number of devices increases, the number of poles increase and trajectories analysis might be confusing.

3.4.2 Singular perturbation techniques for non-linear modeling and large-signal stability studies

Classical analysis methods rely on numerical procedures to approximate the region of attraction of an equilibrium [17]. Analytic approach brought by [125, 126, 127, 128], do not aim at providing best estimation on region of attraction. But they give insights on network structure impact on synchronization.

At odds with the previous method, [125, 126, 127, 128, 96] firstly assume that the droop control is over damped, resulting in a very low time-constant of power dynamics compared to other phenomena. The singular perturbation theory states that faster dynamics have already reached their final states when calculating the solution of a slower differential equation. In this sense, the approximation technique is inherited from the classical phasor approach in power system studies where the electrical transients are neglected compare to slower electromechanical dynamics, as the synchronous generators have inherent inertia. To conclude on the existence on an equilibrium, local-stability, and large signal stability, the power equations are not linearized.

Large-signal stability based on Kuramoto models Proving the convergence to a frequency agreement of an undefined number of droop-controlled VSCs without a linearization of power expression has been made possible with the analogy of Kuramoto models. In the Kuramoto model approach, the focus is not on calculating the maximum stable droop constant, but to give insight into how interaction between droop-controlled simplified sources creates a frequency synchronization or not.

In [127], the authors try to solve the consensus problem of a power-network that converges to a common frequency. They regard the power-network as a system of coupled oscillators. Particularly, they noticed that a reduced model of a machine based power system with overdamped generators characteristics can be approximated with a first-order, non-uniform Kuramoto model and the associated synchronization analysis of non-uniform Kuramoto oscillators.

They further noticed in [125] that droop-controlled VSCs behave as overdamped generators on radial and lossless grid. They can also be represented by Kuramoto oscillator models. The authors tacitly assumed that power filters effect is neglected. Under these approximations, they derive necessary and sufficient conditions for the existence of an equilibrium at a common

frequency shared by all the droop-controlled converters.[126] extends this result to meshed lossless networks. He states that the conditions for the existence of the equilibrium become only a necessary but not sufficient in the case of meshed grids. Once the existence of an equilibria is proved, the local stability of the equilibria can be demonstrated. In the theory developed in [129], Kuramoto oscillators with homogeneous coupling weights (ie, homogeneous frequency droop coefficients), all the stable equilibria exist in the called principal region, $-\frac{\pi}{2} < \delta_0 < \frac{\pi}{2}$, and they are locally stable under the assumptions of lossless static grid, and perfect nodes voltage regulation. This result is also extended to meshed grid in [126] to end with the same conclusion: assuming there exist a steady-state equilibrium between droop-controlled converters, with feasible load-flow, then the equilibrium is locally asymptotically stable if the voltage nodes angle differences are within $-\frac{\pi}{2} < \delta_0 < \frac{\pi}{2}$.

Large-signal model based on dynamics-phasors [105] derived also a large-signal model of two droop-controlled converters based on singular perturbation technique but only neglect loads time-constants and kept line time-constants. He does not consider the power measurement filters. He compares its reduced model with Kuramoto models that neglects lines dynamics. He showed numerically that its reduced model is able to predict unstable local behavior, for high values of frequency-droop coefficients, unpredicted by Kuramoto oscillators theory. The effect of line dynamics on droop-controlled converters was already highlighted in [96]. The local stability of [96] and [105] system is improved by the presence of power filter with sufficient bandwidth by enlarging the range of stable frequency droop coefficient as he showed in[96].

Large-signal stability based on Lyapunov function Frequency droop-controlled converters look like Kuramoto oscillators in the aforementioned papers when they have fixed output voltage amplitude. For taking into account voltage amplitude variation at each nodes, [123] derives a non-linear model of a generalized meshed network. Further, he followed a Lyapunov approach to derive stability conditions on droop gains. In opposition with [125, 130], no assumption of constant voltage or small phase angle difference are made. The converters have variable output voltage amplitude. He also neglects the loads and line dynamics so that the network has an algebraic representation. Lines are predominantly inductive. The power filters, similar to

those of [44, 58] are taken into account. Under the given assumptions, the dynamic states trajectories are found to be bounded for all practical choices of droop-control coefficients and initial power set-points. He concludes that the local stability of an arbitrary lossless meshed grid is independant from frequency droop gains and power set-points, but do depend on voltage droop coefficients. The asymptotic stability property is guaranteed by the Lyapunov approach.

Large-signal stability based on non-linear frequency controls that resemble to droop control only around the stabilized common frequency Some authors tried to break away from conventional frequency droop controls to define a synchronization function from scratch [131, 132]. They define decentralized and non-linear controls that bring the converters to act as oscillators that enter a limit-cycle oscillation where a consensus frequency is found. It can be proved that small-signal perturbation on the system from this equilibrium behave as droop-controlled inverters. Only large-signal is affected as the controllers allows a faster return in the stable region.

Another approach is to add extra non-linear control on existing droop control to help the system to come back to its attractive stable area after a large disturbance [112].

To conclude, overdamped frequency droop-controlled converters can be seen as Kuramoto oscillators which guarantees the existence of a frequency agreement between the units, and the large-signal stability of this equilibrium as long as the voltage angle differences between nodes stay transiently within $-\frac{\pi}{2} < \delta_0 < \frac{\pi}{2}$, and if the converters do not exceed their rated power. Advanced non-linear frequency control can help the transient stability, while conserving the local stable property of droop controls. Taking into account the lines and power filters dynamics, or the voltage-droop of VSCs can restrain the local stability conditions. However, to our best knowledge no studies give an in-depth analysis on the role of power filter time-constant on the global system stability, as noticed recently by [133]. Moreover the analytic analysis on transient stability exposed in this paragraph question the validity of assumptions. Especially in high-power device, the multiple VSC inner controls and limitations can impact positively or negatively the stability of the system during fast electrical transients.

While studying transient stability, it is important to keep in mind that real devices have limitations in the hardware that are hard to predict as it belongs to the manufacturers intellectual

property. Numerical simulations on real system model cannot be avoided in practice to study the large-signal stability of device.

3.5 Transient load-sharing capabilities of droop-controlled voltage-sources

This section illustrates the technical challenge to obtain an acceptable transient behavior of droop-controlled voltage-sources between to stable operating points. The real VSC-based converters have physical limitation of the instantaneous current magnitude that is not taken into account in the small-signal stability studies. Grid-forming converters, represented by perfect voltage-sources, are exposed to large transient currents during network disturbances, such as a line tripping. Output overcurrent spikes are destructive for power electronics devices or require costly oversizing investment. Transient studies involve non-linear differential equation which are more practically analyzed in time-domain using step-by-step numerical integration techniques. Here an EMT simulation software serves to see the impact of network-switching disturbances on a droop-controlled two-voltage-sources. Network-switching disturbances arise from planned and unplanned events (line switching or tripping, system faults or faults clearing).

3.5.1 Transient load-sharing during a line tripping in the transmission grid

The current transient following a line tripping is identified as a critical case for VSC-based grid-forming converters [134]. A time-domain simulation shows that the droop control is unable to prevent the voltage-sources from exceeding their current limits. In a transmission grid, the localization of electricity generation and consumption is variable. Large loads can be electrically close to small rated power units. The grid is built on a highly variable topology, depending on operation conditions or fortuitous external event. A change in topology causes large local variations of power flows. These operating constraints imply large power transients, traditionally supplied by the synchronous generators, that will be handled by the converters. One must certify that the output currents do not exceed instantaneous maximal current values of VSC and share transiently the load.

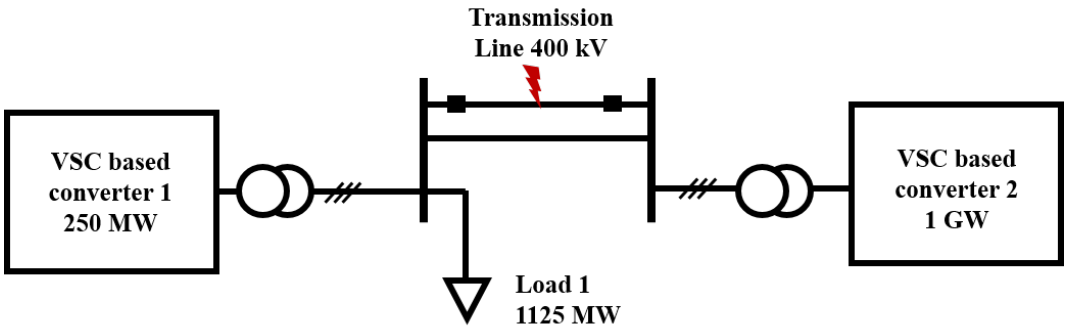

Figure 3.12 – Two voltage-sources system interfaced by a double overhead line, subject to a line tripping

The typical problem of a line tripping is stated in fig. 3.12. A simple network interconnects two droop-controlled voltage-sources representing ideal parallel grid-forming sources with respectively a nominal power for converter 1 $P_{n1} = 250\,MW$ and another nominal power for converter 2 $P_{n2} = 1\,GW$, supplying an active load of 1125 MW. The system is initially at steady-state. The power references of each unit are set to share the load equitably between the sources, $P_{10} = 0.9\,P_{n1} = 225\,MW$ and $P_{20} = 0.9\,P_{n2} = 900\,MW$ at nominal output voltages amplitude and frequency.

The lines parameters used are $R_{line} = 3\,\Omega$, $X_{line} = 30.7\,\Omega$, for each line, which corresponds to a 100 km double line. The load has a reactive compensation of 120MVAR to maintain the voltage in acceptable limits.

The fig. 3.13 and 3.14 show that the closest converters from the load handles temporary the major part of the active power which induces current inrush. The transient comes from the slow reaction of power droop controls to an active power demand variation. The power filter takes few cycles to react to real power change. The droop coefficients that ensure stability of the system, limit the response dynamics. As the voltage-sources do not change instantly their frequency references, a simple transient model can derive roughly the transient overload magnitude in the just after the line trip.

Considering fixed frequency references and fixed amplitude, the output current magnitude of the voltage-sources can be calculated similarly to the short-circuit phase-current in eq. (2.40). However, analyzing the system behavior with both the effect of the fundamental frequency and

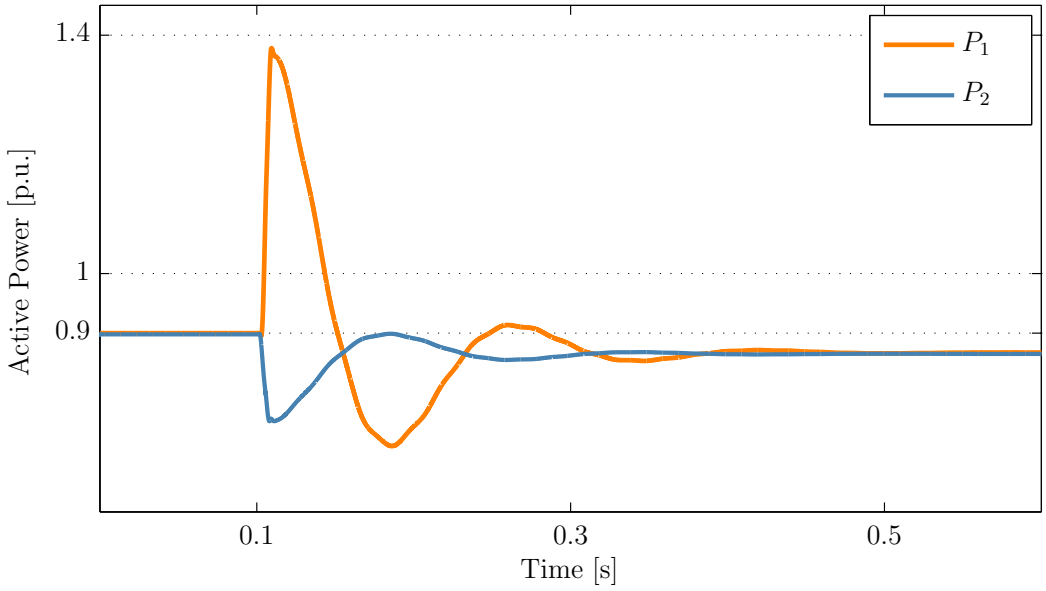

Figure 3.13 – Active power response of two droop-controlled voltage-source following a line opening

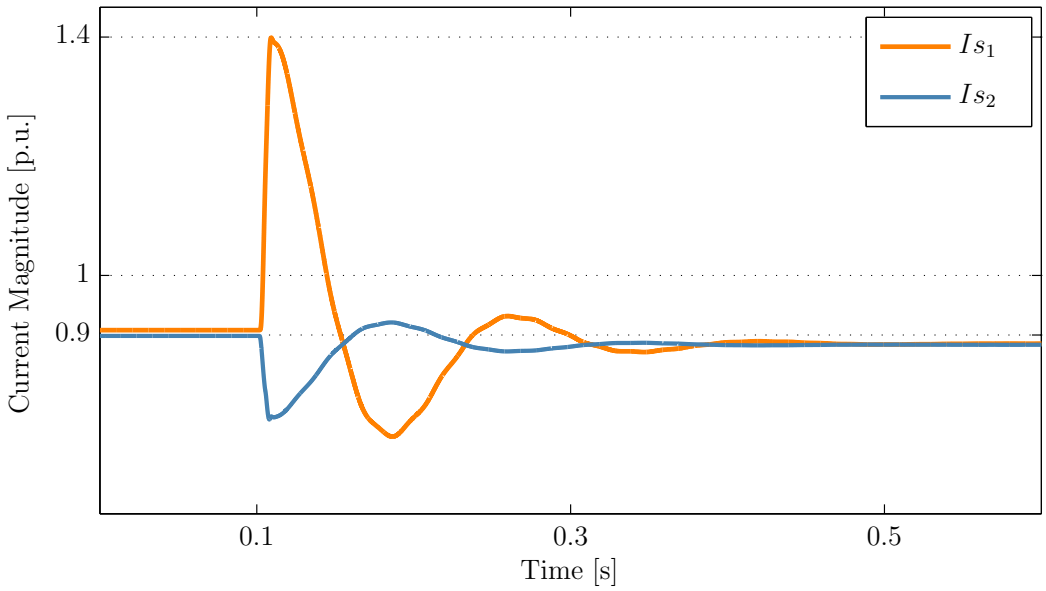

Figure 3.14 – Current envelopes of two droop-controlled voltage-source following a line opening

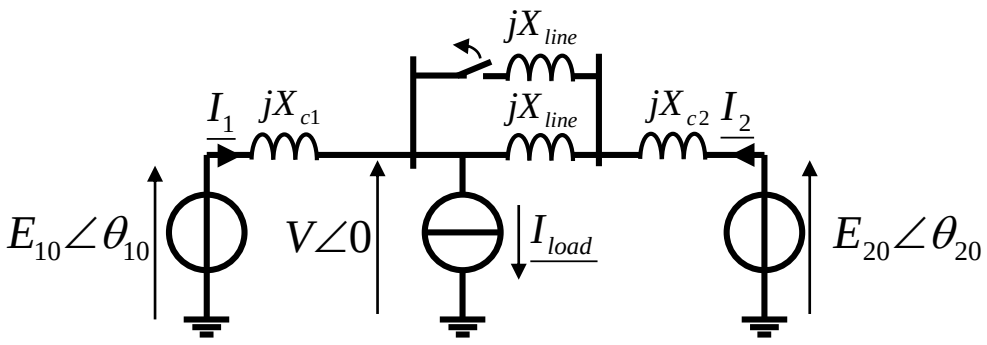

Figure 3.15 – Equivalent circuit describing the initial power sharing

the DC component following the line opening would require much computation efforts. A simplification consists in treating the dc offset separately by eliminating the current derivative term representing the line transient. By removing the derivative term, it is not assumed that the current are constant, but on the contrary, that they change instantaneously following the perturbation. The method is comparable to transient studies on synchronous generators using the fixed voltage E'_d behind its transient reactance X'_d [17]. The output current and active power can thus be roughly calculated using a phasor approach at nominal frequency, where only the reactances of the network are modeled. The loads are neglected. The initial situation is set with voltage magnitudes fixed at $E_{10} = E_{20} = E_0$. The phase origin is taken at the load voltage V, the initial voltage-source phase-angle are then θ_{10} and θ_{20}. Because the converters have distinct power rate, the reactance and the power values are not expressed in per-unit to avoid confusion. The initial steady-state can be written as:

$$\begin{aligned} X_1 &= X_{c1}, \\ X_2 &= X_{c2} + \frac{X_{line}}{2}, \\ P_{10} + P_{20} &= P_{load}, \\ \delta_0 &= \theta_{10} - \theta_{20}, \end{aligned} \tag{3.36}$$

Under the classical assumption of small voltage angle difference $\delta_0 << 1$, the initial load-flow satisfies:

$$\begin{aligned} P_{10} &\approx \frac{E_0^2}{X_1}\theta_{10}, \\ P_{20} &\approx \frac{E_0^2}{X_2}\theta_{20}, \\ X_1 P_{10} - X_2 P_{20} &\approx E_0^2 \delta_0, \\ X_1 P_{10} - X_2 \left(P_{load} - P_{10}\right) &\approx E_0^2 \delta_0, \\ \left(X_1 + X_2\right) P_{10} &\approx E_0^2 \delta_0 + X_2 P_{load}, \end{aligned} \tag{3.37}$$

Just after the line opening, and before the two voltage-sources adapt their frequency references, neither the voltage-angle difference between sources $\delta = \delta_0$, nor the amplitudes $E = E_0$ do change. But the load is instantly fed by the active power from the voltage-source 1 and 2, so that $P_2 + P_1 = P_{load}$. The topological change impacts the X_2 reactance value by $\Delta X_2 = \frac{X_{line}}{2}$, the equation that holds for the first few cycles is then:

$$\left(X_1 + X_2 + \Delta X_2\right) P_1 \approx E_0^2 \delta_0 + \left(X_2 + \Delta X_2\right) P_{load}, \tag{3.38}$$

Replacing (3.37) in the second member of (3.38)

$$\begin{aligned} \left(X_1 + X_2 + \Delta X_2\right) P_1 &\approx \left(X_1 + X_2\right) P_{10} + \Delta X_2 P_{load}, \\ \left(X_1 + X_2 + \Delta X_2\right) \left(P_1 - P_{10}\right) &\approx +\Delta X_2 \left(P_{load} - P_{10}\right), \\ \Delta P_1 &= \frac{\Delta X_2}{X_1 + X_2 + \Delta X_2} P_{20}. \end{aligned} \tag{3.39}$$

Thus, an approximative value of power deviation from optimal load share after the line trip is evaluated from (3.39) and reported in table 3.3.

Those values are the order of magnitude of VSCs output power changes, just after the event. They are conservative as compared to the simulation in fig. 3.13 because the load voltage drop following the line trip has been neglected in the analytic phasor model.

Notably, the transient power variation out of the voltage-source 1 (3.39) is strongly dependent on the reactance between the load and the voltage-source. If the reactance X_1 increases, the real power demand just after the trip is lower.

Table 3.3 – Numerical application

Parameter	Value
X_{line}	30.7 Ω
X_1	61.4 Ω
X_2	30.7 Ω
P_{20}	900 MW
P_{10}	225 MW
ΔP_1	$\approx 128\,MW = 0.57\,Pn1$

3.5.2 Limits of available solutions to improve the transient-load sharing

In the literature, different attempts have been proposed to enhanced the droop control transient behavior. Increasing the droop coefficient m_p is straightforward to fasten the droop control response to reach a steady-state [135]. The stability of the whole system is, however, endangered by high droop coefficients (see section 3.3). Besides, the consequences of m_p on the first current magnitude spike is negligeable [135]. [27] suggested to add a proportional control on the power measurement to directly correct the voltage angle difference, through the phase-angle reference θ_i^*. Using a comparable control technique [109] showed the limitation on system stability, due to the line dynamic.

Speeding-up the droop control is neither desirable as it results in fast frequency reference transients, nor always possible as it degrades the stability.

Conclusion on the synchronization of voltage-sources on transimission system

This chapter analyses the theoretical behavior of interfaced droop-controlled voltage-sources on a transmission grid. Based on the active power dynamics between two sources, a decentralized synchronization of voltage-sources is obtained by the control of each voltage-source frequency reference, defined as an inner state variable. The droop-control makes all the frequency references converge to a common steady-state frequency, in a closed loop and decentralized manner. The droop-controlled voltage-sources exhibits the required property to share, as desired, the active loads in steady-state.

Similarly to the existing synchronization mechanism of synchronous generators, the frequency droop-control ensures the existence of a stable equilibrium between voltage-sources, regardless of the size of the network, under certain conditions. The stability conditions include the nature of the grid, which must be predominantly inductive, the existence of accessible load flow with limited voltage angle differences between voltage-sources, which is always the case on a well designed transmission grid. Other stability conditions restrain the droop coefficient gains to moderate values and require the presence of low-pass power filters to decoupled the droop control action from line resonance at the nominal frequency. The impact of power filter would need a deeper analysis. Alternative frequency controls, as VSM or non-linear frequency controls, belong to the same droop-control family because they provide the same synchronization mechanism around the equilibrium. From a higher perspective, the frequency droop-control recreates the global information on the power demand adequacy between sources, thus allows upper energy management.

Droop-control small-signal stability requirements, however, are not compatible with fast transient load-sharing. This could lead to unacceptable overloaded situations. During sudden but common transmission grid events, such as a line tripping, one VSC might exceed its current limit for a longer time than the hardware can handle. Ensuring both current limiting and large-signal stability is still a hot research field, even if recent propositions have been formulated, including in this thesis. It implies to look deeper in the instantaneous voltage regulation of grid-forming converters.

Chapter 4

Building a grid-forming VSC-PWM for the transmission grid system

Contents

4.1 Design requirements and method 126

4.2 Design of the VSC output filter 129

4.3 Design of the terminal voltage control in closed loop 136

4.4 Robustness of the voltage control in various grid configurations 149

4.5 Analysis of the control robustness through the impedance-based approach 155

Although the VSC devices are intrinsically controllable voltage-sources, they cannot, in practice, be connected directly to a transmission grid to provide grid-forming function. A voltage feedback control must maintain the terminal voltage in case of load changes, in accordance with the technical limitation of the chosen pulse-width-modulated (PWM) technology and with the challenging environment of a transmission grid. The voltage control must be stable in various grid situations from stand-alone to powerful grid-connection made of several other devices. The chapter derives the design method recommendations, from the hardware requirements of the filter, and until the voltage control parameters to face those multiple challenges. The whole VSC system with its control scheme that offers parallel grid-forming capability is drawn in fig. 4.1. As

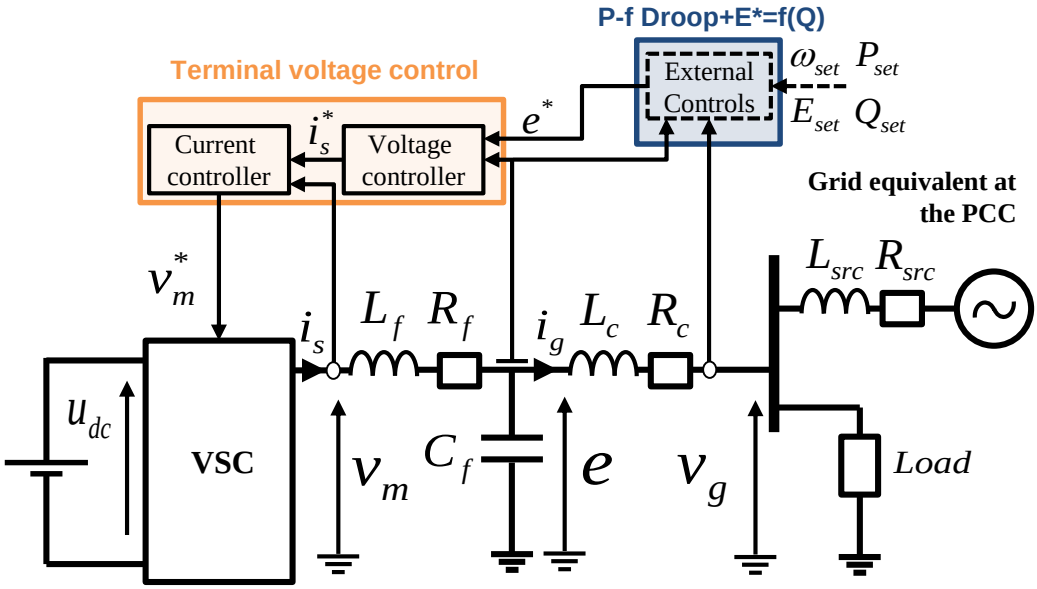

Figure 4.1 – Layout of the PWM-VSC with its output filter and parallel grid-forming controls. Single-phase equivalent representation

the external controls have been treated in the chapter 3, the focus of the chapter is on the filter and the voltage control design.

4.1 Design requirements and method

The terminal voltage control of a grid-forming VSC performs the control and protective functions essential for satisfactory performances. These performances are obtained if the control fulfills the requirements associated with the chosen VSC technology, based on PWM modulation, as well as the system needs in a transmission grid environment. The section recalls the design requirements already announced in chap. 2, adapted to PWM-VSC technology, and describes the voltage control design method.

4.1.1 Design requirements of grid-forming control from PWM-VSC perspective

Regarding the VSC device, the voltage control must address the following requirements:

1. Maintaining the magnitude of its terminal voltage e within acceptable limits when the load varies

2. Ensuring the device survives transient grid-disturbances even with its limited instantaneous overcurrent capability

3. Respecting the technological constraint of the PWM-VSC regarding its limited bandwidth

First, the terminal voltage control can be obtained by adjusting the VSC modulation reference in closed loop to compensate for the dependency of the voltage to the load level. In section 2.1.2, the performance requirement for voltage control states that the RMS value of the terminal voltage must reach ±5 % of the reference, within 10 s (see [16], p215). The voltage reference is given by a setpoint from a centralized operator and usually augmented with a voltage-reactive power droop control.

Then, the voltage control must be designed so that electrical quantities never exceed their constructive limits. In particular interest, the output current i_s must be closely controlled to be kept under the instantaneous overcurrent capability defined in table 2.9.

Finally, the two previous functions must respect the technological constraints of the chosen VSC technology. At high-power, the PWM-VSC based has a limited valves switching frequency because of the switching power losses during commutation. The limited switching frequency has two technical consequences. A second-order output LC filter must be carefully designed to mitigate the voltage harmonics in the terminal voltage e. Secondly, the limited switching frequency results in a limited dynamic response of the VSC modulated voltage, which induces constraints on the inner control design.

The limited PWM-VSC bandwidth due to the switching frequency limitation f_{SW} can be approximated by considering that the pure switching delay is equivalent to a broadly accepted first-order transfer function: [136]

$$\boldsymbol{v}_{mabc}(s) = \frac{1}{1 + \frac{s}{2f_{SW}}} \boldsymbol{v}^*_{mabc}(s) \tag{4.1}$$

A reasonable switching frequency for high-powered device is $f_{SW} = 5\,kHz$, and is used as a reference design value. This value is chosen to be reproducible in laboratory conditions but real

devices at higher power might have different values, during steady-state or transient conditions depending on manufacturers and technologies. It is also worth recalling that MMC technologies might overcome the dynamical constraints presented here.

4.1.2 Design requirements of grid-forming control from power system perspective

From the power system perspective, the voltage control should contribute to an effective control of VSC terminal voltage, while maintaining sufficient stability margins when the VSC is connected to the grid. The required stability is separated in two parts:

1. The small-signal stability is ensured if the potential resonances in the system are sufficiently damped

2. The large-signal stability is ensured if a large disturbance does not lead to loss of synchronization of the VSC, or VSC disconnection, and let the system in an acceptable operating point.

The small-signal stability of voltage control is specifically challenging in a transmission grid environment as the VSC terminal voltage can be connected system either to a standalone passive load or to a powerful grid, containing several converters. No information on the exact composition of the rest of the grid is available. A full power-electronic system is even more challenging as the dynamics and potential resonances of the system depend on the inner control on each devices and not only on physical invariant properties. Then, the dynamic performance of the voltage control must be set independently from the grid dynamics, but the voltage control must be robust in various grid configurations.

The large-signal stability will be strongly affected by the implemented strategy of the overcurrent protection of the VSC device. If the controlled VSC enters in a protecting mode following a stressing event, that can result in loss of control ability or even to disconnection. The voltage control must able to keep the unit connected without disturbing the synchronizing frequency control. The large signal-stability will be analyzed in the next chapter.

4.1.3 VSC grid-forming capability design method

Following the PWM-VSC device requirements and the power system requirements, the design method of a grid-forming function is proposed hereafter and followed in the rest of the chapter. The method includes the output filter design, the voltage control design and the current limitation design. The method of the chapter focuses only on the small-signal performances and stability aspect. Firstly, the output filter is designed, based on the rated power of the VSC and its limited switching frequency. Secondly, a voltage control structure is proposed to regulate the terminal voltage at the filter output. As the rest of the system is uncertain, the control parameters will be tuned depending solely on the filter internal model and the limited dynamic of the VSC. Small-signal approximation allows to neglect the frequency variation from the external droop control and thus to design a linear controller. As the number of measurement sensors is not critical in high-power applications, the load current can be measured and compensated. The small-signal dynamic performances of the VSC with its filter, open-circuited at its terminal, are set to reach the largest available bandwidth to give the grid-forming source the maximum stiffness, and so, a better load rejection. Thirdly, the small-signal stability robustness in various grid-connected situation is assessed using eigenvalues technique. Finally, the eigenvalues technique is completed by an impedance-based approached in frequency domain to understand the external interaction of a voltage controlled VSC. The impedance-based approach integrates the control parameters in equivalent circuit models to help the designer to directly understand the contribution of the connected devices to the stability of the whole power system.

4.2 Design of the VSC output filter

The sections describes the sizing of the hardware elements of a voltage-source converter based on PWM modulation that can be connected to the highest voltage level of the transmission grid. The output filter must fulfill the constraints of transmitting rated power to the point of common coupling (PCC), and must limit the propagation of switching harmonics, even at no load. All recommendations are drawn using per-unit values as defined in chapter 3, considering a converter of 1 GW of nominal power when needed. Note that the author is aware that such high-power PWM-VSC device does not exist. It is assumed, instead, that a 1 GW PWM-VSC converter could

Table 4.1 – Definition of PWM nominal values fig. 4.1 in a common voltage base (U_b =320 kV)

Parameter	Quantity	Value
U_{dc}	Nominal Direct Voltage	640 kV
$U_m(nom)$	Nominal phase-phase VSC output voltage	320 kV (RMS)
f_{SW}	PWM switching frequency	5 kHz

represent an aggregation of multiple devices, interfacing a wind power plant or photovoltaic power plant and connected to the same PCC.

The PWM VSC characteristics are summarized in the table 4.1. The following assumptions are taken into account:

- The direct voltage is considered as a fixed value $u_{dc} = U_{dc}$, because the voltage support from the DC capacitance and from DC voltage regulation of the primary source.
- No over modulation techniques are considered here.
- Without over modulation or third-harmonic rejection, the DC voltage level determines the maximum phase-to-phase RMS value of the modulated voltage v_m, with the eq. 4.2 [137]:

$$U_m(max)\frac{\sqrt{2}}{\sqrt{3}} = \frac{U_{dc}}{2} \tag{4.2}$$

  With the nominal values from table 4.1 it results in, for this specific case:

$$U_m(max) = \frac{U_{dc}}{2}\frac{\sqrt{3}}{\sqrt{2}} = U_m(nom)\frac{\sqrt{3}}{\sqrt{2}} = 1.22\,U_m(nom) \tag{4.3}$$

  A maximum value of $U_m(max) = 1.22\,U_m(nom)$ gives a satisfactory range of accessible voltage for an effective voltage control as stated by [38].

- The filter is assumed to be balanced on the three phases.
- In the harmonized base voltage level, the transformer is modeled by a series impedance $L_c - R_c$ in fig. 4.1, and has a Delta-wye configuration. The zero sequence of the current i_g is then always null.

Given these assumptions and requirements, a filter design is deduced through an analytic process that lists all the design constraints, and ends with the synthesis of filter parameters.

4.2.1 Criterion for rated power delivery

The total interconnection inductance combines the transformer leakage inductance L_c that is naturally present, completed by the filter inductance L_f to be determined. A minimal value of the total interconnection inductance is physically required to decouple the VSC-based sinusoidal voltage-source from the PCC voltage variation, according to the sources interconnection law. On the other hand, the interconnection inductance has to be kept low enough to ensure the rated active and reactive power to flow within the voltage operatin limits [138]. Ideally, the interconnection impedance is purely inductive to avoid power losses.

The maximal value of the total interconnection inductance is determined from steady-state expression of active and reactive power transfer from the VSC to the PCC, at nominal frequency. The power values are given by:

$$\begin{aligned} P &= \frac{U_m U_g \sin(\delta)}{x_{tot}}, \\ Q &= \frac{\left(U_m U_g \cos(\delta) - U_g^2\right)}{x_{tot}}. \end{aligned} \tag{4.4}$$

Where x_{tot} represents the total interconnection reactance between the valves-bridge and the PCC. U_m is the phase-to-phase RMS value of the modulated voltage, U_g is the phase-to-phase RMS value of the PCC voltage, and δ is the phase-angle differences between the two voltages. The filter capacitance causes a marginal reactive current contribution and is therefore neglected at steady-state. This assumption is validated later. The total reactance is then defined solely by $x_{tot} = \left(l_f + l_c\right)$, in per-unit.

Two steady-state criteria determine the maximal value of x_{tot}:

- At nominal active power delivery, the voltage angle difference δ must be kept sufficiently low to maintain a linear characteristic of $P(\delta)$, requiring a limitation of $|\delta| < 30°$ [38]. Indeed, the external power-frequency droop control has a similar behavior on all the operating points only if the power-angle relationship is linear. Here, the angle is limited to $|\delta| < 20°$ to add some margin.

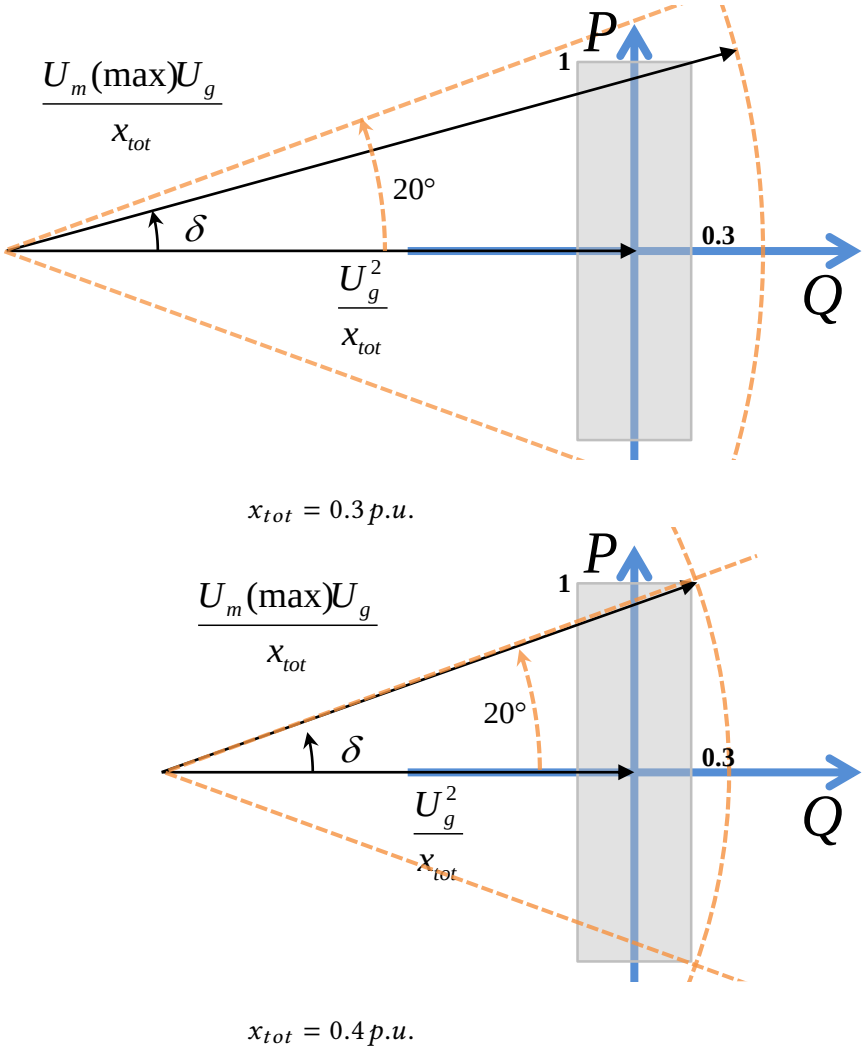

Figure 4.2 – Power delivery in steady-state depending on the total filter inductance. The normal operation area is filled in grey. Dot lines delimits the accessible points for a given value of x_{tot}.

- At nominal active power and maximum reactive power delivery, the value U_m of the modulated voltage must be kept under 1.2 per-unit because of the DC voltage limitation expressed in eq. 4.3.

Though exact determination of parameters is possible based on (4.4), a graphical method provides a better overview on the total inductance design constraint as shown in fig. 4.2. The graphical method is well documented in [137, 38].

To cover all the normal operation area in fig. 4.2, the total interconnection reactance is limited by:

$$x_{tot} < 0.3\,p.u. \tag{4.5}$$

Further, recalling that the transformer linkage gives $l_c = 0.15\,p.u.$ and that $x_{tot} = (l_f + l_c)$, the limitation of filter inductance dictated by the steady-state power delivery requirements is:

$$l_f < 0.15\,p.u. \tag{4.6}$$

4.2.2 Criterion of PWM harmonics attenuation

Before the connection to the grid, the switching harmonics from the PWM modulation must be filtered out from the filter output voltage e [139]. Considering the relatively low switching frequency in high-power application VSCs, the filtering action of a simple inductive filter would result in a large and costly investment to respect the harmonics attenuation requirements [138, 137]. A small shunt capacitance provides a low impedance path at high-frequency to permit harmonic currents to flow while being negligible at nominal frequency [140]. Meanwhile, the introduction of a real capacitance smooths the variation of the voltage (e), resulting in easier measurement and control of this introduced filter state.

To choose the LC filter parameters couple, a broadly accepted criterion is based on a frequency-domain consideration. Filter output voltage with a THD below 5% requires the LC cut-off frequency to fit above ten times the nominal frequency and below five to ten times the switching frequency [38, 46, 31, 138].

$$10\,\omega_n < \omega_{lc} = \frac{\omega_n}{\sqrt{l_f c_f}} < \frac{2\pi f_{SW}}{10}, \tag{4.7}$$

With a switching frequency of $f_{SW} = 5$ kHz, one possible solution is:

$$\frac{1}{\sqrt{l_f c_f}} = 10. \tag{4.8}$$

To further choice l_f value over c_f value, [140] suggested to minimize distortion by maximizing the capacitance c_f and to minimize the filter inductance l_f. On the other hand, the value of the filter capacitance c_f must be kept as small as reasonable to limit the impact of the capacitance on the rating because of the provided reactive power.

4.2.3 Criterion of limitation of output current ripples

The design of the filter inductor l_f is dictated by physical limits of current variation in the valves. At the switching time-scale, the shunt capacitor c_f enforces the ac voltage-source nature at the filter output. Then, the capacitance voltage e can be approximated by its average value over a switching period to precisely estimate the current ripples in the filter inductance l_f and in the valves. These current ripples must be kept below 20% (in most of the IEEE standards) to have a good trade-off between current ripple and inductor size [141].

Considering a fixed capacitor e voltage at no load, the filter inductance l_f is calculated from the current ripple limitation [139, 138]. For a triangular modulation the peak-to-peak ripple is [140, 141]:

$$\Delta\tilde{i_s} = \frac{1}{8}\frac{U_{dc}}{\frac{l_f}{\omega_n} f_{SW}} \tag{4.9}$$

From (4.9), a limited current ripple of $\Delta\tilde{i_s} < 20\%$ below 20% gives a minimal value of l_f in per-unit:

$$l_f > 0.048 \tag{4.10}$$

4.2.4 Filter design synthesis

Recalling the two design criteria for the filter inductance (4.6) and (4.10), the following limits that holds are:

$$0.048\,p.u. < l_f < 0.15\,p.u. \tag{4.11}$$

Combined with the LC filter requirement (4.8), the capacitor size is limited by:

$$0.066\,p.u. < c_f < 0.21\,p.u. \tag{4.12}$$

A degree of freedom still exists in the choice of l_f, c_f. Various optimization objectives under cost, size, or stored energy constraints can guide the choice of LC filter passive elements. The choice was made here to maximize the filter inductor l_f to minimize as far as possible the current dynamics in short-circuit, which is always a critical feature in high-power application [142].

Table 4.2 – LCL filter parameters

Parameter	Quantity	Value
l_f	filter inductor	$0.15\,p.u.$
r_f	filter series resistance	$0.005\,p.u.$
c_f	filter shunt capacitance	$0.066\,p.u.$
l_c	connection inductance	$0.15\,p.u.$
r_c	connection series resistance	$0.005\,p.u.$

Moreover, a capacitor value limited to 6.6 % does not degrade too much the power factor at rated power as assumed first [143, 141].

With these numerical values, the resonance frequency of the LCL filter is calculated to check that its value is away from low order harmonics and from modulation harmonics [143, 31, 138, 144]. With the minimal value of c_f in (4.12), the value of the LCL resonance is:

$$\begin{aligned} \omega_{LCL} &= \sqrt{\frac{l_f + l_c}{l_c l_f c_f}}\omega_n \\ \omega_{LCL} &= 14.2\,\omega_n \end{aligned} \tag{4.13}$$

The LCL resonance frequency of (4.13) is found to above ten times the fundamental frequency, and below half of the switching frequency, which is satisfactory according to [143, 144]. The losses have been neglected in the analysis, but are present in reality. At high power (>1 MVA), the inductive components have generally series losses of 3% with respect to the total impedance. The determined filter parameters are summarized in table 4.2, and give coherent results with existing PWM converters design in high power applications [137, 145].

Following the characteristic of a PWM-VSC for high-power applications, and according to the specified requirements for nominal operation, an output filter design has been deduced. There is, however, a room for manufacturers to optimize the size of the filter elements with additional economical criteria.

Fig. 4.3 shows the EMT simulation of the switched model of the designed VSC with its filter with the parameter in Table 4.1 and 4.2. Due to the highest value chosen for l_f, the current ripple in i_{sa} is largely limited below 20% of the rated current. The filter line output voltage e_a

on (b) exhibits a very low harmonics content. The voltage $e_a(pwm)$ from the switching model filts perfectly the $e_a(avg)$ from the averaged model . At no load, however, note that there exists a poor damped harmonics at 500 Hz due to the LC-filter resonance at ω_{LC}, excited by the numerical computation. This resonance underlines the need for closed-loop control of the voltage to bring additional damping.

4.3 Design of the terminal voltage control in closed loop

The design of the voltage controller is based on the PWM-VSC averaged model and the output filter model. The dynamic performance are fixed from an open-circuited situation at its terminal voltage. The filter is modeled in dq-frame to control constant values in steady-state. The dynamic performances characteristics will be set regarding the frequency response of the system.

4.3.1 Filter model in dq-frame

The equation of electrical quantities are written in the dq-frame (called also synchronous frame) rotating at $\theta^*(t)$, the integration of the frequency reference $\omega^*(t)$ given by the external power-frequency droop control. The rotating reference is defined locally by each inverter. In this frame, the filter equations between complex space vectors representation of electrical quantities are:

$$\begin{aligned}\left(\frac{l_f}{\omega_n}\frac{d}{dt} + r_f + j\omega^*\frac{l_f}{\omega_n}\right)\boldsymbol{i}_{sdq} &= \boldsymbol{v}_{mdq} - \boldsymbol{e}_{dq}\\ \left(\frac{c_f}{\omega_n}\frac{d}{dt} + j\omega^*\frac{c_f}{\omega_n}\right)\boldsymbol{e}_{dq} &= \boldsymbol{i}_{sdq} - \boldsymbol{i}_{gdq}\\ \left(\frac{l_c}{\omega_n}\frac{d}{dt} + r_c + j\omega^*\frac{l_c}{\omega_n}\right)\boldsymbol{i}_{gdq} &= \boldsymbol{e}_{dq} - \boldsymbol{v}_{gdq}\end{aligned} \tag{4.14}$$

The time dependency has been removed for clarity when it is unambiguous. The frequency reference $\omega^*(t)$ is moving slowly at the electrical variation scale. The differential equations in (4.14) can be made made linear by considering the reference angle frequency stays at its steady-state initial values $\omega^* = \omega_0$.

As seen in (4.14), the d and q components of electrical quantities in the filter are interdependent but constant in steady-state. As the equations in (4.14) have been made linear by using $\omega^* = \omega_0$, the relationship between quantities can readily be expressed in Laplace replacing $\frac{d}{dt}$ by the Laplace variable 's':

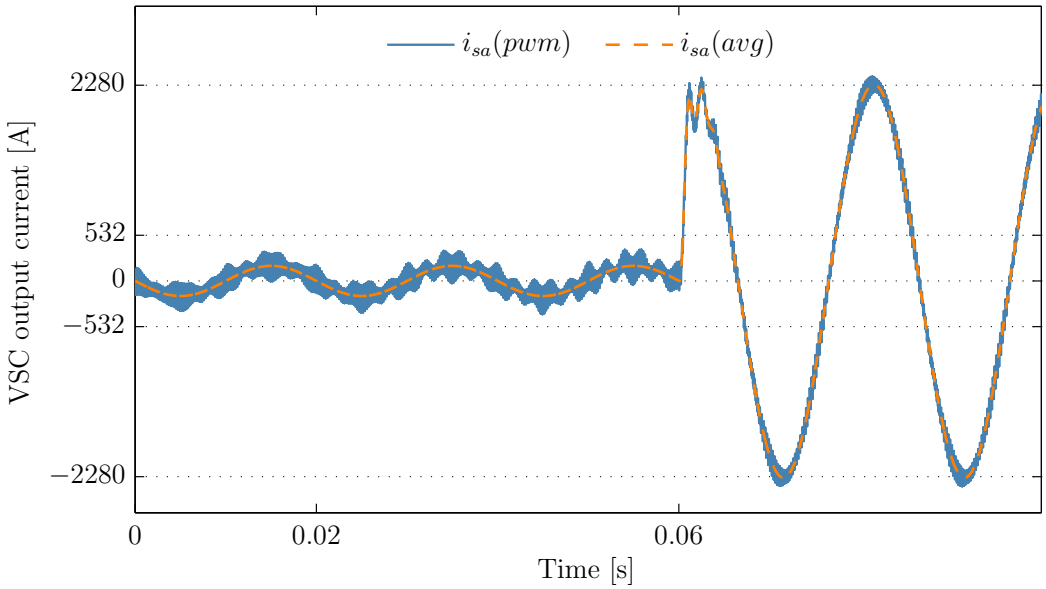

(a)

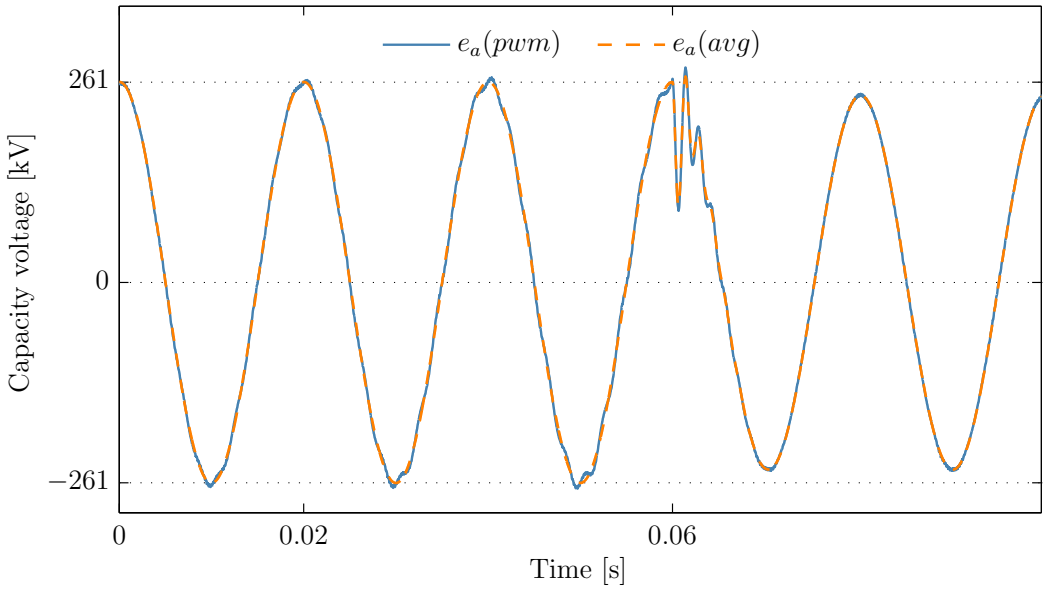

(b)

Figure 4.3 – EMTP simulation of VSC output phase-current (a), and filter output capacity phase-to-ground voltage (b). The full VSC switched model is compared with the averaged model over a switching period. Initially no load is connected. At $t = 0.06$ s, a load of $P_{load} = 1$ p.u. and $Q_{load} = 0.3$ p.u. is connected to the PCC.

$$\begin{aligned}\left(\frac{l_f}{\omega_n}s + r_f + j\omega_0\frac{l_f}{\omega_n}\right)\boldsymbol{i}_{sdq}(s) &= \boldsymbol{v}_{mdq}(s) - \boldsymbol{e}_{dq}(s)\\ \left(\frac{c_f}{\omega_n}s + j\omega_0\frac{c_f}{\omega_n}\right)\boldsymbol{e}_{dq}(s) &= \boldsymbol{i}_{sdq}(s) - \boldsymbol{i}_{gdq}(s)\\ \left(\frac{l_c}{\omega_n}s + r_c + j\omega_0\frac{l_c}{\omega_n}\right)\boldsymbol{i}_{gdq}(s) &= \boldsymbol{e}_{dq}(s) - \boldsymbol{v}_{gdq}(s)\end{aligned} \tag{4.15}$$

The derived model of the filter in dq-frame is linear and independent of the reference angle θ^* if the variation of ω^* are slow enough. Based on this model, filter states can be controlled independently from the reference angle determination of the external droop control.

4.3.2 Design of the cascaded structure of the VSC voltage control

Regarding the PWM-VSC with its output filter, the voltage control basically adjusts the VSC modulated voltage amplitude reference to maintain the terminal voltage, measured at the filter output, regardless the demanded load.

The filter represented in dq-frame by (4.14) will be the physical process to be regulated. The advantage of the controlling of filter states in dq-frame is to handle constant values in steady-state. PI compensators on dq components ensure zero steady-state errors between the measured sinusoidal values and their references. Besides, as the magnitude is directly controlled, magnitude limitation are easier to implement without clipping the voltage waveform. Alternatively, stationary frame line voltages and currents or their $\alpha\beta$ components in stationary frame could be controlled using resonant controller [141, 97]. Performances for balanced systems are equivalent [146]. The analysis here only focuses on the positive-sequence tracking of electrical quantities. For the control of the negative-sequence, in case of unbalanced loads for example, a second reference dq-frame rotating at $-\omega^*$ could be implemented. As unbalanced loads are not common at the transmission grid level, they are not considered.

A cascaded structure of PI compensators (fig. 4.4) is deduced to control the inductance current i_s in l_f and the terminal voltage e across the capacitor voltage c_f. The deduction method is inherited from the principe of the model inversion [147]. Details on the methods are found in [148]. Other states feedback options are studied in [48], such as the capacitor current feedback, but were shown to be less effective for disturbance rejection.

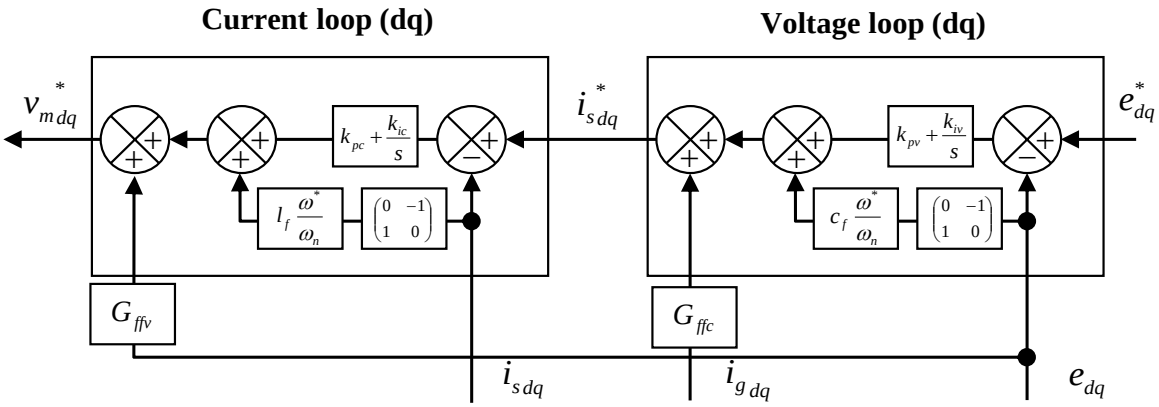

Figure 4.4 – Scheme of the inner control of AC filter output voltage. Two cascaded loops in dq-frame including cross-decoupling terms, capacitor voltage and grid current feedforward.

Cascaded loops have been employed successfully in UPS and Microgrids [48, 149, 46, 31, 58, 40, 150]. The inner current loop explicitly controls the converter output current which is convenient for overcurrent protection [46, 149]. In addition, all the classical grid-following converters at transmission level already embed a current-vector control [151, 7]. They could then be upgraded in grid-forming converters by adding an extra voltage control loop. Finally, cascaded loops appears to be more intuitive for industrial applications, answering the requirement of simplicity of developed solution in this thesis. Fig. 4.4 gives the overall layout of the cascaded structure.

The current controller forces the current $\boldsymbol{i}_{sdq}$ to follow its reference $\boldsymbol{i}_{sdq}*$. Cross-coupling terms decouples the d and q axis so that the control is made independent from the operating frequency $\omega^* = \omega_0$. Feedforward gains g_{ffv} help the current control to compensate for a capacitor voltage changes and thus enhance the current control accuracy against output voltage disturbance [142]. The PI control nullifies the error on steady-state. Note here this property is not

compulsory as the main point is to control the voltage precisely. A proportional control could be sufficient.

If the currents $\boldsymbol{i}_{sdq}$ and the voltages $\boldsymbol{e}_{dq}$ equal their measured values, the VSC reference voltage is given by:

$$\boldsymbol{v}^*_{mdq} = \left(k_{pc} + \frac{k_{ic}}{s}\right)\left(\boldsymbol{i}^*_{sdq} - \boldsymbol{i}_{sdq}\right) + j\frac{l_f}{\omega_n}\omega_0 \boldsymbol{i}_{sdq} + g_{ffv}\boldsymbol{e}_{dq} \tag{4.16}$$

From the current-loop time-scale perspective, the time delay occasioned by the computation and switching is neglected. The time delay may influence high harmonics as shown by [152, 136, 153], but high harmonics are not of interest in this thesis. With a no-delay assumption in the VSC control, the VSC output voltage equals its reference: $\boldsymbol{v}_{mdq} = \boldsymbol{v}^*_{mdq}$. The eq. (4.16) can be re-injected in the filter equation (4.15) in frequency domain.

$$\begin{aligned}
\left(\frac{l_f}{\omega_n}s + r_f + j\omega_0\frac{l_f}{\omega_n}\right)\boldsymbol{i}_{sdq} &= \left(k_{pc} + \frac{k_{ic}}{s}\right)\left(\boldsymbol{i}^*_{sdq} - \boldsymbol{i}_{sdq}\right) + j\frac{l_f}{\omega_n}\omega_0\boldsymbol{i}_{sdq} + g_{ffv}\boldsymbol{e}_{dq} - \boldsymbol{e}_{dq}, \\
\left(\frac{l_f}{\omega_n}s + r_f + k_{pc} + \frac{k_{ic}}{s}\right)\boldsymbol{i}_{sdq} &= \left(g_{ffv} - 1\right)\boldsymbol{e}_{dq} + \left(k_{pc} + \frac{k_{ic}}{s}\right)\boldsymbol{i}^*_{sdq}. \\
\boldsymbol{i}_{sdq} &= \frac{\left(k_{pc} + \frac{k_{ic}}{s}\right)\boldsymbol{i}^*_{sdq}}{\left(\frac{l_f}{\omega_n}s + r_f + k_{pc} + \frac{k_{ic}}{s}\right)} - \frac{\left(1 - g_{ffv}\right)\boldsymbol{e}_{dq}}{\left(\frac{l_f}{\omega_n}s + r_f + k_{pc} + \frac{k_{ic}}{s}\right)},
\end{aligned} \tag{4.17}$$

From the expressions in (4.17), it is remarkable that the feedforward gain g_{ffv} nullifies output current sensitivity to the voltage disturbance, closing the gap with an ideal current-controlled source with infinite Norton impedance in parallel. To feed a random passive load autonomously, under its nominal conditions, the current references must be provided by the outer AC voltage control. Similarly to the current control, the voltage control compensates for the error on the voltage components of $\boldsymbol{e}_{dq}$ with a PI compensator. The d and q components are decoupled. The grid current $\boldsymbol{i}_{gdq}$ is considered as a disturbance that should be rejected to maintain the voltage. As the grid current is already measured for the output power calculation, this disturbance can then be feedforwarded at the voltage control output to improve the disturbance rejection of the connected load. It is worth mentioning that the feedforward of disturbance signals is delayed in practice due the measurement and computation time. The delays can degrade the expected performances or lead to an unstable situation. Delays are not taken in consideration in the following, resulting in an optimistic design.

$$\boldsymbol{i}^*_{sdq} = \left(k_{pv} + \frac{k_{iv}}{s}\right)\left(\boldsymbol{e}^*_{dq} - \boldsymbol{e}_{sdq}\right) + j\frac{c_f}{\omega_n}\omega_0 \boldsymbol{e}_{dq} + g_{ffi}\boldsymbol{i}_{gdq} \tag{4.18}$$

The current loop and the voltage loop of the cascaded structure are tuned independently, based on the time decoupling principle.

4.3.3 Setting the dynamic performance of the cascaded voltage and current loop

Current loop tuning The PI parameters of current-control k_{pc} and k_{ic} are tuned to obtain the highest closed loop bandwidth, in accordance with the VSC bandwidth limitation. The current-control bandwidth in closed loop is limited by the time-decoupling assumption with the natural VSC bandwidth imposed by its switching delay. Neglecting the resulting VSC intrinsic dynamics given by (4.1) from the current-control time-scale requires to impose a current-control closed loop bandwidth ten times lower than the VSC bandwidth. For f_{SW}= 5 kHz, it yields a current bandwidth of:

$$\begin{aligned} \omega_{nc} &= \frac{2f_{SW}}{10}, \\ \omega_{nc} &= 1000\, rad.s^{-1}. \end{aligned} \tag{4.19}$$

From (4.17), if the voltage e variation are neglected, the transfer function of the current closed-loop is:

$$\begin{aligned} \Delta\boldsymbol{i}_{sdq}(s) &= \frac{\left(k_{pc}s + k_{ic}\right)}{\left(\frac{l_f}{\omega_n}s^2 + \left(r_f + k_{pc}\right)s + k_{ic}\right)}\Delta\boldsymbol{i}^*_{sdq}(s), \\ \Delta\boldsymbol{i}_{sdq}(s) &= G_c(s)\Delta\boldsymbol{i}^*_{sdq}(s) \end{aligned} \tag{4.20}$$

In (4.20), the dynamic response of the capacity voltage $\boldsymbol{e}_{dq}$ is supposed to be neglected from current dynamic perspective or completely compensated by the voltage feedforward action ($g_{ffv} = 1$). $G_c(s)$ represents the ideal current closed-loop transfer when the capacity voltage dynamics is ignored. The current closed-loop dynamics can then be fixed following the poles placement techniques, by identifying the denominator of (4.20) with:

$$\left(\frac{s^2}{\omega_{nc}^2} + \frac{2\zeta_c s}{\omega_{nc}} + 1\right) \tag{4.21}$$

Table 4.3 – Numerical values

Parameter	Name	Value
ω_{nc}	Current closed loop bandwidth	$1000\,rad.s^{-1}$
ζ_c	Current closed loop damping	$0.7\,p.u.$
k_{pc}	Proportional gain	$0.62\,p.u.$
k_{ic}	Integral gain	$477.5\,rd.s^{-1}$
T_rc	Time response at 5%	$3\,ms$

Where ω_{nc} represents the desired current closed-loop control bandwidth, and ζ_c is the desired damping. The identification from (4.20) to (4.21) gives the PI parameter expression:

$$\begin{aligned} k_{pc} &= 2\zeta_c l_f \frac{\omega_{nc}}{\omega_n} - r_f, \\ k_{ic} &= \frac{k_{pc}\omega_{nc}}{2\zeta_c - \frac{r_f\omega_n}{l_f\omega_{nc}}}. \end{aligned} \tag{4.22}$$

The current control parameters are summarized in table 4.3.

If the voltage dynamic of $\boldsymbol{e}_{dq}(t)$ is not neglected or not perfectly compensated, the states of $\boldsymbol{i}_{sdq}$ depends on $\boldsymbol{e}_{dq}$ and the closed loop performance is slightly affected. The fig. 4.5 shows a dependency of the closed loop bandwidth with the connected load. Without the voltage feed-forward $g_{ffv} = 0$, the frequency response of the real current closed loop gain exhibits a cut-off frequency of 200 $rd.s^{-1}$ at no load, and of 10 $rd.s^{-1}$ with a resistive load of 1 p.u. Compared with the presence of the voltage feedforward, the highest frequencies (above 1000 $rd.s^{-1}$) are less damped.

Voltage loop tuning A conventional approach [58, 31, 124] for cascaded loop, is to set the outer voltage loop with a bandwidth 5 to 10 times lower than the innermost current loop. Under this time decoupled assumption, the voltage controller considers that the current has already reached its reference value by the time it starts changing the current reference. Considering therefore that $\boldsymbol{i}_{sdq} = \boldsymbol{i}^*_{sdq}$, (4.18) is injected into (4.15):

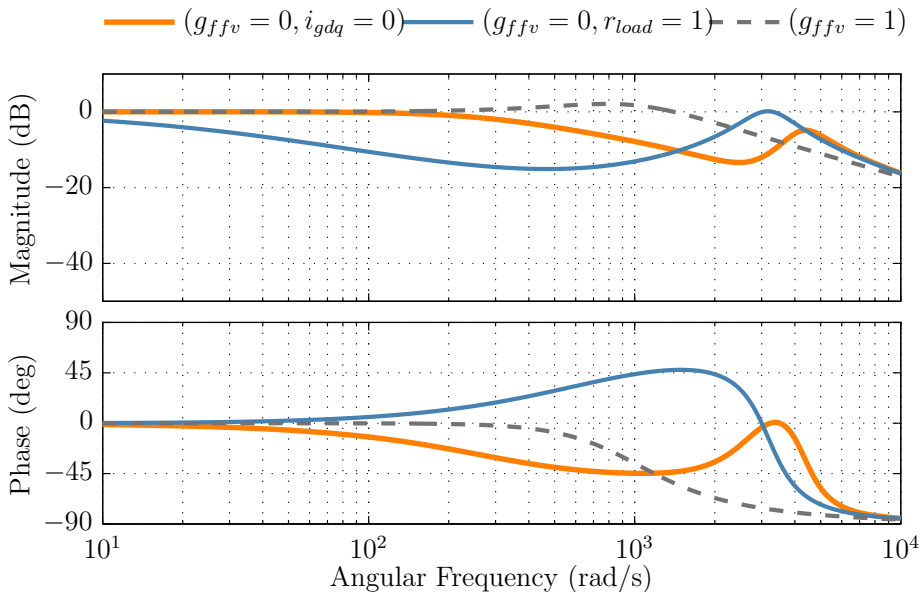

Figure 4.5 – Bode diagram of three current closed-loop transfer functions. With ideal e_{dq} voltage feedforward ($g_{ffv} = 1$), no voltage feedforward at no-load ($g_{ffv} = 0$, $\boldsymbol{i}_{gdq} = 0$), and no voltage feedforward at full load ($g_{ffv} = 0$, $r_{load} = 1$ p.u.).

$$
\begin{aligned}
\left(\frac{c_f}{\omega_n}s + j\frac{c_f}{\omega_n}\omega_0\right)\boldsymbol{e}_{dq} &= \left(k_{pv} + \frac{k_{iv}}{s}\right)\left(\boldsymbol{e}^*_{dq} - \boldsymbol{e}_{sdq}\right) + j\frac{c_f}{\omega_n}\omega_0\boldsymbol{e}_{dq} + g_{ffi}\boldsymbol{i}_{gdq} - \boldsymbol{i}_{gdq},\\
\left(\frac{c_f}{\omega_n}s\right)\boldsymbol{e}_{dq} &= \left(k_{pv} + \frac{k_{iv}}{s}\right)\left(\boldsymbol{e}^*_{dq} - \boldsymbol{e}_{sdq}\right) + \left(g_{ffi} - 1\right)\boldsymbol{i}_{gdq},\\
\left(\frac{c_f}{\omega_n}s + k_{pv} + \frac{k_{iv}}{s}\right)\boldsymbol{e}_{dq} &= \left(k_{pv} + \frac{k_{iv}}{s}\right)\boldsymbol{e}^*_{dq} + \left(g_{ffi} - 1\right)\boldsymbol{i}_{gdq},\\
\boldsymbol{e}_{dq} &= \frac{k_{pv} + \frac{k_{iv}}{s}}{\left(\frac{c_f}{\omega_n}s + k_{pv} + \frac{k_{iv}}{s}\right)}\boldsymbol{e}^*_{dq} - \frac{1 - g_{ffi}}{\left(\frac{c_f}{\omega_n}s + k_{pv} + \frac{k_{iv}}{s}\right)}\boldsymbol{i}_{gdq},
\end{aligned}
\tag{4.23}
$$

The relationship between the filter output voltage $\boldsymbol{e}_{dq}$ in (4.23) an the voltage reference $\boldsymbol{e}^*_{dq}$ is given by the closed-loop gain $\boldsymbol{G}_v(s)$,

$$
G_v(s) = \frac{\Delta\boldsymbol{e}_{dq}}{\Delta\boldsymbol{e}^*_{dq}} = \frac{k_{pv}s + k_{iv}}{\left(\frac{c_f}{\omega_n}s^2 + k_{pv}s + k_{iv}\right)} \tag{4.24}
$$

The closed loop gain $G_v(s)$ is a transfer function with real coefficients because of the decoupling gains and because the dynamic of the current loop has been neglected. The whole closed-loop control system is split, approximately, into two decoupled single-input-single-output control loops for the d and q components of $\boldsymbol{e}_{dq}$. Note from the expression of (4.23) that the grid current

Table 4.4 – Numerical values

Parameter	Name	Value
ω_{nv}	voltage closed loop bandwidth	$100\,rad.s^{-1}$
ζ_v	Voltage closed loop damping	$0.7\,p.u.$
k_{pv}	Proportional gain	$0.03\,p.u.$
k_{iv}	Integral gain	$2.1\,rd.s^{-1}$
T_rv	Time response at 5%	$30\,ms$

feedforward ($g_{ffc} = 1$) weakens the dynamic interaction between the grid and the controlled VSC.

The voltage closed-loop dynamics is fixed following the same method as previously. The voltage control parameters are summarized in table 4.4.

The Bode diagrams of the voltage closed-loop transfer in fig. 4.6 confirms that the current loop dynamic does not influence the desired voltage-closed loop bandwidth, if the latter is designed at least five time slower than the inner loop.

To assess the performance of the voltage control, the controlled VSC is submitted to the connection of large load connection (500 MW, 300 MVAR) and to a voltage reference change. The fig. 4.7 gives the time-responses from simulations in ETMP-RV. Two simulated models are superimposed. One modeling the valves switches (PWM), and one using an averaged model of the VSC over a switching period (avg). The averaged model replaces the switching valves by an ideal ac voltage-source. In fig. 4.7 the VSC initially operates at half nominal load. When the load is connected to the PCC at 0.01 s, the nominal power is reached. Transiently, the terminal voltage magnitude drops until the controllers compensate. The voltage returns to its nominal value with a significant overshot and oscillations. Compared to the performance set at no load, this behavior result from a poor instantaneous load current compensation due to the current loop time response delay. However, the duration of the overshot has not been considered as critical. The reference change of Δe_d^*=-0.1 p.u., applied at t=0.11 s, gives a time-response of the terminal voltage between 30 and 40 ms which is the expected performance. On the lower plot, it can be seen that the output currents follows tightly their references. The averaged model and the

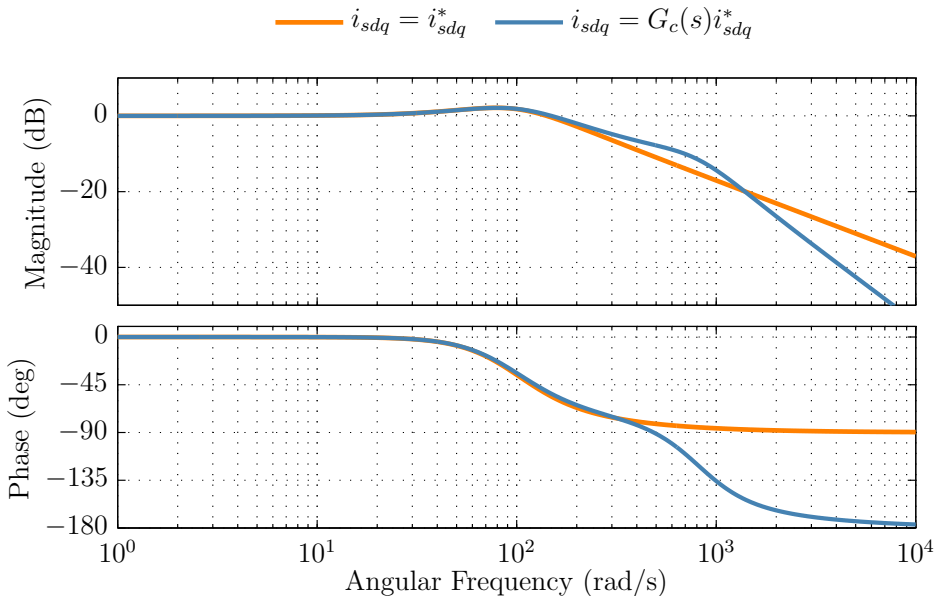

Figure 4.6 – Bode diagram of two voltage closed-loop transfer functions: considering a perfect inner current control ($i_{sdq} = i^*_{sdq}$) and taking into account the closed-loop current dynamic ($i_{sdq} = G_c(s)i^*_{sdq}$).

instantaneous model with the valves switches are well superimposed. This observation justifies that the voltage-controlled VSC will be represented solely by its averaged model in the rest of the thesis.

4.3.4 Current limitation in cascaded loop

Limiting the VSC output current i_{sdq} in cascaded loop may appear as straightforward as it follows exactly its reference i^*_{sdq}. In grid-forming control, there is no need to define a current priority on d or q axis. It will depend on the load. To prevent the voltage controller to command excessive current, the module of the output current reference is then limited whereas the phase angle is conserved:

$$i^*_{sdq,lim} = \begin{cases} i^*_{sdq} \quad if \quad \sqrt{i^{*2}_{sd} + i^{*2}_{sq}} < I_{sat} \\ \frac{I_{sat} i^*_{sdq}}{\sqrt{i^{*2}_{sd} + i^{*2}_{sq}}} \quad if \quad \sqrt{i^{*2}_{sd} + i^{*2}_{sq}} > I_{sat} \end{cases} \tag{4.25}$$

Such a current limiting strategy is called "latch-up" because it holds the voltage controller output in a current-limit and return to normal-operation after the event. The strategy is common for

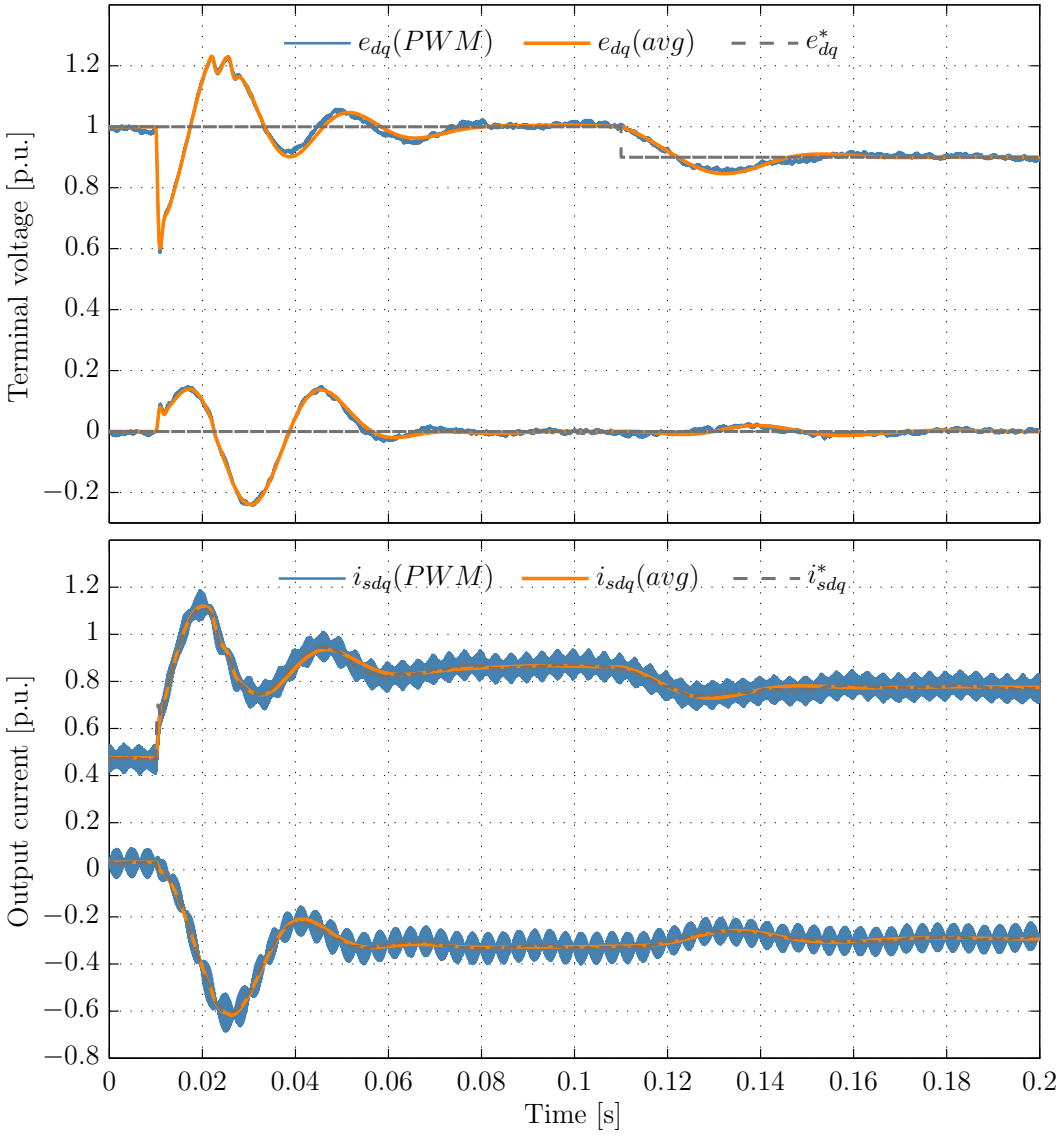

Figure 4.7 – Time-domain response of the voltage closed-loop. (a) The load (r_{load}=0.5 p.u., l_{load}=0.3 p.u.) is connected at 0.01 s, and Δe^*_d=-0.1 p.u. at t=0.11 s.

cascaded loop structure [20, 154, 63, 155]. Trip and reset conditions can be defined differently as reviewed in [63], and comparison with limitation in the natural abc-frame can be found in [155]. Here, we defined I_{sat} according to table 2.9. Reset strategy depend on the expected behavior of the VSC once the fault is cleared. The subject is wide and not treated here but detailed analysis can be found in [97].

Imposing a limitation on the current reference out of the voltage control necessitates to stop the integration in the voltage PI controller to avoid the wind-up. Anti-wind up strategies inherited from motor drives have been extensively studied and some example are reported in [154]. In our case, the dynamic calculation of integral limits is used in the digital integration of the controller in EMTP software. It consists in the limits of the integral action at each sampling period in order to ensure that the sum of proportional plus integral action never exceeds the output limits of the regulator [154].

To prove its ability to limit the output current, the current limiting strategy has been tested on three-phase resistive short-circuit, applied at the terminal voltage (e in 4.1). The external controls were not considered. It will be shown later that this current limitation technique is not sufficient when the external controls are included because of stability issue during the limitation. Another current limiting strategy will then be suggested in the next chapter.

4.3.5 Conclusion on the voltage control design

The first role of the voltage control is to imposed a voltage waveform at its filter output with a controlled amplitude in closed-loop. The voltage amplitude reference comes from the external regulation. The inner control keeps filter states under control during transients with the highest bandwidth to protect the device and reject the load variation.

The dynamic performances of the inner control can only be set precisely on a defined system. Accordingly, the choice was made to tune the control based on the open-circuited filter model, at no load. The load current disturbances are compensated by feedforward gain.

Time-domain simulations with an EMT software validate the tuning method on passive loads by verifying the expected response times with valves-switching dynamics. The grid-forming capability of the designed voltage-controlled VSC has then be proved.

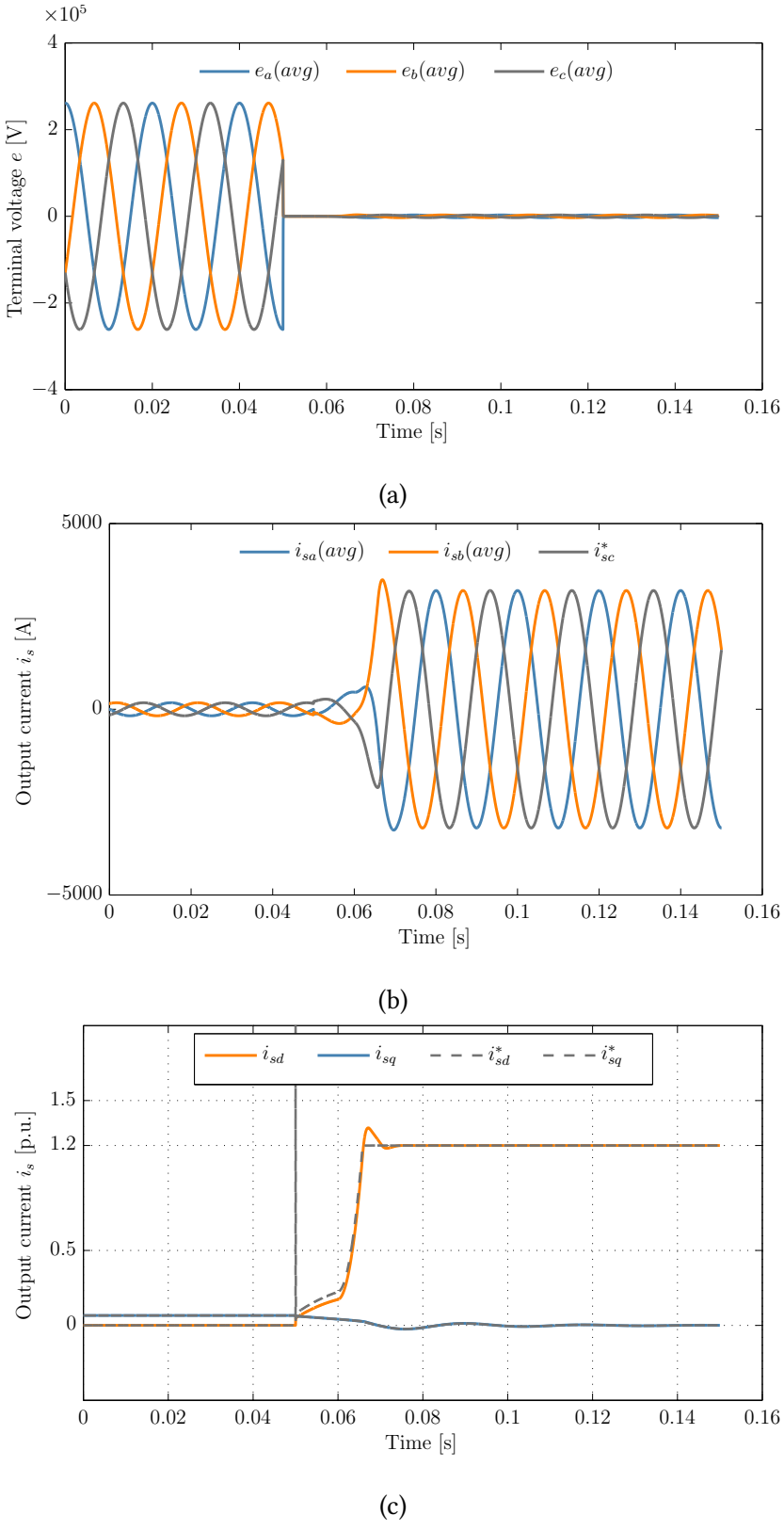

Figure 4.8 – Current-limiting strategy during short-circuit at terminal voltage ($R_{fault} = 1\Omega$). (a) Terminal voltages. (b) VSC output currents. (c) VSC output currents in dq-frame.

The system exhibits satisfactory performances for rated passive loads. However, the dynamic performances no longer stands when the rest of the grid has different dynamics. In this case, a stability robustness analysis must be conducted using eigenvalues technique.

4.4 Robustness of the voltage control in various grid configurations

The voltage control showed satisfactory performance on a passive load. The present section shows how the control stability is endangered when the voltage-controlled VSC is connected to a strong grid. Accordingly, the role of the voltage feedforward gain is highlighted. Transmission grid have variable and unpredictable topologies. The voltage-control must remain stable in any grid-connected situation. This ability of a VSC to face a standalone situations as well as grid-connected situation with the same control is known as "flexibility" [156, 108]. The instability which arises in grid-connected mode is characterized according to the short-circuit capacity of the linked network.

4.4.1 Grid stiffness and short-circuit capacity definition

Each device will need to interact with a grid composed of interconnected converters. Unlike Microgrids or UPS system, the VSCs will not be able to determine if they are linked to a grid or not. Neither could be predicted the short-circuit capacity of this grid as it will depend on external parameters. Accordingly, the developed controls must be assessed under grid-connected conditions with an equivalent source of variable "stiffness". The "stiffness" or the "strength" of a grid is defined by its ability to preserve its voltage magnitude whatever the current flowing through. In a series Thevenin equivalent of the grid as presented in fig. 4.1, the "stiffness" is characterized by the value of the series impedance parameters L_{src} and R_{src}. In power system, the short-circuit capacity at the PCC is the indicator traditionally used instead, based on the phasor impedance value in nominal conditions ($Z_{src} = jL_{src}\omega_n + R_{src}$).

$$S_{sc} = \frac{3V_{src}}{|Z_{src}|} \tag{4.26}$$

To characterize the impact of the short-circuit capacity S_{sc} on the VSC control, this power is expressed per-unit values with respect to the VSC rating. The short-circuit ratio is the defined by (4.26).

$$SCR = \frac{S_{sc}}{S_b} \tag{4.27}$$

The grid series inductance and resistance expressed in per-unit in the VSC base, using l_{src} and r_{src} notation. In transmission grid system, $l_{src} >> r_{src}$, so that:

$$SCR \approx \frac{1}{l_{src}} \tag{4.28}$$

Note that an other definition exits using the nominal active power instead of the nominal apparent power. Regarding today requirements for the generation connection at the transmission grid level, the VSC interfaces must face a grid inductance variation of $0.05\,p.u. < l_{src} < 0.6\,p.u.$ (see section 3.1) and [16]. The equivalent range of the short circuit ratio is $1.7 < SCR < 20$. At $1 < SCR < 3$, the grid is considered to be "weak" [66].

4.4.2 Small-signal stability limit of the voltage controlled VSC in various grid-connected situations

To assess the stability limits of a grid-connected grid-forming converters, a small-signal stability analysis has been conducted using eigenvalues technique of the state-space model of the system. The new considered system is the voltage-controlled VSC with its filter connected to the grid equivalent as shown in fig. 4.1. The load is neglected. Equations (4.18) and (4.17) of voltage and current loop still hold, along with the equation of the grid current dynamic ($\boldsymbol{i}_{gdq}$), determined by the transformer impedance, in series with the equivalent grid impedance.

$$\left(\frac{l_c + l_{src}}{\omega_n}s + r_c + r_{src} + j\omega_0\frac{l_c + l_{src}}{\omega_n}\right)\boldsymbol{i}_{gdq}(s) = \boldsymbol{e}_{dq}(s) - \boldsymbol{v}_{srcdq}(s) \tag{4.29}$$

The filter equations (4.15), the control equations (4.16), (4.18), and the grid current expresion (4.29) can be rewritten in state-space form as shown in [58, 124, 150] to form a ten states model.

The derivation of the system eigenvalues is realized, assuming a perfect synchronization between the VSC and the grid ($\omega^* = \omega_{src} = \omega_0$). Fig. 4.9 shows the behavior of the system with

the evolution of the poles for a *SCR* growing from 0.25 to 20. Clearly, the poles with an angular frequency around 100-200 $rd.^{-1}$ are shifted to the right-hand-side when the *SCR* increases. The stability limit, marked with a red cross, is reached when $l_{src} = 2.95$ and $r_{src} = 0.295$, so for $SCR = 0.34$. This exhibits the poor stability of a voltage-controlled source connected to a strong grid. At an extreme point, it can be easily understood that controlling the voltage of an infinite bus is impossible.

The influence of the voltage control parameters already studied in [124]. Through sensitivity analysis, [124] showed that the increase of inner current loop bandwidth, the decrease of voltage feedforward gain, lowering the voltage bandwidth, the increase of the capacitance stabilize the system. In microgrids, small inverters usually embed fast current control or relatively large filter capacitance. In high-power VSC devices, speeding-up the current bandwidth is not possible due to the limited switching frequency. On the other hand, increasing the capacitor size induces higher cost. In the following, the stabilizing effect of a lower voltage feedforward gain is illustrated.

4.4.3 Improving the robustness against grid stiffness with the voltage feedforward gain

Instabilities arise when the series impedance of the Thevenin equivalent model decreases. This means that the dynamics of the current flowing through the grid are faster. The voltage control bandwidth is not large enough compared to the voltage variation observed across the filter capacitor. A straightforward solution would be to design a large voltage control bandwidth [124] or to slow down the terminal voltage variation by increasing the capacitors value. Unfortunately, these directions are neither technically feasible for high-power converters, nor desirable in transmission system applications. As an alternative way, the author considered the opportunity of lowering the stiffness of the controlled voltage source formed by the VSC system and its voltage control by acting on the voltage feedforward gain. The fig. 4.10 shows the impact of voltage feedforward gain on grid-connected stability.

Compared to fig. 4.9, fig. 4.10 does not show unstable poles of the system for a feedforward gain of ($g_{ffv} = 0.5$). At $SCR = 20$, however, two poles marked with a cross in the fig. 4.10 (b) are really closed to the imaginary axis. The situation is at the stability limit.

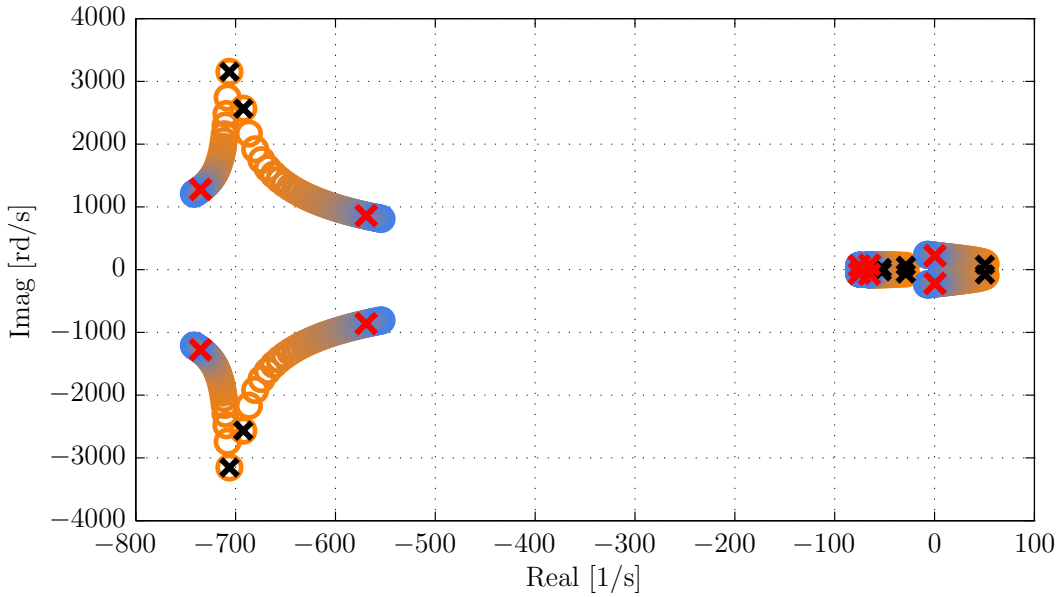

(a)

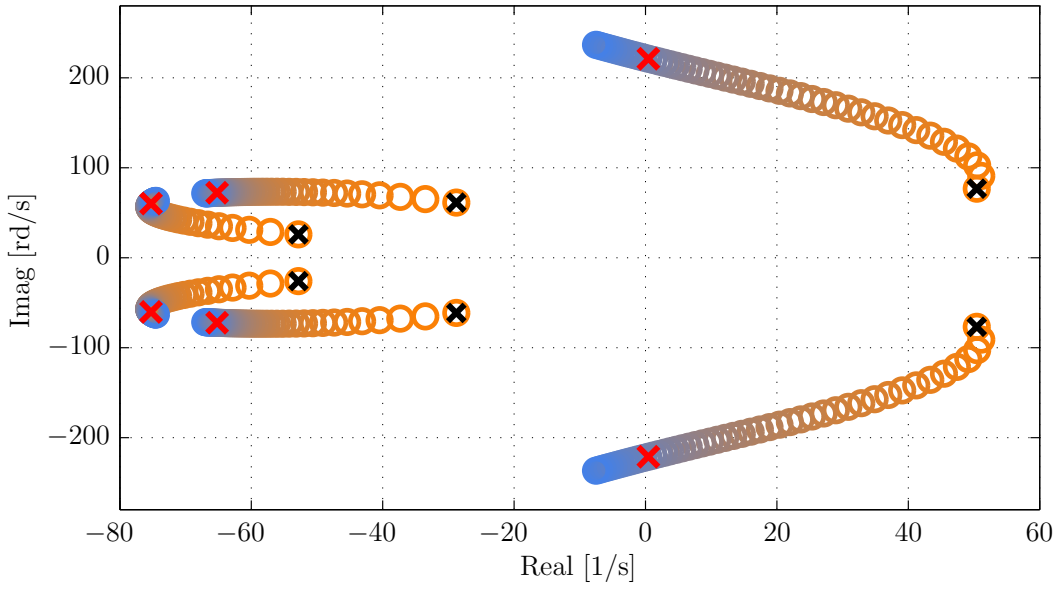

(b)

Figure 4.9 – Poles-map of a grid-connected VSC with voltage-control with *SCR* growing from 0.25 blue (dark) to 20 orange (light),($g_{ffv} = 1$). (a) The whole eigenvalues. (b) Zoom on slower modes.

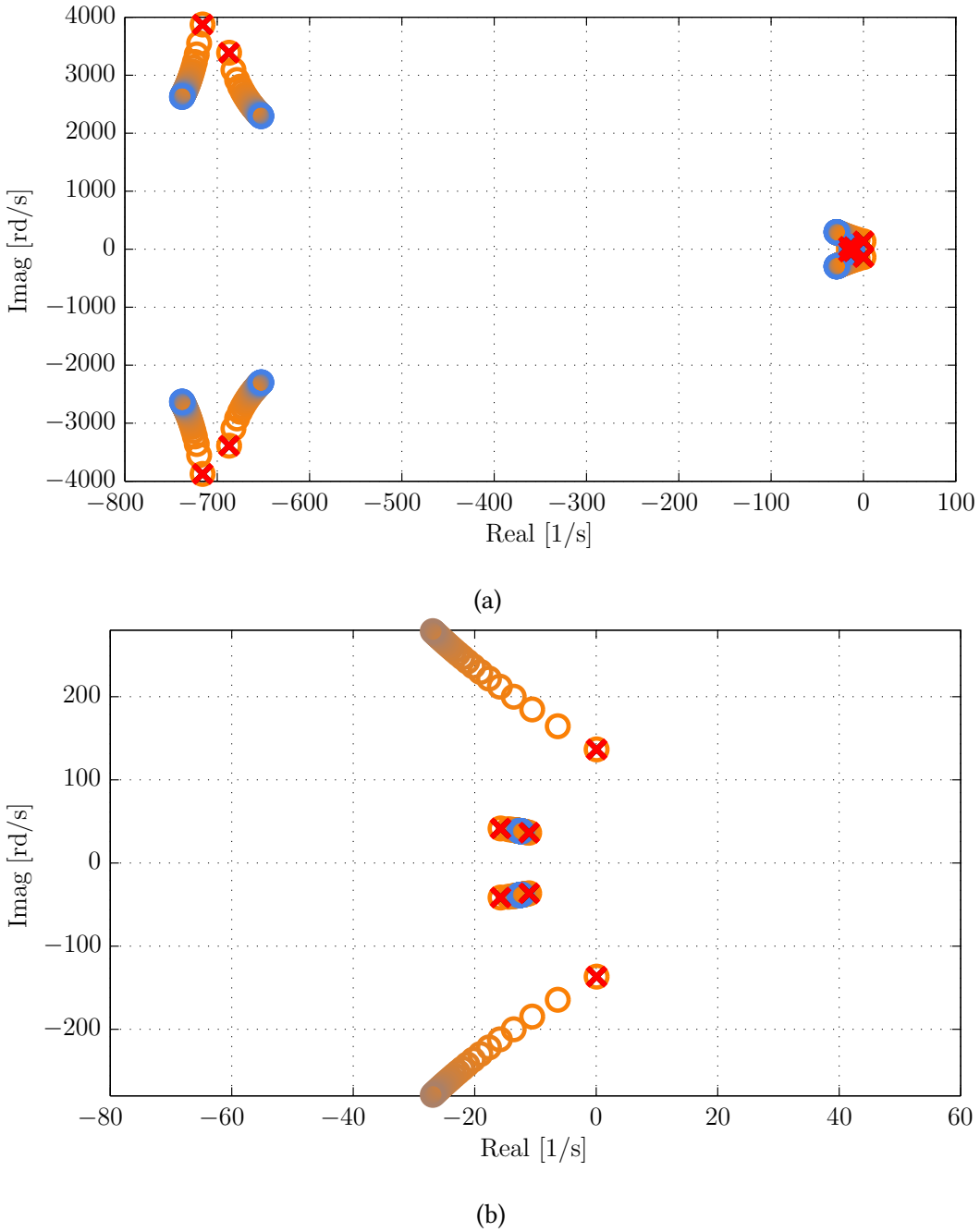

Figure 4.10 – Poles-map of a grid-connected VSC with voltage-control with *SCR* growing from 0.25 blue (dark) to 20 orange (light) ($g_{ffv} = 0.5$). (a) The whole eigenvalues. (b) Zoom on slower modes.

Changing the control parameters impacts its performances on disturbance rejection but also on tracking capability. The poles maps show that the unstable poles are around 100-200 $rd.s^{-1}$ can be effectively damped by lowering the voltage feedforward. Very slow and poorly damped modes are, however, introduced around 20 $rd.s^{-1}$. Sensivity analysis showed that these poorly damped poles are associated with voltage control. Therefore, the voltage controlled VSC responds slowly to a voltage reference change but is less affected by disturbance, as load changes. This consequence is desirable for standalone regulation but the external control can suffer from the sluggish response of the voltage reference tracking.

4.4.4 Conclusion on VSC voltage control robustness

When a voltage controlled VSC is connected to other voltage sources, the loop dynamic used in section 4.3 to tune the controllers parameters no longer stands. The load current rejection is not effective when the connected grid has fast current dynamics, eg. a large short-circuit capacity. A small-signal stability analysis based on eigenvalue technique gave a stability limit of $SCR = 0.34$ meaning that such a grid-forming VSC can only be attached to a one-third less powerful voltage source. As an example, the positive impact on stability of lowering the terminal voltage feedforward gain has been emphasized. Optimization process such as [124] can be easily implemented to find the most stable point according to the range of grid situations.

The representation of the grid by a Thevenin voltage source has validity limits. In a larger system with multiple VSCs, pole maps cannot be directly used due to the larger number of eigenvalues. Physical insights on instability origins must come from participation factors analysis or parameter sensitivity analysis. Alternatively, to understand the contribution of the voltage control to the power system small-signal (in)stability, another approach looks at the frequency representation of the equivalent output impedance of the VSCs. The VSC and associated controls are then observed from the external point of view of the grid, so that the control parameters are integrated in an equivalent circuit model.

4.5 Analysis of the control robustness through the impedance-based approach

Building a VSC based power system requires a comprehensive analysis of external behavior of converters, and their interactions with the rest of the grid to predict unstable behavior. Following this objective, the impedance-based approach, exposed originally in [157], has recently regained interest to predict instabilities of grid-connected, grid-feeding, converters, in the frequency domain [158, 159, 71, 153, 160]. This section details how to transpose the concept of passivity and impedance-based stability to grid-forming converters. The passivity is first explained with a simple open-loop VSC (without feedback control), and its LCL filter. Then, it is shown how voltage control modifies the shape of the output equivalent impedance. Thus, the influence of the control parameters on the output impedance passivity is highlighted. Recommendations on the voltage control parameters tuning are submitted for higher robustness, with the consequence of slowing down the voltage control dynamic.

4.5.1 Concept of passivity of the equivalent output impedance

Origin of the VSCs interactions with the system resonances In opposition to electromechanical devices, VSC devices the main dynamics of VSC-based interfaces are dictated by their controls that might interact with the rest of the system. Instabilities of grid-connected converters originates from three main causes: the forced switching commutations can excite resonances on the system, the controls can be wrongly designed and thus induce instabilities even in a standalone situation, or the controls can deteriorate the damping of resonances or modes, that are already present in the connected system.

Nowadays, power system have identified resonances, classified by [153] as follows:

- Harmonics resonances from 100 Hz, to kHz. Caused by lines, cables, LCL filters interaction. Those harmonics resonances might by stimulated by switching modulation, current or voltage controls or VSC.

- Near fundamental resonances from 50 Hz, 100Hz especially observed in weak grid conditions. But also subsynchronous resonances, traditionally caused by torsional modes of

electromechanical devices or by series compensated lines. Those resonances can be stimulated by the inner controls as well as by the external synchronization and power controls.

Listing the resonances for a full VSC based system is ambitious as it depends mainly on the controls chosen for the VSC devices. Harmonics resonances will still be present, whereas near fundamental resonances could be cause by three-phases lines resonance interacting with the inner controls, external power and synchronization controls of grid-forming VSCs. Also, the grid-feeding controls of VSCs, with tightly regulated power are prone to destabilize the system at new modes [161].

In the present study, the harmonics resonances are disregarded, as well as the impact of the VSC switching dynamics. The VSC is modeled by its averaged model. If no feedback controls are applied to the VSC (open-loop), all the possible resonances listed above would be naturally damped by the physical resistances of the LCL filter. Indeed, a resistance dissipates the energy at all frequencies. When the voltage control is implanted, the controlled VSC actively injects or absorbs energy when needed to fulfill the control requirements. Concretely, when energy is respectively absorbed or injected at certain modes, the damping of the modes are improved or degraded. The positive of negative contribution of a controlled VSC can be represented by drawing the frequency-response of its equivalent output impedance.

Equivalent output impedance of a VSCs device and passivity definition The equivalent output impedance of a VSC is formed by a combination of passive circuit components of the filter and active control elements. The control structure and the control parameters play a significant role in the frequency profile of the equivalent output impedance. Using notation of Fig. 4.1, the output impedance is defined in small-signal sens, by the response of the PCC voltage to a grid current incremental variation:

$$Z_{out}(j\omega) = \frac{-\Delta v_g(j\omega)}{\Delta i_g(j\omega)} \tag{4.30}$$

In particular, the negative or positive real-part of this impedance depicts the negative or a positive equivalent resistance presented, at certain frequencies, to the rest of the system. When a positive resistance is presented, the concerned frequencies are damped, and the system behaves as a passive device in this frequency range. A more formal definition of the passivity in frequency-domain of a linear transfer function $Z(s)$, with real coefficients is recalled by [162]:

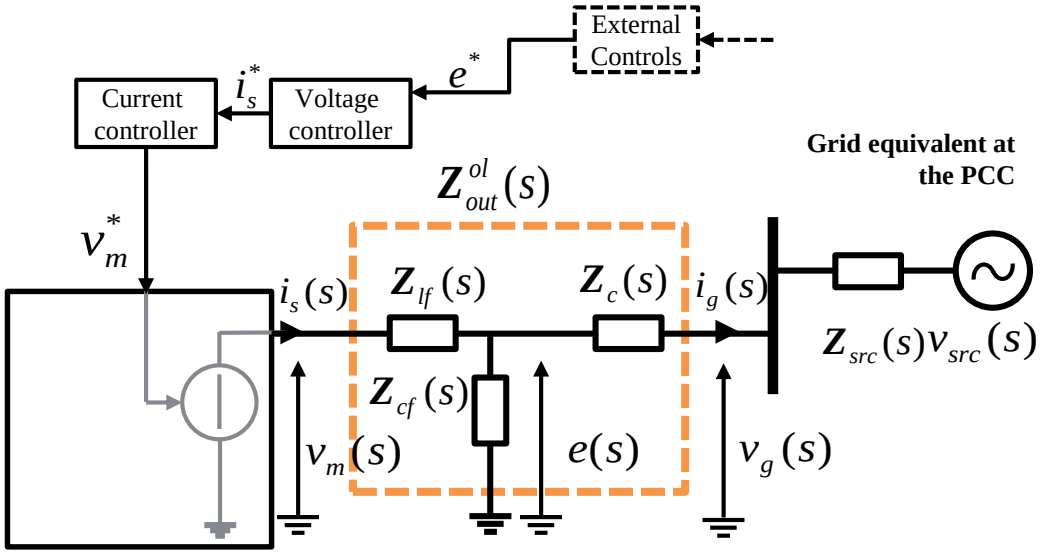

Figure 4.11 – Equivalent representation of the VSC in open-loop modeled by a voltage-source, and a open-loop output impedance $Z_{out}^{ol}(s)$.

1. $Z(s)$ has no Right Half-Plane (RHP) poles

2. $\Re(Z(j\omega)) > 0 \Leftrightarrow arg(Z(j\omega)) \in [-90; 90]\ \forall \omega > 0$

The concept of passivity is illustrated in the next subsections by first only considering the VSC in open loop with its LCL filter. Then the impact of the voltage control is shown. It is reminded here that the external controls are not considered in this section, and their action on the output impedance shape is not treated.

4.5.2 Output impedance shape and passivity of a VSC in open-loop

As seen from the PCC, the equivalent output impedance of the system is shaped only by the LCL filter dynamic as shown on 4.11. Following the definition of (4.30), the output impedance can be expressed both in the natural abc-frame or in the synchronously rotating dq-frame. The dq-frame representation has the advantage of offering simpler expression of the output impedance when the controller will be added. However, the different frame references induce differences in the frequency representation as illustrated here, with the simple example of the open-loop impedance.

Open-loop output impedance model in the natural abc-frame As the filter elements are balanced, the output impedance is the same for each phase.

$$\left[Z_{out}^{ol}(s)\right]_{abc} = \frac{-\Delta v_{ga}(s)}{\Delta i_{ga}(s)} \tag{4.31}$$

$$-\Delta v_{ga}(s) = \left[\frac{l_c}{\omega_n}s + r_c + \frac{\frac{l_f}{\omega_n}s + r_f}{\left(\frac{l_f}{\omega_n}s + r_f\right)\left(\frac{c_f}{\omega_n}s\right) + 1}\right]\Delta i_{ga}(s) \tag{4.32}$$

$$\left[Z_{out}^{ol}(s)\right]_{abc} = \frac{l_c}{\omega_n}s + r_c + \frac{\frac{l_f}{\omega_n}s + r_f}{\frac{l_f c_f}{\omega_n}s^2 + \frac{r_f c_f}{\omega_n}s + 1} \tag{4.33}$$

In natural frame, $\left[Z_{out}^{ol}(s)\right]_{abc}$ has only real coefficients that depends on LCL filter characteristics. The frequency response of $\left[Z_{out}^{ol}(j\omega)\right]_{abc}$ is plotted in orange/light line on the Bode diagram in fig. 4.12. The two characteristic frequencies of the filter are also plotted on the figure: the LC filter cut-off frequency ω_{lc} from eq. (4.8), and the LCL filter resonant frequency ω_{lcl} given by eq: (4.13).

Results from the frequency response of $\left[Z_{out}^{ol}(j\omega)\right]_{abc}$ plotted in orange/light line on the fig. 4.12 indicate that the output impedance of the LCL filter presents a very high magnitude at ω_{lc}, and a very low magnitude at ω_{lcl}. Indeed, the filter inductance l_f and filter capacitance c_f trap the currents components at the designed cutoff frequency ω_{lc}. As a consequence, the phase currents at a frequency close to ω_{lc} cannot flow between the VSC device, and the grid. The impedance is then high at this particular frequency. On the other hand, ω_{lcl} is the natural resonant frequency of the LCL filter. The LCL filter offers a preferable path for the phase current whose frequency is around ω_{lcl} inducing low impedance magnitude at this frequency.

Looking further at the real-part of $\left[Z_{out}^{ol}(j\omega)\right]_{abc}$ plotted in orange/light line on the fig. 4.13, one can observe that the real-part, equal to $r_f + r_c = 0.01$, is constant over the whole frequency range excepted in a narrow band around ω_{lc}. The conclusion can be formulated as follows. In the case where no controls are applied, the resistive behavior (positive real-part) is due to the presence of physical resistances r_f and r_c, providing damping at all frequencies, excepted around ω_{lc}. The harmonics currents are trapped because of the path offered by the shunt capacitor c_f and the filter inductance l_f resulting in high damping of this frequency.

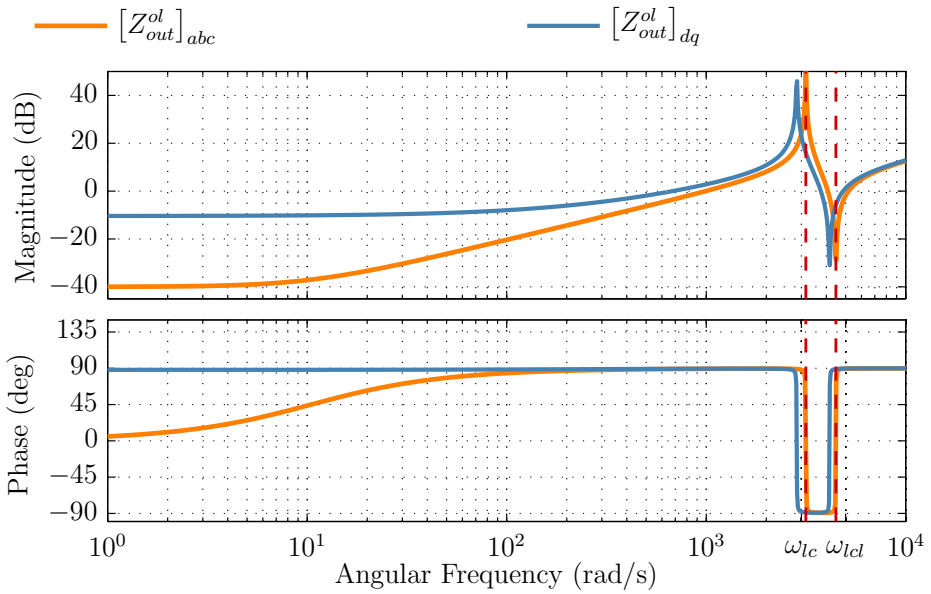

Figure 4.12 – Bode diagram of the VSC open-loop output impedance for positive frequencies. $\left[Z_{out}^{ol}(j\omega)\right]_{abc}$ is expressed in the natural abc-frame, and $\left[Z_{out}^{ol}(j\omega)\right]_{dq}$ is expressed in the dq-frame rotating at $\omega^* = \omega_n$.

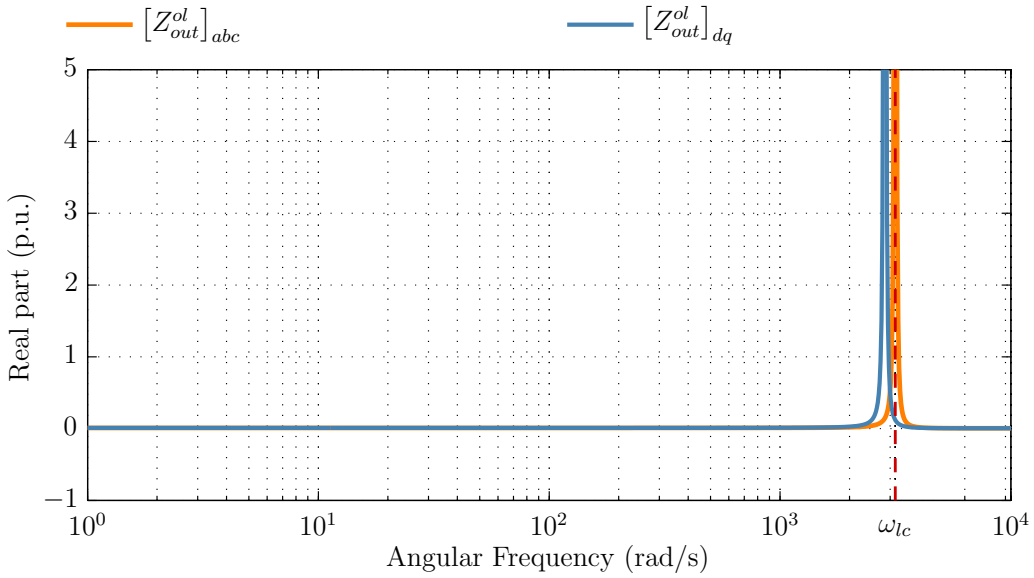

Figure 4.13 – Real-part of the VSC open-loop output impedance for positive frequencies. $\left[Z_{out}^{ol}(j\omega)\right]_{abc}$ is expressed in the natural abc-frame, and $\left[Z_{out}^{ol}(j\omega)\right]_{dq}$ is expressed in the dq-frame rotating at $\omega^* = \omega_n$.

Open-loop output impedance model in the synchronously rotating dq-frame Unlike in the abc-frame, the frequency responses of dq-components can not be expressed independently. Instead, four real transfer functions in a matrix must be defined. For illustration, the voltage response v to a current i in a three-phase series r-l line is given in frequency domain by:

$$\begin{bmatrix} \Delta v_d(s) \\ \Delta v_q(s) \end{bmatrix} = \begin{bmatrix} \frac{l}{\omega_n}s + r & -\frac{l}{\omega_n}\omega^* \\ \frac{l}{\omega_n}\omega^* & \frac{l}{\omega_n}s + r \end{bmatrix} \begin{bmatrix} \Delta i_d(s) \\ \Delta i_q(s) \end{bmatrix} \tag{4.34}$$

Nonetheless, when the modeled system is symmetric, its frequency response is represented by a symmetric transfer matrix, such as in eq. (4.34). Without loosing information, complex transfer functions between complex space vectors can be defined instead of matrice transfer [163]. Complex transfer function are denoted with bold and capital letters in (4.35):

$$\begin{aligned} \Delta \boldsymbol{v}_{dq}(s) &= \left(\frac{l}{\omega_n}s + r + j\omega^*\frac{l}{\omega_n}\right)\Delta \boldsymbol{i}_{dq}(s) \\ \Delta \boldsymbol{v}_{dq}(s) &= \boldsymbol{Z}_l(s)\Delta \boldsymbol{i}_{dq}(s) \end{aligned} \tag{4.35}$$

To derive the VSC output impedance frequency response when no voltage-control is applied, the LCL filter equations (4.15) can be directly used to obtain the complex transfer function of equivalent output impedance in dq-frame.

$$\begin{aligned} \boldsymbol{Z}_{lf}(s)\boldsymbol{i}_{sdq}(s) &= \boldsymbol{v}_{mdq}(s) - \boldsymbol{e}_{dq}(s) \\ \boldsymbol{Y}_{cf}(s)\boldsymbol{e}_{dq}(s) &= \boldsymbol{i}_{sdq}(s) - \boldsymbol{i}_{gdq}(s) \\ \boldsymbol{Z}_c(s)\boldsymbol{i}_{gdq}(s) &= \boldsymbol{e}_{dq}(s) - \boldsymbol{v}_{gdq}(s) \end{aligned} \tag{4.36}$$

$$\begin{aligned} \boldsymbol{Z}_{lf}(s) &= \frac{l_f}{\omega_n}s + r_f + j\omega^*\frac{l_f}{\omega_n} \\ \boldsymbol{Y}_{cf}(s) &= \frac{c_f}{\omega_n}s + j\omega^*\frac{c_f}{\omega_n} \\ \boldsymbol{Z}_c(s) &= \frac{l_c}{\omega_n}s + r_c + j\omega^*\frac{l_c}{\omega_n} \end{aligned} \tag{4.37}$$

$$-\Delta \boldsymbol{v}_{gdq}(s) = \left[\boldsymbol{Z}_c(s) + \frac{\boldsymbol{Z}_{lf}(s)}{\boldsymbol{Z}_{lf}(s)\boldsymbol{Y}_{cf}(s) + 1}\right]\Delta \boldsymbol{i}_{gdq}(s) \tag{4.38}$$

$$\left[\boldsymbol{Z}_{out}^{ol}(s)\right]_{dq} = \boldsymbol{Z}_c(s) + \frac{\boldsymbol{Z}_{lf}(s)}{\boldsymbol{Z}_{lf}(s)\boldsymbol{Y}_{cf}(s) + 1} \tag{4.39}$$

in fig. 4.12, the frequency response of the complex transfer function $\left[Z_{out}^{ol}(j\omega)\right]_{dq}$ is plotted with the blue/dark line on the same Bode diagram than $\left[Z_{out}^{ol}(j\omega)\right]_{abc}$. Curves from fig. 4.12 show a frequency shift of $\omega^* = \omega_n$, between the frequency responses expressed in the two reference frames. The frequency translation is explained in the next paragraph, but one can already note that the frequency response of subsynchronous frequencies in the natural frame ($\omega < \omega_n$) are missing in the case of $\left[Z_{out}^{ol}(j\omega)\right]_{dq}$ because they are shifted to negative frequencies plan.

Discussion on frequency response of generic signals in the synchronously rotating dq-frame compared to abc-frame The dq-transformation of real electrical quantities phase signals implies a translation of their frequency spectrum of $\omega_{dq} \rightarrow \omega_{abc} - \omega^*$ [163, 71, 153]. This frequency translation has consequences as the frequency responses of dq-signals cannot be considered as symmetric on positive and negative frequencies. An analytic explanation is briefly described in the following, but more details can be found in [163].

In the general case, the complex space representation of a sinusoidal three-phase signal, with no zero-sequence, oscillating at a given frequency ω, is composed of a positive and a negative sequence in time domain, denoted as:

$$\boldsymbol{x}^{abc}(t) = X_+ e^{j\omega t} + X_- e^{-j\omega t} \tag{4.40}$$

The corresponding complex space representation in dq-frame is defined by:

$$\boldsymbol{x}^{dq}(t) = \frac{2}{3} e^{-j\omega^* t} \boldsymbol{x}^{abc}(t) = \frac{2}{3} \left(X_+ e^{j(\omega-\omega^*)t} + X_- e^{-j(\omega+\omega^*)t} \right) \tag{4.41}$$

As an example, the positive sequence of a real signal at fundamental frequency ω_n in abc-frame, is turned into a DC component if the qd-frame is also rotating at $\omega^* = \omega_n$. This property of dq-frame is expected. The negative sequence, in the other hand, is turned into a $-2\omega_n$ component, so that the negative sequence in abc-components induces $2\omega_n$ oscillations in dq-components. When the electrical system is assumed to be symmetric, the three-phase signals are commonly supposed to be balanced, and the negative-sequence is often disregarded. However, it has been shown in section 2.3.2 and eq. (2.11), that the phase currents out of the VSC, have unbalanced transient DC components when a bold three-phase fault is applied at the terminal voltage. The DC components in real phase signals result in oscillating signals at $-\omega^*$ in the dq-frame. Hence,

to take into account the system response to small-signal perturbation of DC components in phase signal, the frequency response of dq-component must be studied also on negative frequencies.

Note here that the expression of (4.39) could have been directly obtained from (4.33) with the transformation $s \longrightarrow s + j\omega^*$ [153, 163] because of the frequency translation between the abc-frame and the dq-frame.

To summarize:

- Complex transfer functions are only valid to simplify the representation of symmetric models. In case of unbalance, transfer matrices must be used instead.
- When complex transfer function have only real coefficient, their frequency response on negative frequencies verifies $\boldsymbol{G}(-j\omega) = \boldsymbol{G}(j\omega)^*$, so that the magnitude is even and the phase is odd. The frequency response of real complex transfer functions can be plotted on positive frequencies only. In the presence of complex coefficient, the frequency-responses must be plotted on the whole frequency domain $-\infty < \omega < \infty$.
- In practice, the frequency boundary ω_{max} is limited by the validity of VSC model considered as a ideal voltage source. In our case, ω_{max} is fixed by the VSC bandwidth, so by its switching frequency. The maximum frequency of the frequency domain is taken as the Nyquist frequency: $\omega_{max} = \frac{2\pi f_{SW}}{2}$.
- Complex transfer function are compatible with gain-margin and phase-margin definition, as given in[163].

To validate the statements above, the frequency response of $\left[Z_{out}^{ol}(j\omega)\right]_{abc}$ and $\left[\boldsymbol{Z}_{out}^{ol}(j\omega)\right]_{dq}$ are plotted in fig. 4.14 on the full frequency range. The frequency response of $\left[Z_{out}^{ol}(j\omega)\right]_{abc}$ is symmetrical on positive and negative frequency, but this is not the case for $\left[\boldsymbol{Z}_{out}^{ol}(j\omega)\right]_{dq}$. The very low impedance in abc-frame for DC components is represented by low impedance magnitude in dq-frame around $\omega = -\omega_n$. As detailed later, this low impedance at $-\omega_n$ could be critical. in fig. 4.15, the real part of both frequency response is plotted, and the effect of frame change is not clearly visible except for the frequency translation.

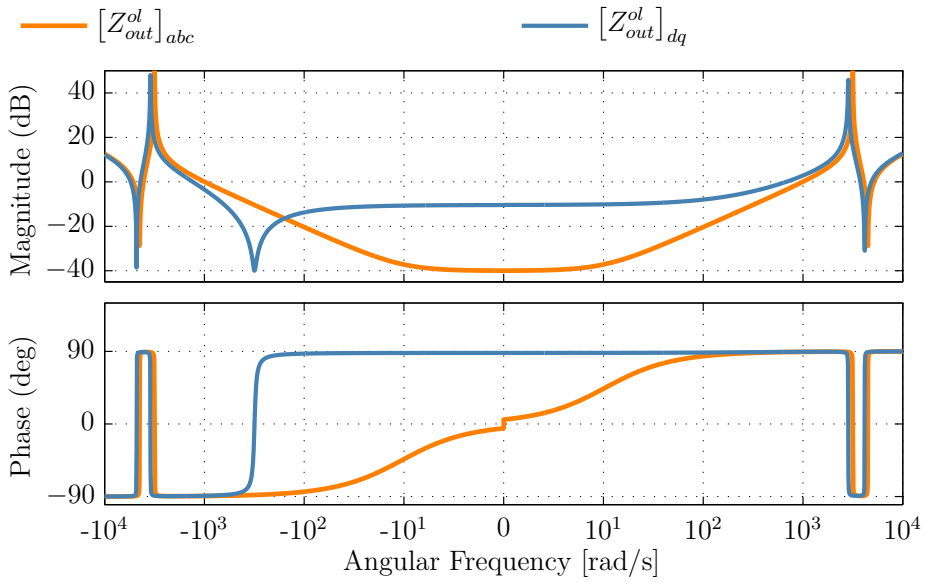

Figure 4.14 – Bode diagram of the VSC open-loop output impedance for positive and frequencies. $\left[Z_{out}^{ol}(j\omega)\right]_{abc}$ is expressed in the natural abc-frame, and $\left[Z_{out}^{ol}(j\omega)\right]_{dq}$ is expressed in the dq-frame rotating at $\omega^* = \omega_n$.

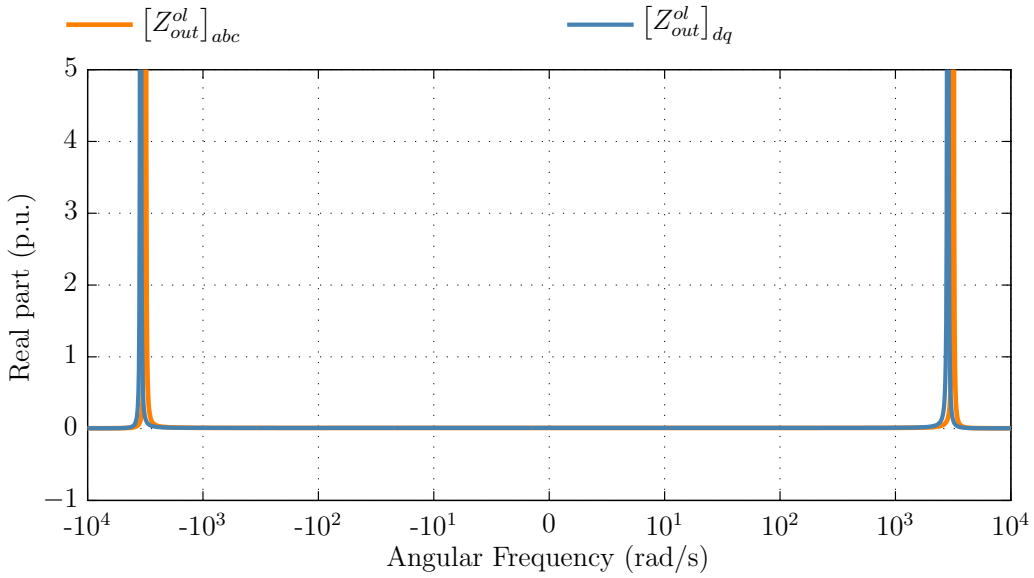

Figure 4.15 – Real-part of the VSC open-loop output impedance for positive and frequencies. $\left[Z_{out}^{ol}(j\omega)\right]_{abc}$ is expressed in the natural abc-frame, and $\left[Z_{out}^{ol}(j\omega)\right]_{dq}$ is expressed in the dq-frame rotating at $\omega^* = \omega_n$.

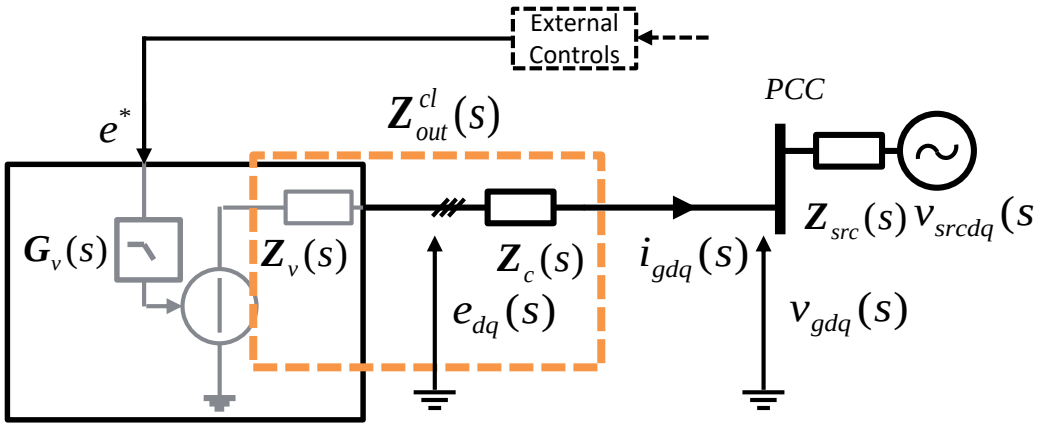

Figure 4.16 – Representation of the voltage-controlled VSC with its reference tracking transfer gain $G_v(s)$ and its closed-loop output impedance $Z_{out}^{cl}(s)$.

4.5.3 Output impedance shape and passivity of voltage-controlled VSC in closed-loop

The presence of a voltage-control strongly affects the impedance profile. Assuming a perfect synchronization with the grid ($\omega^* = \omega_{src} = \omega_n$) the voltage-controlled VSC can be represented by a reference transfer gain and an closed-loop output impedance as shown in fig. 4.16.

Closed-loop impedance model of voltage-controlled VSC As the cascaded voltage and current controllers are symmetrically applied to d and q components, the complex transfer function can be used to represent the closed-loop output impedance. To obtain the output impedance complex transfer function, the controlled current expression in (4.17) is rewritten in :

$$\boldsymbol{i}_{sdq} = G_c(s)\boldsymbol{i}_{sdq}^* - Y_i(s)\boldsymbol{e}_{dq}, \tag{4.42}$$

With:

$$\begin{aligned} G_c(s) &= \frac{\left(k_{pc} + \frac{k_{ic}}{s}\right)}{\left(\frac{l_f}{\omega_n}s + r_f + k_{pc} + \frac{k_{ic}}{s}\right)} \\ Y_i(s) &= \frac{\left(1 - g_{ffv}\right)}{\left(\frac{l_f}{\omega_n}s + r_f + k_{pc} + \frac{k_{ic}}{s}\right)}, \end{aligned} \tag{4.43}$$

The current closed-loop dynamic given by (4.43) is associated with the voltage control (4.18), and the complex transfer model of the filter (4.36), to form the terminal expression in closed-loop using complex transfer functions:

$$\boldsymbol{e}_{dq} = \boldsymbol{G}_v(s)\boldsymbol{e}^*_{dq} - \boldsymbol{Z}_v(s)\boldsymbol{i}_{gdq}, \tag{4.44}$$

The complete expression of $\boldsymbol{G}_v(s)$, and $\boldsymbol{Z}_v(s)$ are :

$$\begin{aligned} \boldsymbol{G}_v(s) &= \frac{\boldsymbol{G}_c(s)\left(k_{pv} + \frac{k_{iv}}{S}\right)}{\boldsymbol{G}_c(s)\left(k_{pv} + \frac{k_{iv}}{S}\right) + \boldsymbol{Y}_i(s) + j\frac{c_f}{\omega_n}\omega^*\left(1 - \boldsymbol{G}_c(s)\right) + \frac{c_f}{\omega_n}s} \\ \boldsymbol{Z}_v(s) &= \frac{\left(1 - g_{ffc}\boldsymbol{G}_c(s)\right)}{\boldsymbol{G}_c(s)\left(k_{pv} + \frac{k_{iv}}{S}\right) + \boldsymbol{Y}_i(s) + j\frac{c_f}{\omega_n}\omega^*\left(1 - \boldsymbol{G}_c(s)\right) + \frac{c_f}{\omega_n}s} \end{aligned} \tag{4.45}$$

$\boldsymbol{G}_v(s)$ represents the closed loop complex transfer function of the voltage tracking reference at no load condition. $\boldsymbol{Z}_v(s)$ is the complex transfer function representing the sensitivity of regulated voltage to the output current perturbations. The complex transfer $\boldsymbol{Z}_v(s)$ can also be regarded as the stiffness of the regulated voltage against grid disturbance [164].

As seen in fig. 4.16, the closed loop output impedance $\boldsymbol{Z}^{cl}_{out}(s)$ is formed by:

$$\boldsymbol{Z}^{cl}_{out}(s) = \boldsymbol{Z}_v(s) + \boldsymbol{Z}_c(s) \tag{4.46}$$

Where $\boldsymbol{Z}_c(s)$ is the connection impedance given by (4.37).

Comparison of the closed-loop and open-loop output impedance models The frequency-response of $\boldsymbol{Z}^{cl}_{out}(j\omega)$ in fig. 4.17 is compared with $\boldsymbol{Z}^{ol}_{out}(j\omega)$. Their real-parts are also plotted on positive and negative frequencies in fig. 4.18.

Fig. 4.17 reveals that the voltage control decreases the output impedance magnitude at low frequency, which is expected to improve the voltage stiffness. The integral action of the voltage control ensures a perfect control of the terminal voltage $\boldsymbol{e}_{dq}$, so that $\boldsymbol{Z}_v(s \approx 0) \approx 0$, and then $\boldsymbol{Z}^{cl}_{out}(j\omega)$ is only formed by the connection impedance $\boldsymbol{Z}_c(s)$ at low frequencies. Indeed, a constant magnitude of $|\boldsymbol{Z}^{cl}_{out}(j\omega)| \approx 20log(l_c) = -16.5$ is reported for approximately $-60\,rd.s^{-1} =< \omega < 60\,rd.s^{-1}$.

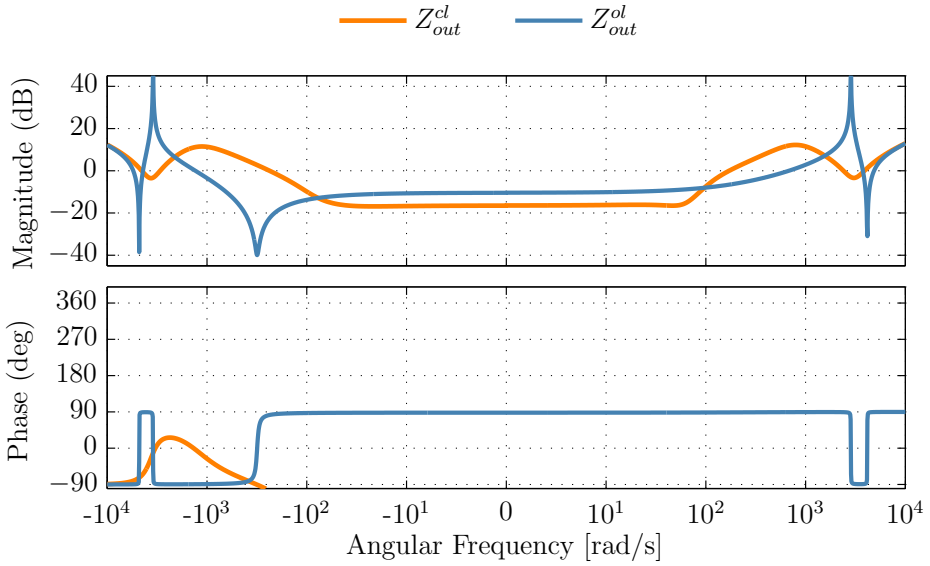

Figure 4.17 – Frequency-response comparison of the closed-loop and open-loop output impedance models in dq-frame.

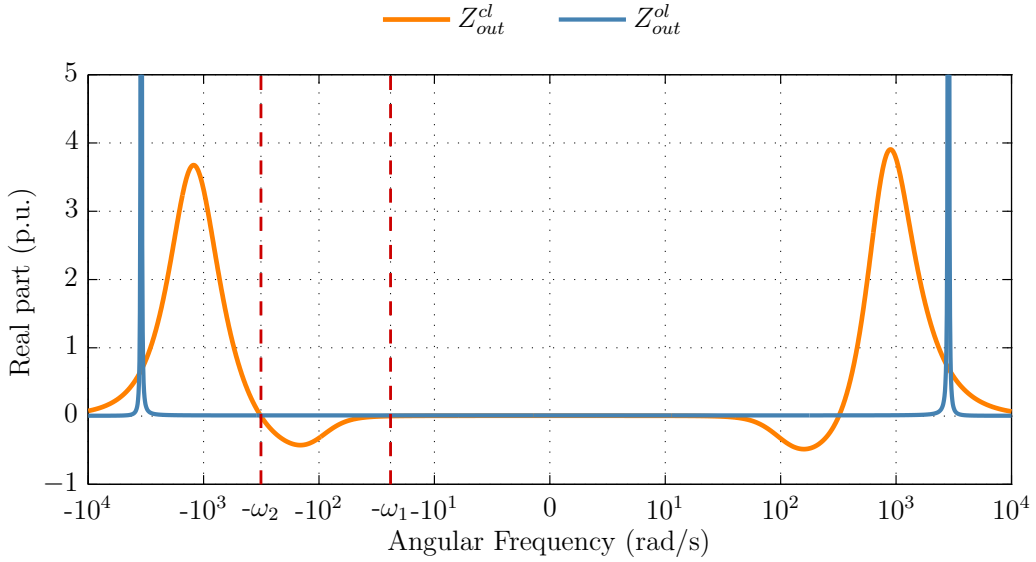

Figure 4.18 – Real-part comparison of the closed-loop and open-loop output impedance models. $\omega_1 = 24\,rd.s^{-1}$ and $\omega_2 = 319\,rd.s^{-1}$.

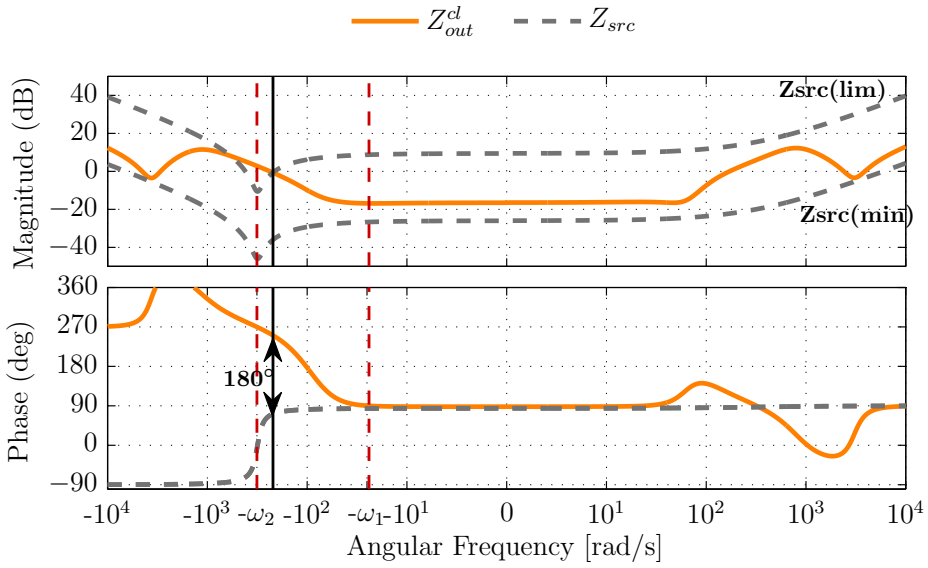

Figure 4.19 – Frequency-response in dq-frame of the closed-loop output impedance of the controlled VSC $Z_{out}^{cl}(j\omega)$ and of two values of the grid impedance $Z_{src}(j\omega)$. $\omega_1 = 24\,rd.s^{-1}$ and $\omega_2 = 319\,rd.s^{-1}$.

Fig. 4.18 shows the damping contribution of the voltage around $\omega = 1000\,rd.s^{-1}$ and $\omega = 1000\,rd.s^{-1}$ where the real-part of $Z_{out}^{cl}(j\omega)$ is high. The voltage-controlled VSC is then passive at high frequencies. However, The voltage-control creates large region of negative real-part, for both positive and negative frequencies, between $\omega_1 = 24\,rd.s^{-1} < |\omega| < \omega_2 = 319\,rd.s^{-1}$. As consequence, the voltage tuning conventional method detailed in the previous section could adversely affect the stability of the system. This prediction is coherent with the frequency of unstable poles in fig. 4.9 in grid-connected situation. To understand if the VSC effectively destabilizes the system, the output impedance must be compared with the equivalent impedance of the rest of the system.

4.5.4 Interaction between the closed-loop output impedance and the grid impedance

To understand how the output impedance of the voltage-controlled VSC can interact adversely with the grid impedance in grid-connected situations, the expression of the PCC voltage $\boldsymbol{v}_g$ is derived to deduce a stability requirement. The grid impedance Z_{src} from fig. 4.16 is modeled by

complex transfer function in the same dq-frame under the assumption: $\omega^* = \omega_{src} = \omega_n$. The external controls are still neglected as they are assumed to provide a perfect synchronization.

$$Z_{src}(s) = \frac{l_{src}}{\omega_n}s + r_{src} + j\omega^*\frac{l_{src}}{\omega_n} \tag{4.47}$$

Definition of the impedance-based criterion for voltage-controlled VSC Given the voltage-controlled VSC, connected through its filter to a generic grid formed by a stable voltage source $\boldsymbol{v}_{srcdq}$ and its own dynamic represented by $\boldsymbol{Z}_{src}(s)$ (see Fig. 4.16). The grid current flowing through the PCC can be written as:

$$\boldsymbol{i}_{gdq}(s) = \frac{\boldsymbol{v}_{gdq}(s) - \boldsymbol{v}_{srcdq}(s)}{\boldsymbol{Z}_{src}(s)} \tag{4.48}$$

Recalling that the PCC voltage is given by:

$$\boldsymbol{v}_{gdq}(s) = \boldsymbol{G}_v(s)\boldsymbol{e}^*_{dq} - \boldsymbol{Z}_{out}(s)\boldsymbol{i}_{gdq}(s) \tag{4.49}$$

Combining (4.48) and (4.49):

$$\boldsymbol{v}_{gdq}(s) = \frac{1}{1 + \frac{\boldsymbol{Z}_{out}(s)}{\boldsymbol{Z}_{src}(s)}}\left(\boldsymbol{G}_v(s)\boldsymbol{e}^*_{dq} + \frac{\boldsymbol{Z}_{out}(s)}{\boldsymbol{Z}_{src}(s)}\boldsymbol{v}_{srcdq}(s)\right) \tag{4.50}$$

The closed-loop voltage gain $\boldsymbol{G}_v(s)$ is stable by construction, and we assume that $\boldsymbol{Z}_{src}(s)$ is passive and has no RHP zeros. The ratio of the controlled VSC output impedance $\boldsymbol{Z}_{out}(s)$ to the grid impedance $\boldsymbol{Z}_{src}(s)$ can be regarded as the open loop gain of a closed-loop with unit feedback gain. Hence, the stability of $\boldsymbol{v}_{gdq}$ can be evaluated by the classic Nyquist criterion applied to complex transfer function. Application examples of Nyquist criterion on Nyquist plots are shown in the appendix A.2 for the grid-connected stability and in [165] for the stability of a two grid-forming VSCs system. In the following, the stability requirements on the impedance shape are deduce from this stability criterion.

Stability requirements for the closed-loop output impedance VSC The stability of the grid-connected VSC requires the Nyquist curve of the impedance ratio does not encircle the critical point -1. A necessary condition to encircle -1 is that the phase difference between the

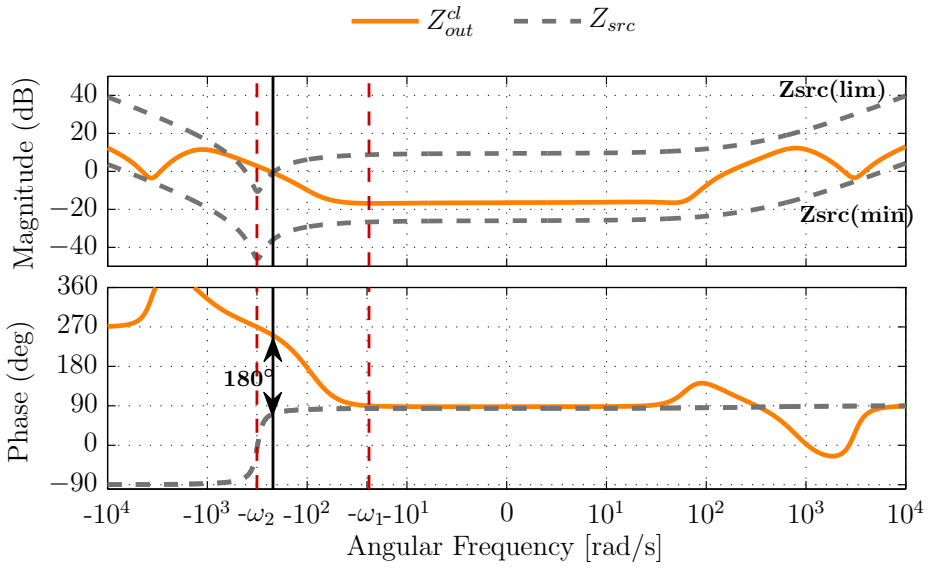

Figure 4.20 – Frequency-response in dq-frame of the closed-loop output impedance of the controlled VSC $Z_{out}^{cl}(j\omega)$ and of two values of the grid impedance $Z_{src}(j\omega)$. The negative real-part of $Z_{out}^{cl}(j\omega)$ is delimited by $\omega_1 = 24\,rd.s^{-1}$ and $\omega_2 = 319\,rd.s^{-1}$.

$Z_{out}(j\omega)$ and $Z_{src}(j\omega)$ goes below -180°. Since $Z_{src}(s)$ is passive, its phase is confined in [-90°,90°]. If the closed-loop impedance is also passive, the phase difference is limited over -180°. Therefore, the passivity of the closed-loop impedance is a sufficient condition for the system stability. One other necessary condition to encircle -1 is that the the magnitude of $Z_{out}(j\omega)$ is equal or superior to $Z_{src}(j\omega)$ for certain frequencies. As a result, even if closed-loop impedance is not passive, the stability is ensured if the magnitude of $Z_{src}(j\omega)$ is over the magnitude of $Z_{out}(j\omega)$ in the negative real-part region. Those observations are illustrated in fig. 4.20 where their frequency responses superimposed on the same Bode diagram

Two extreme values of the grid impedance are plotted in fig. 4.20. The minimal value ($l_{src}(min) = 0.05\,p.u.$, $r_{src}(min) = 0.005\,p.u.$) modeling a stiff grid situation that led to instabilities (see section 4.4), and the limit value of the impedance that led to a stable situation of the grid-connected VSC (($l_{src}(lim) = 2.95\,p.u.$, $r_{src}(lim) = 0.95\,p.u.$)). The frequency range of negative real-part region is delimited by $-\omega_2$ and $-\omega_2$, in the negative frequency plan. The frequency responses show that the magnitude $|Z_{src}(min)(j\omega)|$ is under the magnitude $|Z_{out}^{cl}(j\omega)|$, in the negative real-part region of $Z_{out}^{cl}(j\omega)$. Thus, the interaction between the VSC closed-loop

impedance and the grid impedance is likely to be unstable. The stability limit is obtained when the grid impedance is superior to the controlled VSC output impedance (eg, $|Z_{src}(lim)(j\omega_{180})| > |Z^{cl}_{out}(j\omega_{180})|$) at the frequency ω_{180}, where $arg(Z_{out}(j\omega_{180})) - arg(Z_{srcM}(j\omega_{180}))$ =-180°.

Conclusion The representation of the output impedance in frequency domain gives insights on potential adversely interaction with the grid. It opens the path to output impedance shaping techniques developped for grid-feeding converters [70, 98, 67, 166, 153]. Their purpose is to modify magnitude and phase around certain frequencies. A popular approach seeks at modifying only the impedance module at certain frequencies to stay under the grid-impedance module [152, 167]. Another approach tries to extend the passivity region [162, 168]. In our case, the grid impedance is unknown so that it is more robust to decrease the negative real-part region as much as possible and to shift it far from the grid-impedance resonance or regions where the grid-impedance module is always higher than the closed-loop impedance module.

4.5.5 Output impedance shaping to improve its passivity

The frequency-response of $Z_{out}(j\omega)$ is influenced by the voltage control parameters. Here is detailed the impact of the parameters on real-part of $Z_{out}(j\omega)$ to increase the non-negative frequency domain.

Influence of voltage feedfoward gain The fig. 4.21 illustrates the influence of the feedforward gain g_{ffv}, on $Z_{out}(j\omega)$. Clearly, the negative real-part region grows with g_{ffv}.

Influence of voltage loop bandwidth As seen in fig. 4.22, decreasing the speed of the voltage regulation loop, compared to the fixed designed bandwidth of the current loop, decreases also the region of negative real-part.

Influence of integral gain of current controller The integral gain of the most inner current controller is not needed in practice, as there is an integration already in the voltage loop to follow the reference with no steady-state error. Also, some cases identified the integral gain to cause instabilities [93]. The evolution of the real-part of $Z_{out}(j\omega)$ with the integral gain is plotted on

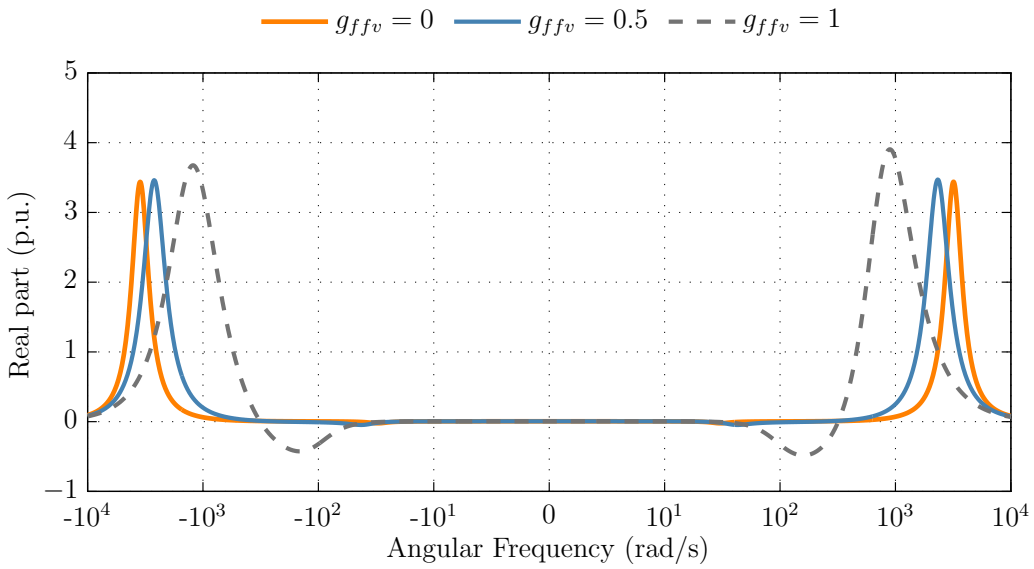

Figure 4.21 – Real part of the frequency-response of $Z_{out}(j\omega)$ for three different voltage feed-forward gains.

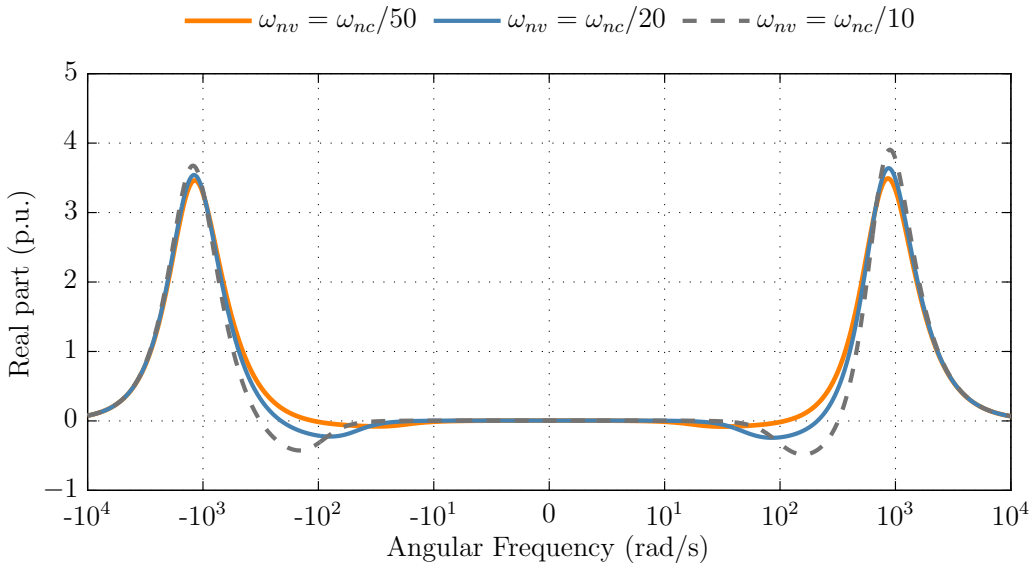

Figure 4.22 – Real part of the frequency-response of $Z_{out}(j\omega)$ for three different voltage loop designed bandwidths.

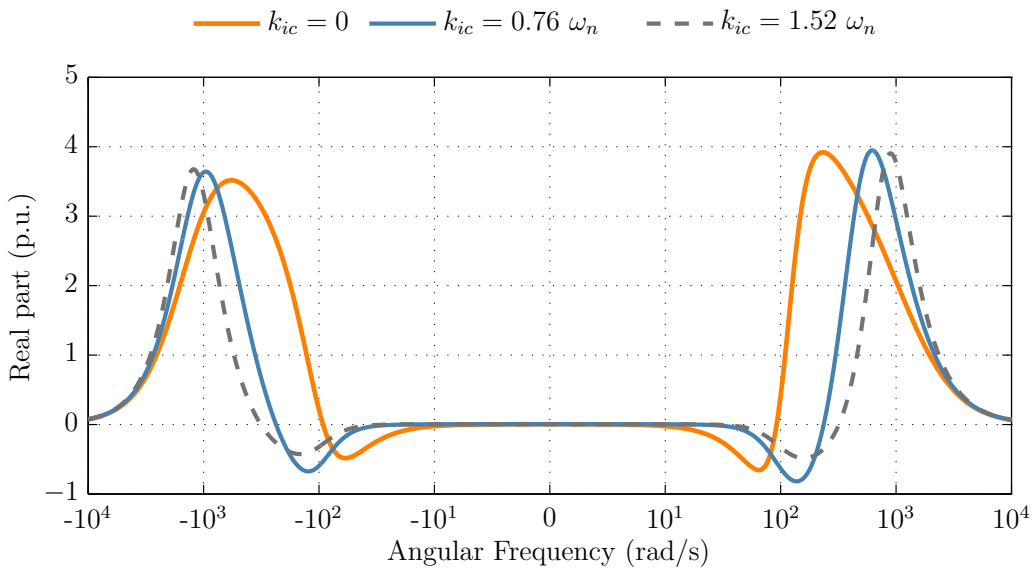

Figure 4.23 – Real part of the frequency-response of $Z_{out}(j\omega)$ for three different integral gain of the current loop controller.

4.23. Results says that suppressing the integral gain of the current control shift the negative real-part region to lower frequencies, with a narrower band: $4\,rd.s^{-1} < |\omega| < 200\,rd.s^{-1}$. However, suppressing the integral gain does not guarantee sufficient passivity.

Conclusion on impedance shaping To decrease the destabilizing effect of the voltage control, two parameters changes has shown their effectiveness: lowering the voltage feedforward gain g_{ffv} in the current controller, or lowering the designed voltage loop bandwidth ω_{nv}. In return, the voltage tracking performance at no load, modeled by the voltage gain $G_v(s)$, will also be affected as shown in fig. 4.24. The figure clearly shows that the voltage gain bandwidth moves from $149\,rd.s^{-1}$ for the original design, to $42\,rd.s^{-1}$ in the case of $g_{ffv} = 0$, and to $28\,rd.s^{-1}$ when $\omega_{nv} = \omega_{nc}/50$.

However, the voltage control performance of grid-forming units is not precisely defined in the system requirement, as long as the voltage is controlled in steady-state and reaches its reference value within 10 s. There exists then a large room for parameters optimization in grid-forming controls with the objective of increasing the stability of external interactions with the grid. The

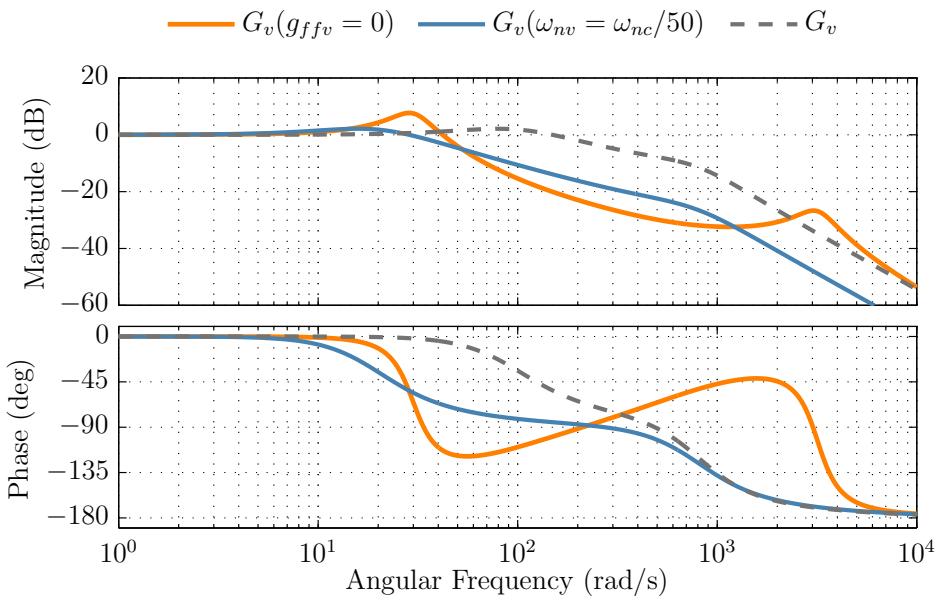

Figure 4.24 – Frequency-response of $G_v(j\omega)$ for $g_{ffv} = 0$ and $\omega_{nv} = \omega_{nc}/50$, compared to the originally designed function.

tuning criterion must then be the external interactions limitation rather than the control speed maximization.

4.5.6 Conclusion on impedance-based approach

A conventional design approach for the voltage control showed satisfactory performances in standalone situation but suffers from instability issues when the VSC is connected to a grid above a certain short-circuit ratio. Interaction between the VSCs and the grid is ruled by the shape of the equivalent output series impedance in frequency domain. The impedance shape depends on control parameters. In this section, some example of parameters impact on the output impedance shape are discussed. Results showed that lowering the voltage feedforward gain or the designed voltage loop bandwidth improves its passivity and thus the damping provided by the VSC to the rest of the system, at the expense of the voltage tracking performances.

Compared to the pole map tool, the impedance-based approach and the passivity property directly give insight of the positive or negative contribution of a grid-forming converter, without knowledge of the remaining system. Moreover, this technique is well suited to TSOs, since they do not always have information on internal control structure and parameters of the power elec-

tronic devices. The frequency-response of the closed-loop output impedance can be estimated by external measurements on real devices or on replica. The impedance shape also gives a common framework to compare the external behavior of converters with different controls. One can imagine that the impedance shape will become a requirement in future grid-codes for converter connection to the transmission system.

Provided the closed-loop impedance model, the stability the grid-forming converter can be directly assessed, using the Nyquist criterion applied to the impedance ratio. Based on this criterion, an optimal output shaping tuning could be performed to find the best trade-off between parameters as made by [160]. Nevertheless, it relies on estimation of the grid impedance [169], which is not always feasible. To overcome this diffuclty, a promising robust technique to shape the output impedance along with the tracking performances is suggested in [170], using H-infiny method.

The impedance-based approach could be generalized to include external controls. In that case, the modeled system will not be symmetric on d and q components, so that the output impedance must be imperatively expressed by mean of transfer matrices. A generalized Nyquist criterion must be then used for the impedance-based stability criterion [163, 75]. Note that asymmetric models introduce a dependency of the output impedance elements on the power operating point [71].

Conclusion on VSC-PWM grid-forming control design method

This chapter proposed a design method of grid-forming that respects the PWM-VSC physical constraints and the transmission grid needs. Cascaded loop structure has been employed for its simplicity and its ability to explicitly control the VSC output current and terminal voltage. As the connected system is unpredictable, the control performance are initially set at no load conditions, treating the load current as a disturbance that can be compensated. However, the small-signal stability is endangered when the voltage-controlled VSC is connected to a strong grid. Small-signal stability is traditionally evaluated with eigenvalues technique. The poles map tool is easily readable for a single inverter system, but its complexity raises with the number of devices. Physical interpretation of instabilities is also missing. Instead, an analysis of stability requirements is proposed for grid-forming converter using the impedance-based approach.

The impedance-based approach is interesting from the TSOs perspective as the output impedance can be externally measured without the knowledge of VSCs internal controls. It also gives a common framework to quickly compare the potential interactions of different control structure with the rest of the system. Moreover, the passivity property of the equivalent output impedance of a voltage-controlled VSC gives a sufficient stability condition without knowledge of the grid model. Passivity appears then as an interesting control objective, but increasing passivity could has consequences on the voltage reference tracking. Although the transmission system need requirements are not demanding for the tracking performance of the voltage, it could have consequences during large-disturbance as illustrated in the next chapter.

Chapter 5

Enhancing the large-signal stability of parallel grid-forming converters

Contents

5.1 Overcurrent limiting strategy for improving the VSC transient stability 178

5.2 Simulation EMT of a two-VSCs parallel grid-forming system 190

5.3 Simulation EMT of a three-VSCs parallel grid-forming system in a meshed grid 195

Combining the external controls designed in chapter 3 with the terminal voltage control from chapter 4 gives the VSC the parallel grid-forming function, stable in small-signal sense. This last chapter specifically addresses large-signal stability issues of the developed controls during faults or large grid transients. A specific current limiting strategy has been developed to avoid saturation of the control references in order to keep the system under control. The chapter further validates the solution by simulating simple systems comprising two and three converters. The systems are excited by various grid events to observe the resulting dynamics and validate the stability. The designed control solution is shown to be a good candidate to operate a future full VSC-based power system.

5.1 Overcurrent limiting strategy for improving the VSC transient stability

Transient stability of a power system is obtained if all the generators remain synchronized and return to normal operation after a fault or a grid event. In converter based system, this transient stability is affected by the current strategy limit. Grid-forming converters are exposed to large transient currents during network disturbances, such as a large load connection or line tripping. Output overcurrent spikes are destructive for power electronics devices or require costly oversizing investment. In high-rating devices such as those integrated in transmission grid, the manufacturers include protection scheme to saturate the output current. However, reaching saturation level of inner current reference is undesirable in a multi-loop control as it neutralizes the voltage control action. Without voltage control, the VSC may be subject to loss of synchronization. A current limiting strategy is proposed in this section to specifically address the transient overcurrent issue in a VSC based power system.

5.1.1 The loss of transient stability with conventional current limitation

The section 3.5 showed the sensitivity of parallel grid-forming converters to transient overcurrents during grid events. As seen from the VSC perspective, the grid events have basically two possible consequences. A sudden drop of the voltage amplitude at the PCC when a short-circuit occurs, and or a sudden phase-angle shift when a topological change rearranges the power flow on the grid. The section focuses particularly on phase-shift angle perturbation. The short-circuits certainly require a specific protection scheme that depends deeply on the fault clearance time [60], and are thus excluded from the analysis

To assess the transient stability of the developed parallel grid-forming converter, the fully controlled VSC of fig. 4.1 is considered. The external controls by active power-frequency droop and reactive power-voltage from chapter 3 are included, as well as the voltage control previously designed, comprising the conventional current limitation by saturation of the inner current reference detailed in section 4.3.4. To model a transient event, the voltage of the grid equivalent is affected by a large phase-angle shift $\Delta\phi$:

$$\begin{bmatrix} v_{srca}(t) \\ v_{srcb}(t) \\ v_{srcc}(t) \end{bmatrix} = \begin{bmatrix} V_{src}\cos(\omega_0 t + \phi_0 + \Delta\phi) \\ V_{src}\cos(\omega_0 t + \phi_0 + \Delta\phi - \frac{2\pi}{3}) \\ V_{src}\cos(\omega_0 t + \phi_0 + \Delta\phi + \frac{2\pi}{3}) \end{bmatrix} \tag{5.1}$$

The response of the controlled VSC following a $\Delta\phi = -\frac{\pi}{6}$ is plotted in fig. 5.1. The magnitude of VSC output current shown on plot (b) shows that the current is limited at the saturation level of $I_{max} = 1.2 p.u.$ in the first cycles following the disturbance. This is caused by the latch-up of the current reference by the current limitation module detailed in section 4.3.4. However, the system does not manage to keep the synchronization with the grid as illustrated by the frequency reference of the VSC on plot (c).

Reaching saturation level of inner current reference opens the voltage loop and thus neutralizes the voltage-control and the power-frequency droop control. The reference saturation in the inner control of a cascaded structure has already been identified as critical in previous works [64, 171, 154]. The loss of synchronization process when during the current loop saturation is particularly well illustrated in [171].

To keep the synchronization during transients, some authors suggested to insert a PLL that operates when the VSC-based source is turned into current-source mode by the reference saturation [66, 55, 154]. Thus, the source operates transiently in grid-feeding mode during faults. Introducing such switching-mode control is, however, a challenging topic for the stability of the system. Moreover, the presence of a PLL based synchronization is hazardous if the VSC faces a standalone situation [72] and is avoided in this thesis.

In high-rating devices such as those connected at the transmission grid level, the manufacturers always include protection schemes to saturate the output current and protect the hardware. The following developments aim at preventing the voltage loop from commanding exceeding current by the implementation of a threshold virtual impedance.

5.1.2 Threshold-virtual impedance concept for limiting the overcurrent

As demonstrated in 2.3 and 3.5, the magnitude of transient currents after faults and line switching are dictated by the output reactance of the VSCs. The *Threshold Virtual Impedance* (TVI) concept proposes to virtually increase the output impedance by of the controlled VSC, Z_{vi} when needed

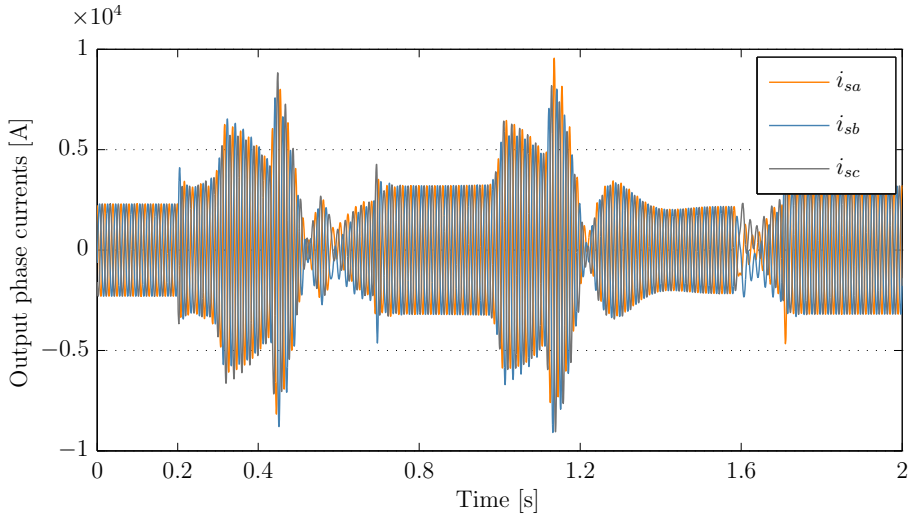

(a)

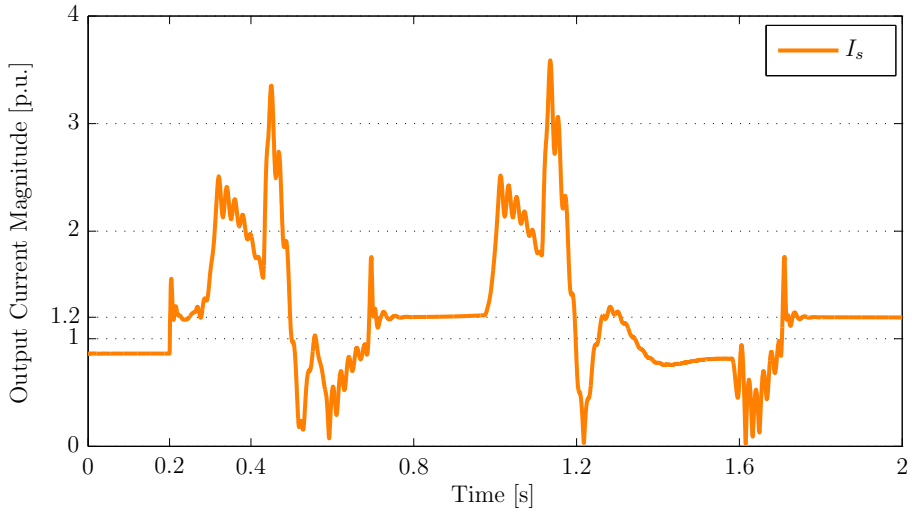

(b)

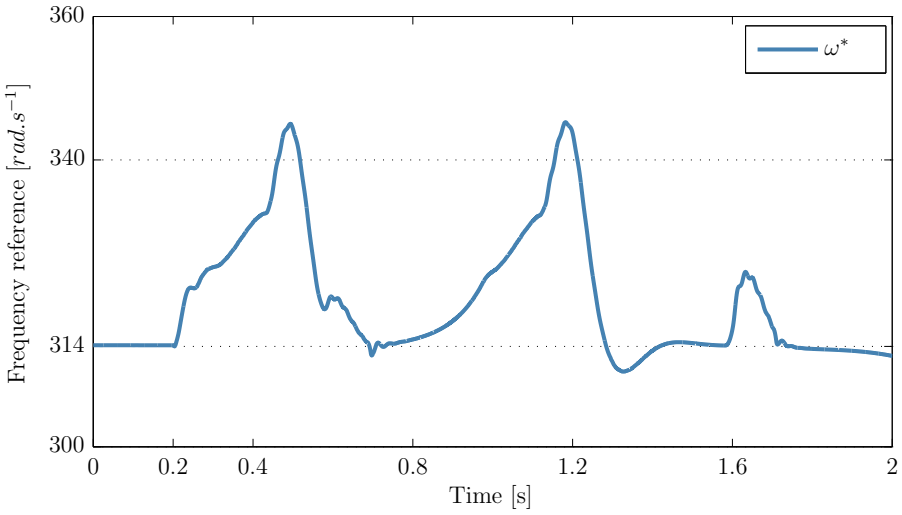

(c)

Figure 5.1 – Time-domain response of fully controlled VSC after a grid voltage phase-angle shift at 0.2 s. (a) VSC output phase-currents (b) Magnitude of the VSC output current (c) Frequency reference.

but only when the VSC output current magnitude exceeds a defined threshold. This strategy is best suited to limit the overcurrent in a grid-forming converter before reaching the current reference saturation level. The virtual impedance is a wide VSC control concept and [172] reviews the different possible applications. This idea is applied here for current limitation in the grid-forming converters. A similar current limitation by voltage reference modification is already presented in [149, 50] and more recently in [64], in different application goals. They propose a signal $\Delta \boldsymbol{v}_{VIdq}$, given by the TVI module to be subtracted to the voltage control reference as in eq. (5.2):

$$\begin{aligned} e_d^* &= E^* - v_{VId}, \\ e_q^* &= -v_{VIq}. \end{aligned} \tag{5.2}$$

Threshold-virtual impedance structure Modifying the form of the actual VSC series output impedance by a virtual impedance term Z_{vi} requires to analyze the benefit of adding more resistive or more inductive behavior between the VSC and the PCC during grid disturbances. From a rough analysis in 3.5, it has been concluded that first current peak following a line switch or, more generally, an phase-angle shift, is determined by the inductive component of the VSC output impedance. A purely resistive, as the one presented in [149] is excluded. Besides, emulating numerically inductive impedance is not straightforward task due to the differentiation operation. An algebraic representation of quasi-static impedance is, however, easy to implement in the dq-rotating frame, as follows:

$$\begin{aligned} Z_{vi} &= r_{vi} + jx_{vi}, \\ v_{VId} &= r_{vi} i_{sd} - x_{vi} i_{sq}, \\ v_{VIq} &= r_{vi} i_{sq} + x_{vi} i_{sd}. \end{aligned} \tag{5.3}$$

The overcurrent detection is added to form the voltage drop $\Delta \boldsymbol{v}_{VIdq}$ signal out of the TVI as shown in fig. 5.2.

For smoother transition between normal operation and current limiting operation, the resistance and reactance values are chosen to be progressive in respect with the overcurrent.

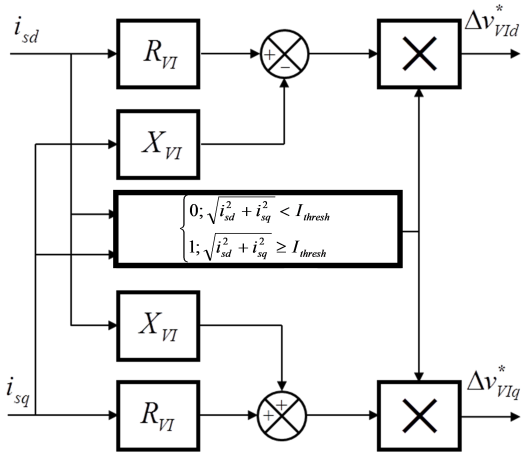

Figure 5.2 – The threshold virtual impedance control scheme is implemented in dq-frame. The virtual impedance is active only if the VSC output current magnitude (I_s) exceeds the defined threshold value I_{tresh}.

$$\begin{aligned} r_{vi}(I_s) &= k_R|I_s - I_{thresh}| \\ x_{vi}(I_s) &= k_R|I_s - I_{thresh}|\rho_{X/R} \end{aligned} \tag{5.4}$$

The two TVI parameters to be defined are the gain k_R and the ratio $\rho_{X/R}$ of the reactive part to the resistive part of TVI. I_{sd} and i_{sq} are the VSC output currents expressed in the rotating dq-frame. The following paragraph explains how to choose the gain k_R given a maximum acceptable current magnitude, and how to determine $\rho_{X/R}$ to maintain the stability of the droop controls when the TVI is active.

Threshold-virtual impedance tuning The value of k_R is chosen to keep the output current under the fixed limit I_{max} in steady-state. The amplitude of the transient disturbance are impossible to predict so that k_R is determined in the worst case of a three-phases bold short-circuit at the PCC. Fig. 5.3 illustrates the electrical circuit after of a short-circuit when the steady state is recovered. Since then the TVI becomes active, the steady-state output current expression is:

$$I_{ssc} = \frac{E_0}{Z_c + Z_{VI}(I_{ssc})} \tag{5.5}$$

Assuming that $I_{ssc} = I_{max}$ during the short-circuit, introducing (5.4) in (5.5) yields k_R to be solution of:

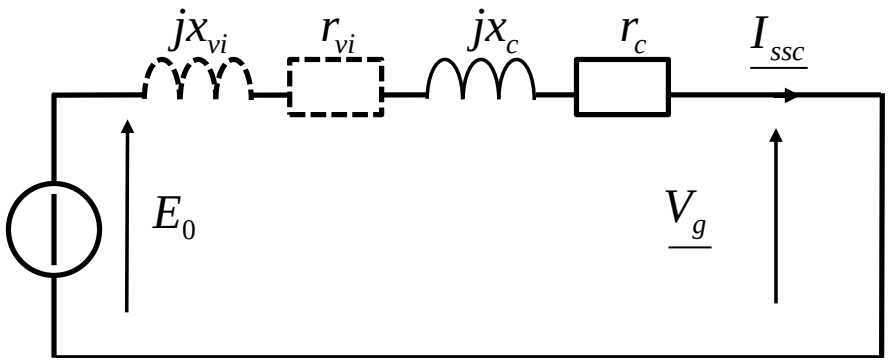

Figure 5.3 – Steady state representation of the system after short-circuit, for the calculation of k_R value.

$$\left(\frac{E_0}{I_{max}}\right)^2 = (r_c + r_{vi}(I_{max}))^2 + (x_c + x_{vi}(I_{max}))^2 \tag{5.6}$$

Keeping the positive solution of the second order equation (5.6) gives the value or k_R, depending on the value of $\rho_{X/R}$. To further determine the couple of parameters (k_R, $\rho_{X/R}$), a stability study is performed. The aim is to ensure that the external controls are not disturbed by the presence of the virtual impedance. The TVI is highly non-linear so the large-signal stability is complicated to assess analytically. Instead, a small-signal stability analysis is conducted considering that the TVI is continuously activated (switched-on). First, the trade-off between the influence of the resistive and reactive component of Z_{VI} on the dynamic behavior of the system is assessed. Then, with the chosen $\rho_{X/R}$ value, a pole map is plotted for all range of values taken by the Z_{VI} when the output current is comprised between $I_{thresh} < I_s < I_{max}$. For the clarity of the results, the voltage-control has been disregarded and the voltage-controlled VSC is approximated by a controllable voltage-source. The impact of the TVI is then focused on the interaction with the external controls, especially with the power-frequency droop control. The considered system is given in fig. 5.4.

The simplified system has five remaining states: two associated with first order filters of the active and reactive power, the d and q components of the i_g current, and the phase-angle reference θ^* resulting from the integration of the frequency reference ω^*. First of all, it is interesting to compare the impact of the TVI on the poles of the system, with the impact of a real additional

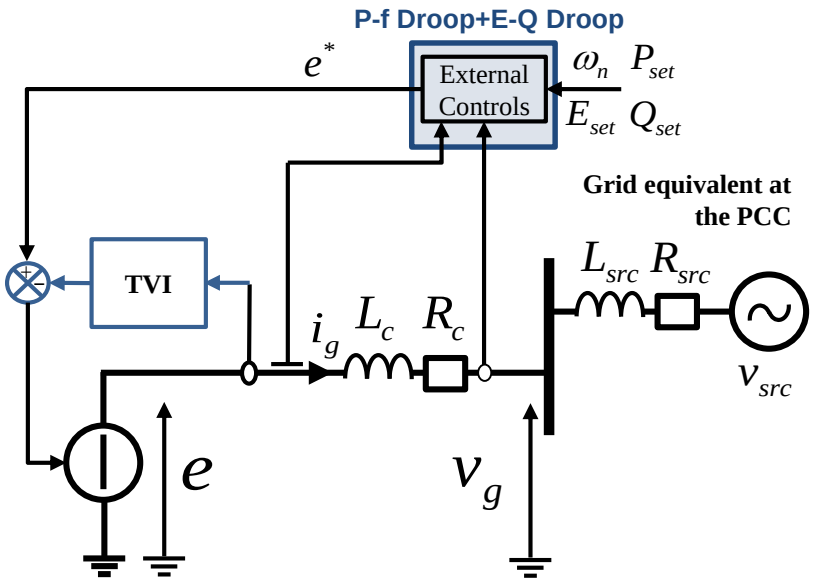

Figure 5.4 – Considered system for the tuning of the TVI. The terminal voltage-control is disregarded. The source impedance value is taken as $l_{src} = 0.15$ p.u. $r_{src} = 0.15$ p.u.

Table 5.1 – Comparison of eigenvalues from fig. 5.5

Eigenvalue	Real impedance	Equivalent TVI
λ_{1-2}	$-53.12 \pm 313.5j$	$-172.0 \pm 1017j$
λ_{3-4}	$-15.56 \pm 12.43j$	$-15.65 \pm 12.26j$
λ_5	-31.74	-31.74

inductance of equivalent size in steady-state. As shown in fig. 5.5 and the corresponding table 5.1, the TVI and the real impedance have the same eigenvalues corresponding to the three slowest modes λ_{3-4} and λ_{3-4}. These eigenvalues are related to the external control. The fastest modes λ_{1-2}, related to the currents, are increased in frequency by the presence of the TVI but keep the same damping. As a conclusion, the TVI resembles to a real impedance at low frequency which was expected.

From the situation of fig. 5.5, the value of $\rho_{X/R} = 10$ is progressively decreased to $\rho_{X/R} = 0.1$. The poles trajectories are plotted in fig. 5.6.

As previously mentioned, the TVI cannot be purely resistive. However, increasing relatively the resistive component of the TVI provides more damping at high frequencies. The slowest

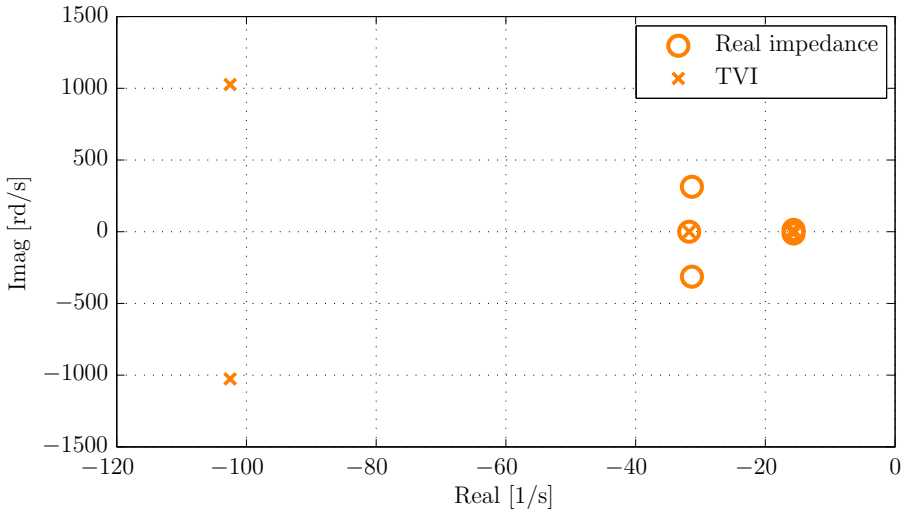

Figure 5.5 – Poles map of the simplified system in the presence of a real additional series impedance compared to the presence of the equivalent TVI. $\rho_{X/R} = 10$, $I_s = I_{max}$.

modes have a significatively reduced damping once $\rho_{X/R} < 1$. Indeed, the external controls have been designed based on the assumption of series impedances dominated by their inductive component. Consequently, the value of $\rho_{X/R} = 5$ is chosen to preserve the inductive behavior of the line, as seen by the external controls.

The last poles map ensures that all the values taken by the TVI do not destabilize the system when the current is comprised between $I_{thresh} < I_s < I_{max}$. The result in fig. 5.7 shows that the small-signal stability of the system is not drastically affected by the permanent presence of the TVI. However, this is not a proof of large-signal stability of the complete system during grid transient events. Time-domain simulation on hard transients must be conducted on EMT software to validate the effectiveness of the TVI

5.1.3 Implementation of the Threshold-virtual impedance in the parallel grid-forming VSC

The implementation of the TVI on the fully controlled system must take into account the limitation of the voltage tracking performance. If the voltage-control is sluggish to adjust the terminal voltage amplitude, the current spike can not be mitigated soon enough. Moreover, the design

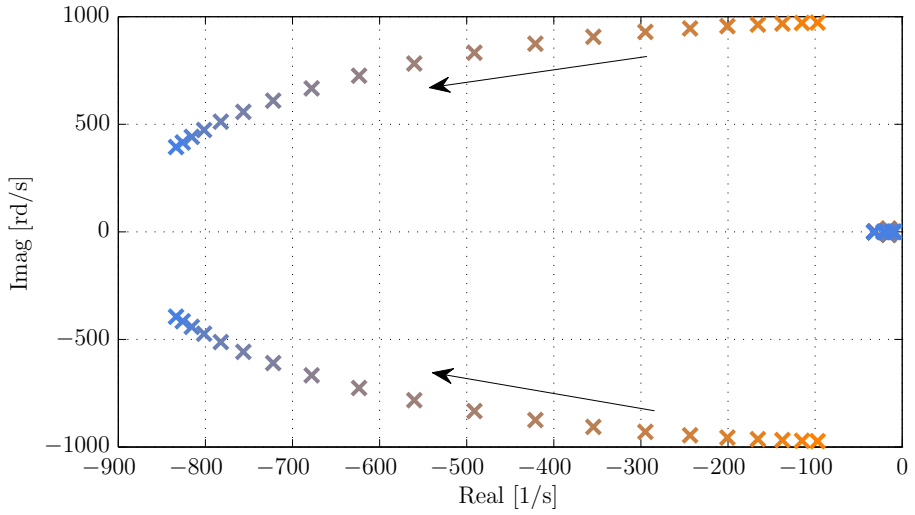

(a)

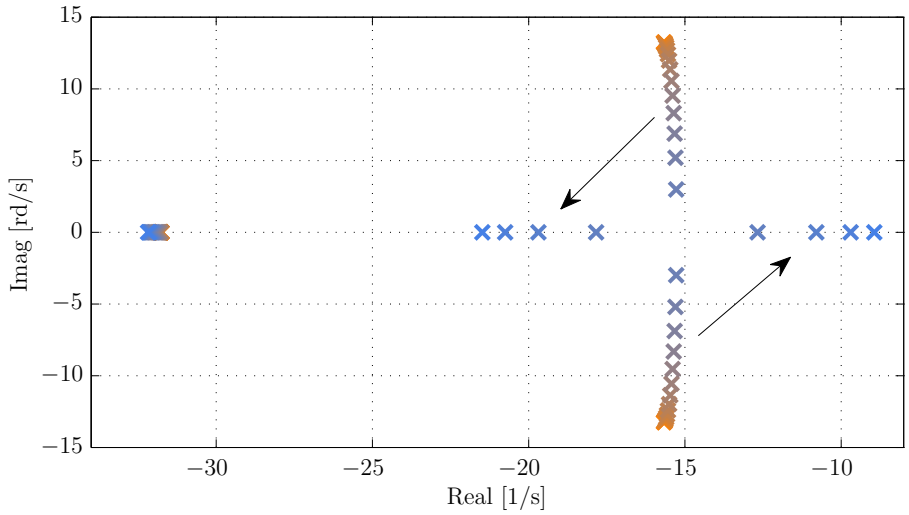

(b)

Figure 5.6 – Poles trajectories of the simplified system with the presence of an active TVI (a) and zoom on the slowest modes (b). $\rho_{X/R}$ = is moving from 10 (orange/light) to 0.1 (blue/dark), $Z_{VI} = Z_{VI}(I_s = I_{max})$.

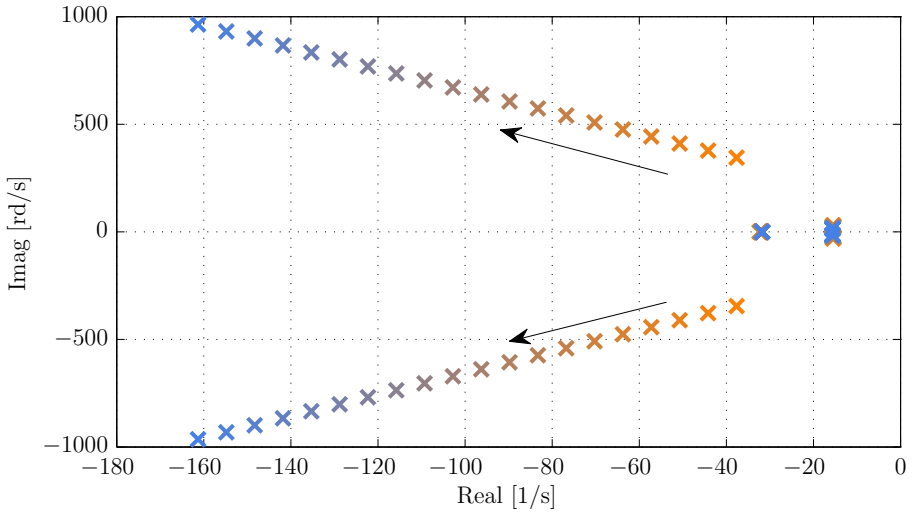

(a)

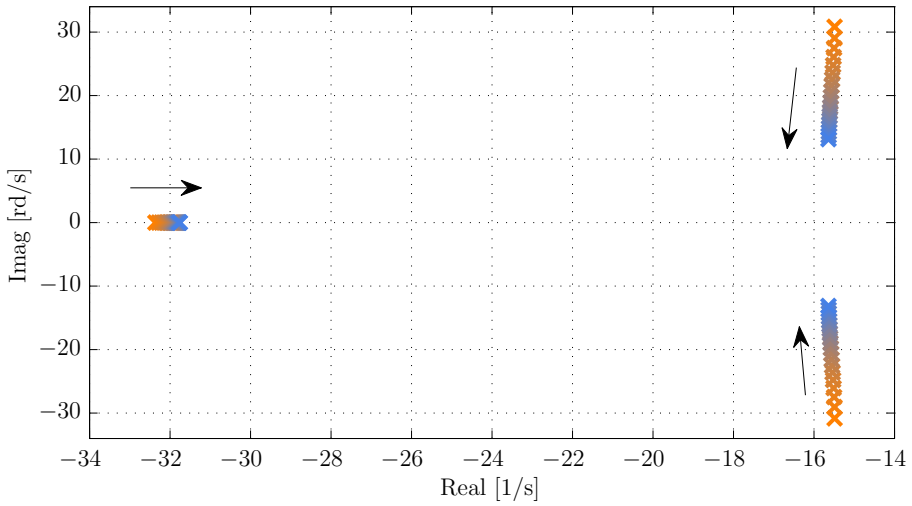

(b)

Figure 5.7 – Poles trajectories of the simplified system with the presence of an active TVI (a) and zoom on the slowest modes (b). $\rho_{X/R}$ =5, Z_{VI} is moving from $Z_{VI}(I_s = 1)$ (orange/light) to $Z_{VI}(I_s = I_{max})$ (blue/dark).

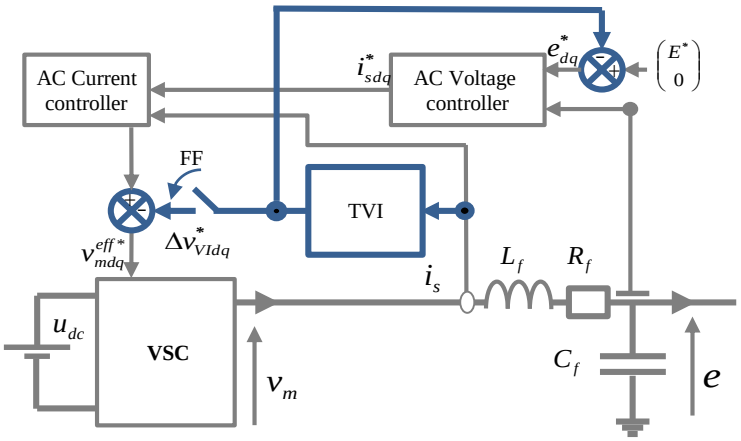

Figure 5.8 – Implementation of the TVI within the cascaded loops of the voltage-control.

recommendations of section 4.5 specify to decrease the voltage control dynamic to increase the system robustness.

To by-pass the voltage-control during critical events, the TVI signals v_{VIdq} have to be applied as close as possible from the VSC modulation, in order to speed up the response to overcurrent. In the present implementation, v_{VIdq} signals are subtracted directly to the VSC modulation reference (v^*_{mdq}) given by the current control output, to form the reference (v^{eff*}_{mdq}) effectively applied to the converter modulation:

$$\begin{aligned} v^{eff*}_{md} &= v^*_{md} - v_{VId}, \\ v^{eff*}_{mq} &= v^*_{mq} - v_{VIq}. \end{aligned} \tag{5.7}$$

The signals v_{VIdq} are still subtracted from the voltage control tracking reference, otherwise, the inner voltage control tries to compensate the threshold virtual impedance action. The implementation of TVI in the internal multi-loop control is summarized on the scheme fig. 5.8.

This feedforwarded implementation of the TVI (TVI-FF) is compared to the implementation on the voltage reference only. The fig. 5.9 displays the time-domain curves of quantities following a grid event modeled by $\Delta\phi = -\frac{\pi}{6}$. The activation of the TVI certainly affects the behavior of the inner current loop. Depending on the requirement during transient, the current loop parameters tuning could be improved in the presence of the TVI.

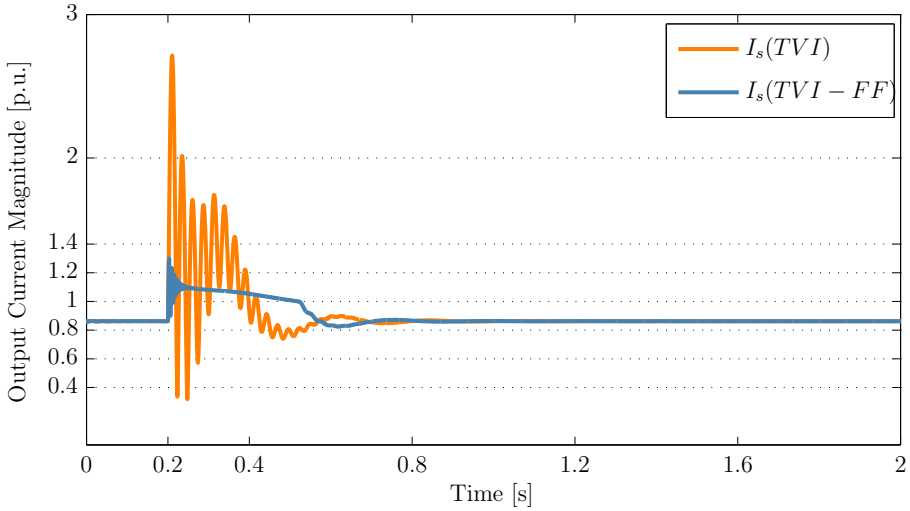

(a)

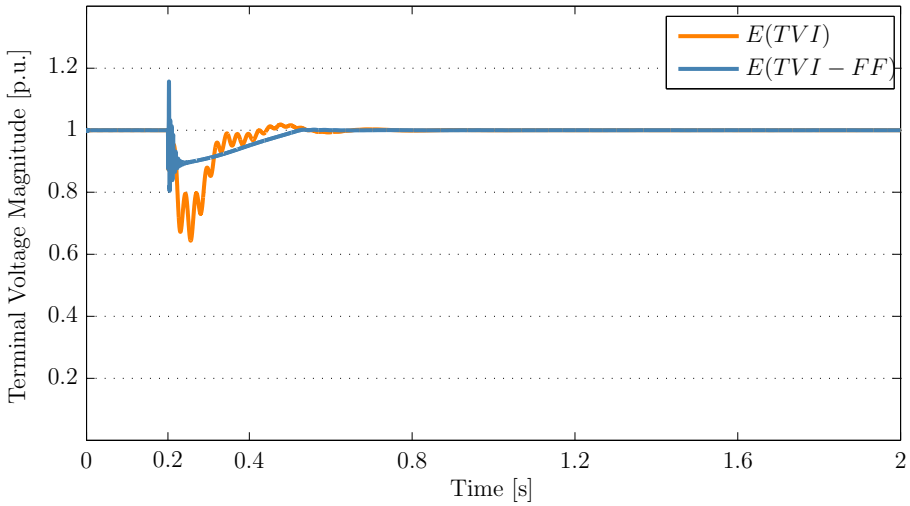

(b)

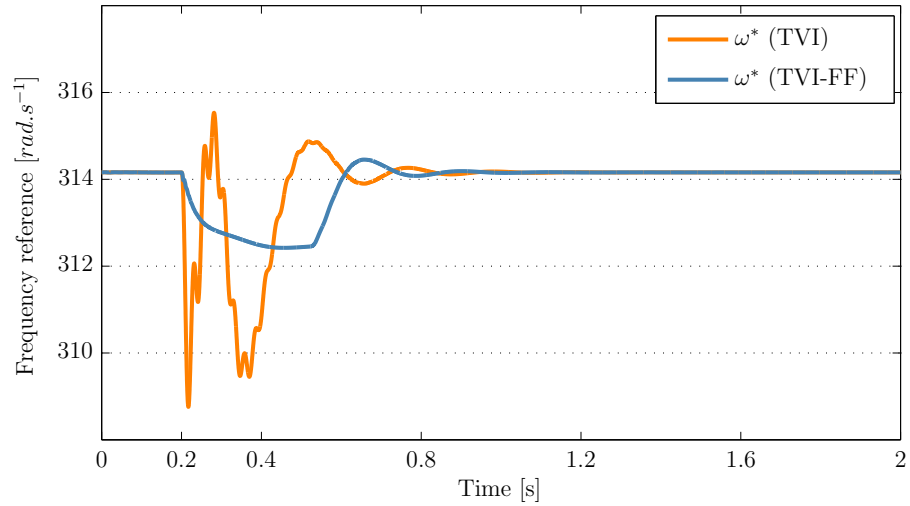

(c)

Figure 5.9 – Time-domain response of fully controlled VSC with the TVI after a grid voltage phase-angle shift at 0.2 s. (a) Amplitude of the VSC output current (b) Amplitude of the VSC terminal voltage (c) Frequency reference.

5.1.4 Conclusion on the new overcurrent limiting strategy

The TVI principle is to avoid that the demanded current reaches the current limit in the inner current loop. The activation on threshold does not disturb the controlled VSC behavior when it is far from its current limit. In other words, the grid-forming VSC acts as a stiff voltage source as long as its nominal output current is not exceeded. Once the current limit is reached, the equivalent output impedance of the controlled VSC is drastically increased, and thus the voltage stiffness property is abandoned to protect the device. This behavior seems desirable for future parallel grid-forming converters.

The main difficulty of the TVI design is the analytic analysis of the transient-stability of the system. The design procedure here only ensures that the external controls are not significantly disturbed when the TVI is activated. Investigations on formal proof of the stability of the TVI would be more rigorous. At the moment, the large-signal stability of the TVI has been only evaluated using numerical simulations on possible but demanding situations of future VSC-based transmission system.

5.2 Simulation EMT of a two-VSCs parallel grid-forming system

The first considered system is the two-VSCs system of fig. 3.12 presented in the chapter 3. One objective of the simulation is to validate that the overcurrent risk predicted in this previous chapter has been mitigated by the developed controls.

5.2.1 System model and parameters

The two-VSCs system includes all the parallel grid-forming controls developed in this thesis, as detailed on the left hand side converter in fig. 5.10. The two VSCs have different ratings of 1 GW and the 250 MW power rates, connected to the highest voltage level (400kV) of the French transmission grid. The parameters are recalled in tables 5.2, 5.3, and 5.4. Notably, the effect of the reactive power droop has been disabled by making $n_q = 0$ as it is not of interest here.

The inverters are interfaced with a double overhead line of 100 km, whose parameters are recalled in table 5.5.

Table 5.2 – Nominal values of two VSC based sources

Parameter	Quantity	Value	per-unit
P_{n1}	Nominal active power of VSC 1	$1\,GW$	0.96
S_{b1}	Base apparent power of VSC 1	$1044\,MVA$	1
P_{n2}	Nominal active power of VSC 2	$250\,MW$	0.96
S_{b2}	Base apparent power of VSC 2	$261\,MVA$	1
U_b	Base voltage	$400\,kV$	1
ω_n	Nominal angular frequency	$2\pi 50\,rad.s^{-1}$	1

Table 5.3 – LCL filters parameters

Parameter	Quantity	Value
l_f	filter inductor	$0.15\,p.u.$
r_f	filter series resistance	$0.005\,p.u.$
c_f	filter shunt capacitance	$0.066\,p.u.$
l_c	connection inductance	$0.15\,p.u.$
r_c	connection series resistance	$0.005\,p.u.$

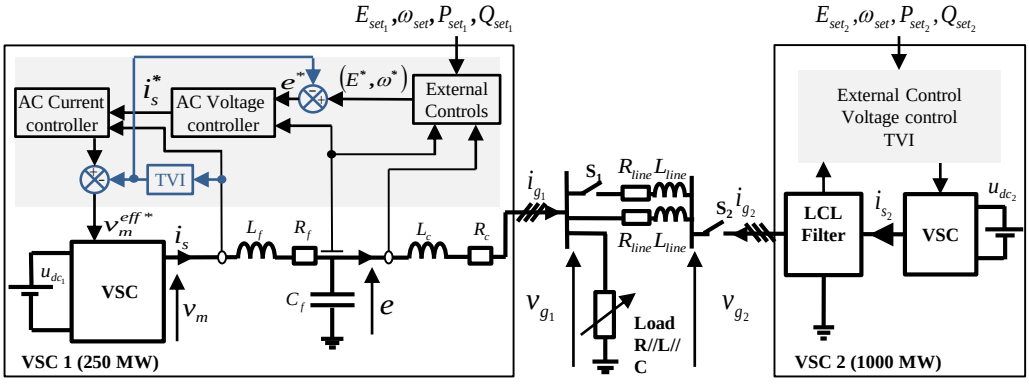

Figure 5.10 – Layout of a power system based on two parallel grid-forming VSC

Table 5.4 – Control parameters

Parameter	Name	Value
m_p	Frequency droop gain	$0.04\omega_n\ rd.s^{-1}$
n_q	Reactive power droop gain	$0\,p.u.$
ω_{LP}	Power filter cut-off frequency	$\omega_n/10\ rd.s^{-1}$
k_{pc}	Proportional gain	$0.62\,p.u.$
k_{ic}	Integral gain	$477.5\ rd.s^{-1}$
g_{ffv}	Voltage feedforward gain	$0\,p.u.$
k_{pv}	Proportional gain	$0.03\,p.u.$
k_{iv}	Integral gain	$2.1\ rd.s^{-1}$
g_{ffc}	Current feedforward gain	$1\,p.u.$
k_R	TVI gain	$0{,}67\,p.u.$
$\rho_{X/R}$	TVI ratio	$5\,p.u.$

Table 5.5 – Typical 400 kV overhead line on transmission grid

Parameter	Quantity	Value
r_{line}	distributed line series resistance	$0.024\ \Omega.km^{-1}$
x_{line}	distributed line series reactance at ω_n	$0.24\ \Omega.km^{-1}$
b_{line}	distributed line shunt susceptance at ω_n	$3.974.10^{-6}\ \Omega^{-1}.km^{-1}$

5.2.2 Response to a line switch, load change, and power setpoint modification

The two-VSC system is initially loaded with P_{load} = 1125 MW of resistive load. The first simulated event opens one of the lines (S_1 opens) between the two VSCs at 0.1 s. This situation has been identified as particularly challenging for parallel grid-forming converter in section 3.5. Then, the load sharing capability of the system is evaluated through the increase of 150 MW (+12 %) of the active load at 0.8 s. Lastly, the adjustment of the active power setpoint is evaluated by increasing P_{set2} from 0.85 to 0.95 p.u. at 1.5 s. The resulting electrical quantities are plotted in fig. 5.11 in their respective per-unit bases.

The output current magnitude I_{s1} of the smallest VSC (VSC 1) following the line switch is limited by the TVI action. Whereas the current could theoretically reach 1.4 p.u. for few cycles if the VSC was idealy controlled in voltage (see fig. 3.14), the actual current remain limited here under 1.05 p.u. As a direct consequence, the terminal voltage E_1 drops to 0.96 p.u. but returns to its nominal value in around 100 ms which is an acceptable dynamic considering the present system requirements. It may be noted, that the total power demand decreased after the line switch because of the small load voltage drop due to the larger impedance separating the load and the VSC 2. Still, the load is shared equitably.

The load increases at 0.8 s is electrically closer from VSC 1, resulting in a larger transient seen by the VSC 1. Before the P-f droop control reacts, the TVI is activated to avoid transient overcurrents. In steady-state, however, the load level of each converter is well shared. The power setpoint modification of P_{set2} = +0.1 p.u. reliefs the smallest inverter from part of the load. This action shows how an outer and centralized controller could restore the power margins of different units.

Looking at the frequency reference in fig. 5.12, it should be noted that the units keep the synchronization after each events. Because of the droop characteristic, the common frequency in steady-state gives the information of the disequilibrium between the power setpoints and the actual load level. It shows also that the power setpoint modification of P_{set2} = +0.1 p.u. can restore the frequency.

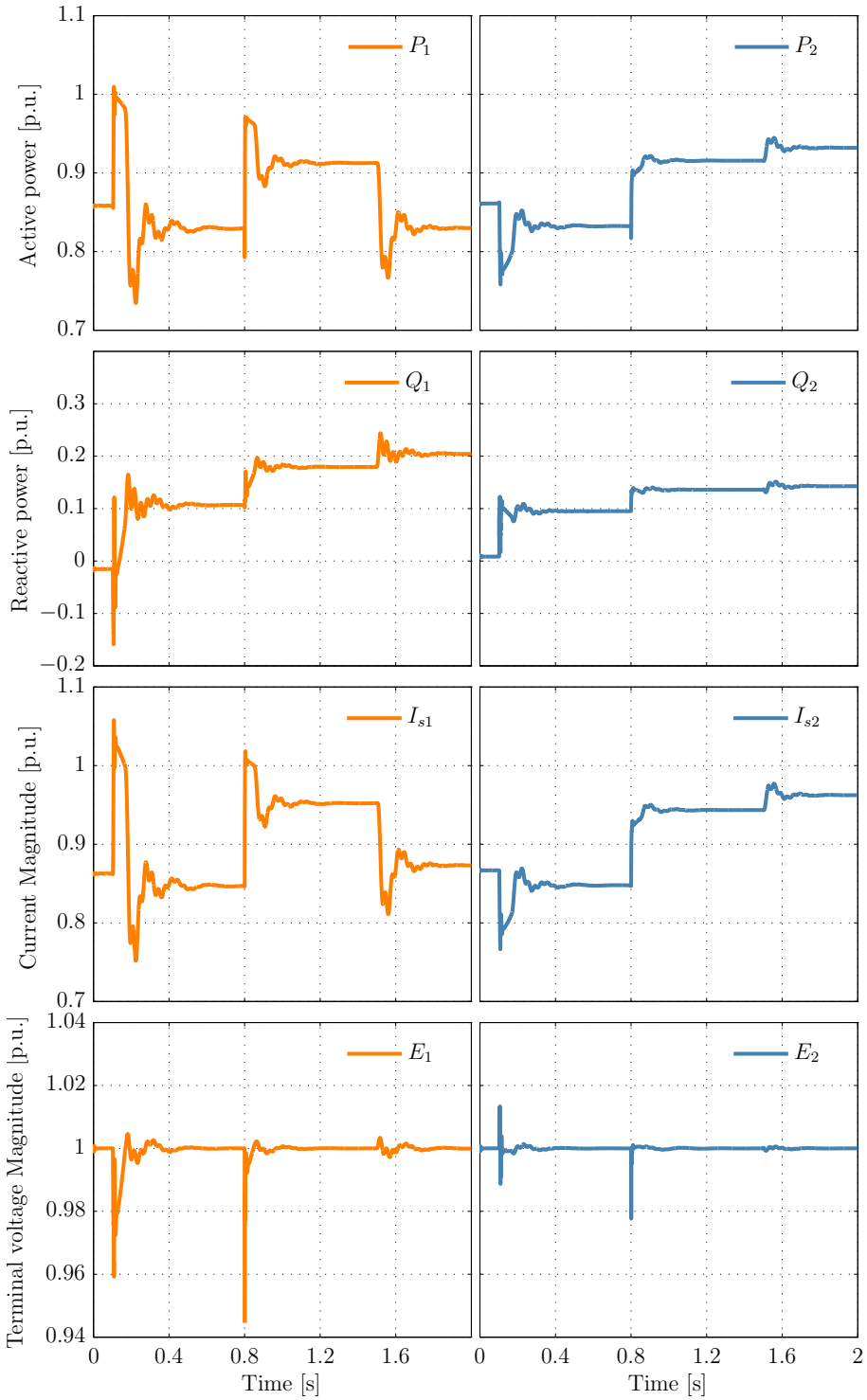

Figure 5.11 – Time-domain response of electrical quantities of the two-VSC system (fig. 5.10) expressed in respective per-unit base S_{b1}=261 MVA, S_{b1}=1044 MVA. At t=0.1 s, S_1 opens, t=0.8 s P_{load} = +150 MW, t=1.5 s P_{set2} = +0.1 p.u.

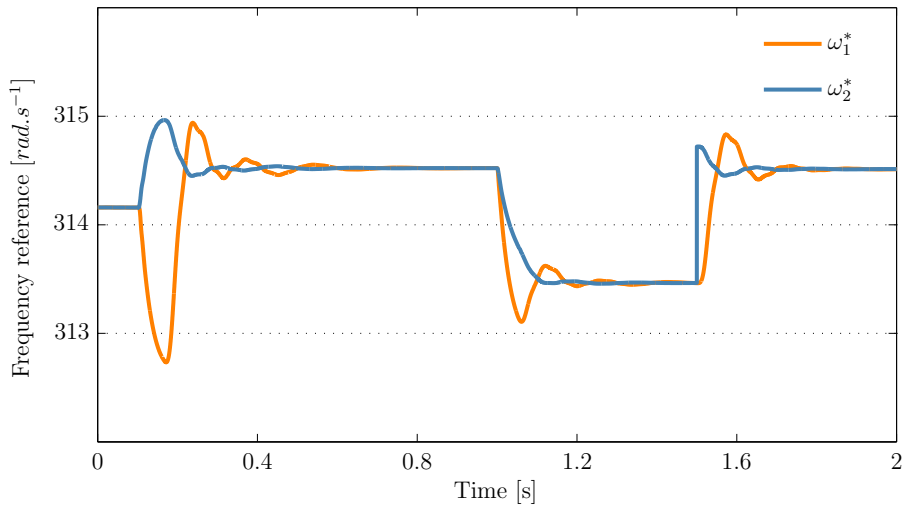

Figure 5.12 – Time-domain responses of the frequency references of the two VSCs (fig. 5.10). At t=0.1 s, S_1 opens, t=0.8 s P_{load} = +150 MW, t=1.5 s P_{set2} = +0.1 p.u.

5.2.3 Response to islanding

In this second simulated case, the load is readjusted to P_{load} = +250 MW and is initially shared among the two units. At 0.1 s, The largest units is separated from the rest of the system. The fig. 5.13 shows how the system recovers from this severe outage. Clearly, the figure illustrates that the VSC 1 manages to feed the load in standalone under nominal terminal voltage, whereas the VSC 2 is successfully islanded with no load. The units are not connected anymore so the frequency references diverge from each other (see 5.14).

5.3 Simulation EMT of a three-VSCs parallel grid-forming system in a meshed grid

In this second simulated case, three VSCs are interfaced through a meshed grid. The impact of topological changes are assessed.

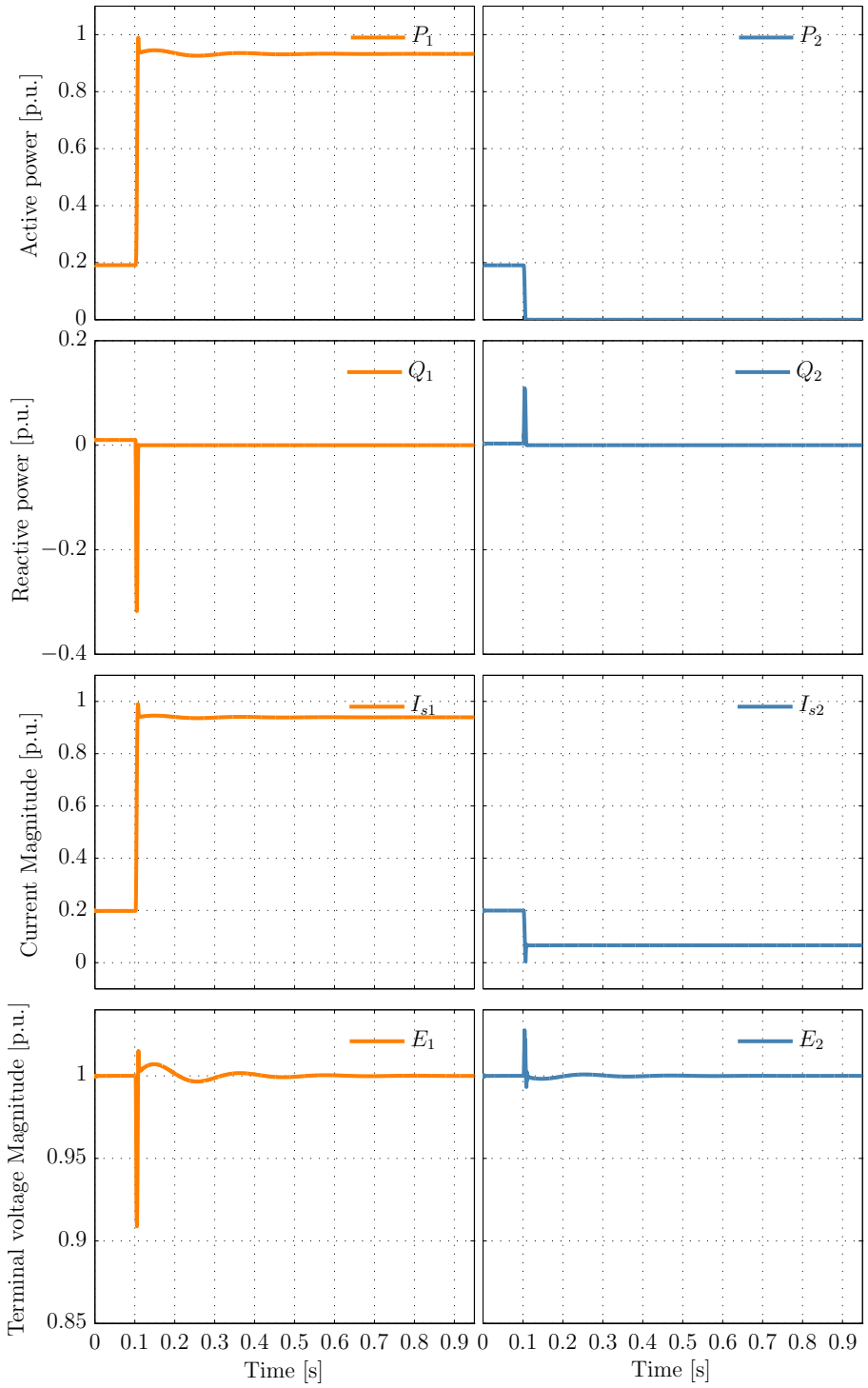

Figure 5.13 – Time-domain response of electrical quantities of the two-VSC system (fig. 5.10) expressed in respective per-unit base S_{b1}=261 MVA, S_{b2}=1044 MVA. At t=0.1 s, S_2 opens.

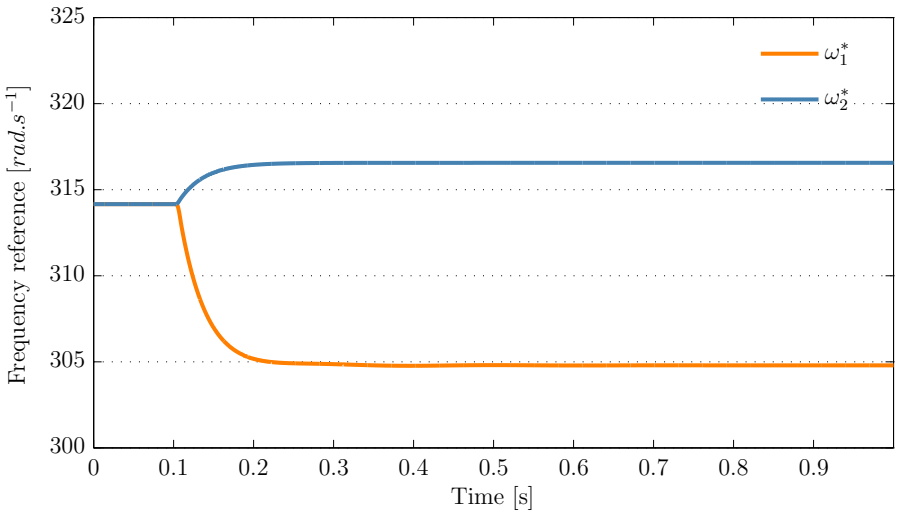

Figure 5.14 – Time-domain responses of the frequency references of the two VSCs (fig. 5.10). At t=0.1 s, S_1 opens, t=0.8 s P_{load} = +150 MW, t=1.5 s P_{set2} = +0.1 p.u.

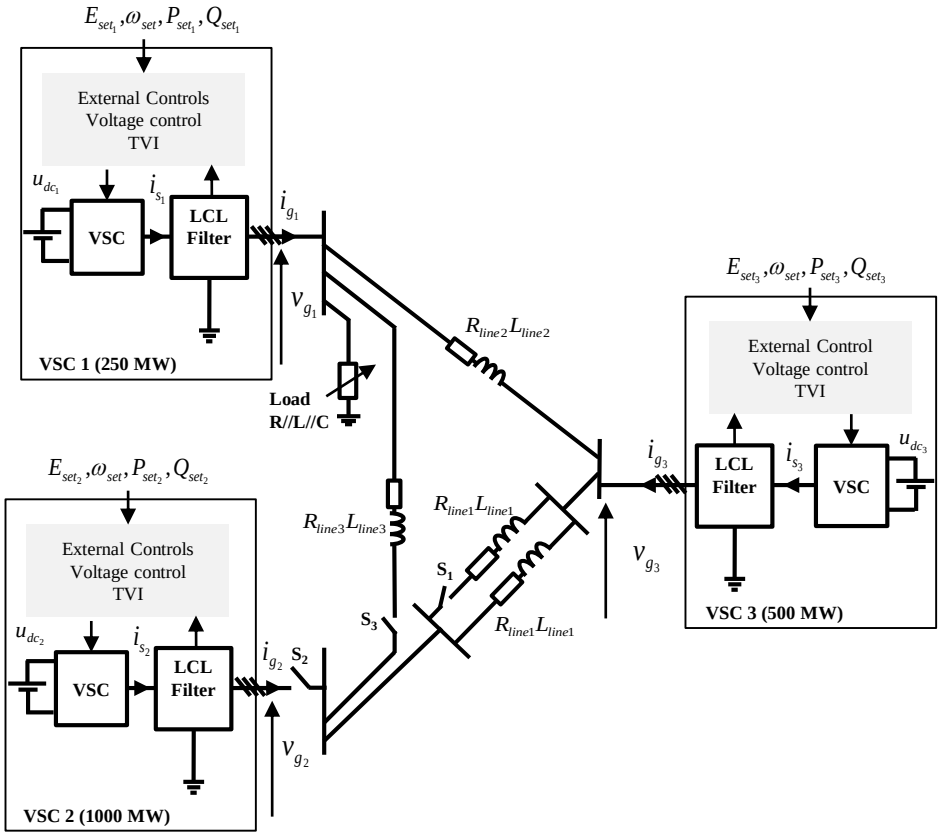

Figure 5.15 – Layout of a power system based on three parallel grid-forming VSC

Table 5.6 – Nominal values of three VSC based sources

Parameter	Quantity	Value	per-unit
P_{n1}	Nominal active power of VSC 1	$1\,GW$	0.96
S_{b1}	Base apparent power of VSC 1	$1044\,MVA$	1
P_{n2}	Nominal active power of VSC 2	$250\,MW$	0.96
S_{b2}	Base apparent power of VSC 2	$261\,MVA$	1
P_{n3}	Nominal active power of VSC 2	$500\,MW$	0.96
S_{b3}	Base apparent power of VSC 2	$522\,MVA$	1
U_b	Base voltage	$400\,kV$	1
ω_n	Nominal angular frequency	$2\pi 50\,rad.s^{-1}$	1

Table 5.7 – Chosen lines length

400kV line	Length
$Line1$	$100\ km$
$Line2$	$125\ km$
$Line3$	$25\ km$

5.3.1 System model and parameters

Compared to the previous study case, a new VSC-based source of 500 MW of nominal power is added as seen in table 5.6. The filters and control parameters (given in tables 5.3,and 5.4) are identical for the three converters, in respect with their base power.

The overhead lines have the same characteristics (given in table 5.5) but different lengths as described in table 5.7.

5.3.2 Response to line switches and power setpoints modification

The three-VSC system is initially loaded with $P_{load} = 1050$ MW of resistive load. The opening of the switch S_3 corresponds to a sudden line trip between the smallest converter (VSC 1) and the largest converter (VSC 2). Following the fault, the active power flows are instantaneously re-

dispatched and the VSC 1 must handle transiently a high load level. The phenomenon is visible in fig. 5.16 at 0.1 s. The action of the TVI is visible when the current I_{s1} exceeds its limit. The TVI keeps the VSC 1 in an acceptable operation range and the synchronization stability is maintained as shown in fig. 5.17. Later, the opening of one line between the VSC 1 and the VSC 3 is simulated at t=0.8 s. The VSC 1 is electrically too far from the event to be seriously affected. Lastly, the power setpoint of VSC 2 is modified by $P_{set2} = -100$ MW at t=1.5 s. Consequently, the two-other converters have an increased active power, and the frequency drops.

5.3.3 Response to a VSC-based generator outage

This subsection focuses on what happens if the the largest unit (VSC 2) trips. The remaining VSC-based production of 750 MW nominal power is apparently not sufficient to feed the 1050 MW of the load. The switch S_2 opens at t=0.1 s and the simulation results are plotted in fig. 5.18. The curve of I_{s1} shows that the current stays over 1 p.u. meaning that the TVI is constantly activated. As a consequence, the terminal voltage E_1 drops until 0.83 p.u. lowering the active power demand of the load due to its impedance characteristic. In this specific case, the TVI acts as a load self regulation. The situation is not sustainable regarding the electrical quality requirements of the transmission system, but it is interesting to note that the system is kept stable even during overloaded situations. However, the frequency ($\omega_1^* = \omega_2^*$) is stabilized with a small drop (see fig. 5.19), so that the defense plan based on frequency measurement for load shedding may be not activated. The protection strategy must therefore be adapted to the new dynamics of VSC-based transmission system.

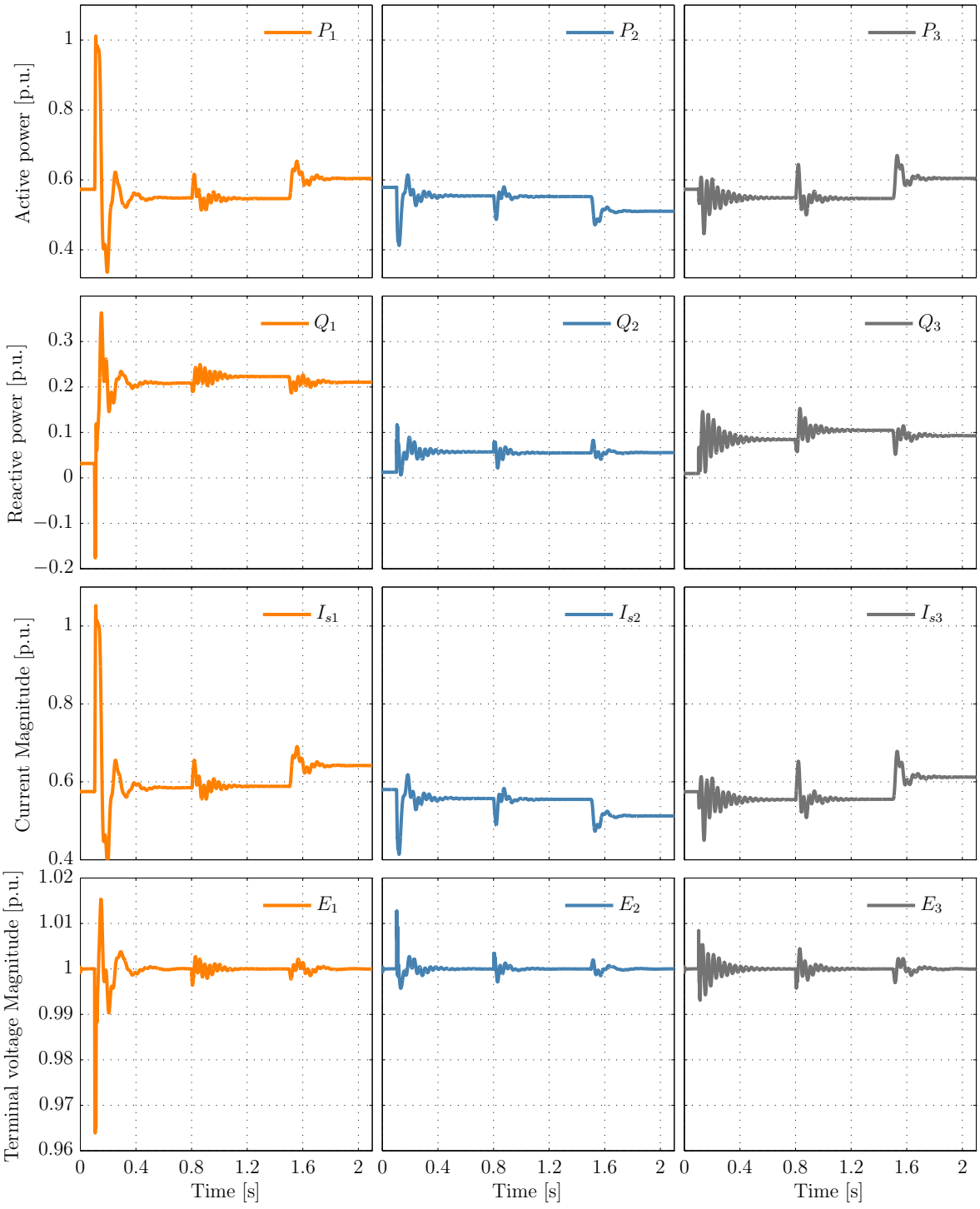

Figure 5.16 – Time-domain responses of electrical quantities of the three-VSC system (fig. 5.15) expressed in respective per-unit base S_{b1}=261 MVA, S_{b2}=1044 MVA, S_{b3}=522 MVA. At t=0.1 s, S_3 opens, t=0.8 s S_1 opens, t=1.5 s P_{set2} = +0.1 p.u.

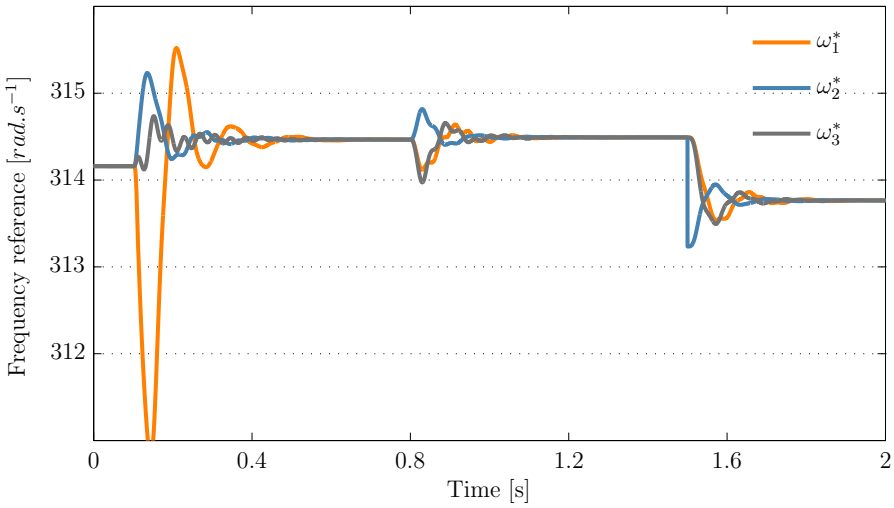

Figure 5.17 – Time-domain responses of the frequency references for the three VSCs (fig. 5.15). At t=0.1 s, S_3 opens, t=0.8 s S_1 opens, t=1.5 s P_{set2} = +0.1 p.u.

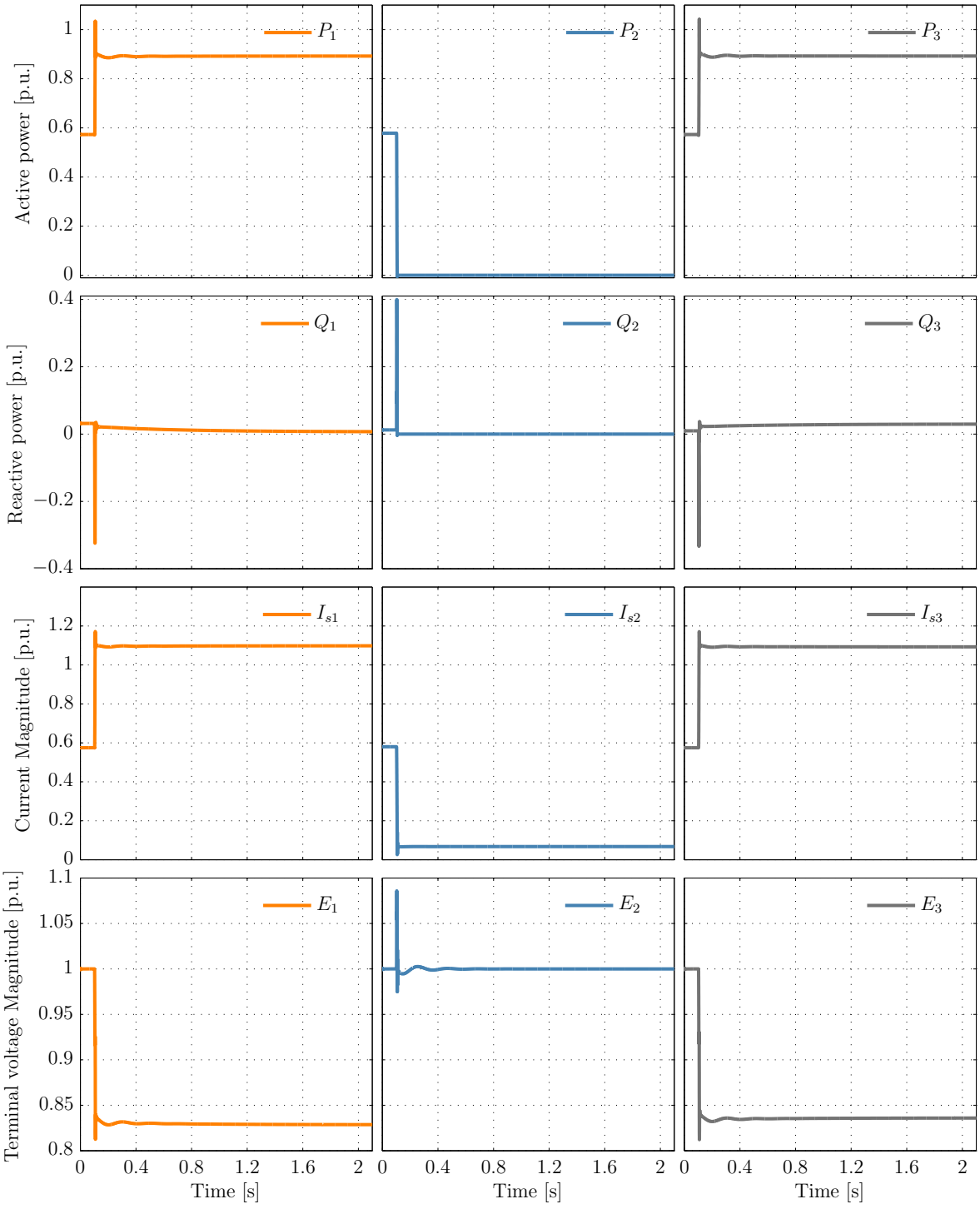

Figure 5.18 – Time-domain responses of electrical quantities of the three-VSC system (fig. 5.15) expressed in respective per-unit base S_{b1}=261 MVA, S_{b2}=1044 MVA, S_{b3}=522 MVA. At t=0.1 s, S_2 opens

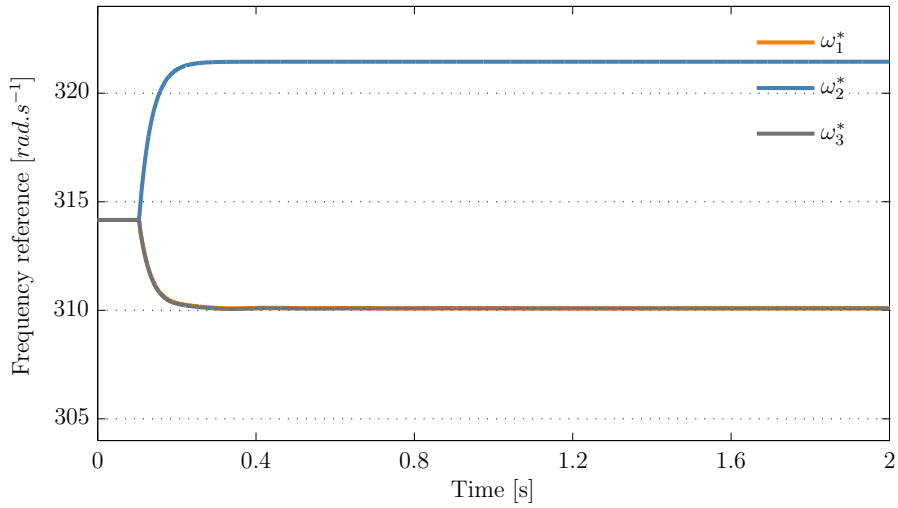

Figure 5.19 – Time-domain responses of the frequency references for the three VSCs (fig. 5.15). At t=0.1 s, S_2 opens.

The chapter exhibits the limit of the inner current reference latch-up after grid-events. The controlled VSC did not manage to return to an acceptable operating point. Instead, a new current limiting strategy, based on a Threshold Virtual Impedance, is proposed to keep stability of the external controls, and to suit the voltage control designed previously. In purpose, the TVI falls down the voltage stiffness of the grid-forming VSC only when the operating limits of the device are reached transiently. The large-signal improvement of the TVI is shown through numerical EMT simulations in typical situation of one, two and three fully controlled VSCs. Interestingly, one specific case of overloaded situation following a generator outage lead to the stabilization to a lower voltage. It raises the question of modifying defense strategy such as frequency-based load shedding to adapt to the parallel grid-forming behavior.

Chapter 6

Conclusion and perspectives

6.1 Summary and discussion around the achievements

This thesis investigated the operating conditions for a full-VSC based power system, giving insight on analysis tools that must be employed, as well as design methods and requirements to build parallel grid-forming devices. From system needs analysis, three-challenges have notably been discussed, the synchronization process of ideal voltage-sources, the small-signal stability of a voltage-controlled VSC in various grid-configurations, and the enhancement of large-signal stability with a specific current limitation strategy based on a threshold virtual impedance. The resulting dynamics of the new controlled system are resumed roughly on fig. 6.1. Main contributions and findings are summarized here.

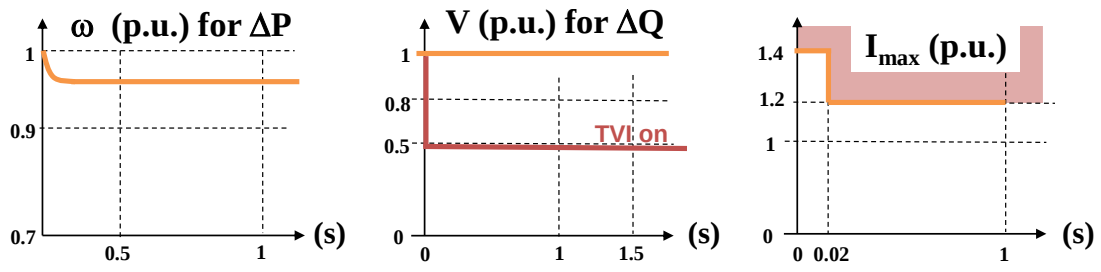

(a) Frequency dynamic (b) Voltage magnitude dynamic (c) Overcurrent capability

Figure 6.1 – Properties of the grid-forming fonction of the controlled VSC

Future challenges of VSC-based power system As opposed to the discussion on the flexibility that fast power-electronics can bring to the power system, the chapter 2 conducts a reflection on what are the stiffness the system must rely on to operate at sufficient level of reliability and security. Among the fundamental needs, the stiffness of the voltage amplitude and frequency have been supported historically by the physical properties of synchronous generators and their associated controls. The amplitude stiffness is usually quantified by the "short-circuit power", and the frequency stiffness by the "inertia". These properties have been redefined here as grid-forming capability which is required from power-electronics based sources to operate a full power-electronics interfaced power system. Further, the stability of the interconnected system is a basic requirement for reliable operation of multi-sources system. Thus, the ability of electrical sources to stay synchronized and to converge to an acceptable equilibrium following a grid disturbance has been defined as the parallel grid-forming capability. The requirement of grid-forming capability increases the sensitivity of sources to overcurrent, which faces the technological current limitation of VSC-based converters. As a consequence, the VSCs must be tightly controlled in closed-loop and their output current must be actively limited. Active control actions on VSCs modifies the sources behavior which could be different during small-signal disturbances, or large disturbances. The traditional notions of "inertia" and "short-circuit power" are then reconsidered throughout the thesis to take into account the specificity of VSCs on transmission grid.

Synchronization stability of ideal grid-forming sources The chapter 3 specifically outlines the trade-off between synchronization stability between ideal voltage-sources and their sensitivity to transient overloads. It turns out that introducing an elasticity between frequency references and delivered power creates conditions for the convergence of all units toward a common steady-state frequency. This elasticity takes the form a droop coefficient that is completely determined by the desired excursion limits of the frequency variation. The frequency variation dynamic is ruled by a second fundamental parameter, the power filter cut-off frequency. On one hand, high value of the filter cut-off frequency results in rapid convergence to the final state, avoiding large transient overloads or oscillating behavior. On the other hand, the small-signal stability of droop-controlled converters and the frequency stiffness are reinforced by a lower value of the filter cut-off frequency.

For multi-sources system of droop-controlled voltage source, the existence of an equilibrium and the exponential convergence to this equilibrium has been proved in the literature, provided a power filter with sufficient filtering action. The synchronization stability mechanism is easily understood as it resembles to synchronous generators synchronization. The control schemes based on "virtual synchronous machine" are also effective because they are similar to the filtered droop control and can be placed in a droop-like control family. From the author point of view, the terms "virtual synchronous machine" or "virtual inertia" must be carefully employed. Droop-controlled VSCs and synchronous generators share some common behavior for slow and small deviations around an equilibrium, but their characteristic time constants and dynamic damping characteristics are very different. The time constant of synchronous generators is determined by its non-chosen mechanical inertia, whereas the droop control time constant is fixed after the power filter choice for stability reasons. Moreover, some dynamics of the synchronous generators are not desirable and it would be unproductive to blindly introduce them into the VSCs dynamics.

Droop-like controls that improves transients load share exist in the literature. They propose either to fasten or suppress the power filter, or to add a derivative gain on the measured power to adjust the frequency. As the stability of such improved controls have not been proved yet, the author considered rather to treat separately the trade-off between synchronization stability and transient overload. More precisely, the VSC control speed should be increased exclusively when the VSC exceeds its operating limits, which motivates the choice of a threshold virtual impedance to limit the current.

Grid-forming control design for a PWM VSC To meet the technical challenges of building a grid-forming source based on a PWM-VSC, a terminal voltage control in closed loop has been developed in chapter 4. It was found out that the small-signal stability the controlled converter is endangered as soon as it is connected to a grid with sufficient stiffness. To analyze the contribution of the voltage control to the grid instabilities, its external behavior has been represented through its equivalent output impedance. From this closed-loop impedance model, the passivity property is identified a highly desirable feature for grid-connected converters as it is a sufficient condition for stability. The chosen cascaded current and voltage structure has a strong implication in the non-passivity of the output designed closed-loop impedance, due to the time

decoupling constraint between loops. In particular, the feedforward gains, that compensate for the load disturbance, play a major role in the output impedance shape even if their tuning is often skipped in the literature. Passivity based design could overcome the limitation of the classical design of the cascaded-voltage control. It gives a solid theoretical background to develop solutions based on active-damping, or on lead-lag compensation at certain frequencies.

The output impedance model has the advantage to represent the behavior of a controlled converter on all the frequency range. It clearly exhibits the short-term response in its high-frequencies, the steady-state behavior at nominal frequency, as well as potential subsynchronous interactions for lower frequencies. Moreover, the output impedance can easily be observed experimentaly without knowledge of the control structure.

Overcurrent protection The traditional current reference saturation is not applicable in parallel grid-forming control as it opens the cascaded loop structure, resulting in loss of voltage control and of synchronization control. Instead, the TVI, proposed in chapter 5, reacts to overcurrent by dropping the terminal voltage and preventing the current reference from reaching its saturation level. Transient overloads are thus limited and the external regulation is kept effective after a grid-event. The use of the TVI reveals that even if the fast-control of power-electronics is not a system requirement under normal operation of the system, it is useful to prevent damages and to recover after faults and grid events.

Simulations on two and three VSCs systems validate the large-signal stability on hypothetical but realistic networks. The overloaded situation raised new questions for power-electronics based system. Indeed, it turns out that the constantly overloaded sources react by dropping the voltage of the whole system to reach a new stable operating point without large frequency drop. This completely new behavior when the VSC are closed to their limits must be understood to reconsider the defense plan. For example, the frequency-based load shedding might not be effective anymore.

6.2 Perspectives

Beyond the studies presented in this document, certain research directions deserve more investigations to alleviate the remaining challenges.

Output impedance as comparative framework between solution TSOs could take the opportunity to define impedance pattern requirements for either grid-forming of grid-feeding VSC in future grids. However, the external controls also shape the output impedance, especially at subsynchronous frequencies. The non-linearity of the external controls induce complication in the incremental impedance shape determination. The non-linearity is due to a PLL or due to a power calculation. These particularities should be explored.

Voltage control design optimization The design method presented in this thesis could be improved using robust control theory (such as infinite control theory), or through parameters optimization algorithm provided the range of variation of the grid model. In particular, a desired impedance shape or a passivity property could be obtained with optimal determination of the tuning parameters.

Other synchronization techniques In the present thesis, it has been chosen to rely only on droop-control technique to synchronize grid-forming converters during parallel operation. However, PLL-based solutions exist and can be better explored to improve the transient behavior with droop control. Also, non-linear synchronization techniques such as "virtual oscillators" are promising. Finally, information from GPS signal or from remote PMU measurement could be employed to improve the response of the system.

Impact of the DC regulation In the whole thesis, the DC voltage was considered as fixed. The DC bus control impact has often been studied for grid-feeding converters but rarely for grid-forming converters. As commented in section 2.3.2, one could fear that the DC voltage control adversely impacts the AC stability or the way around depending of the choice of compensating the DC voltage variation or not.

Application to MMC devices Some stability issues of the voltage-control are linked to the dynamics limitation of PWM-VSC with high power rates. However, at the transmission level, the biggest converters are now built with the MMC topology. The MMC technology can change its modulated voltage almost instantaneously. Besides, the output filter does not require a capacitor for harmonic filtering in grid-connected applications. Applying parallel grid-forming requirements to MMC devices opens a whole new research area.

Large-system analysis The present study limited the simulation cases to a three-VSC system. The developed solutions are expected to be applied on larger systems. The simulations of such systems could be time-consuming. Efforts should be undertaken to reduce the presented models while keeping the physical meaning of states variables.

Large-signal stability Analytical proof of the large-signal stability of droop-controlled converters with current limitation strategy is missing. Especially, the addition of the TVI changes drastically the VSC behavior depending on whether it operates in normal condition, or under overloaded condition.

Short-circuit fault ride-through As we are convinced that short-circuits would require a specific management action (including the unit disconnection and reconnection), they have not been treated in this thesis. Some simulations of the developed controls with the TVI showed that the current is can be limited during voltage sag, but that the frequency reference from droop control diverges during the very low voltage. The divergence is due to the impossibility to export the desired active power under low voltage, so that the power reference is never reached. One ongoing solution, currently investigated, adapts the power reference with the terminal voltage level to block the angle integration in the droop control during short-circuits.

Migrate Project To address part of the future researches, the EU has recently funded, through the Research and Innovation programme Horizon 2020, a project focused on maximizing the penetration of power electronics devices in the electrical grid. This project, named MIGRATE for “Massive InteGRATion of power Electronic devices”, decomposes the expected issues in subtasks. Amongst the subjects of the overall MIGRATE project, a work package specifically address

a particular aspect, namely the operation of a grid with only Power Electronic (PE) devices. Responses to some of the perspectives mentioned above are defined as the project outputs. A substantial contribution of the Migrate project will be the validation the chosen strategies through an experimental mock-up.

Appendix A

Appendix

A.1 Electromechanical model of a synchronous generator

The analytic model of synchronous generators have been deeply detailed in the literature for power system studies [17] [5] [173]. Main assumptions and equations are recalled here to exhibit later the grid-forming functions of the synchronous generator. The following modeling assumptions hold in all the section:

- The generator is a bipolar synchronous generator,
- The stator windings have a sinusoidal distribution,
- The magnetic saturation is neglected,
- The system is balanced, such that the homopolar components are always equal to 0,
- All the physical quantities are expressed in per-unit, except for the time constants and frequencies.

A.1.1 The mechanical equation

The mechanical equation rules the dynamic rotation of the rotor shaft:

$$\frac{2H}{\omega_n}\frac{d\omega_r}{dt} = \Gamma_m - \Gamma_e \tag{A.1}$$

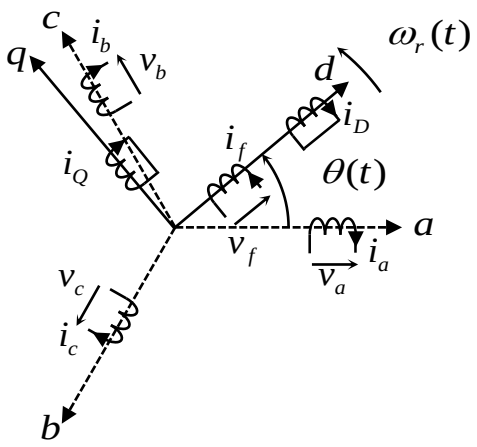

Figure A.1 – Stator windings and rotor windings relative positions.

Where H is the mechanical inertia constant in per-unit, Γ_m the mechanical torque provided by the primary energy sources, Γ_e the electromechanical torque depending on the electrical circuit quantities and ω_r is the instantaneous rotating speed of the rotor defined as the derivative of the angular position θ of the rotor winding axis, relatively to the axis of the first phase stator winding as represented on fig. A.1.

$$\omega_r = \frac{d\theta}{dt} \tag{A.2}$$

A.1.2 The electrical equations

The electrical equations are written in a rotating dq-frame attached with the rotating rotor winding axis, forming a angle θ with the axis of the first stator winding that respects the equation (A.2). The stator electrical quantities are linked by:

$$\begin{cases} v_d = \frac{d\psi_d}{dt} - \psi_q \omega_r - r_a i_d \\ v_q = \frac{d\psi_q}{dt} + \psi_d \omega_r - r_a i_q \end{cases} \tag{A.3}$$

On the rotor, the three circuits of the inductor on the d-axis, and dampers on d and q-axis respect:

$$\begin{cases} v_f = r_f i_f + \frac{d\psi_f}{dt} \\ 0 = r_D i_D + \frac{d\psi_D}{dt} \\ 0 = r_Q i_Q + \frac{d\psi_Q}{dt} \end{cases} \tag{A.4}$$

The equations set is completed by the magnetic relationship coupling the flux and the currents between the rotor and the stator:

$$\begin{bmatrix} \psi_d \\ \psi_f \\ \psi_D \end{bmatrix} = \begin{bmatrix} l_d & m_{af} & m_{aD} \\ m_{af} & l_{ff} & m_{fD} \\ m_{aD} & m_{fD} & l_{DD} \end{bmatrix} = \begin{bmatrix} i_d \\ i_f \\ i_D \end{bmatrix} \tag{A.5}$$

$$\begin{bmatrix} \psi_q \\ \psi_Q \end{bmatrix} = \begin{bmatrix} l_q & m_{aQ} \\ m_{aQ} & l_{QQ} \end{bmatrix} = \begin{bmatrix} i_q \\ i_Q \end{bmatrix} \tag{A.6}$$

Where l_d and l_q denote the synchronous self inductances of the stator along each axis ($l_d = l_q$ if the saliency of the rotor is neglected), l_{ii} denote the self inductance of the i-winding and, m_{ij} the mutual inductance between the i-winding and the j-winding.

The electromechanical torque is deduced after the instantaneous expression of the active power delivered at the stator terminal:

$$\begin{aligned} p_e &= v_d i_d + v_q i_q, \\ p_e &= \left(i_d \frac{d\psi_d}{dt} + i_q \frac{d\psi_q}{dt} \right) + \left(\psi_d i_q - \psi_q i_d \right) \omega_r - r_a \left(i_d^2 + i_q^2 \right). \end{aligned} \tag{A.7}$$

In the second member of (A.7), the first term corresponds to the variation of the magnetic energy stored in the magnetic circuits, the second term corresponds to the mechanical power transformed into electrical power, and the third represents the electrical losses in the stator circuits. The electromechanical torque is then (in per-unit of $\Gamma_{base} = \frac{S_{base}}{\omega_n}$):

$$\Gamma_e = \left(\psi_d i_q - \psi_q i_d \right) \omega_n \tag{A.8}$$

A.1.3 Steady-state representation of the synchronous generators at fixed speed

In steady-state, the electrical equations (A.3) and (A.4), and magnetic eq. (A.5) and (A.6) simplify in :

$$\begin{cases} v_d = -\psi_q \omega_0 - r_a i_d \\ v_q = +\psi_d \omega_0 - r_a i_q \\ v_f = r_f i_f \end{cases} \tag{A.9}$$

$$\begin{cases} \psi_d = -l_d i_d + m_{af} i_f \\ \psi_q = -l_q i_q \end{cases} \tag{A.10}$$

At no load, in steady-state, eq. (A.10) and (A.9) give:

$$\begin{cases} v_d = 0 \\ v_q = m_{af} \omega_0 i_f \end{cases} \tag{A.11}$$

As seen on eq. (A.11), the voltage terminal at no load is sinusoidal of frequency ω_0 and amplitude of $m_{af}\omega_0 i_f$. In other words, the synchronous generator with a fixed rotation speed is a sinusoidal voltage source with a controllable voltage amplitude in steady-state, depending on the field current i_f. The no-load terminal voltage is called the electromotive force (emf), e_{emf}:

$$e_{emf} = m_{af} \omega_0 i_f \tag{A.12}$$

With a load, the terminal voltages are then:

$$\begin{cases} v_d = l_q \omega_0 i_q - r_a i_d \\ v_q = e_{emf} - l_d \omega_0 i_d - r_a i_q \end{cases} \tag{A.13}$$

From (A.13) worth noting that the load current deeply affects the terminal voltage magnitude in steady-state, as the reactance value is around $l_d\omega_0 \approx l_q\omega_0 = 2\,p.u.$ when ω_0 is closed to the nominal frequency ω_n. Maintaining the terminal voltage in an acceptable range requires an adaptation of the current field i_f to the load level through a slow acting voltage control.

In loaded conditions, an electromechanical torque is created, which impacts the rotor speed by the mechanical law (A.1). To maintain a constant frequency, the mechanical power represented by the torque Γ_m must be adapted through a rotor speed control. The electromechanical torque, induced by the load, can easily be derived in steady-state by representing the electrical value in a complex phasor diagram. The vector corresponding to the e.m.f. e_{emf} forms an angle difference δ with the terminal voltage vector. This angle δ is called the internal angle. Neglecting saliency, so that $l_d = l_q$, the steady-state couple expression is:

$$\Gamma_e = \frac{E_{emf} V}{l_d \omega_0} sin(\delta) \tag{A.14}$$

Table A.1 – Typical parameters of synchronous generators with round pole in power system [5]

Parameters	Value
r_a	0.003 p.u.
$l_d\omega_n$	2 p.u.
$l_q\omega_n$	2 p.u.
T'_d	1.2 s
T''_d	0.04 s
T'_q	0.6 s
T''_q	0.04 s
T'_{d0}	10 s
T''_{d0}	0.05 s
T'_{q0}	2 s
T''_{q0}	0.4 s
T_D	0.02 s

Where v is the terminal voltage magnitude $V = \sqrt{v_d^2 + v_q^2}$.

Before reaching the long-term steady-state, the behavior of the synchronous generator depends on its electrical transient equation.

A.1.4 Transient electrical representation of the synchronous generators at fixed speed

At fixed speed, the electrical and magnetic equations are linear and can be studied in Laplace domain.

From equations (A.3), (A.4), (A.5), (A.6) in Laplace domain, and after some computation efforts detailed in [17] [5], it comes:

$$\begin{cases} \psi_d = -l_d(s)i_d + g(s)v_f \\ \psi_q = -l_q(s)i_q \end{cases} \tag{A.15}$$

Where $l_d(s)$, and $l_q(s)$ are the direct and quadrature frequency varying inductances, and $g(s)$ the voltage gain transfer function. Using traditional parameters of synchronous generators listed in table A.1, their expressions are:

$$\begin{aligned} l_d(s) &= l_d \frac{\left(1+T'_d s\right)\left(1+T''_d s\right)}{\left(1+T'_{d0} s\right)\left(1+T''_{d0} s\right)}, \\ l_q(s) &= l_q \frac{\left(1+T'_q s\right)\left(1+T''_q s\right)}{\left(1+T'_{q0} s\right)\left(1+T''_{q0} s\right)}, \\ g(s) &= \frac{maf}{r_f} \frac{1+T_D}{\left(1+T'_{d0} s\right)\left(1+T''_{d0} s\right)}. \end{aligned} \tag{A.16}$$

$T'_d, T''_d, T'_{d0}, T''_{d0}$ are characteristic time constant related of the synchronous generators related to its external behavior as viewed from terminal. The time constants respect:

$$\begin{aligned} T_D < T''_d < T''_{d0} < T'_d < T'_{d0} \\ T''_q < T''_{q0} < T'_q < T'_{q0} \end{aligned} \tag{A.17}$$

And more specifically from table A.1:

$$\begin{aligned} T''_d << T'_d \\ T''_{d0} << T'_{d0} \end{aligned} \tag{A.18}$$

A.2 Impedance-based Nyquist criterion

The impedance stability criterion, first proposed by [157] for dc power electronic systems, relates the system stability to the ratio between the source and load impedances. The interest of the method for grid-connected grid-following inverters has been raised in [158] arguing for its simplicity over system poles in case of high-order interconnected system. In this section, the impedance stability criterion is adapted to voltage-controlled grid-forming converter designed previously.

From the equation (4.50), the interconnected system is stable if and only if the ratio of the controlled VSC output impedance $Z_{out}(s)$ to the rest of the system dynamics $Z_{src}(s)$ fulfills the Nyquist criterion. Applied to complex transfer functions, the Nyquist curve of the ratio $Z_{out}(j\omega)$ to $Z_{src}(j\omega)$, must be drawn from on positive and negative frequencies.

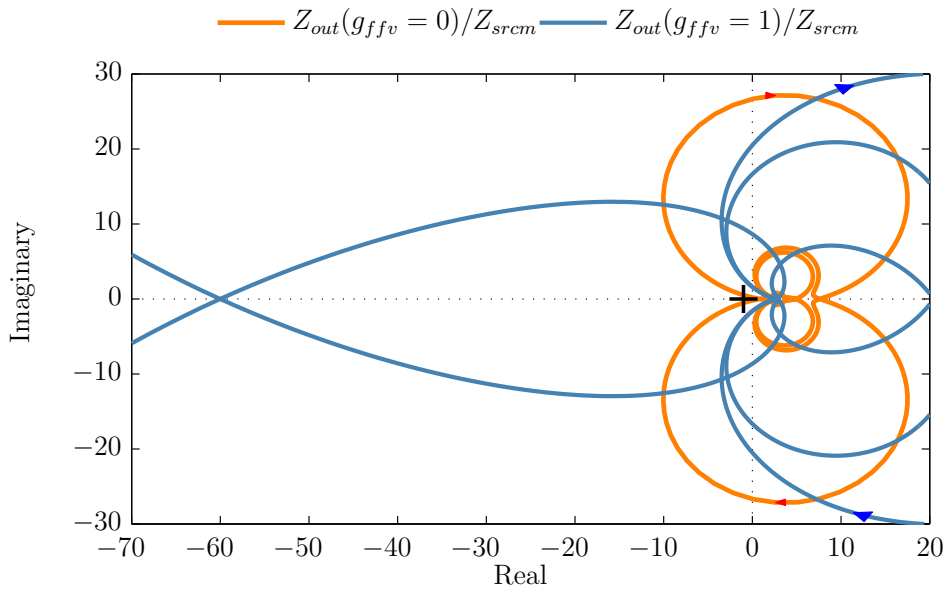

Figure A.2 – Nyquist diagram of the ratio $Z_{out}(j\omega)$ to $Z_{srcm}(j\omega)$ for $g_{ffv} = 0$ and $g_{ffv} = 1$.

Application to the stability of a grid-connected and voltage-controlled VSC As an application example, the output impedance of the voltage-controlled VSC $Z_{out}(j\omega)$ is compared to the minimal series impedance grid impedance $Z_{srcm}(s)$ defined previously. The Nyquist curve of the impedances ratio is plotted on fig. A.2 for two different values of the feedforward gain g_{ffv}.

In the case where $g_{ffv} = 1$, the Nyquist curve does encircle -1 (marked by the black cross), confirming the unstable situation. In the case where $g_{ffv} = 0$, the Nyquist curve does not encircle -1 (marked by the black cross), leading to a stable situation.

Conclusion on the impedance-based stability criterion Although the Nyquist criterion on output admittance of grid-feeding VSC has already been developed in [158], we showed here that it can be extended to grid-forming VSC when applied to the equivalent output impedance.

The Nyquist criterion to the ratio of the voltage-controlled VSC to the minimal grid-impedance, gives the same conclusion on stability than poles plot in section 4.4. The grid impedance can successfully by replaced by a more complex impedance shape, as the output impedance of an other grid-forming VSC as demonstrated in [165].

Bibliography

[1] NREL. Renewable Electricity Futures Study. *www.nrel.gov/analysis/re_futures*, 2012.

[2] ADEME. Un mix électrique 100% renouvelable ? *www.ademe.fr/mix-electrique-100-renouvelable-analyses-optimisations*, 2015.

[3] Thomas Ackermann, Thibault Prevost, Vijay Vittal, Andrew J. Roscoe, Julia Matevosyan, and Nicholas Miller. A Future without Inertia is Closer than you Think. *IEEE Power & Energy Magazine (to be published)*.

[4] I Erlich, B Paz, M Koochack Zadeh, S Vogt, C Buchhagen, C Rauscher, A Menze, and J Jung. Overvoltage Phenomena in Offshore Wind Farms Following Blocking of the HVDC Converter. pages 1–5, 2016.

[5] Philippe Barret. *Régimes transitoires des machines tournantes électriques*. Eyrolles, 1987.

[6] P. L. Francos, S. S. Verdugo, H. F. Alvarez, S. Guyomarch, and J. Loncle. INELFE - Europe's first integrated onshore HVDC interconnection. In *Proc. 2012 IEEE Power and Energy Society General Meeting, San Diego, CA*, pages 1–8. IEEE, jul 2012.

[7] Frede Blaabjerg, Remus Teodorescu, Senior Member, Marco Liserre, Adrian V Timbus, and Student Member. Overview of Control and Grid Synchronization for Distributed Power Generation Systems. 53(5):1398–1409, 2006.

[8] Karel De Brabandere. *Voltage and frequency droop control in low voltage grids by distributed generators with inverter front-end*. PhD thesis, Phd Thesis, Katholieke Universiteit Leuven, 2006.

[9] Joan Rocabert, Alvaro Luna, Frede Blaabjerg, and Pedro Rodríguez. Control of power converters in AC microgrids. *IEEE Transactions on Power Electronics*, 27(11):4734–4749, nov 2012.

[10] Ye Wang, Vera Silva, and Miguel Lopez-Botet-Zulueta. Impact of high penetration of variable renewable generation on frequency dynamics in the continental Europe interconnected system. *IET Renewable Power Generation*, 10(1):10–16, 2014.

[11] Mengran Yu, Andrew J. Roscoe, Campbell D. Booth, Adam Dysko, Richard Ierna, Jiebei Zhu, and Helge Urdal. Use of an inertia-less virtual synchronous machine within future power networks with high penetrations of converters. *Power Systems Computation Conference (PSCC 2016)*, 2016.

[12] H2020 Migrate Project: Deliverable 1.1. Report on systemic issues. *www.h2020-migrate.eu/downloads.html*, 2016.

[13] Ye Wang, Gauthier Delille, Herman Bayem, Xavier Guillaud, and Bruno Francois. High wind power penetration in isolated power systems-assessment of wind inertial and primary frequency responses. *IEEE Transactions on Power Systems*, 28(3):2412–2420, 2013.

[14] Gauthier Delille, Bruno François, and Gilles Malarange. Dynamic Frequency Control Support by Energy Storage to Reduce the Impact of Wind and Solar Generation on Isolated Power System ' s Inertia. *IEEE Transactions on Sustainable Energy*, 3(4):931–939, 2012.

[15] RTE. Mémento de la sûreté du système électrique. *www.rte-france.com*, 2004.

[16] RTE. *Documentation technique de référence*. 2017.

[17] Prabha Kundur, NJ Balu, and MG Lauby. *Power system stability and control*, volume 23. McGraw-hill New York, 1994.

[18] Julian Freytes, Gilbert Bergna, Jon Are Suul, Salvatore D'Arco, Francois Gruson, Frederic Colas, Hani Saad, and Xavier Guillaud. Improving Small-Signal Stability of an MMC with CCSC by Control of the Internally Stored Energy. *IEEE Transactions on Power Delivery*, 8977(c):1–10, 2017.

[19] Henri Foch, François Forest, and Thierry Meynard. Onduleurs de tension, structures, principes, applications. *Techniques de l'ingénieur*, d3176, 1998.

[20] Cornelis a. Plet and Timothy C. Green. A method of voltage limiting and distortion avoidance for islanded inverter-fed networks under fault. In *Power Electronics and Applications (EPE 2011), Proceedings of the 2011-14th European Conference on*, pages 1–8, 2011.

[21] Amir H. Etemadi, Edward J. Davison, and Reza Iravani. A decentralized robust control strategy for multi-DER microgrids; part I: fundamental concepts. *IEEE Transactions on Power Delivery*, 27(4):1843–1853, oct 2012.

[22] Amir H. Etemadi, Edward J. Davison, and Reza Iravani. A Decentralized Robust Control Strategy for Multi-DER Microgrids;Part II: Performance Evaluation, 2012.

[23] Amir H. Etemadi, Edward J. Davison, and Reza Iravani. A Generalized Decentralized Robust Control of Islanded Microgrids, 2014.

[24] Mohammad Sadegh Golsorkhi, Dylan Dah Chuan Lu, and Josep M. Guerrero. A GPS-based decentralized control method for islanded microgrids. *IEEE Transactions on Power Electronics*, 32(2):1615–1625, 2017.

[25] Mukul C. Chandorkar, Deepakraj M. Divan, and Rambabu Adapa. Control of parallel connected inverters in standalone ac supply systems. *IEEE Transactions on Industry Applications*, 29(1):136–143, 1993.

[26] Mukul C. Chandorkar. *Distributed Uninterruptible Power Supply Systems*. PhD thesis, University of Wisconsin–Madison., 1995.

[27] Josep M Guerrero, Luis Garcia de Vicuna, José Matas, Miguel Castilla, and Jaume Miret. A wireless controller to enhance dynamic performance of parallel inverters in distributed generation systems. *IEEE Transactions on Power Electronics*, 19(5):1205–1213, sep 2004.

[28] Josep M Guerrero, Luis García De Vicuña, José Matas, and Miguel Castilla. Output impedance design of parallel-connected UPS inverters with wireless load-sharing control. *IEEE Transactions on Industrial Electronics*, 52(4):1126–1135, 2005.

[29] Yun Wei Li and Ching-Nan Kao. An accurate power control strategy for power-electronics-interfaced distributed generation units operating in a low-voltage multibus microgrid. *IEEE Transactions on Power Electronics*, 24(12):2977–2988, 2009.

[30] Karel De Brabandere, Bruno Bolsens, Jeroen Van Den Keybus, Achim Woyte, Johan Driesen, and Ronnie Belmans. A voltage and frequency droop control method for parallel inverters. *IEEE Transactions on Power Electronics*, 22(4):1107–1115, 2007.

[31] Y. Mohamed and E.F. El-Saadany. Adaptive decentralized droop controller to preserve power sharing stability of paralleled inverters in distributed generation microgrids. *IEEE Transactions on Power Electronics*, 23(6):2806–2816, nov 2008.

[32] Ritwik Majumder, Arindam Ghosh, Gerard Ledwich, and Firuz Zare. Angle droop versus frequency droop in a voltage source converter based autonomous microgrid. In *Proc. IEEE PES General Meeting*, number July, pages 1–8, 2009.

[33] Robert H Lasseter and Paolo Piagi. Microgrid: A Conceptual Solution. (June), 2004.

[34] A. Engler and N. Soultanis. Droop control in LV-grids. In *2005 International Conference on Future Power Systems*, pages 6 pp.–6. IEEE, 2005.

[35] J A Peças Lopes, C L Moreira, and A G Madureira. Defining control strategies for MicroGrids islanded operation. *IEEE Transactions on Power Systems*, 21(2):916–924, 2006.

[36] F. Katiraei and M Reza Iravani. Power Management Strategies for a Microgrid With Multiple Distributed Generation Units. *IEEE Transactions on Power Systems*, 21(4):1821–1831, nov 2006.

[37] F. Katiraei, M.R. Iravani, and P.W. Lehn. Small-signal dynamic model of a micro-grid including conventional and electronically interfaced distributed resources, 2007.

[38] Robert Lasseter and Paolo Piagi. Control and Design of Microgrid Components. *PSERC Publication 06*, 03, 2006.

[39] Alaa Mohd, Egon Ortjohann, Danny Morton, and Osama Omari. Review of control techniques for inverters parallel operation. *Electric Power Systems Research*, 80(12):1477–1487, dec 2010.

[40] Josep M Guerrero, Mukul C. Chandorkar, Tzung-Lin Lee, and Poh Chiang Loh. Advanced control architectures for intelligent microgrids—Part I: Decentralized and hierarchical control. *IEEE Transactions on Industrial Electronics*, 60(4):1254–1262, apr 2013.

[41] Josep M Guerrero, Poh Chiang Loh, Tzung-Lin Lee, and Mukul C. Chandorkar. Advanced Control Architectures for Intelligent Microgrids—Part II: Power Quality, Energy Storage, and AC/DC Microgrids. *IEEE Transactions on Industrial Electronics*, 60(4):1263–1270, apr 2013.

[42] Johannes Schiffer, Daniele Zonettib, Romeo Ortegab, Aleksandar Stankovicc, Tevfik Sezid, and Jorg Raischa. Modeling of microgrids—from fundamental physics to phasors and voltage sources. pages 1–15, 2015.

[43] Allal M Bouzid, Josep M Guerrero, Ahmed Cheriti, Mohamed Bouhamida, and Pierre Sicard. A Survey on Control of Electric Power Distributed Generation Systems for Microgrid Applications. 2015.

[44] E.A.A. Coelho, P.C. Cortizo, and P.F.D. Garcia. Small-signal stability for parallel-connected inverters in stand-alone AC supply systems. *IEEE Transactions on Industry Applications*, 38(2):533–542, aug 2002.

[45] E. Barklund, Nagaraju Pogaku, Milan Prodanovic, C. Hernandez-Aramburo, and Timothy C. Green. Energy management in autonomous microgrid using stability-constrained droop control of inverters. *IEEE Transactions on Power Electronics*, 23:2346–2352, 2008.

[46] Timothy C. Green and M. Prodanović. Control of inverter-based micro-grids. *Electric Power Systems Research*, 77:1204–1213, 2007.

[47] Poh Chiang Loh, Michael John Newman, Daniel Nahum Zmood, and Donald Grahame Holmes. A comparative analysis of multiloop voltage regulation strategies for single and three-phase UPS systems. *IEEE Transactions on Power Electronics*, 18:1176–1185, 2003.

[48] Poh Chiang Loh and D.G. Donald Grahame Holmes. Analysis of multiloop control strategies for LC/CL/LCL-filtered voltage-source and current-source inverters. *IEEE Transactions on Industry Applications*, 41(2):644–654, 2005.

[49] Irvin J Balaguer, Qin Lei, Shuitao Yang, and Uthane Supatti. Control for grid-connected and intentional islanding operations of distributed power generation. *IEEE Transactions on Industrial Electronics*, 58(1):147–157, 2011.

[50] Jinwei He and Yun Wei Li. Analysis, design, and implementation of virtual impedance for power electronics interfaced distributed generation. *IEEE Transactions on Industry Applications*, 47(6):2525–2538, nov 2011.

[51] Alireza Kahrobaeian. *Modeling, Analysis and Control of Single and Multiple Micro-grid-Based Active Distribution Grids*. PhD thesis, University of Alberta, 2014.

[52] Yun Wei Li and D. Mahinda Vilathgamuwa. Design , Analysis , and Real-Time Testing of a Controller for Multibus Microgrid System. *IEEE Transactions on Power Electronics*, 19(5):1195–1204, 2004.

[53] Seyed Mahdi Ashabani and Yasser Abdel Rady Ibrahim Mohamed. A flexible control strategy for grid-connected and islanded microgrids with enhanced stability using nonlinear microgrid stabilizer. *IEEE Transactions on Smart Grid*, 3:1291–1301, 2012.

[54] Alireza Kahrobaeian and Yasser Abdel Rady Ibrahim Mohamed. Interactive distributed generation interface for flexible micro-grid operation in smart distribution systems. *IEEE Transactions on Sustainable Energy*, 3(2):295–305, 2012.

[55] M. Amin Zamani, Amirnaser Yazdani, and Tarlochan S. Sidhu. A control strategy for enhanced operation of inverter-based microgrids under transient disturbances and network Faults. *IEEE Transactions on Power Delivery*, 27(4):1737–1747, oct 2012.

[56] Jaehong Kim, Josep M JM Guerrero, Pedro Rodriguez, and Remus Teodorescu. Mode adaptive droop control with virtual output impedances for an inverter-based flexible AC microgrid. *IEEE Transactions on Power Electronics*, 26(3):689–701, 2011.

[57] Fang Gao and M.R. Iravani. A control strategy for a distributed generation unit in grid-connected and autonomous modes of operation. *IEEE Transactions on Power Delivery*, 23(2):850–859, apr 2008.

[58] Nagaraju Pogaku, Milan Prodanovic, and Timothy C. Green. Modeling, analysis and testing of autonomous operation of an inverter-based microgrid. *IEEE Transactions on Power Electronics*, 22(2):613–625, mar 2007.

[59] Shivkumar V. Iyer, Madhu N. Belur, and Mukul C. Chandorkar. A generalized computational method to determine stability of a multi-inverter microgrid. *IEEE Transactions on Power Electronics*, 25(9):2420–2432, 2010.

[60] Nathaniel Bottrell, Milan Prodanovic, and Timothy C. Green. Dynamic Stability of a Microgrid with an Active Load. *IEEE Transactions on Power Electronics*, 28(11):5107–5119, 2013.

[61] D. Mahinda Vilathgamuwa, Poh Chiang Loh, and Yun Wei Li. Protection of microgrids during utility voltage sags. *IEEE Transactions on Industrial Electronics*, 53(5):1427–1436, 2006.

[62] Fouad Salha, Frederic Colas, and Xavier Guillaud. Virtual resistance principle for the overcurrent protection of PWM voltage source inverter. In *2010 IEEE PES Innovative Smart Grid Technologies Conference Europe (ISGT Europe)*, pages 1–6. IEEE, oct 2010.

[63] Nathaniel Bottrell and Timothy C. Green. Comparison of Current-Limiting Strategies During Fault Ride-Through of Inverters to Prevent Latch-Up and Wind-Up. *IEEE Transactions on Power Electronics*, 29(7):3786–3797, jul 2014.

[64] Andrew D. Paquette and Deepak M. Divan. Virtual impedance current limiting for inverters in microgrids with synchronous generators. *IEEE Transactions on Industry Applications*, 51(2):1630–1638, mar 2015.

[65] Xiaonan Lu, Jianhui Wang, Josep Guerrero, and Dongbo Zhao. Virtual Impedance Based Fault Current Limiters for Inverter Dominated AC Microgrids. *IEEE Transactions on Smart Grid*, 3053(c):1–1, 2016.

[66] Lidong Zhang. *Modeling and control of VSC-HVDC links connected to weak AC systems*. PhD thesis, Royal Institute of Technology, Stockholm, Sweden, 2010.

[67] Khaled Mohammad Alawasa and Yasser Abdel-Rady I. Rady I Mohamed. Impedance and damping characteristics of grid-connected VSCs with power synchronization control strategy. *IEEE Transactions on Power Systems*, 30(2):952–961, mar 2015.

[68] Martyn Durrant, Herbert Wemer, and Keith Abbottt. Robust Control of a VSC HVDC Terminal Attached to a Weak AC System. *Control Applications, 2003. CCA 2003. Proceedings of 2003 IEEE Conference on*, pages 173–177, 2003.

[69] D. Jovcic, L.a. Lamont, and L. Xu. VSC transmission model for analytical studies. *2003 IEEE Power Engineering Society General Meeting (IEEE Cat. No.03CH37491)*, 3:1–6, 2003.

[70] Lennart Harnefors, Massimo Bongiorno, and Stefan Lundberg. Input-admittance calculation and shaping for controlled voltage-source converters. *IEEE Transactions on Industrial Electronics*, 54(6):3323–3334, 2007.

[71] Mauricio Cespedes and Jian Sun. Impedance Modeling and Analysis of Grid-Connected Three-Phase Converters. *IEEE Transactions on Power Electronics*, 29(3):1254–1261, 2014.

[72] Dong Dong, Bo Wen, Dushan Boroyevich, Paolo Mattavelli, and Yaosuo Xue. Analysis of phase-locked loop low-frequency stability in three-phase grid-connected power converters converters considering impedance interactions. *IEEE Transactions on Industrial Electronics*, 62(1):310–321, jan 2015.

[73] Seyed Mahdi Ashabani, Francisco Freijedo, Saeed Golestan, and Senior Member. Inducverters : PLL-Less Converters with Auto- Synchronization and Emulated Inertia Capability. *IEEE Transactions on Smart Grid*, 2015.

[74] Seyed Mahdi Ashabani, Yasser Abdel-Rady Ibrahim Mohamed, Mojtaba Mirsalim, and Mohammad Aghashabani. Multivariable Droop Control of Synchronous Current Converters in Weak Grids/Microgrids With Decoupled dq-Axes Currents. *IEEE Transactions on Smart Grid*, 6(4):1610–1620, jul 2015.

[75] Bo Wen, Dushan Boroyevich, Rolando Burgos, Paolo Mattavelli, and Zhiyu Shen. Analysis of D-Q small-signal impedance of grid-tied inverters. *IEEE Transactions on Power Electronics*, 31(1):675–687, 2016.

[76] George C. Konstantopoulos, Qing Chang Zhong, and Wen Long Ming. PLL-Less Nonlinear Current-Limiting Controller for Single-Phase Grid-Tied Inverters: Design, Stability Analysis, and Operation under Grid Faults. *IEEE Transactions on Industrial Electronics*, 63(9):5582–5591, 2016.

[77] Salvatore D'Arco and Jon Are Suul. Virtual synchronous machines - Classification of implementations and analysis of equivalence to droop controllers for microgrids. *2013 IEEE Grenoble Conference PowerTech, POWERTECH 2013*, 2013.

[78] Salvatore D'Arco and Jon Are Suul. Equivalence of virtual synchronous machines and frequency-droops for converter-based microgrids. *IEEE Transactions on Smart Grid*, 5(1):394–395, jan 2014.

[79] Salvatore D'Arco, Jon Are Suul, and Olav B. Fosso. A Virtual Synchronous Machine implementation for distributed control of power converters in SmartGrids. *Electric Power Systems Research*, 122:180–197, 2015.

[80] Toshinobu Shintai, Yushi Miura, and Toshifumi Ise. Oscillation damping of a distributed generator using a virtual synchronous generator. *IEEE Transactions on Power Delivery*, 29(2):668–676, 2014.

[81] Yan Du, Josep M. Guerrero, Liuchen Chang, Jianhui Su, and Meiqin Mao. Modeling , Analysis , and Design of a Frequency- Droop-Based Virtual Synchronous Generator for Microgrid Applications. 2013.

[82] Jia Liu, Yushi Miura, Hassan Bevrani, and Toshifumi Ise. Enhanced virtual synchronous generator control for parallel inverters in microgrids. *IEEE Transactions on Smart Grid*, 7401122(c):1–10, 2016.

[83] Qing-chang Zhong and George Weiss. Synchronverters : Inverters that mimic synchronous generators. *IEEE Transactions on Industrial Electronics*, 58(4):1259–1267, 2011.

[84] Lidong Zhang, Lennart Harnefors, Senior Member, and Hans-Peter Nee. Modeling and control of VSC-HVDC links connected to island systems. *IEEE Transactions on Power Systems*, 26(2):783–793, 2011.

[85] K Visscher and S. W. H. De Haan. Virtual synchronous machines (VSG's) for frequency stabilisation in future grids with a significant share of decentralized generation. In *CIRED SmartGrids for Distribution*, number 0118, pages 1–4, 2008.

[86] M. P N Van Wesenbeeck, S. W H De Haan, P. Varela, and K. Visscher. Grid tied converter with virtual kinetic storage. In *IEEE Bucharest PowerTech: Innovative Ideas Toward the Electrical Grid of the Future*, 2009.

[87] T. Vu Van, K Visscher, J Diaz, V Karapanos, A Woyte, M Albu, J Bozelie, T Loix, and D Federenciuc. Virtual synchronous generator: An element of future grids. In *2010 IEEE PES Innovative Smart Grid Technologies Conference Europe (ISGT Europe)*, pages 1–7. IEEE, oct 2010.

[88] Miguel A Torres and Luiz a. C. Lopes. A Virtual Synchronous Machine to Support Dynamic Frequency Control in a Mini-Grid That Operates in Frequency Droop Mode. *Energy and Power Engineering*, 05(03):259–265, 2013.

[89] Miguel A Torres and Luiz A C Lopes. Virtual Synchronous Generator: A Control Strategy to Improve Dynamic Frequency Control in Autonomous Power Systems. *Energy and Power Engineering*, 05(02):32–38, 2013.

[90] Johan Morren. *Grid support by power electronic converters of Distributed Generation units*. PhD thesis, 2006.

[91] Hans-peter Beck and Ralf Hesse. Virtual synchronous machine. In *9th International Conference on Electrical Power Quality and Utilisation, EPQU*, 2007.

[92] Yong Chen, Ralf Hesse, Dirk Turschner, and Hans-peter Beck. Comparison of methods for implementing virtual synchronous machine on inverters. In *nternational Conference on Renewable Energies and Power Quality (ICREPQ'12)*, Santiago de Compostela, Spain, 2012.

[93] I. Erlich, A. Korai, T. Neumann, M. Koochack Zadeh, S. Vogt, C. Buchhagen, C. Rauscher, A. Menze, and J. Jung. New Control of Wind Turbines Ensuring Stable and Secure Operation Following Islanding of Wind Farms. *IEEE Transactions on Energy Conversion*, 8969(c):1–9, 2017.

[94] T Neumann, I Erlich, B Paz, A Korai, M Koochack Zadeh, S Vogt, C Buchhagen, C Rauscher, A Menze, and J Jung. Novel Direct Voltage Control by Wind Turbines. pages 1–5, 2016.

[95] Qing-Chang Zhong and Tomas Hornik. *Control of Power Inverters In Renewable Energy and Smart Grid Integration.* JohnWiley & Sons IEEE press, 2013.

[96] V Mariani, F Vasca, and Josep M Guerrero. Analysis of droop controlled parallel inverters in islanded microgrids. In *ENERGYCON 2014 - IEEE International Energy Conference*, pages 1304–1309, 2014.

[97] Nathaniel Bottrell. *Small-signal Analysis of Active Loads and Large-signal Analysis of Faults in Inverter Interfaced Microgrid Applications.* PhD thesis, Imperial College London, 2014.

[98] Amr Ahmed A Radwan and Yasser Abdel Rady I Mohamed. Analysis and active-impedance-based stabilization of voltage-source- rectifier loads in grid-connected and isolated microgrid applications. *IEEE Transactions on Sustainable Energy*, 4(3):563–576, 2013.

[99] Remus Teodorescu, Marco Liserre, Pedro Rodriguez, and Pedro Rodríguez. *Grid Converter For Photovoltaix and Wind Power System.* 2011.

[100] Ahmadreza Tabesh and M Reza Iravani. Multivariable dynamic model and robust control of a voltage-source converter for power system applications. *IEEE Transactions on Power Delivery*, 24:462–471, 2009.

[101] K. De Brabandere, Bruno Bolsens, J. Van Den Keybus, J. Driesen, M Prodanovic, and R Belmans. Small-signal stability of grids with distributed low-inertia generators taking into account line phasor dynamics. In *18th International Conference and Exhibition on Electricity Distribution (CIRED 2005)*, volume 2005, pages v4–75–v4–75. IEE, 2005.

[102] Xiaoqiang Guo, Zhigang Lu, Baocheng ; Wang, Xiaofeng Sun, Lei Wang, and Josep M Guerrero. Dynamic phasors-based modeling and stability analysis of droop-controlled

inverters for microgrid applications dynamic phasors based modeling and stablity analysis of droop-controlled inverters for microgrid applications. *IEEE Transactions on Smart Grid*, 5(6):2980–2987, 2014.

[103] Lidong Zhang, Lennart Harnefors, and Hans-Peter Nee. Power-synchronization control of grid-connected voltage-source converters. *IEEE Transactions on Power Systems*, 25(2):809–820, may 2010.

[104] Xianwei Wang, Fang Zhuo, Haiping Guo, Liang Meng, Meijuan Yang, and Jinjun Liu. Stability analysis of droop control for inverter using dynamic phasors method. In *IEEE Energy Conversion Congress and Exposition: Energy Conversion Innovation for a Clean Energy Future, ECCE 2011, Proceedings*, pages 739–742, 2011.

[105] Valerio Mariani, Francesco Vasca, Juan C. Vasquez, and Josep M. Guerrero. Model Order Reductions for Stability Analysis of Islanded Microgrids With Droop Control. *IEEE Transactions on Industrial Electronics*, 62(7):4344–4354, 2015.

[106] Lidong Zhang, Hans-peter Nee, and Lennart Harnefors. Analysis of Stability Limitations of a VSC-HVDC Link Using Power-Synchronization Control Lidong. *IEEE Transactions on Power Systems*, 26(3):1326–1337, 2011.

[107] Lidong Zhang and Hans Peter Nee. Multivariable feedback design of VSC-HVDC connected to weak AC systems. *2009 IEEE Bucharest PowerTech: Innovative Ideas Toward the Electrical Grid of the Future*, 1(1):1–8, 2009.

[108] Josep M. Guerrero, Juan Carlos Vasquez, Jóse Matas, Miguel Castilla, L.G. de Vicuna, Juan C. Vásquez, Jóse Matas, Miguel Castilla, and Lui García de Vicuna. Control strategy for flexible microgrid based on parallel line-interactive UPS systems. *IEEE Transactions on Industrial Electronics*, 56(3):726–736, 2009.

[109] Ritwik Majumder, Student Member, Balarko Chaudhuri, and Arindam Ghosh. Improvement of Stability and Load Sharing in an Autonomous Microgrid Using Supplementary Droop Control Loop. *IEEE Transactions on Power Systems*, 25(2):796–808, 2010.

[110] Lennart Harnefors, Lidong Zhang, and Massimo Bongiorno. Frequency-domain passivity-based current controller design. *IET Power Electronics*, 1(4):455–465, 2008.

[111] Ernane Antonio Alves Coelho, P.C. Cortizo, and P.F.D. Garcia. Small signal stability for single phase inverter connected to stiff AC system. In *Industry Applications Conference, 1999. Thirty-Fourth IAS Annual Meeting. Conference Record of the 1999 IEEE*, volume 4, pages 2180–2187, 1999.

[112] Seyed Mahdi Ashabani, Yasser Abdel-Rady I. Mohamed, Senior Member, Mahdi Ashabani, Yasser Abdel-Rady I. Mohamed, and Senior Member. Integrating VSCs to weak grids by nonlinear power damping controller with self-synchronization capability. *IEEE Transactions on Power Systems*, 29(2):805–814, mar 2014.

[113] Josep M. Guerrero, Juan C. Vasquez, José Matas, Luis García de Vicuna, and Miguel Castilla. Hierarchical Control of Droop-Controlled AC and DC Microgrids—A General Approach Toward Standardization, 2011.

[114] Josep M Guerrero, José Matas, Luis García De Vicuña, and Miguel Castilla. Wireless-Control Strategy for Parallel Operation of Distributed-Generation Inverters. *IEEE Transactions on Industrial Electronics*, 53(5):1461–1470, 2006.

[115] Philip J. Hart, Austin Nelson, R. H. Lasseter, and T. M. Jahns. Effect of power measurement filter properties on CERTS microgrid control performance. *2015 IEEE 6th International Symposium on Power Electronics for Distributed Generation Systems, PEDG 2015*, 00(1), 2015.

[116] MA Abusara, SM Sharkh, and JM Guerrero. Improved droop control strategy for grid-connected inverters. *Sustainable energy, grids and*, 2015.

[117] Salvatore D'Arco, Jon Are Suul, and Olav B. Fosso. Small-signal modeling and parametric sensitivity of a virtual synchronous machine in islanded operation. *International Journal of Electrical Power & Energy Systems*, 72:3–15, nov 2015.

[118] Jia Liu, Yushi Miura, and Toshifumi Ise. Comparison of Dynamic Characteristics between Virtual Synchronous Generator and Droop Control in Inverter-Based Distributed Generators. *IEEE Transactions on Power Electronics*, 31(5):3600–3611, 2016.

[119] Ritwik Majumder. Some Aspects of Stability in Microgrids. *IEEE Transactions on Power Systems*, 28(3):3243–3252, aug 2013.

[120] Alexander Micallef, Maurice Apap, Cyril Spiteri-Staines, Josep M. Guerrero, and Juan C. Vasquez. Reactive power sharing and voltage harmonic distortion compensation of droop controlled single phase islanded microgrids. *IEEE Transactions on Smart Grid*, 5(3):1149–1158, 2014.

[121] Qobad Shafiee, Josep M. Guerrero, and Juan C. Vasquez. Distributed Secondary Control for Islanded MicroGrids - A Novel Approach. *IEEE Transactions on Power Electronics*, 29(2):1018–1031, 2014.

[122] Qobad Shafiee, Vahidreza Nasirian, Josep M Guerrero, Frank L Lewis, and Ali Davoudi. Team-oriented adaptive droop control for autonomous AC microgrids. In Press IEEE, editor, *Proceedings, IECON 2014 - 40th Annual Conference of the IEEE Industrial Electronics Society*, pages 1861–1867, 2014.

[123] Johannes Schiffer, Romeo Ortega, Alessandro Astolfi, Jörg Raisch, and Tevfik Sezi. Conditions for stability of droop-controlled inverter-based microgrids. *Automatica*, 50(10):2457–2469, oct 2014.

[124] Salvatore D'Arco, Jon Are Suul, and Olav Fosso. Automatic tuning of cascaded controllers for power converters using eigenvalue parametric sensitivities. *IEEE Transactions on Industry Applications*, 9994(c):1–1, 2014.

[125] John W Simpson-porco, Florian Dörfler, and Francesco Bullo. Synchronization and power sharing for droop-controlled inverters in islanded microgrids. *Automatica*, 49(9):2603–2611, 2013.

[126] Nathan Ainsworth and Santiago Grijalva. A structure-preserving model and sufficient condition for frequency synchronization of lossless droop inverter-based AC networks. *IEEE Transactions on Power Systems*, 28(4):4310–4319, 2013.

[127] Florian Dörfler and Francesco Bullo. Synchronization and Transient Stability in Power Networks and Non-Uniform Kuramoto Oscillators. *SIAM Journal on Control and Optimization*, 50(3):1616–1642, oct 2012.

[128] Johannes Schiffer, Romeo Ortega, and Alessandro Astolfi. Stability of synchronized motions of inverter-based microgrids under droop control. (2002), 2013.

[129] Dirk Aeyels and Jonathan a. Rogge. Existence of Partial Entrainment and Stability of Phase Locking Behavior of Coupled Oscillators. *Progress of Theoretical Physics*, 112(6):921–942, 2004.

[130] Johannes Schiffer, J; Goldin, Jörg Raisch, and T Sezi. Synchronization of droop-controlled microgrids with distributed rotational and electronic generation. In *Proc. 52nd IEEE CDC*, pages 2334–2339, Florence, Italy, 2013.

[131] BB Brian B Johnson, SV Sairaj V Dhople, Abdullah O Hamadeh, and Philip T Krein. Synchronization of parallel single-phase inverters with virtual oscillator control. *IEEE Transactions on Power Electronics*, pages 1–14, 2014.

[132] Mohit Sinha, Florian Dorfler, Brian B. Johnson, and Sairaj V. Dhople. Uncovering droop control laws embedded within the nonlinear dynamics of van der Pol oscillators. *IEEE Transactions on Control of Network Systems*, PP(99):1–12, 2015.

[133] Philip J Hart, Robert H. Lasseter, and T. M. Jahns. Reduced-Order Harmonic Modeling and Analysis of Droop-Controlled Distributed Generation Networks. In *Power Electronics for Distributed Generation Systems (PEDG), 2016 IEEE 7th International Symposium on*, pages 1–9, 2016.

[134] G Denis, T Prevost, P Panciatici, X Kestelyn, F Colas, and X Guillaud. Review on potential strategies for transmission grid operations based on power electronics interfaced voltage sources. In *2015 IEEE Power & Energy Society General Meeting*, pages 1–5. IEEE, jul 2015.

[135] Andrew D. Paquette. *Power Quality and Inverter-Generator Interactions in Microgrids Power Quality and Inverter-Generator Interactions in Microgrids*. PhD thesis, 2014.

[136] F De Bosio, M Pastorelli, and F D Freijedo. Enhanced current and voltage regulators for stand-alone applications. pages 1–6, 2016.

[137] Gauthier Delille. *Contribution du Stockage à la Gestion Avancée des Systèmes Électriques, Approches Organisationnelles et Technico-économiques dans les Réseaux de Distribution.* PhD thesis, ÉCOLE CENTRALE DE LILLE, 2010.

[138] Kamram Jalili and Steffen Bernet. Design of LCL filters of active-front-end two-level voltage-source converters. *IEEE Transactions on Industrial Electronics*, 56(5):1674–1689, 2009.

[139] Milan Prodanovic and Timothy C. Green. Control and Filter Design of Three-Phase Inverters for High Power Quality Grid Connection. 18(1):373–380, 2003.

[140] Khaled H. Ahmed, S J Finney, and B W Williams. Passive filter design for three phase inverter interfacing in distributed generation. In *2007 Compatibility in Power Electronics*, pages 1–9, Gdansk, Poland, 2007.

[141] Remus Beres, Xiongfei Wang, Frede Blaabjerg, Claus Leth Bak, and Marco Liserre. A review of passive filters for grid-connected voltage source converters. In *IEEE Applied Power Electronics Conference and Exposition - APEC 2014*, pages 2208–2215, 2014.

[142] Khaled Mohammad Alawasa, Yasser Abdel Rady Ibrahim Mohamed, and Wilsun Xu. Active mitigation of subsynchronous interactions between PWM voltage-source converters and power networks. *IEEE Transactions on Power Electronics*, 29(1):121–134, 2014.

[143] Marco Liserre, Frede Blaabjerg, and Steffan Hansen. Design and Control of an LCL -Filter-Based Three-Phase Active Rectifier. *IEEE Transactions on Industry Applications*, 41(5):1281–1291, 2005.

[144] a a Rockhill, Marco Liserre, Remus Teodorescu, and Pedro Rodriguez. Grid Filter Design for a Multi-Megawatt Medium-Voltage Voltage Source Inverter. *I E E E Transactions on Industrial Electronics*, 58(4):1205–1217, 2011.

[145] Pierre Rault. *Modélisation Dynamique et Commande des Réseaux à Courant Continu Multi-Terminaux Haute Tension.* PhD thesis, Phd Thesis, Ecole centrale de Lille, 2014.

[146] Yun Wei Li, D. Mahinda Vilathgamuwa, Poh Chiang Loh, Three-phase Three-wire Microgrid Applications, Senior Student Member, A Control, and Shunt Inverter. A grid-interfacing power quality compensator for three-phase three-wire microgrid applications. *IEEE Transactions on Power Electronics*, 21(4):1021–1031, 2006.

[147] Jean-paul Hautier, Jean Faucher, and Jean-pierre Caron. Le Graphe Informationnel Causal , Un outil pour analyser, comprendre, représenter. In *Journées 3EI*, pages 1–18, 1999.

[148] Peng Li. *Formalisme pour la Supervision des Systèmes Hybrides Multi-Sources de Générateurs d'Energie Répartie : Application à la Gestion d'un Micro Réseau.* PhD thesis, Phd Thesis, Ecole centrale de Lille, 2009.

[149] Fouad Salha. *Microréseaux îlotables: étude et coordination des protections des générateurs et du réseau.* PhD thesis, Phd Thesis, Ecole Centrale de Lille, 2010.

[150] Salvatore D'Arco, Jon Are Suul, and OB Olav B. Fosso. Small-signal modelling and parametric sensitivity of a Virtual Synchronous Machine. *Power Systems Computation ...*, 2014.

[151] M.P. Kazmierkowski and L. Malesani. Current control techniques for three-phase voltage-source PWM converters: a survey. *IEEE Transactions on Industrial Electronics*, 45(5):691–703, 1998.

[152] Xiongfei Wang, Frede Blaabjerg, Marco Liserre, Zhe Chen, Jinwei He, and Yun Wei Li. An active damper for stabilizing power-electronics-based AC systems. *IEEE Transactions on Power Electronics*, 29(7):3318–3329, 2014.

[153] Lennart Harnefors, Xiongfei Wang, Alejandro G. Yepes, and Frede Blaabjerg. Passivity-Based Stability Assessment of Grid-Connected VSCs—An Overview. *Ieee Journal of Emerging and Selected Topics in Power Electronics*, 4(1):116–125, mar 2016.

[154] Giuseppe Guidi, Salvatore D'Arco, J. Are Suul, Giuseppe Guidi, and J. Are Suul. Embedded limitations and protections for droop-based control schemes with cascaded loops in the synchronous reference frame. In *IPEC-Hiroshima 2014 - ECCE-ASIA*, pages 1544–1551, 2014.

[155] Iman Sadeghkhani, Mohamad Esmail Hamedani Golshan, Josep M. Guerrero, and Ali Mehrizi-sani. A Current Limiting Strategy to Improve Fault Ride-Through of Inverter Interfaced Autonomous Microgrids. *IEEE Transactions on Smart Grid*, 2016.

[156] G Denis, T Prevost, P Panciatici, X Kestelyn, F Colas, and X Guillaud. Improving robustness against grid stiffness, with internal control of an AC voltage-controlled VSC. In *Proc. 2016 IEEE Power and Energy Society General Meeting (PESGM), Boston, MA, Jul.*, pages 1–5, 2016.

[157] R D Middlebrook. Input filter considerations in design and application of switching regulators. In *IEEE Ind. Appl. Soc. Annu. Meeting*, pages pp. 366–382, 1976.

[158] Jian Sun. Impedance-based stability criterion for grid-connected inverters. *Power Electronics, IEEE Transactions on*, 26(11):3075–3076, 2011.

[159] Xiongfei Wang, Frede Blaabjerg, and Weimin Wu. Modeling and Analysis of Harmonic Stability in an AC Power-Electronics-Based Power System. *IEEE Transactions on Power Electronics*, 29(12):1–1, 2014.

[160] Maher A. Azzouz and Ehab F. El-Saadany. Multivariable DG Impedance Modeling and Reshaping for Impedance Stabilization of Active Distribution Networks. *IEEE Transactions on Smart Grid*, PP(99), 2016.

[161] Amr Ahmed A Radwan and Yasser Abdel Rady Ibrahim Mohamed. Modeling, analysis, and stabilization of converter-fed AC microgrids with high penetration of converter-interfaced loads. *IEEE Transactions on Smart Grid*, 3(3):1213–1225, 2012.

[162] Xiongfei Wang, Frede Blaabjerg, and Poh Chiang Loh. Proportional derivative based stabilizing control of paralleled grid converters with cables in renwable power plants. *2014 IEEE Energy Conversion Congress and Exposition, ECCE 2014*, pages 4917–4924, 2014.

[163] L. Harnefors. Modeling of Three-Phase Dynamic Systems Using Complex Transfer Functions and Transfer Matrices. *IEEE Transactions on Industrial Electronics*, 54(4):2239–2248, 2007.

[164] Fernando Briz del Blanco, Michael W. Degner, and Robert D. Lorenz. Dynamic analysis of current regulators for AC motors using complex vectors. *IEEE Transactions on Industry Applications*, 35(6):1424–1432, 1999.

[165] G. Denis, Thibault Prevost, Xavier Kestelyn, Frederic Colas, Patrick Panciatici, and Xavier Guillaud. Internal control stability assessment method of a VSC-based transmission grid. In *2016 18th European Conference on Power Electronics and Applications (EPE'16 ECCE Europe)*, pages 1–10. IEEE, sep 2016.

[166] Yong Tao, Quanwei Liu, Yan Deng, Xunhao Liu, and Xiangning He. Analysis and mitigation of inverter output impedance impacts for distributed energy resource interface. *IEEE Transactions on Power Electronics*, 30(7):3563–3576, jul 2015.

[167] Mauricio Cespedes and Jian Sun. Impedance shaping of three-phase grid-parallel voltage-source converters. *Conference Proceedings - IEEE Applied Power Electronics Conference and Exposition - APEC*, pages 754–760, feb 2012.

[168] Lennart Harnefors, Alejandro G. Yepes, Ana Vidal, and Jesús Doval-Gandoy. Passivity-based controller design of grid-connected VSCs for prevention of electrical resonance instability. *IEEE Transactions on Industrial Electronics*, 62(2):702–710, 2015.

[169] Maher Abdelkhalek Azzouz and Ehab F. El-Saadany. Multivariable Grid Admittance Identification for Impedance Stabilization of Active Distribution Networks. *IEEE Transactions on Smart Grid*, 8(3):1116–1128, may 2017.

[170] Jorge Perez, Santiago Cobreces, Robert Grino, and Francisco Javier Rodriguez Sanchez. H∞ current controller for input admittance shaping of VSC-based grid applications. *IEEE Transactions on Power Electronics*, 32(4):3180–3191, 2017.

[171] Huanhai Xin, Linbin Huang, Leiqi Zhang, Zhen Wang, and Jiabing Hu. Synchronous instability mechanism of P-f droop-controlled voltage source converter caused by current saturation. *IEEE Transactions on Power Systems*, pages 1–2, feb 2016.

[172] Xiongfei Wang, Yun Wei Li, Frede Blaabjerg, and Poh Chiang Loh. Virtual impedance based control for voltage source and current source converters. *IEEE Transactions on Power Electronics*, 30(12):7019–7037, dec 2015.

[173] P. Anderson and A. Fouad. *Power System Control and Stability*. J.Wiley & Sons, 2002.

Les nouvelles stratégies de contrôle d'onduleurs pour un système électrique 100% interfacé par électronique de puissance

Résumé Dans un contexte de développement des énergies renouvelables et des liaisons HVDC dans les systèmes électriques, les travaux présentés s'attachent au fonctionnement technique de tels systèmes. La génération éolienne, photovoltaïque et les liaisons HVDC sont interfacées par dispositifs d'électronique de puissance au réseau de transport électrique. Dès lors, serait-il envisageable d'alimenter la demande électrique uniquement via des sources électriques interfacées par des convertisseurs statiques? Le pilotage du système électrique par électronique de puissance constitue un changement radical du fonctionnement dynamique des réseaux. La traditionnelle stratégie de commande « grid-following » des onduleurs a montré ses limites lorsque la pénétration de ces dispositifs devient importante. Elle doit être révisée au profit de stratégies dîtes « parallel grid-forming ». Dans cette thèse, les besoins fondamentaux du système électrique sont d'abord analysés pour définir les exigences de la stratégie « parallel grid-forming », ainsi que les défis associés. Selon ces spécifications, une méthode de synchronisation de sources « grid-forming » est ensuite proposée ainsi qu'un contrôle de tension, adapté aux limitations physiques des convertisseurs de tension PWM. La stabilité de la solution est discutée pour différentes configuration de réseau. Enfin, une stratégie de limitation du courant a été spécifiquement développée pour palier la sensibilité des VSC aux surcourants, lors d'évènements réseaux éprouvant. Les idées développées sur un convertisseur unique sont appliquées à petits réseaux afin de tirer des interprétations physiques à partir de simulations temporelles.

Mots-clés : Convertisseur de tension, Contrôle distribué, Réseau de transport électrique, Gestion des transitoires.

From grid-following to grid-forming: The new strategy to build 100 % power-electronics interfaced transmission system with enhanced transient behavior

Summary In the context of renewable energy and HVDC links development in power systems, the present work concerns the technical operations of such systems. As wind power, solar photovoltaics and HVDC links are interfaced to the transmission grid with power-electronics, can the system be operated in the extreme case where the load is fed only through static converters? Driving a power system only based on power electronic interfaced generation is a tremendous change of the power system paradigm that must be clearly understood by transmission grid operators. The traditional "grid-feeding" control strategy of inverters exhibits a stability limit when their proportion becomes too important. The inverter control strategy must be turned into a "parallel grid-forming" strategy. This thesis first analyses the power system needs, proposes the requirements for "parallel grid-forming" converters and describes the associated challenges. Accordingly, the thesis gives a method for designing a stable autonomous synchronization controls so that grid-forming sources can operate in parallel with a good level of reliability. Then, a method is proposed to design a voltage control for a grid-forming PWM source taking into account the limited dynamic of powerful converters. The robustness of the solution is discussed for different configuration of the grid topology. A current limiting strategy is presented to solve the current sensitivity issue of grid-forming converters, subject to different stressing events of the transmission grid. The ideas developed on a single converter are then applied on small grids with a limited number of converters to allow a physical interpretation on the simulation results.

Keywords: Converters, Distributed control, Overcurrent protection, Power system dynamic stability, Power system transients, Transmission line, Voltage control